BEHAVIOR OF CTT-NODES IN REINFORCED CONCRETE STRUT-AND-TIE MODELS

APPROVED:

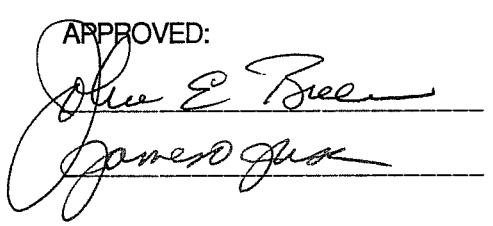

BEHAVIOR OF CTT-NODES IN REINFORCED CONCRETE STRUT-AND-TIE MODELS

BY

ROBERT B. ANDERSON, B.S.

THESIS

Presented to the Faculty of the Graduate School of

The University of Texas at Austin

in Partial Fulfillment

of the Requirements

for the Degree of

MASTER OF SCIENCE IN ENGINEERING

THE UNIVERSITY OF TEXAS AT AUSTIN

December, 1988

ACKNOWLEDGEMENTS

The research reported herein was conducted at the Phil M. Ferguson Structural Engineering Laboratory of the The University of Texas at Austin. Financial support for the study was provided by the Texas State Department of Highways and Public Transportation under Project 3-4-87-1127.

This project was supervised jointly by Drs. John E. Breen, James O. Jirsa, and Michael E. Kreger. I would like to thank these faculty members for their guidance throughout the project. I feel privileged to have been able to gain from their advice and encouragement. The efforts of Dr. Breen as the principal director of this study and Dr. Jirsa who served on the thesis committee are appreciated.

The staff of the Phil M. Ferguson Structural Engineering Laboratory: Pat Ball, Sharon Cunningham, Maxine DeButts, Jean Gehrke, Laurie Golding, Robert Gracia, Wayne Little, Dick Marshall, Irene Saathoff, Blake Stasney, and Alec Tahmassebi are acknowledged for their valuable assistance.

I wish to thank Erico Products, Incorporated of Cleveland, Ohio for supplying the LENTON® mechanical connectors which were an essential part of the test setup.

The assistance, and especially the friendship, of my fellow graduate students is recognized and greatly appreciated. A personal thanks goes to Dave Barton who coauthored Chapter 2 and helped in preparing and testing several specimens. Sincere thanks are also extended to Richard Beaupre and Willy Ramirez. I would like to acknowledge the work of Olivier Burdet who was kind enough to perform the finite element analysis of the dapped beam. I am

grateful to John Myers, Andreas Savvides, and Mike Hebert who served as research assistants and were instrumental in the successful completion of this project.

Lastly, special thanks are due to my wife Deb and the members of both our families. I am always grateful for their continued interest and moral support.

TABLE OF CONTENTS

Chapter 1 Introduction

1.1 General....1
1.2 Objectives and Scope of the Study....6

Chapter 2 The Strut-and-Tie Model

2.1 Introduction....9
2.2 Basic Principles....10
2.2.1 Background and Assumptions....10
2.2.2 Types of Strut-and-Tie Models....12
2.2.3 Design Procedure....16
2.3 Elements of the Strut-and-Tie Model....18
2.3.1 Ties....18
2.3.2 Struts....19
2.3.3 Nodes....20
2.4 Effective Concrete Strength Limits....35
2.5 Modelling....42
2.5.1 General Guidelines....42
2.5.2 Model Development....46
2.6 Summary....49

Chapter 3 Test Program

3.1 Introduction....52
3.2 Specimen Identification....54
3.3 Specimen Design....55
3.4 Specimen Details....59
3.5 Materials....63
3.5.1 Concrete....63
3.5.2 Reinforcing Steel....70
3.5.3 Mechanical Connectors....73
3.6 Instrumentation....74
3.6.1 Strain Gages....74
3.6.2 Hydraulic Force and Pressure Measurements....81
3.6.3 Linear Potentiometers....83
3.6.4 Data Acquisition System....83
3.7 Specimen Fabrication....85
3.8 Test Setup....89
3.8.1 Concrete Reaction Block....89
3.8.2 Loading and Reaction System....92
3.9 Preparation for Testing....97
3.9.1 Positioning the Specimen....97

3.9.2 Equalization of Reinforcement Stresses 101
3.10 Testing Procedure 103
3.11 Data Reduction and Interpretation 108
3.12 Summary 108

Chapter 4 Test Results

4.1 Introduction 110
4.2 Interpretation of Individual Test Results 110
4.2.1 General 110
4.2.2 Comprehensive Interpretation of Test Results for Specimen HFNC 118
4.3 Specimen Behavior 127
4.3.1 General 127
4.3.2 Prototype Beam Specimen 131
4.3.3 Specimen HFSR-A 137
4.3.4 Specimen HFSR-B 139
4.3.5 Specimen LFSR 141
4.3.6 Specimen LFNC 143
4.3.7 Specimen HHSR 146
4.3.8 Specimen LHSR 146
4.3.9 Specimen HFSB 149
4.3.10 Specimen LFAC 151
4.4 Comparisons of Specimen Behavior 156
4.4.1 Crack Patterns 158
4.4.2 Comparison of Strains 158
4.4.3 Percentage of Applied Tensile Force at Gage Locations 165
4.4.4 Validity of Node Tests 169
4.5 Summary 171

Chapter 5 Evaluation of Strut-and-Tie Model

5.1 Introduction 173
5.2 Dimensions and Configuration of the Compression Strut 174
5.2.1 Stress Trajectories and Actual Crack Patterns 174
5.2.2 Estimating the Geometry of the Compressive Stress Fields 178
5.3 Comparison of Test Results with Effective Concrete Strength Limits 183
5.4 Comparison of Test Results with ACI and AASHTO Provisions for Development 187
5.4.1 General 187
5.4.2 Background of ACI and AASHTO Design Provisions for Development 189

5.4.3 Evaluation of Node Specimen Behavior 192
5.5 Design Guidance for CTT-Nodes 199
5.5.1 Classifying Tie Anchorage Details 199
5.5.2 Design Checks for Ties Anchored Through Development Length 205
5.6 Design Implications 213
5.6.1 Ramifications of Major Findings 213
5.6.2 Practical Considerations 216

Chapter 6 Summary and Conclusions

6.1 Summary 221
6.2 Conclusions 222
6.3 Needs for Further Research 225

References 227

Appendix

A.1 Supplemental Crack Patterns 230
A.2 Supplemental Strain Graphs for Transverse Reinforcement 233
A.3 Supplemental Strain Graphs for Longitudinal Reinforcement 241
A.4 Supplemental Bar Graphs Showing Percentage of Load at Gage Locations 250

LIST OF TABLES

Table		Page
2.1	Effective Concrete Strength Limits Proposed by Schlaich et al. (1)	43
2.2	Effective Concrete Strength Limits Proposed by MacGregor (14)	43
3.1	Summary of Test Specimens	65
3.2	Concrete Mix Design for Specimen HFSR-A	66
3.3	Concrete Mix Design for Specimen LFSR, LHSR, and LFNC	67
3.4	Concrete Mix Design for Specimen HFSR-B, HHSR, HFNC, and HFSB	68
3.5	Concrete Mix Design for Specimen LFAC	69
3.6	Load Stages for Specimen LFAC	107
4.1	Summary of Node Specimen Test Results	129
4.2	Crack Widths	130
4.3	Comparison of Percentages of Applied Force at Transverse Gage Locations	167
4.4	Comparison of Percentages of Applied Force at Longitudinal Gage Locations	168
5.1	Comparison of Node Test Results with Efficiency Factors (υ) from Selected Authors Based on Available Bearing Surface	185
5.2	Comparison of Node Test Results with Efficiency Factors (υ) from Selected Authors Based on Estimated Strut Width	185
5.3	Nominal Development Lengths for Unconfined Specimens HFNC and LFNC	196
5.4	Nominal Development Lengths for Unconfined Specimen LFAC	196
5.5	Comparisons Between the Predicted Capacity of Tie Based Upon Development Length Measured from Boundary of Compression Field	200

LIST OF FIGURES

Figure		Page
1.1	"Details" that may Exist in Actual Structures	4
1.2	Truss Analogy	4
2.1	Examples of Strut-and-Tie Models (From Ref. 1)	11
2.2	Application of Strut and Tie Model to Simple Beam	14
2.3	Examples of B- and D-Regions (From Refs. 1 and 14)	15
2.4	Compression Fields Radiating Outward from Concentrated Loads (D-Regions)	17
2.5	Strut and Tie Model Design Procedure	17
2.6	Basic Types of Struts (Adapted from Ref. 1)	21
2.7	Fan Shaped Compression Stress Field at Beam Support	21
2.8	Bottle Shaped Struts (Adapted from Ref. 1)	22
2.9	Singular and Smeared Nodes (Adapted from Ref. 1)	24
2.10	Examples of Singular Nodes	24
2.11	CCC-Node, Hydrostatic State of Stress (Adapted from Ref. 15)	27
2.12	Bottle Shaped Struts Created by Hydrostatically Dimensioned Node	27
2.13	Constricting Struts Producing Hydrostatic Stress State at the Nodes	28
2.14	Idealization of Tie Forces Within Node	28
2.15	Effects of Decreasing Tie Width (Adapted from Ref. 1)	29
2.16	Effect of Tension Tie Location on Size of Compression Strut (From Ref. 14)	31
2.17	Tie Width as Defined by Mechanical Reinforcement Ratio (Ref. 15)	31

Figure Page

2.18 Proposals for Dimensioning CTT-Nodes with Multiple Layers of Reinforcement (Adapted from Ref. 1) 32

2.19 CTT-Node Compressive Force Distribution in Flanged Member 34

2.20 Effect of CCT-Node Anchorage Detail 34

2.21 Reinforcement in Bottle Shaped Strut 36

2.22 Anchorage of Reinforcement in CTT-Nodes 37

2.23 Anchoring Ties at the Node 37

2.24 Relationship Between Efficiency Factor and Concrete Strength 39

2.25 Strains for Cracked Web (Adapted from Ref. 12) 41

2.26 Relationship Between Efficiency Factor and Strut Angle 41

2.27 Allowable Stresses in Bottle Shaped Struts (From Ref. 1) 44

2.28 Load Path Method for Estimating Stress Paths (Adapted from Ref. 1) 48

2.29 Optimizing the Model (Adapted from Refs. 1 and 14) 50

3.1 Scope of Elemental Study 56

3.2 Determination of Node Boundaries 58

3.3 Geometry and Placement of Steel for Specimens HFSR-A, HFSR-B, and LFSR 60

3.4 Bearing Surfaces Used for Isolated Tests 60

3.5 Details to Provide and Minimize Confinement 62

3.6 Geometry and Placement of Steel for Specimen HFSB 64

3.7 Comparison of Specimen Strut Angles 64

3.8 Geometry and Placement of Steel for Specimen LFAC 65

3.9 Concrete Strength vs. Time for Specimen HFSR-A 66

Figure		Page
3.10	Concrete Strength vs. Time for Specimens LFSR, LHSR, and LFNC	67
3.11	Concrete Strength vs. Time for Specimens HFSR-B, HHSR, HFNC, HFSB	68
3.12	Concrete Strength vs. Time for Specimen LFAC	69
3.13	Stress-Strain Curve for #3-Grade 60 Reinforcement	71
3.14	Stress-Strain Curve for #5-Grade 60 Reinforcement	71
3.15	Stress-Strain Curve for #5-Grade 40 Reinforcement	72
3.16	Mechanical Connectors with Adjusting Nuts for #3 and #5 Bars	75
3.17	Interior Gage Locations for Specimen HFSR-A	76
3.18	Interior Gage Locations for Specimen HFSR-B, HHSR, LFSR, LHSR, LFAC	77
3.19	Interior Gage Locations for Specimen HFSB	78
3.20	Interior Gage Locations for Specimen HFNC and LFNC	79
3.21	Calibration Plot for Horizontal Pressure Transducer	82
3.22	Calibration Plot for Vertical Pressure Transducer	82
3.23	Hydraulic Load Application and Monitoring System	84
3.24	Location of Linear Potentiometers	87
3.25	Assembled Formwork and Reinforcing Cage	87
3.26	Placement and Consolidation of Concrete	88
3.27	Elevation View of Concrete Reaction Block	90
3.28	Reinforcement of Extension Block	93
3.29	Reinforcement of Base Block	93
3.30	Elevation View of Test Setup	95

Figure		Page
3.31	Plan View of Test Setup	96
3.32	View of Actual Test Setup	98
3.33	Roller Support for Horizontal Bearing Beam and Ram	98
3.34	Positioning of Specimen	100
3.35	Hydrostone Grouting Procedure	102
3.36	Specimen Angle Clamp	102
3.37	Loading Forces at Specimen LFAC's Ultimate Capacity	105
4.1	Node Specimen Force Designation	114
4.2	External Transverse Bar Strains for Specimen HFSB	114
4.3	External Longitudinal Bar Strains for Specimen HFSB	115
4.4	Average External Longitudinal Bar Strains for Specimen HFSB	115
4.5	Crack Patterns for Specimen HFNC	119
4.6	Specimen HFNC at Failure (South and End Faces)	120
4.7	Specimen HFNC-Reinforcement Strain Data for Individual Transverse Gage Locations	122
4.8	Tensile Strains Resulting from Slip at 90° Bend	122
4.9	Average Strain at Transverse Locations for Specimen HFNC	125
4.10	Average Strain at Longitudinal Locations for Specimen HFNC	125
4.11	Specimen HFNC-Percentage of Applied Force at Transverse Locations	128
4.12	Specimen HFNC-Percentage of Applied Force at Longitudinal Locations	128
4.13	Prototype Beam Specimen Near Failure	133
4.14	Average Strain at Longitudinal Locations for Prototype Beam Specimen	135

Figure		Page
4.15	Average Strain at Transverse Locations for Prototype Beam Specimen	135
4.16	Prototype Beam Specimen-Percentage of Applied Force at Transverse Locations	136
4.17	Prototype Beam Specimen-Percentage of Applied Force at Longitudinal Locations	136
4.18	Crack Patterns for Specimen HFSR-A	138
4.19	Average Strain at Transverse Locations for Specimen HFSR-A	138
4.20	Crack Patterns for Specimen HFSR-B	140
4.21	Specimen LFSR-Development Failure of Transverse Reinforcement (North and Top Faces)	142
4.22	Crack Patterns for Specimen LFSR	144
4.23	Specimen LFSR-Reinforcement Strain Data for Individual Transverse Gage Locations	144
4.24	Specimen LFNC-Cover Splitting Failure (North and End Faces)	145
4.25	Crack Patterns for Specimen LFNC	147
4.26	Crack Patterns for Specimen LFNC	147
4.27	Average Strain at Transverse Locations for Specimen HHSR	148
4.28	Average Strain at Longitudinal Locations for Specimen HHSR	148
4.29	Specimen LHSR-Compression Strut Crushing Failure (North and South Faces)	150
4.30	Crack Patterns for Specimen LHSR	152
4.31	Average Strain at Longitudinal Locations for Specimen HFSB	152
4.32	Effect of Diagonal Tension Crack Upon Reinforcement Development Length	154
4.33	Crack Patterns for Specimen LFAC	154

Figure		Page
4.34	Specimen LFAC-Development Failure of Longitudinal Reinforcement (North and South Faces)	155
4.35	Average Strain at Transverse Locations for Specimen LFAC	157
4.36	Specimen LFAC-Reinforcement Strain Data for Individual Longitudinal Gage Locations	157
4.37	Reoccurring Crack Pattern and Stress Field for Specimens with 45°-10.6 in. Compression Strut	159
4.38	Reoccurring Crack Pattern and Stress Field for Specimens with 45°-4.0 in. Compression Strut	159
4.39	Crack Pattern and Stress Field for Specimen LFAC with 30°-10.6 in. Compression Strut	159
4.40	Comparison Strain Graph for Location TA	161
4.41	Comparison Strain Graph for Location TB	161
4.42	Comparison Strain Graph for Location TC	162
4.43	Comparison Strain Graph for Location TD	162
4.44	Comparison Strain Graph for Location LA	163
4.45	Comparison Strain Graph for Location LB	163
4.46	Comparison Strain Graph for Location LC	164
4.47	Comparison Strain Graph for Location CA	164
4.48	Comparison Strain Graph for Location CB	166
4.49	Distribution of Compression Strut Force	166
4.50	Crack Pattern Comparison of Specimen HFSR-A and Prototype Beam Specimen	170
4.51	Confining Forces Produced by Test Setup	170
5.1	Comparisons of Design Rationale Used for Nodal Region of Strut-and-Tie Model and Joint of Steel Truss	175

Figure Page

5.2 Principal Stress Vectors and Elastic Stress Trajectories for Prototype Beam and CTT-Node Specimens....177

5.3 Compression Strut Intersecting CTT-Node in Prototype Beam Specimen....179

5.4 Estimated Physical Geometries of Compressive Stress Fields in the Several Types of Node Specimens....182

5.5 Development Length for Straight and Hooked Bars....188

5.6 Comparisons of Transverse Reinforcement Nominal Development Lengths, Cracking Patterns, and Compressive Stress Fields for Specimens HFNC and LFNC....197

5.7 Comparisons of Transverse Reinforcement Nominal Development Lengths, Cracking Patterns, and Compressive Stress Fields for Specimen LFAC....197

5.8 Continuous Reinforcement Details for Anchoring Tensile Ties in CTT-Node....202

5.9 Defining the Effective Width of Continuous Reinforcement Tie Anchors....202

5.10 Design Complications Resulting from Uneven Placements of Reinforcement....203

5.11 Undesirable Effects Resulting from the Use of Continuous Reinforcement Details in Wide Members....203

5.12 Force Transfer in CTT-Node with Simple Reinforcement Layout....206

5.13 Positive and Development Length Anchorage Details....206

5.14 Design Checks for Ties Anchored with Single and Multiple Layers of Reinforcement....209

5.15 Bond Transfer Mechanism (From Ref. 29)....210

5.16 Consequence of Reinforcement Spacing in Dapped Beam....212

5.17 Flowchart Illustrating Design Steps for CTT-Node....214

Figure Page

5.18 Detailing the CTT-Node to Provide Three-Dimensional Confinement 218

5.19 Placement of Reinforcement and Corresponding Strut-and-Tie Model and Termination Point of Straight Bars 220

5.20 Force Transfer Mechanisms at Intersection of Straight Bar with U Reinforcement 220

NOTATION

The following symbols are used in this report. Other symbols which are not listed below are defined in the text where they are used.

A_s	Area of steel reinforcement
A_b	Area of steel reinforcing bar
b	Width of beam
b_w	Width of beam web
C	Compressive force
d_b	Diameter of reinforcement
E_s	Modulus of elasticity of steel
f_{ce}	Effective Concrete strength
f'c	Concrete cylinder strength
f_s	Maximum bar stress
f_y	Yield strength of reinforcement
h	Depth of beam
l_d	Development length for straight deformed bar
l_{dn}	Nominal development length for straight deformed bar
l_{dh}	Development length for standard hook in tension
l_{dhn}	Nominal development length for standard hook in tension
T	Tensile force
α	Strut angle
ε_1	Principal tensile strain normal to the principal compressive stress

ε_x Principal tensile strain parallel to beam's longitudinal axis

ϕ Strength reduction factor

υ Concrete efficiency factor

ω Nondimensional mechanical reinforcement ratio

ξ Constant for development of standard hook

ψ Development length modification factor

CHAPTER 1

INTRODUCTION

1.1 General

The arrival of structural concrete as a dominant structural material in engineered construction is apparent. Concrete construction is marked by increasingly flexible applications. Technological advances have made it possible to combine precast and/or cast-in-place concrete with conventionally reinforced, pretensioned, and/or post-tensioned elements within a single structure. The term "structural concrete" is used to address the wide spectrum of reinforced and prestressed concrete ranging from elements with only nonstressed or "passive" reinforcement to elements with all prestressed or "active" reinforcement. Composite construction with structural steel members is used where economically beneficial. The industry trend is toward higher strength materials, especially higher strength concrete. This growing diversity has added to the complexity of structural design.

Design is far more than analysis to determine member forces and proportioning the members to obtain safe stresses. It requires a certain amount of "detailing" which affects the overall safety, economy, and constructability of the structure. In concrete structures, detailing would encompass: 1) preparation of drawings showing the size and location of structural elements and reinforcement; and 2) specification of bar details such as anchorage provisions and location of splices and overlaps. Detailing should not be confused with the "details" of a structure. Details would include

statical or geometrical discontinuities such as point loads or frame corners, corbels, recesses, holes, and other openings (1). Examples of details which may occur in bridge and building construction are shown in Fig. 1.1. The structural engineer must be concerned with the "detailing" of reinforcement whether he is designing the "details" or other parts of the structure. Details and detailing are equally important in monolithic construction and "mixed" structural systems because they are essential to overall structural integrity.

Neither the ACI Building Code (2) nor the generally similar provisions of the AASHTO Bridge Specifications (3) address detailing of reinforcement extensively or uniformly. Provisions governing development length, lap splices, bar spacing, and reinforcement details such as standard hooks and bends are included. Detailing of transverse or confining reinforcement in members subjected to axial forces or shear is described by general guidelines. Even though the codes offer no general method or philosophy, the designer is able to detail reinforcement in standard portions of structures expeditiously.

However, unusual or complex situations often present the designer with numerous difficulties. There is not a general methodology for "detailing". The ACI Code has some specific provisions for details such as brackets and corbels, anchorage zones, and joints in seismic frames. Additional guidance for design of details is found in documents published by the Prestressed Concrete Institute (4), the Post-Tensioned Concrete Institute (5), and the Concrete Reinforcing Steel Institute (6). Various ACI committees have also developed reports and standards covering details and

detailing. Most of these manuals and standards tend to be empirical in nature, focused on specific applications and lack a conceptual model to assist the designer. Thus, the recommendations are either extremely vague or extremely rigid and it is difficult to extend them to other applications. Empirical methods are inherently plagued with the problem of new design situations falling outside the envelope of empirical results. Empirical guidelines cannot be developed for the innumerable details that may arise. The highly specific "standard" details are sometimes based on rules of thumb without any underlying rationale or logic.

Truss models, because of their transparency and adaptability to many design situations, are seen as attractive alternatives to empirical approaches for detailing structural concrete. Truss models for shear design of reinforced concrete beams were introduced by Ritter (7) near the turn of the century. The procedure was later generalized by Mörsch (8). In truss models for shear, the reinforced concrete beam is represented by an analogous truss. A typical reinforcement scheme in a cracked reinforced concrete beam will mobilize "truss" action as shown in Fig. 1.2. The flexural concrete compression zone is thought of as the top chord of the truss while the tensile reinforcing forms the bottom chord. The top and bottom chords are connected by stirrups acting as vertical tension hangers and pieces of concrete between diagonal tension cracks acting as struts. Important fundamental work, incorporating truss models for reinforced concrete detail design, was carried out and popularized by Leonhardt (9). Various researchers, including Neilsen et al. (10), Lampert and Thürlimann (11), Mitchell and Collins

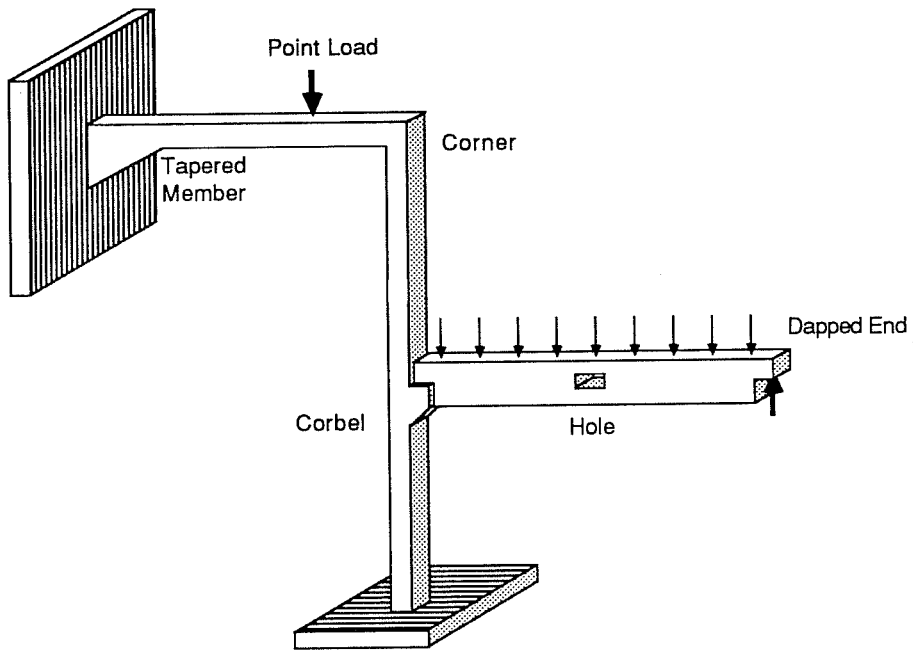

Fig. 1.1 "Details" that May Exist in Actual Structures

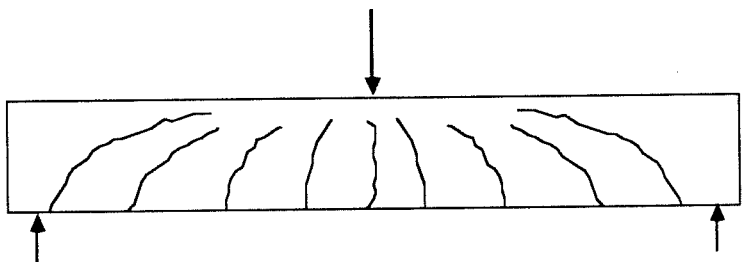

(a) Typical Cracks in Reinforced Concrete Beam

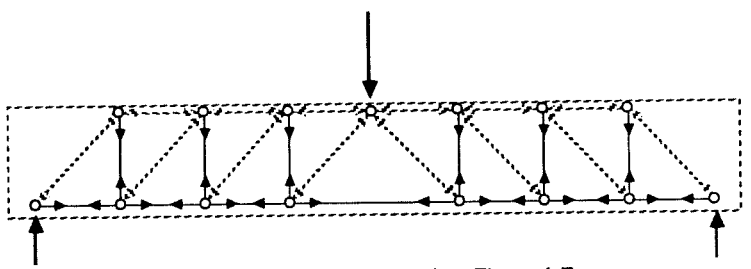

(b) Analogous Truss Representing Flow of Forces

Fig. 1.2 Truss Analogy

(12), and Ramirez (13), have worked to refine and expand the method so it is applicable to shear, torsion, and the interaction of these actions, as well as bending. Recently, MacGregor(14), Marti (15), and Schlaich, Schäfer, and Jennewein (1) have published refined methods for detailing structures using truss models. In a major contribution for English language readers Schlaich, et al. (1) have presented the "strut-and-tie" model as a generalization of previous truss models applicable to the entire structural concrete spectrum. The present study, following the proposal of Schlaich and his co-workers, identifies the strut-and-tie model as a unified design concept applicable to all portions of the structure. This terminology is used in lieu of the more specific truss model which is somewhat lacking in certain specific applications.

Because the strut-and-tie model is a conceptual model, it enables the designer to visualize the flow of forces within the structure. It enhances his understanding of member internal force paths, thus enabling him to design better structures.

Despite considerable recent progress, the strut-and-tie model is still highly conceptual and has not been subjected to comprehensive verification through tests. Empirical expressions developed for the failure criterion of cracked concrete struts are a necessary part of the model and have been widely discussed (10,12,13,16). Also, stress checks at the nodes require highly graphical procedures which are cumbersome during design. Some portions of the method have not been fully developed. Lack of consistent code provisions can allow the designer to make unreasonable assumptions

regarding the flow of forces and subsequent reinforcement detailing. Dimensioning of the strut and tie members and limiting of the strut and nodal concrete stresses must be better quantified before the method can be practically implemented.

1.2 Objectives and Scope of the Study

This study is part of a larger research program whose objective is to develop a comprehensive detailing guide for structural concrete based on refined strut-and-tie models. It is hoped the guide will help designers develop a clearer understanding of the functioning of reinforcement in a wide variety of details in concrete structures. It is envisioned that the designer will approach the detailing of a concrete member using the strut-and-tie model much as he would the detailing of a steel truss. After selecting a suitable truss to carry the applied loads for the given boundary conditions, the designer would analyze the truss for member forces. The truss members would then be proportioned to carry the indicated forces. Lastly, the designer would detail the connections at the nodes. Simple strut-and-tie models could be transparent to numerous design situations.

In the early stages of this study after reviewing the strut-and-tie model in current literature and trying to design members according to its philosophy, it became apparent that the existing state of knowledge was not sufficient for application of the model to complex detailing situations. Particularly troublesome were the nodes. Therefore, the scope of this study was limited to developing an in-depth understanding of an isolated node. The investigation focused on an elemental, but yet essential, part of the strut-

and-tie model. Physical tests were performed to enhance the understanding of the node.

Chapter 2 explains the basis for the strut-and-tie model used in detailing structural concrete. It was coauthored by Barton (17) and presents an overview of the proposals developed by various researchers. The chapter discusses general principles, components, and mechanics of the model. Also presented are brief discussions regarding concrete failure criterion and modelling techniques.

The isolated node test program, described in Chapter 3, studied the behavior of a node joining two tensile ties and one compression strut. This type of node was chosen because it was an often occurring critical node type, was one of the four principal node types referred to in the literature (1), and seemed readily explored with relatively simple tests. The study consisted of nine isolated node specimens. Variables included concrete strength, confinement, strut width, reinforcement anchorage details, and strut angle. The tests were complimentary to tests of full-sized, dapped beams which were part of the larger research program. In the isolated node test specimens, reinforcement patterns similar to those present in the nodes of the full-sized, dapped beams were used.

The results of the laboratory tests are summarized in Chapter 4. The data was analyzed and presented in an effort to understand the distribution and transfer of forces within the node. Comparisons with the full-sized, dapped beam are made. Factors influencing the behavior of the node are explained and quantified.

An evaluation of physical test results is presented in Chapter 5. In particular the study was aimed at providing information about: 1) effective physical dimensions of the node; 2) configuration of stress fields; 3) allowable concrete stresses; 4) detailing considerations; and 5) effects of strut angle change. Comparisons are made with existing theories in order to determine their accuracy. Lastly, the design implications of this research study are discussed.

Chapter 6 briefly summarizes the work of this study. Conclusions, recommendations, as well as, needs for further research are presented.

CHAPTER 2

STRUT-AND-TIE MODEL

2.1 Introduction

As alluded to in Chapter 1, the general practice in detailing of structural concrete has been based on experience, rules of thumb or highly specific "standard" details. Most of these methods do not incorporate conceptual models to assist the designer. The lack of a consistent, rational method for detailing may lead to problems when unique situations are encountered. Strut-and-tie models serve to provide a rational detailing method which may be applied to a variety of structural components and loading conditions.

In the strut-and-tie model, the actual stress distribution within a structure is idealized as a static force system consisting of the following basic elements:

1. Struts
2. Ties
3. Nodes

The strut-and-tie model behaves essentially as a truss. Compressive forces are directed along struts representing compressive stresses within the concrete. Tensile forces in the truss are directed along ties which represent reinforcement. Intersection of struts and ties occurs at nodes which are idealizations of areas in which internal forces are redirected.

By replacing a complex structural system with a strut-and-tie model, it is a simple matter to obtain estimates of the internal forces in the system by analyzing the model with the external forces applied to the system. In most cases, the solution procedure requires only standard truss analysis techniques. The estimates of internal forces may then be used to determine reinforcement requirements, check concrete stresses, and determine anchorage requirements. Some typical examples of strut-and-tie models are illustrated in Fig. 2.1.

In this chapter, a brief overview of the strut-and-tie procedure for design of structural concrete is presented. The development of the strut-and-tie model as a comprehensive design tool for structural concrete "details" is a relatively new undertaking. Consequently, all facets of the procedure are not fully developed and tested. The following discussion is a summary of the proposals of several researchers regarding application of strut-and-tie models. The focus is on design of details for which no rational design method currently exist. Therefore, traditionally well defined applications such as uniformly loaded simple beams are only briefly addressed.

2.2 Basic Principles

2.2.1 Background and Assumptions. The strut-and-tie model is a limit analysis approach to the design of structural concrete. More specifically, the strut-and-tie model is a static or lower bound plasticity solution. Marti (18) explains that strut-and-tie models represent a possible equilibrium system of forces within a structure at its ultimate load.

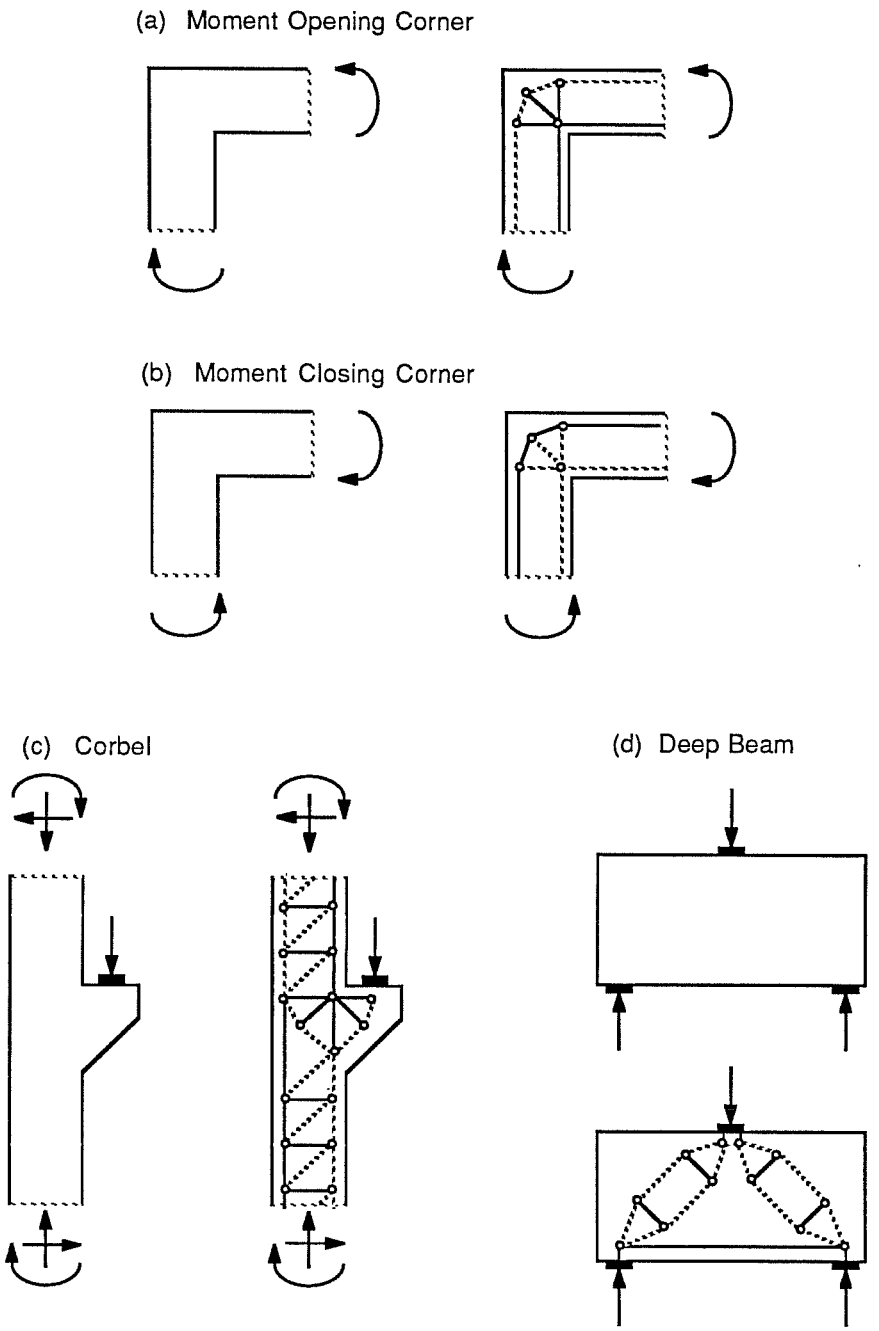

Fig. 2.1 Examples of Strut-and-Tie Models (From Ref. 1)

While the plasticity theory behind the strut-and-tie model is quite complex, it is primarily used to establish a rational basis for the method. For most practical applications, it is only necessary to understand that a properly chosen and dimensioned strut-and-tie model represents a lower bound estimate of the true capacity of a structural element assuming other brittle failures such as stability, local crushing, or anchorage failures are precluded.

Although development of detailed mathematical verification for the strut-and-tie method is unnecessary to understand its application, awareness of the assumptions is important. The most important of these assumptions are summarized below:

1. Failure is due to the formation of a "mechanism" resulting from yielding of one or more ties.
2. Crushing of the concrete struts does not occur prior to yielding of the ties. This is prevented by limiting the stress levels in the concrete.
3. Only uniaxial forces are present in the struts and ties.
4. All external loads are applied at the nodes of the strut-and-tie model. In the case of distributed loads, the model must be adequately detailed to realistically represent the load distribution.
5. The reinforcement is properly detailed so as to prevent local bond failures.

2.2.2 Types of Strut-and-Tie Models. Strut-and-tie models are often divided into two categories based upon the regions of the structure to which they apply (1,14,19,20). The distinction is based on the elastic stress distribution within the structure. While elastic stresses are not necessarily representative of the stress distribution in an actual concrete

structure, they are utilized to characterize different areas of a structure. Division between regions of a structure can be illustrated by considering a simple beam under a central concentrated load as shown in Fig. 2.2 (a). The elastic state of stress in the beam may be characterized by the use of stress trajectories (contours of principal stress). At the concentrated load and the supports, where the stresses are "**D**isturbed" the areas are defined as D-regions. Between D-regions the stress distribution is essentially uniform and regular and the linear strain profile assumption of "**B**ernoulli" is applicable. These areas are identified as B-regions. In the B-regions the elastic principal stresses may be determined directly from the flexural and shear stresses acting on the beam. In the D-regions a more complicated analysis which includes the local effects of the loads is required to determine elastic principal stresses. D-regions may also result from geometrical discontinuities. The subdivision of other types of structures into B- and D-regions is illustrated in Fig. 2.3.

Design of B-regions is accomplished using a special type of strut-and-tie model which is generally termed the "truss analogy". An example of a truss model is illustrated in Fig. 2.2 (b). The truss model has been used extensively as a conceptual model for shear design. In the truss model for a simply supported beam the lower horizontal chord represents longitudinal reinforcement while the upper chord represents the concrete compression zone. The stirrups of the beam are lumped together as the truss vertical members. Inclined compression struts are used to represent the continuous inclined compression fields in the web of the beam.

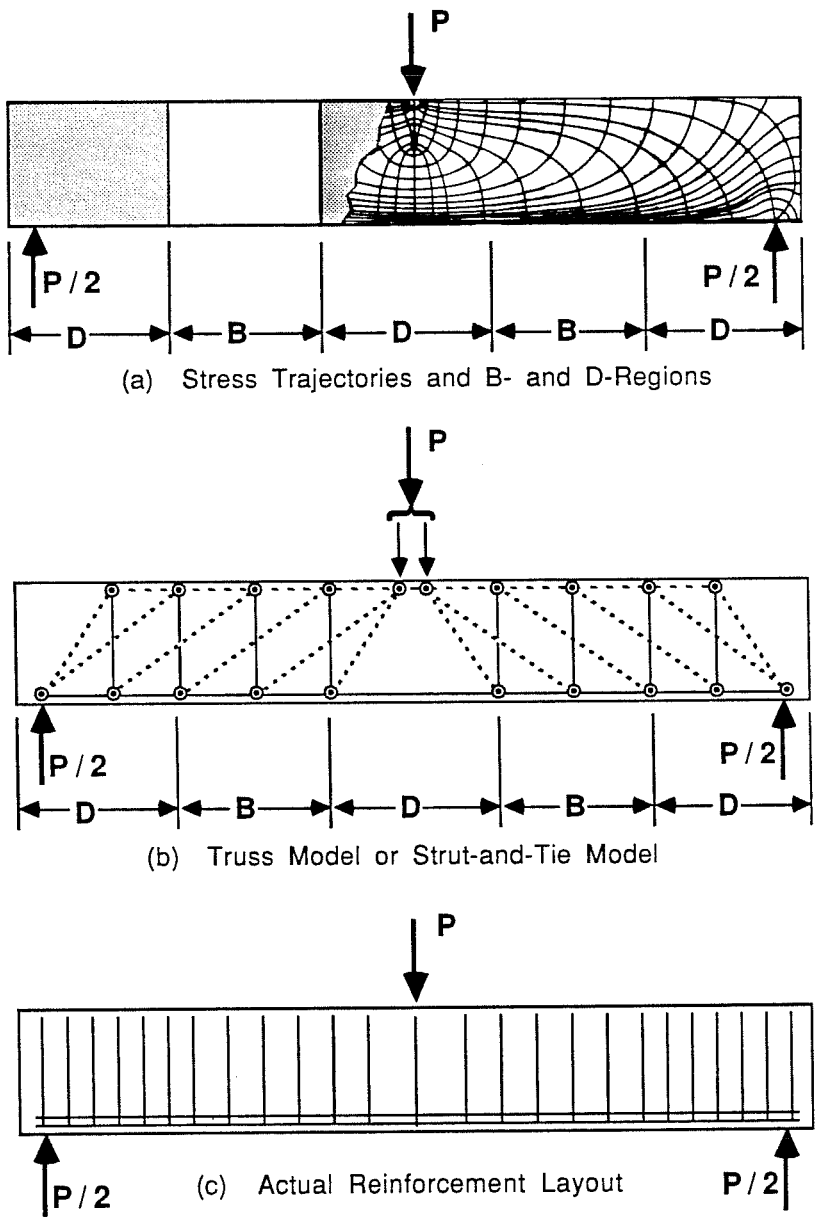

Fig. 2.2 Application of Strut and Tie Model to Simple Beam

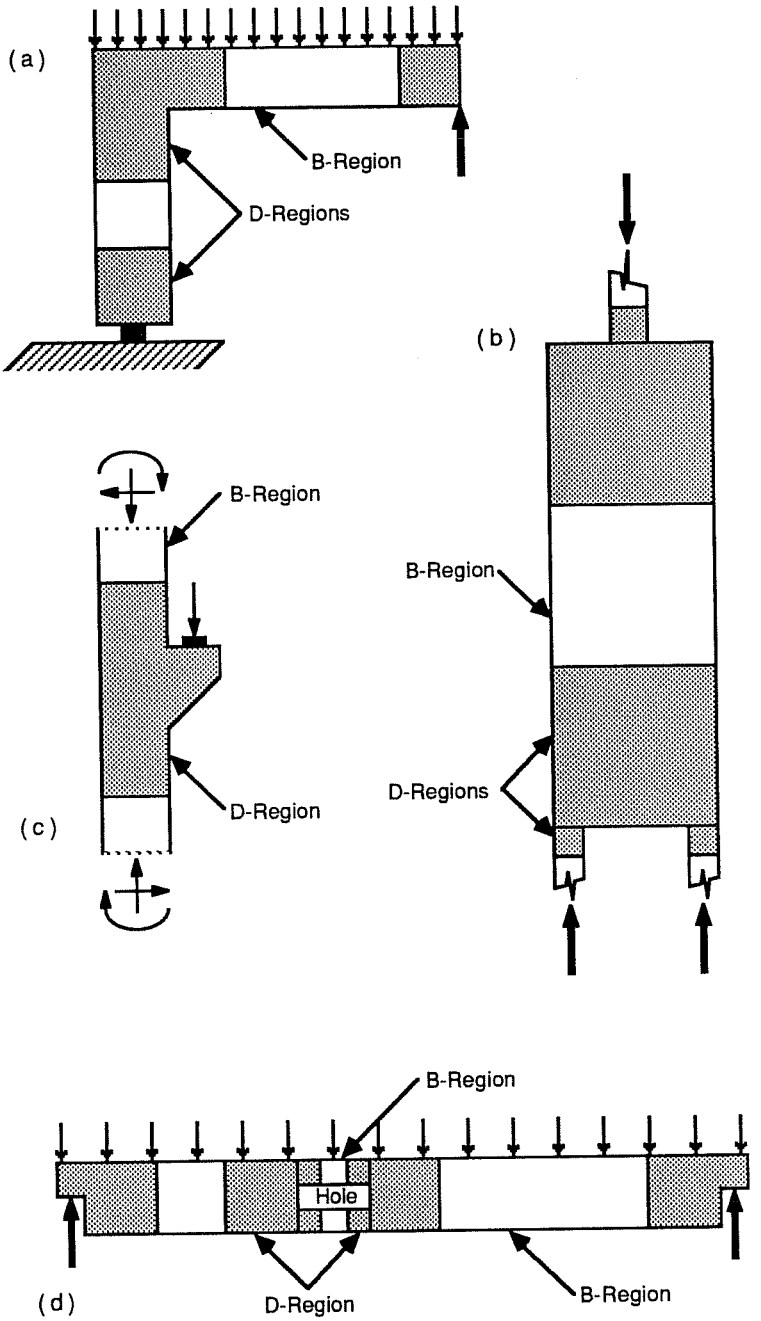

Fig. 2.3 Examples of B- and D-Regions (From Refs. 1 and 14)

The strut-and-tie model is proposed as a generalization of the truss analogy applicable to all portions of a structure. The truss model is limited in scope because it is intended primarily for use in the design of beams. Its use in D-regions is mainly confined to regions of beams in which concentrated loads produce compression fields which radiate outward from the load (See Fig. 2.4). These areas have been treated in the past by extending the truss analogy through the development of new procedures and elements which tend to make the truss analogy seem fragmented and overcomplicated (13). Rather than modifying the truss analogy for each new situation, it is now proposed (1,19,20) that all structures be encompassed in a unified design procedure: the strut-and-tie-model. In the strut- and-tie model, the truss analogy is generalized and extended so that it may be applied to a variety of design situations. The truss analogy is a specialized form of the strut-and-tie model and is used exclusively for the design of B-regions. Other types of models which apply to the wide range of D-regions occurring in structures are then lumped under the more general category of strut-and-tie models.

2.2.3 Design Procedure. The general procedure in applying the strut-and-tie model is summarized in Fig. 2.5. Before the strut-and-tie model is applied, it is necessary to establish a basic structural system, estimate loads and member sizes, and analyze the structure to determine any redundant reactions. The first step in the strut-and-tie model is to isolate each specific area of the structure which is to be designed (the "detail"), estimate dimensions, and determine forces acting on this specific area. The

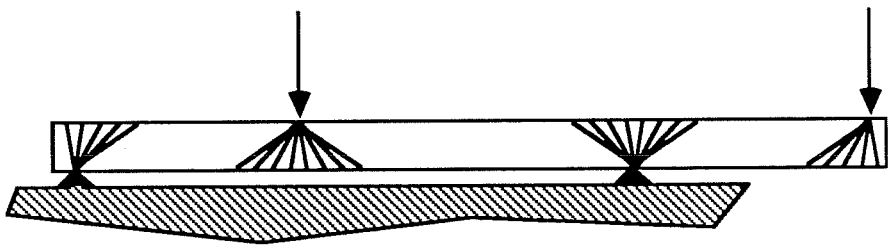

Fig. 2.4 Compression Fields Radiating Outward from Concentrated Loads (D-Regions)

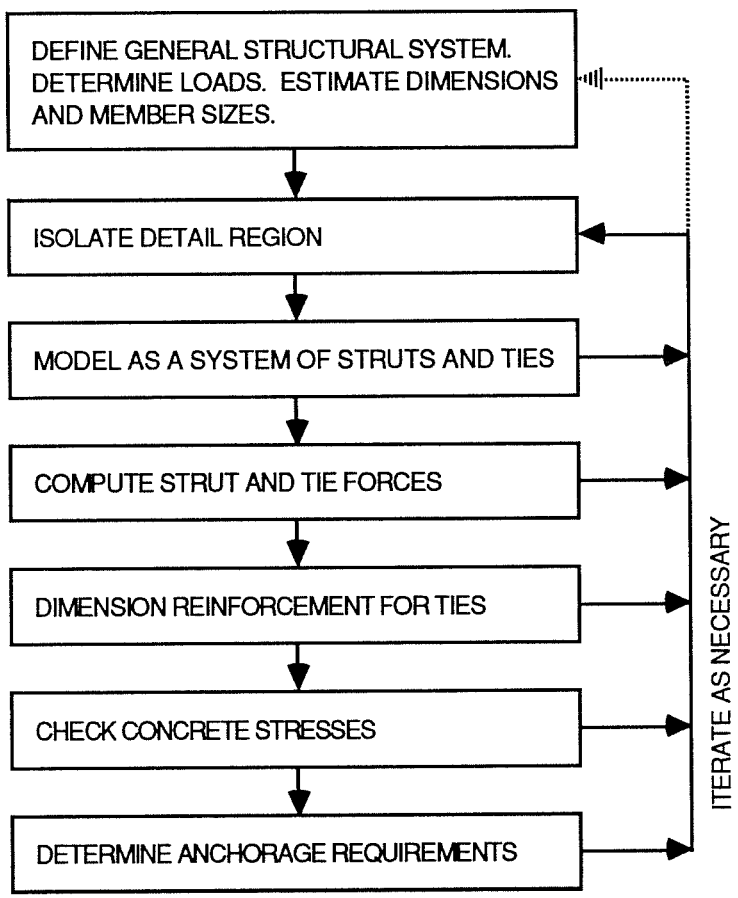

Fig. 2.5 Strut-and-Tie Model Design Procedure

region to be designed (the "detail") can now be replaced by a strut-and-tie model which satisfies equilibrium and the local boundary conditions. Internal forces in the struts and ties are determined from equilibrium and other assumptions of load distribution for indeterminate strut-and-tie models. The reinforcement is then dimensioned using the tie force and the stress levels in the concrete struts are checked. Finally, the nodes are evaluated to ensure proper development of reinforcement and transfer of forces.

Design using the strut-and-tie model is often an iterative procedure as many of the steps are interrelated. The geometry of the model and the detail will likely need to be altered as specific reinforcement sizes, anchorage requirements, etc. are developed. To aid in the process it is recommended that the model be drawn to scale in order to get a "feel" for the force transfer mechanism.

2.3 Elements of the Strut-and-Tie Model

2.3.1 Ties.

Ties are the tension members of the strut-and-tie model. Usually, tie forces are resisted by reinforcement placed symmetrically about the line of action of the force. The reinforcement must extent the entire length of the tie and should be properly anchored at the nodes. The amount of reinforcement to be provided is determined from the tie force. Ideally, the tie should be proportioned so that at the ultimate design load it will just reach yield. In order to ensure a ductile failure mode, sufficient yielding must occur to allow the formation of a mechanism prior to crushing of the concrete.

Tie reinforcement may consist of single or multiple bars or of prestressing strands. However, in many cases it is not readily apparent whether ties should be consist of a few large reinforcing bars or a large number of smaller bars. In addition, the maximum width over which reinforcement may be considered to act as a single tie is unclear because few guidelines regarding the spacing of reinforcement within ties are reported in current literature. Also, the distribution or spacing between reinforcement within a tie is not clearly addressed. Schlaich et al. (1) indicate reinforcement within a tie should undergo similar strains in order to act as a unit or a single tie. However, estimating the variation in strain rates within the actual structure may be difficult. Furthermore, if reinforcement with differing bond characteristics is considered to act as a unit, it may be necessary to neglect or discount the contribution of one of the components if it is strained to a lesser degree.

In Reference 1, refined models are presented that utilize concrete ties or concrete tensile strength. While concrete tensile strength may play a part in the force transfer mechanism, it is generally more convenient to neglect its contribution. This is prudent for design purposes as the tensile strength of the concrete is very small relative to that of reinforcement. Also, the action of creep, shrinkage, and thermal stresses may cause cracking which would eliminate the development of concrete tension ties. For most practical detailing problems, concrete tensile strength may be ignored.

2.3.2 Struts. Compression members of the strut-and-tie model are known as struts. Struts are usually considered to be comprised of concrete.

However, reinforcement will also resist compressive forces if it does not buckle. Struts actually represent stress fields in the concrete. Thus, various struts have been developed to characterize different types of stress fields. Three configurations are sufficient to model most situations (1). These are the prism, fan, and bottle struts illustrated in Fig. 2.6.

A prismatic strut is the simplest idealization of a compressive stress field. The prism is uniform in geometry and has a constant stress along its length. Prisms are generally used to model stress fields having uniform parallel stress trajectories.

Fan shaped stress fields are normally developed at points of concentrated loading or at supports. Figure 2.7 illustrates a fan region such as that which develops at the support in a simple beam. This fan region incorporates a series of trapezoidal struts which act to distribute force to several stirrups.

In some cases, a stress field may tend to narrow near points of concentrated loads or at supports. This is modelled using a bottle shaped strut as shown in Fig. 2.8. The increase in strut width induces tensile stresses normal to the longitudinal axis of the strut. This tensile stress must either be resisted by transverse reinforcement or by the tensile strength of the concrete in order to prevent cracking. Figure 2.8 (b) shows the bottle strut represented by a secondary strut-and-tie model for analysis.

2.3.3 Nodes. Nodes connect the elements of strut-and-tie-models. In strut-and-tie models, nodes represent the pinned joints of a truss. Physically, nodes represent regions in which internal forces are redirected.

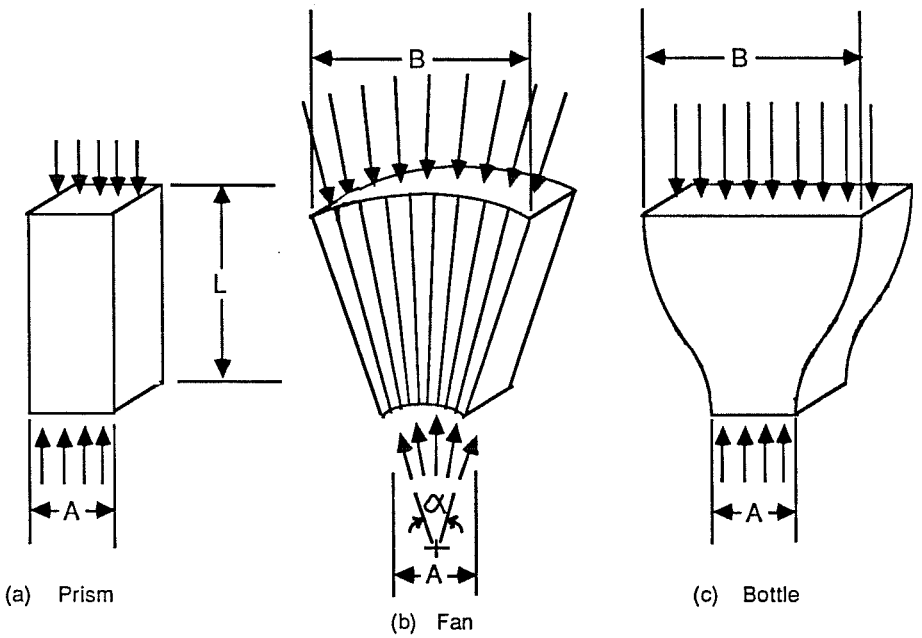

Fig. 2.6 Basic Types of Struts (Adapted from Ref. 1)

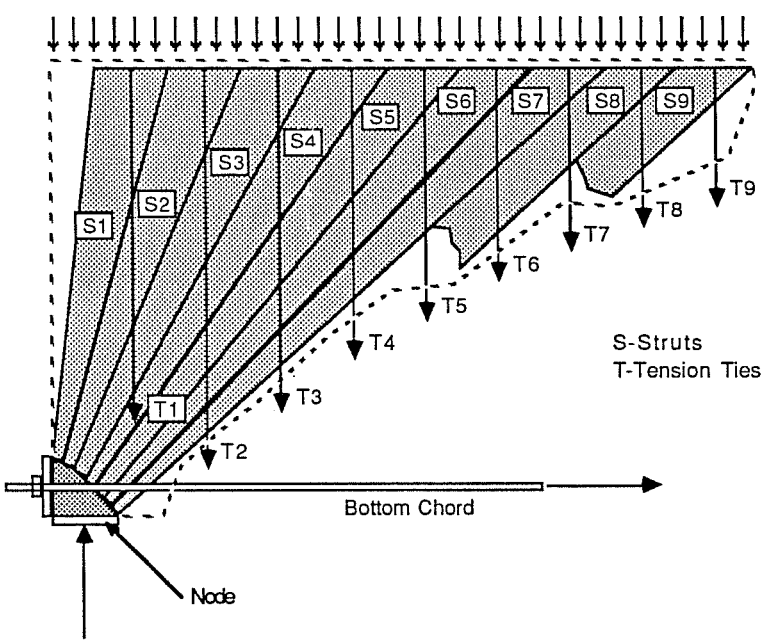

Fig. 2.7 Fan Shaped Compression Stress Field at Beam Support

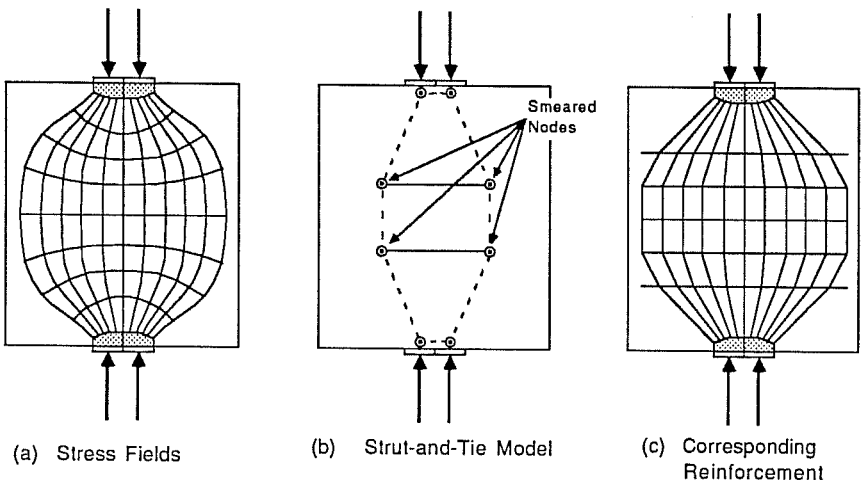

Fig. 2.8 Bottle Shaped Struts (Adapted from Ref. 1)

The importance of nodes in the design process is twofold. First, concrete stress levels in nodal regions must be controlled to allow for the safe transfer of forces. Secondly, dimensioning of nodes is the key to satisfying anchorage requirements for reinforcement.

Nodes may be classified by their relative size and by the struts and ties which they connect (1). Figure 2.9 illustrates the two size designations for nodes. The singular node connects strut-and-tie forces in relatively small areas. Smeared nodes, in contrast, join wide stress fields or consist of a number of ties with distributed reinforcement. Of the two types of nodes, the singular node is generally the more critical since the force transfer is more abrupt which creates higher stress concentrations. Thus, much of the following discussion is focused on singular nodes.

Singular and smeared nodes may be grouped into subsets relating to the type of elements which they join. For instance, a node joining two compression struts and one tension tie is termed a CCT-node. Examples of various singular nodes are shown in Fig. 2.10.

In order to evaluate nodes some background on the state of stress within nodes is helpful. Marti (15) describes the equilibrium system of three planar strut forces using Mohr's circle. Marti shows that if the stresses on each face of the node are equal, both principal stresses within the nodal region will equal the stress at the boundary of the node. This condition is known as a state of planar hydrostatic stress.

Evaluation of the nodes includes checking the node boundary stresses and determining anchorage requirements for nodes which contain tension ties.

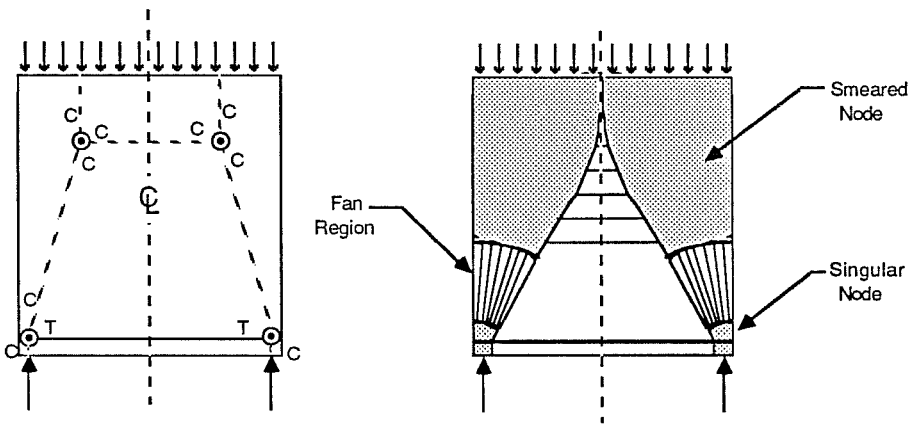

Fig. 2.9 **Singular and Smeared Nodes** (Adapted from Ref. 1)

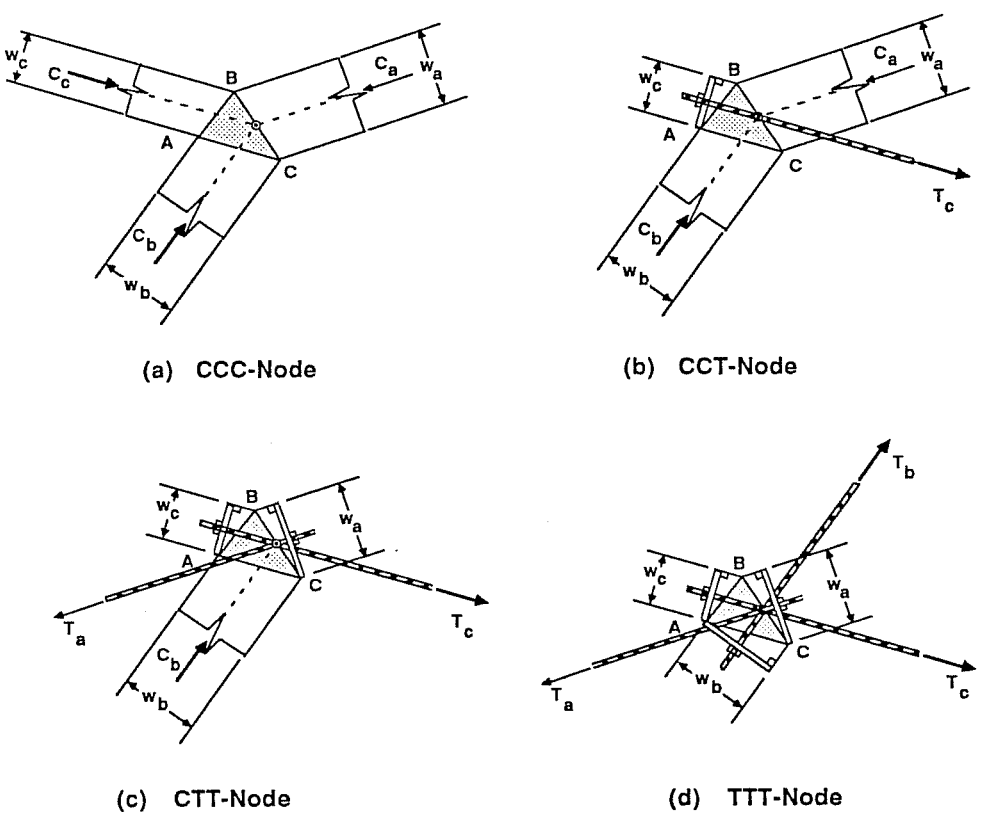

Fig. 2.10 Examples of Singular Nodes

Each of these steps requires the determination of the physical boundaries of the node. The "dimensioning" of nodes is largely determined by two constraints. The first constraint is that all the lines of actions of struts and ties as well as any external forces must coincide. Secondly, the widths and relative angles of the struts and ties will further constrain the node geometry.

Dimensioning of the node and checking of boundary stresses are somewhat interrelated. Beyond the constraints previously discussed, some freedom often remains in selecting the node geometry. In these cases, the geometry should be chosen to minimize the stresses within the node. This is accomplished by selecting a geometry in which the stresses along the border of the node do not exceed the limiting value of the concrete stress (see Sec. 2.4 for limiting stresses). Furthermore, Schlaich, Schäfer, and Jennewein (1) recommend dimensioning the node so that a state of planar hydrostatic stress results. This state of stress in the node is achieved by choosing the node geometry so that the stresses on all the node faces are equal. An example of a CCC-node under a hydrostatic stress state is shown in Fig. 2.11. Because the node stress is hydrostatic, strut forces are proportional to their width and the sides of the node are perpendicular to the axis of each of the struts.

It should be recognized that the geometries of the model may not allow for equalization of the boundary stresses. Such a situation is shown in Fig. 2.12 (a). Schlaich et al. (1) indicate that this stress state may be tolerable if the maximum ratio of stresses between any two sides does not exceed 2.0. The node shown in Fig. 2.12 (a) may be dimensioned for hydrostatic stress by

changing the width of the compression struts in the vicinity of the node as shown in Fig. 2.12 (b). The intersection of the strut centerlines actually lies outside the nodal region in this case. Bottle shaped struts are often used where one of the node boundaries is fixed as in the case of a node adjacent to a bearing plate. A reduction of the width of the struts is required to produce a hydrostatic node. An example of this situation occurring in a deep beam without web reinforcement is shown in Fig. 2.13.

Nodes anchoring tension ties are dimensioned similar to the CCC-node. This is made possible by assuming the tie forces act from behind the node to compress the nodal region (1). The anchorage of reinforcement is often visualized as a plate even though most reinforcement is anchored by simply providing sufficient development length (See Fig. 2.14). The dimensions of nodes joining ties is often controlled by the width of the tie. Thus, placement of reinforcement can be critical to the design of nodes. The use of multiple layers of reinforcement increases the width of the tie and thereby reduces stress levels in the node (Fig. 2.15). MacGregor (14) points out that the location of the reinforcement in the tensile tie affects the size of the nodes and intersecting struts as illustrated in Fig. 2.16. If the reinforcement is positioned closer to the tension side of the beam, the size of both the node and adjoining strut decrease. This can be detrimental to the strength of the member because the stress levels in the strut and the node will increase as the node decreases in size. The examples illustrate that the determination of tie widths is critical to the evaluation of nodes containing ties. However, in many cases the determination of tie widths is unclear.

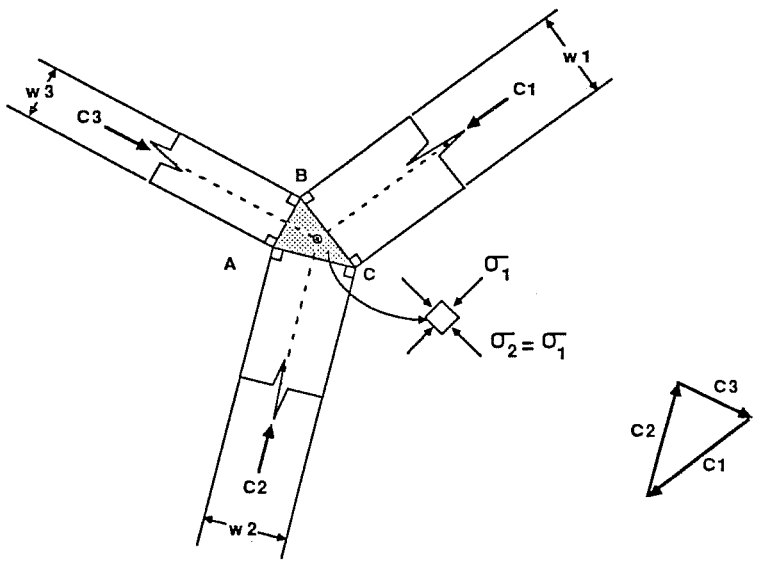

Fig. 2.11 CCC-Node, Hydrostatic State of Stress (Adapted from Ref. 15)

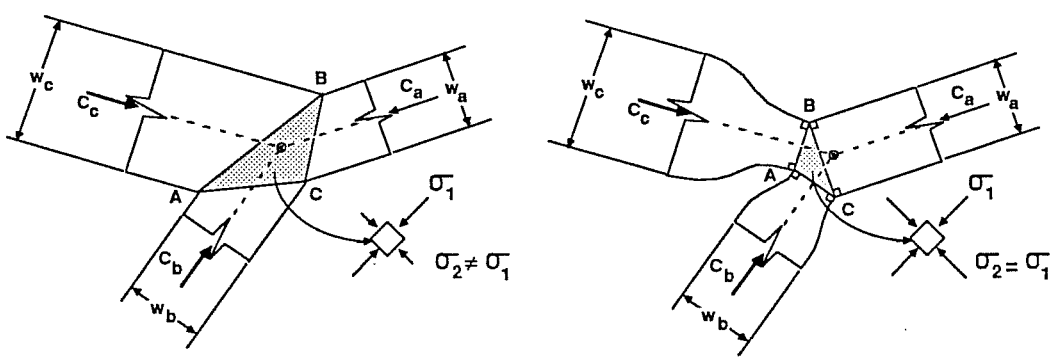

(a) CCC-Node with Unequal Pressures at Borders

(b) CCC-Node Designed to be Planer Hydrostatic

Fig. 2.12 Bottle Shaped Struts Created by Hydrostatically Dimensioned Node

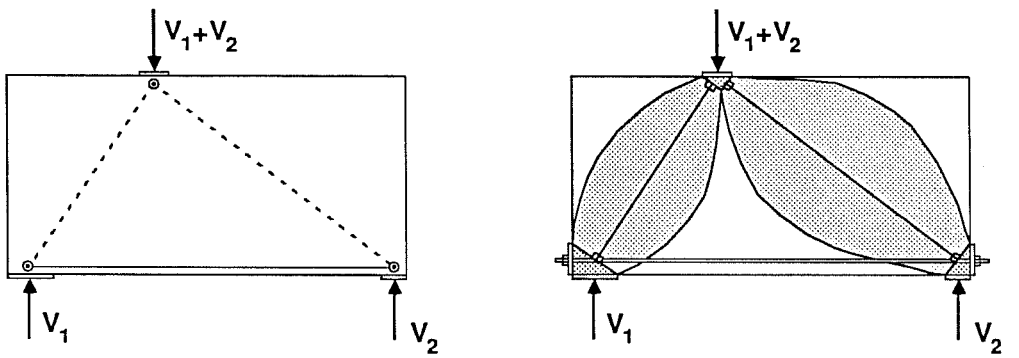

(a) Strut and Tie Model for Deep Beam

(b) Stress Fields, Nodes, and Corresponding Reinforcement

Fig. 2.13 Constricting Struts Producing Hydrostatic Stress State at the Nodes

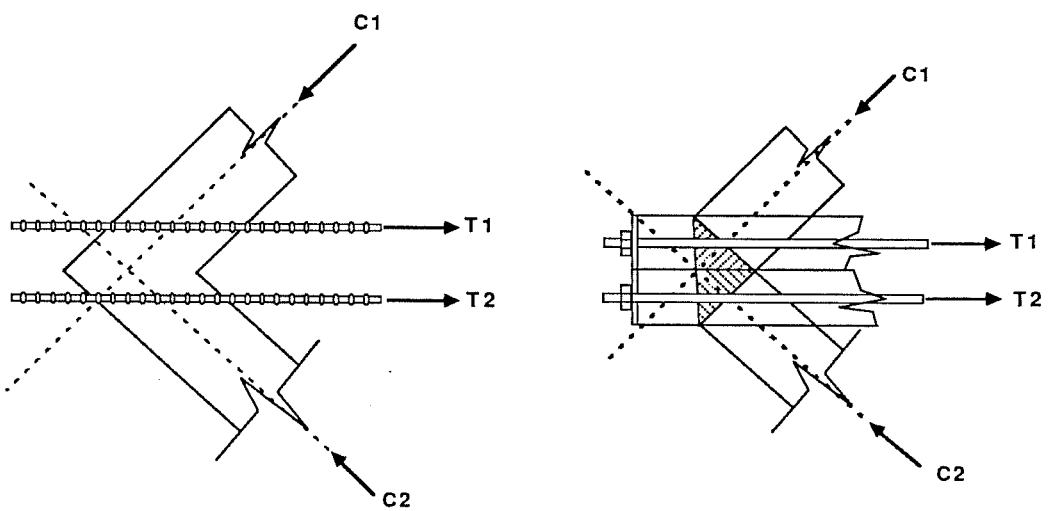

(a) Actual Reinforcement Layout

(b) Idealized Tie Anchors

Fig. 2.14 Idealization of Tie Forces Within Node

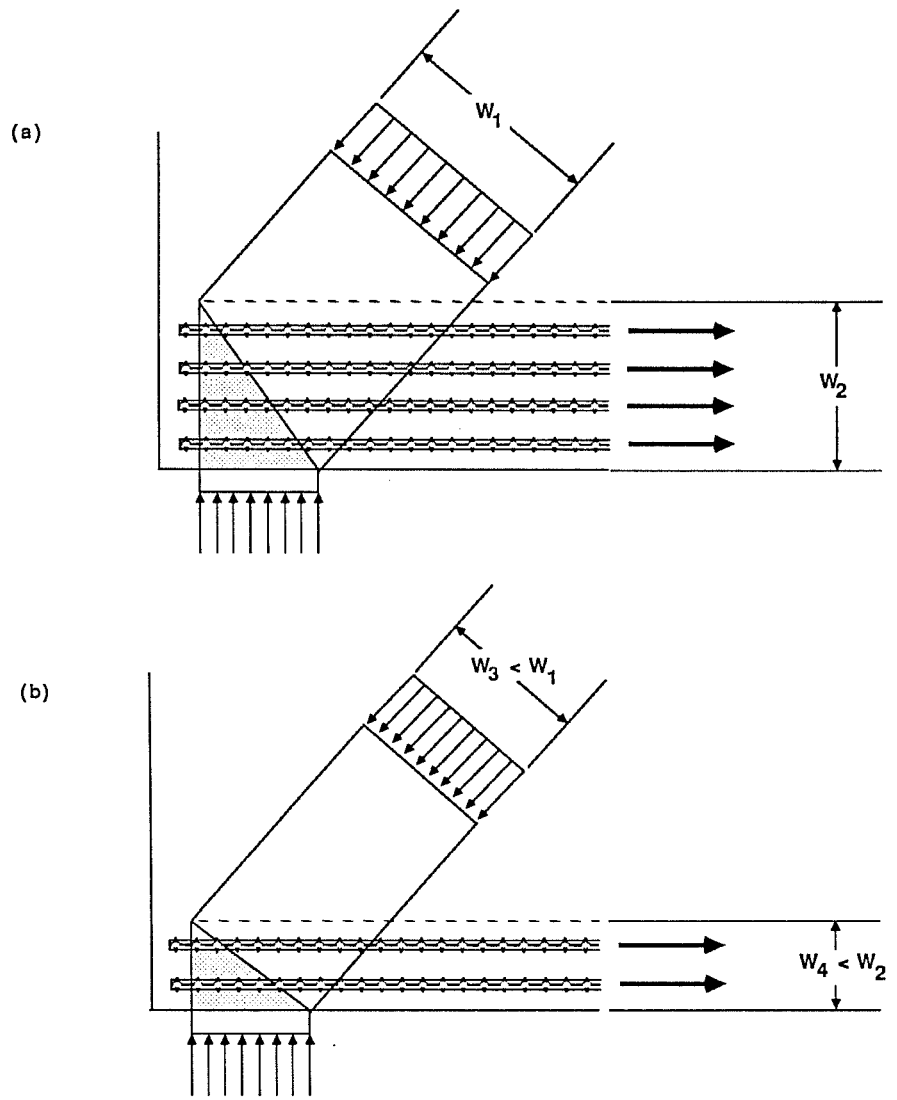

Fig. 2.15 Effects of Decreasing Tie Width (Adapted from Ref. 1)

One of the most commonly occurring nodes is the CCT-node located at the supports of beams (Fig. 2.16). Even though the nodes in this figure are not designed to be planar hydrostatic, their dimensions are defined by the width of the tension tie. Where the reinforcement is relatively close to the bottom of the beam, the tie width is defined by Schlaich, Schäfer, and Jennewein (1) as being twice the distance from the center of gravity of the reinforcement to the bottom of the beam. It is obvious, however, that as the center of gravity of the reinforcement is moved further from the bottom of the beam there must be a limit on the tie width. Marti (15) therefore, defines the tie width "ωh" as:

$$\omega h = \frac{A_s f_y}{b(\upsilon f'_c)} \qquad (2.1)$$

where

ω	=	Nondimensional mechanical reinforcement ratio
h	=	Depth of the beam
A_s	=	Area of flexural reinforcement
f_y	=	Yield strength of flexural reinforcement
b	=	Width of the beam
υ	=	Concrete efficiency factor (See Sec. 2.4)
f'c	=	Concrete cylinder strength

This is illustrated in Fig. 2.17. Further proposals by Schlaich and his co-workers (1) are shown in Fig. 2.18. Schlaich et al., suggest that dimensions of the CCT-node are dependent on factors such as the relative magnitude of stress fields and the amount of tie reinforcement. For instance, in Fig. 2.18 where σ_2 is less than σ_1 and there are multiple layers of reinforcement, the width of the tensile tie may be as much as 20 percent of the length of the entire D- region. In the opposite case when σ_2 is greater than σ_1 and only one row of tie reinforcement is used, the tie has virtually zero width.

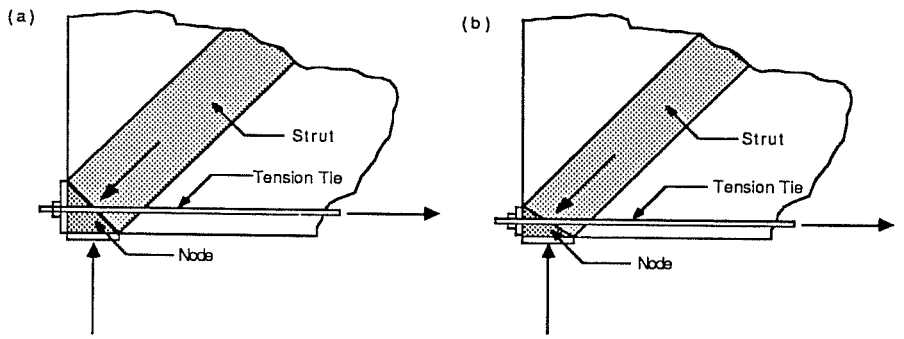

Fig. 2.16 Effect of Tension Tie Location on Size of Compression Strut (From Ref. 14)

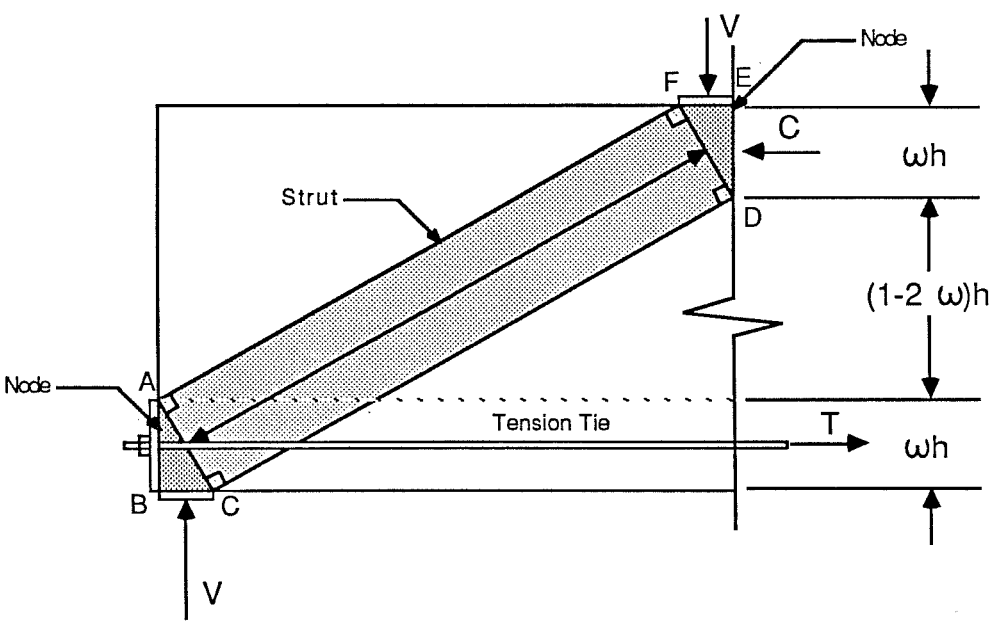

Fig. 2.17 Tie Width as Defined by Mechanical Reinforcement Ratio (Ref. 15)

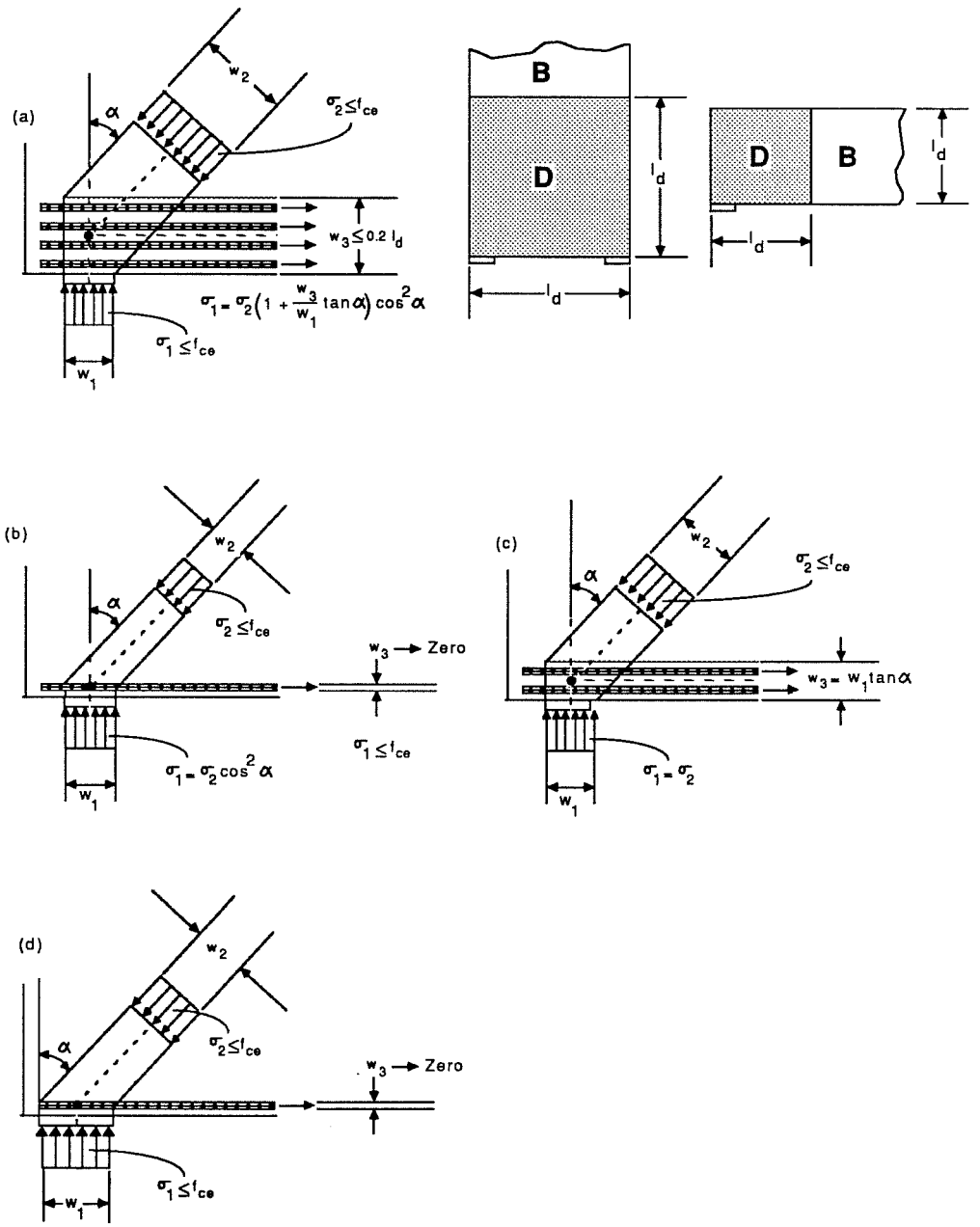

Fig. 2.18 Proposals for Dimensioning CTT-Nodes with Multiple Layers of Reinforcement (Adapted from Ref. 1)

It is apparent that further research is needed to clarify the dimensioning of nodes anchoring ties. Only a few node configurations have been addressed to a degree that would allow designers to use them with confidence. Fundamental node dimensioning techniques have not been verified experimentally, therefore, it is difficult to extend them to more complex design situations. In this study, several examples where present proposals lack adequate definition were identified. One problem is the modelling of nodes in flanged members. Figure 2.19 (a) shows a side view of the CCT-node that occurs at the support of a simple beam. If the beam is flanged, the forces will tend to spread out as they move from the web into the flange. However, the spreading angle of the forces is not defined (See Fig. 2.19 (b)). Determining the geometry of the node becomes complex where compression struts are narrowing in the plane of the beam's longitudinal axis and is widening in the lateral direction.

Other problems are encountered when evaluating varying reinforcement distributions and anchorage details. For example, Fig. 2.20 shows CCT-nodes where tie reinforcement is anchored using straight and hooked bars. The effect of the hook on node geometry has not been well addressed in current literature. Another problem is illustrated in Fig. 2.21 which shows the strut-and-tie model for a bottle shaped strut. The design checks needed for nodes B and C are unclear. If a single layer of bars is used to reinforce tie BC, nodes B and C would be considered as singular nodes based upon definitions proposed by Schlaich and his co-workers (1). If several layers of reinforcement are used and are distributed over a width "w" as

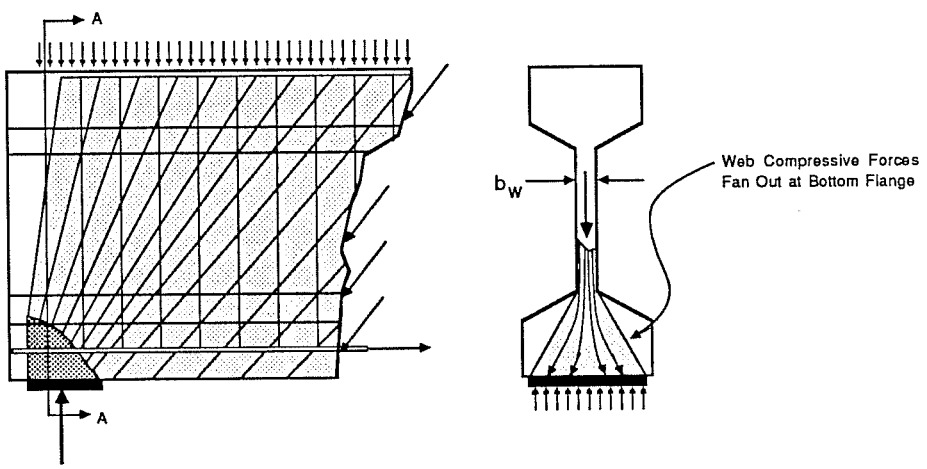

Fig. 2.19 CTT-Node Compressive Force Distribution in Flanged Member

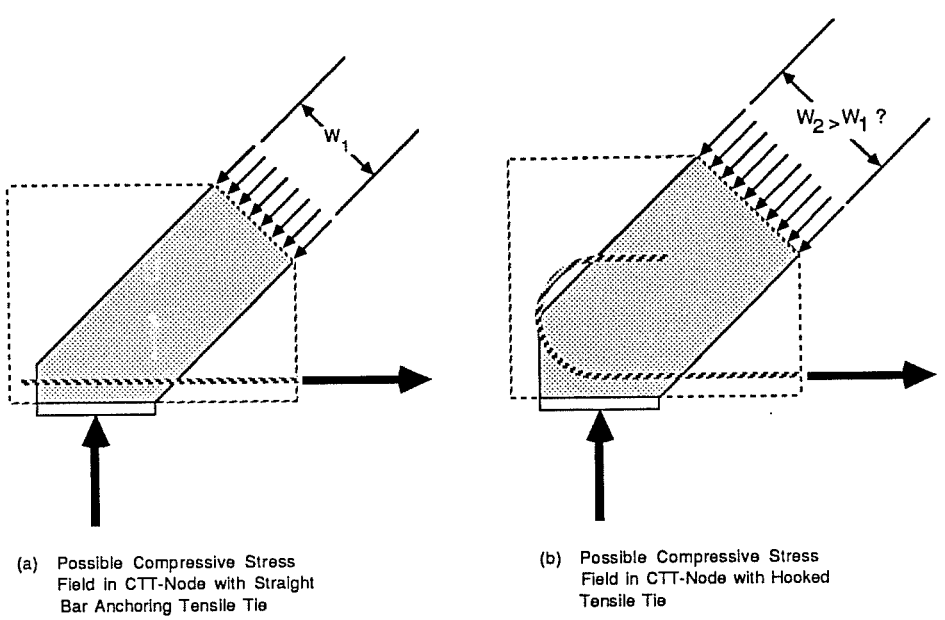

Fig. 2.20 Effect of CCT-Node Anchorage Detail

shown in Fig. 2.21 (b), it seems logical that a smeared node approach should be followed. In the latter case, Schlaich et al. (1) state that the check of the stresses in the node is unnecessary because singular nodes within the structure will be more critical. However, it is not clear where the transition from a singular node to a smeared node occurs.

The final step in evaluating nodes is ensuring that tie reinforcement is properly anchored in singular and smeared nodes. Anchorage is achieved by providing proper development length or in special circumstances by attaching the reinforcement to bearing plates or other fixed components. The key to determining anchorage requirements is selecting the point at which the reinforcement must be fully developed. In the case of the CCT- node at a beam support shown in Fig. 2.22, the anchorage is considered to begin at the inside of the support because of the favorable compression from the reaction (1). Except for the singular CTT-node, little guidance is given for determining the point where anchorage begins. Still, it is conservative to anchor tie forces entirely behind the node if the node dimensions are known (See Fig. 2.23). If sufficient space is not available for hooks or normal development lengths, end plates or continuous reinforcement details such as U's may be utilized. Also, confining hoops or spirals may be used to improve development.

Dimensioning, stress checks, and anchorage requirements for CTT-nodes will be discussed further in Chapter 5.

2.4 Effective Concrete Strength Limits

The general goal in structural concrete design is to produce members in which the critical section will exhibit ductile behavior under extreme

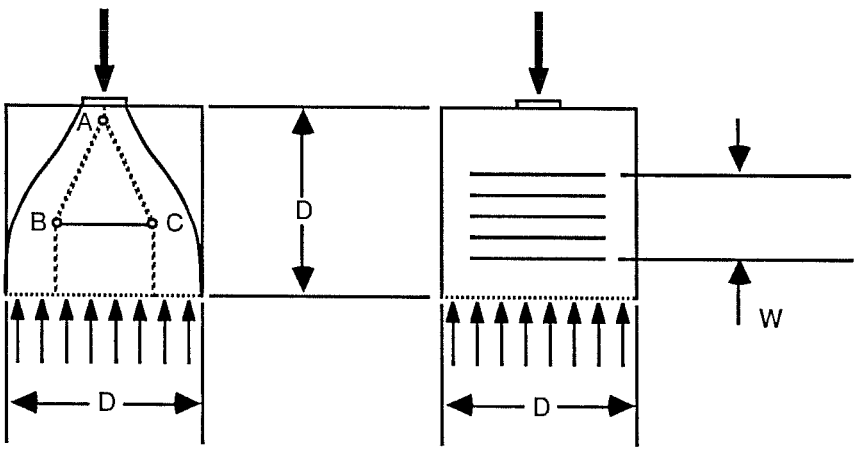

(a) Strut-and-Tie Model (b) Placement of Tie BC's Reinforcement

Fig. 2.21 Reinforcement in Bottle Shaped Strut

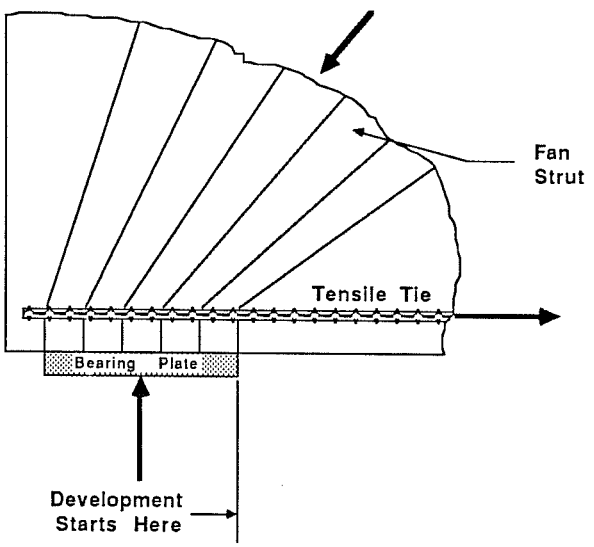

Fig. 2.22 Anchorage of Reinforcement in CTT-Nodes

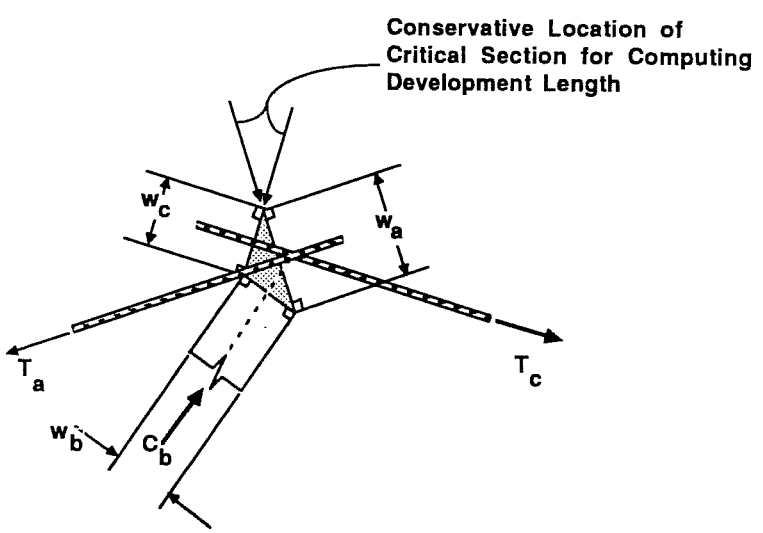

Fig. 2.23 Anchoring Ties at the Node

overload. This is done by ensuring that failure occurs after the reinforcement yields. To ensure ductile behavior, it is necessary to limit stress levels in the concrete. These are termed effective concrete strength limits. In this manner, the strut-and-tie model promotes the use of "underreinforced" sections.

In general, the effective strength limit in the compression struts is chosen as some portion of the concrete compressive strength, f'c. The effective strength, f_{ce}, is equal to υf'c where υ is an efficiency factor and f'c is the 28-day compressive strength. Because the strut-and-tie model is associated with the ultimate limit state, substantial cracking may be expected which will act to reduce the concrete's compressive strength. Furthermore, in the strut-and-tie model, the struts are assumed to be loaded uniaxially. Actually, frictional forces, aggregate interlock, and dowel forces are present which may also affect concrete strength. Hence, an efficiency factor, υ, is introduced to reflect this decrease.

Considerable research has been conducted in an effort to determine the limiting stress for compression struts. Much of this work has focused on the webs of beams. Empirical relations for the compressive strength of concrete struts in beam webs as suggested by Neilsen et al. (10), Grob and Thürliman (16), and Ramirez (13) are summarized in Fig. 2.24.

Mitchell and Collins (12) present a more detailed method of determining the limiting stress in compression struts which is based on results of tests on shear panels. The compressive strength is related to the

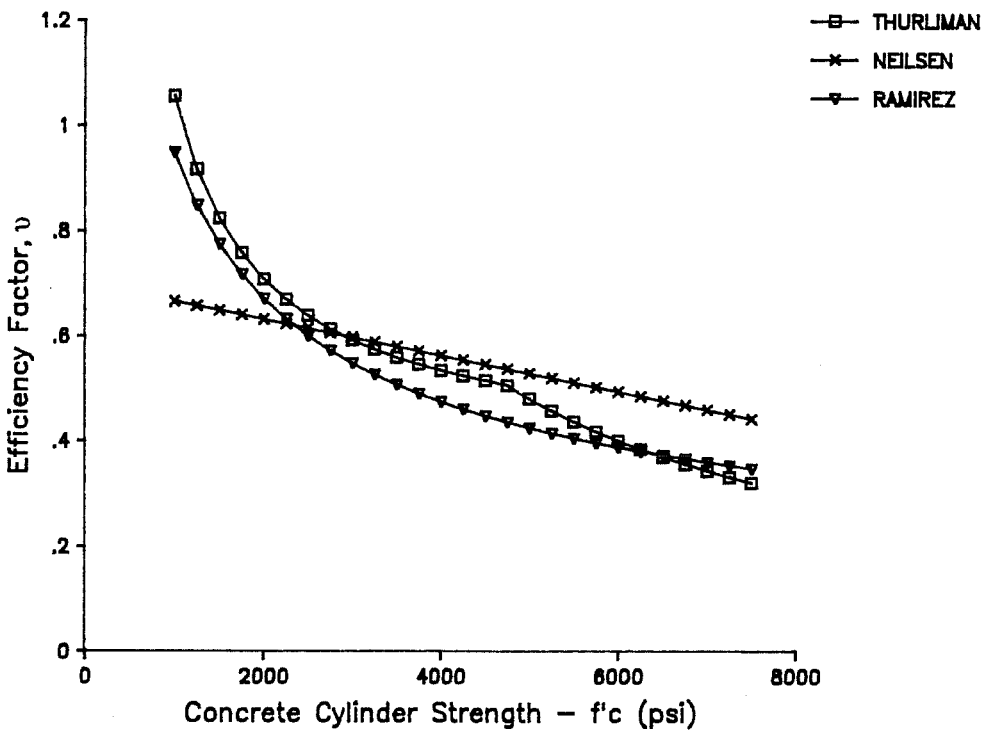

Fig. 2.24 Relationship Between Efficiency Factor and Concrete Strength

principal tensile strain along with the cylinder compressive strength. The proposed equation is given below :

$$f_{ce} = \upsilon f'c = \left(\frac{f'c}{0.8 + 170\ \varepsilon_1}\right) f'c \qquad (2.2)$$

where:

f_{ce} = Effective concrete strength
υ = Concrete efficiency factor
$f'c$ = Cylinder compressive strength
ε_1 = Principal tensile strain normal to the principal compressive stress

The principal strain may be determined from Mohr's circle of strain using the strut angle, principal compressive strain and the strain parallel to the beam axis (Fig. 2.25). Mitchell and Collins indicate that a value of 0.002 may be used for both the principal compressive strain (ε_1) and the strain along the beam's axis (ε_x) in lieu of a more accurate analysis. The principal tensile strain may then be determined as shown in Fig. 2.25. The relationship between the efficiency factor for varying strut angles is presented in graph form in Fig. 2.26 (21).

The various proposals for effective concrete strength limits are based on tests of continuous compression fields either in beams or shear panels. In more general applications, recommendations must consider isolated struts and nodes where the state of stress may be quite different from the continuous compression fields.

In References 1 and 14, proposals for effective concrete strength limits incorporate factors such as the stress state. These methods indicate that uniformity of strains influences concrete strengths. The crushing

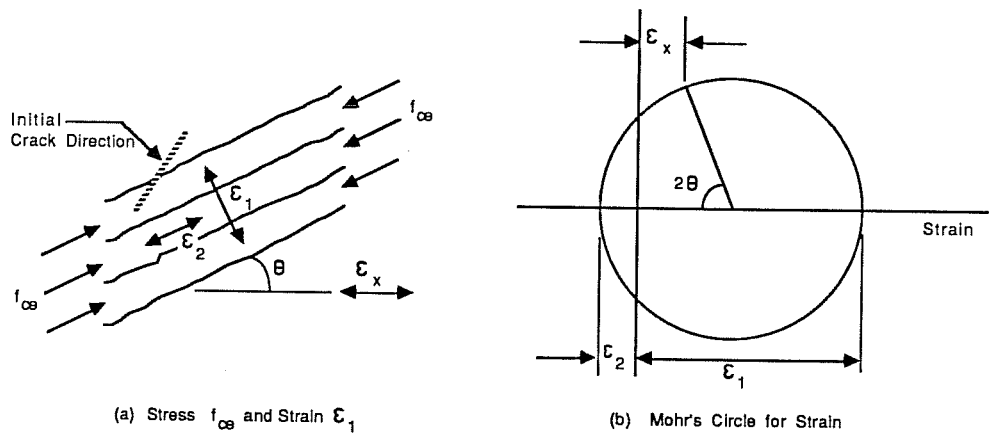

(a) Stress f_{ce} and Strain ε_1 (b) Mohr's Circle for Strain

Fig. 2.25 Strains for Cracked Web (Adapted from Ref. 12)

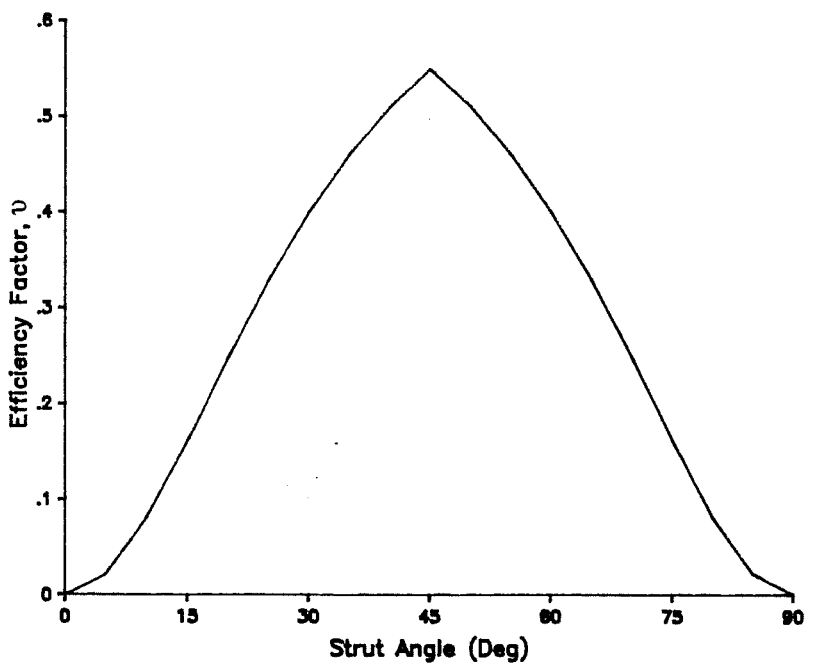

Fig. 2.26 Relationship Between Efficiency Factor and Strut Angle

strengths of nodes and struts with highly localized strain conditions are generally found to be higher than in more uniformly strained compression fields presumably due to the influence of adjacent, lower stressed concrete. Recommendations for effective concrete stresses from References 1 and 14 are summarized in Tables 2.1 and 2.2.

In addition, Schlaich et al. (1) present a method by which the compressive strength of bottle shaped struts may be evaluated using Fig. 2.27. The safe pressure acting on the bottle "neck" is related to the amount of transverse reinforcement, the aspect ratio of the strut, and the concrete compressive strength.

2.5 Modelling

2.5.1 General Guidelines. One of the key elements in the application of the strut-and-tie model is the selection of an appropriate model for a specific detail. Model development is constrained by the following considerations:

1. Ease of Fabrication
2. Equilibrium
3. Ductility
4. Serviceability

In many cases, practicality and ease of fabrication will have the greatest influence upon the configuration of the design model. Models which result in details that are overly congested or difficult to fabricate should be avoided. The reinforcement pattern for the detail region should follow the reinforcement scheme used in adjacent portions of the structure.

State of Stress and/or Reinforcement Layout for Strut or Node	$f_{ce}=\upsilon f'_c$
Undisturbed and uniaxial state of compressive stress that may exist for prismatic struts and CCC-nodes.	0.85 f'c
Tensile strains and/or reinforcement perpendicular to the axis of the strut may cause cracking parallel to the strut with normal crack width; this applies also to nodal regions where reinforcement is anchored or crossing.	0.68 f'c
Tensile strains causing skew cracks and/or reinforcement at skew angles to the strut's axis.	0.51 f'c
For skew cracks with extraordinary crack width. Skew cracks would be expected if modelling of the struts departs significantly from the theory of elasticity's flow of internal forces. Considerable redistribution of internal forces would be required to exploit the member's ultimate capacity.	0.34 f'c

Table 2.1 Effective Concrete Strength Limits Proposed by Schlaich et al. (1)

Structural Member	$f_{ce}=\upsilon f'_c$
Truss Nodes:	
Joints bounded by compressive struts and bearing areas	0.85 f'c
Joints anchoring one tension tie	0.65 f'c
Joints anchoring tension ties in more than one direction	0.50 f'c
Isolated compression struts in deep beams or D-regions	0.50 f'c
Severely cracked webs of slender beams:	
α =30°	0.25 f'c
α =45°	0.45 f'c

Table 2.2 Effective Concrete Strength Limits Proposed by MacGregor (14)

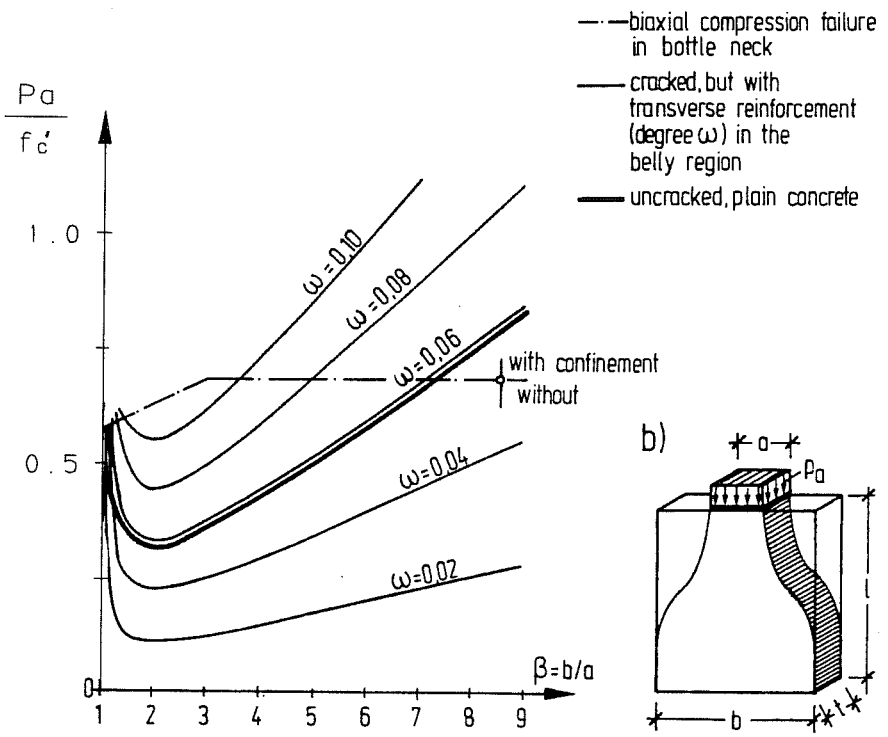

$$\omega = \frac{A_s f_y}{t f'c}$$

where

A_s = Area of Reinforcemnt per Unit Length

f_y = Yield Strength of Reinforcement

t = Thickness of the Member

$f'c$ = Concrete Cylinder Strength

Fig. 2.27 Allowable Stresses in Bottle Shaped Struts (From Ref. 1)

Model geometry must also conform to the assumptions and limitations of strut-and-tie model theory. In order to satisfy the requirements of the theory of plasticity, a model must be in equilibrium under the applied loads. However, if the selected force system or "truss" is to fully develop, the load carrying capacity of the strut-and-tie elements and the rotational capacity of the nodes must not be exceeded before the ties yield. To fulfill the latter ductility requirement, it is suggested (1,19) that the model be oriented so as approximate the elastic stress trajectories. The relationship between design models and elastic stress distribution will be further discussed in Sec. 2.5.2.

Another fundamental consideration in any design process is serviceabilty. According to Schlaich et al. (1,19), crack control is provided by orienting the strut-and-tie model according to the elastic stress trajectories. In addition, accepted standards for bar spacings, minimum reinforcement, and control of creep and shrinkage should be followed.

In the B-regions of beams, inclined compression strut angles are limited to promote better serviceability behavior. It may be shown that the choice of a strut angle determines the relative amounts of longitudinal and transverse reinforcement. A very low strut angle requires a large amount of longitudinal reinforcement relative to transverse reinforcement while the converse is true for steep strut angles. In either case extreme strut angles may result in excessive cracking. Although various limits have been proposed, there is some agreement that strut angles should be between 30 and 60 degrees in beams. Limits on strut angles have not been fully addressed for structural components other than beams even though it is apparent that

similar problems may be encountered in other detailing situations. In more general details, however, it is difficult to establish a frame of reference from which to measure strut angles.

2.5.2 Model Development. Some authors, in particular Schlaich et al. (1), emphasize developing a model which conforms to the elastic stress trajectories within the structure. The elastic stress distribution in a structural element may be determined from a finite element analysis. Still, guidelines for model development using elastic stress trajectories are vaguely defined. A design model can only follow the continuous elastic stress distribution in a very general sense because a strut-and-tie model condenses internal forces along discrete lines of action.

An example of the concept of model orientation along elastic stress trajectories is illustrated in Fig. 2.2 for the case of a truss model of a simple beam. In the upper portion of the beam, principal compressive stress are nearly parallel to the beam axis and are represented in the truss model by the upper horizontal strut. In the same manner the lower tension tie represents principal tensile stresses in the lower portion of the beam. Rather than selecting the location of the upper and lower chords based on the elastic stress distribution the distance between the upper and lower chords is chosen for the ultimate moment capacity of the section. Inclined compression struts are aligned with the curvature of compression trajectories near mid-depth of the beam but deviate from the compression stress directions at other locations. The same is true of stirrups (vertical ties) which correspond to principal tensile stresses only near the top of the beam and are oriented vertically

primarily for ease of fabrication. The geometry of a truss model for a simple beam represents only an approximation of the elastic stress trajectories.

While much research has been performed in verifying the geometry of the truss model for beams, little guidance is given as to what constitutes an acceptable model for more general applications. While this situation has not been addressed in detail, there are indications that major struts should not deviate from the elastic stress trajectories by more than 15 degrees (1).

An alternative method for developing strut-and-tie models based on estimated load paths is presented by Schlaich and his co-workers (1). Figure 2.28 demonstrates the load path method for a typical D-region. First, the equilibrium of the D-region is satisfied. The internal stresses on the boundaries are then computed. The boundary stresses are subdivided and force resultants determined so that each resultant force has a counterpart on the opposite boundary. A suitable load path between the resultant forces is then drawn. Load paths should follow the most direct route between forces and should not cross one another. After drawing the load paths a strut-and-tie model may be constructed. This approach may also be used in conjunction with elastic stress trajectories as an aid in model development.

The model selection procedure is complicated by the fact that, for any given detail, there may be more than one valid model configuration. A consideration in evaluating alternative model configurations is that loads will follow the path with the least deviations. Since the concrete struts are for the most part undeformable in comparison to the tension ties, the model should be

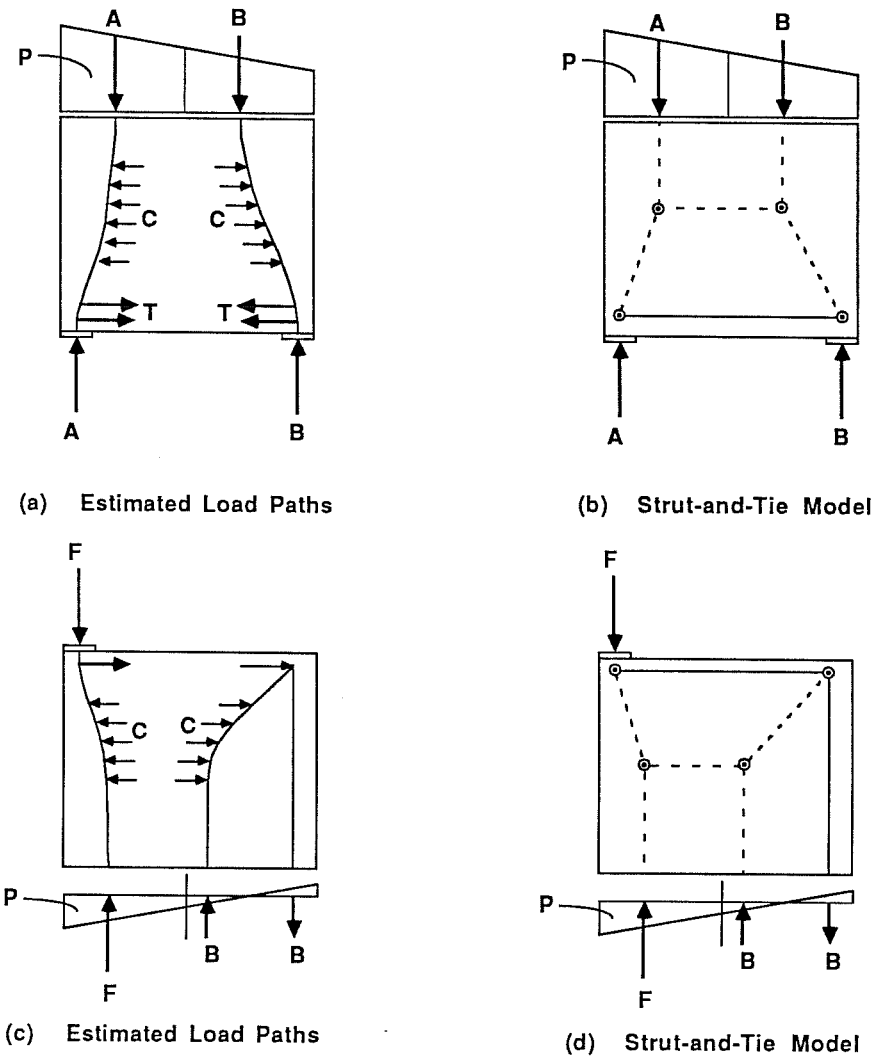

Fig. 2.28 Load Path Method for Estimating Stress Paths (Adapted from Ref. 1)

chosen to minimize the volume of reinforcement (1). Figure 2.29 illustrates two examples of this concept.

In summary, specific guidelines for model development have not been proposed. The designer must rely heavily on judgement and practical considerations in combination with strut-and-tie model principles in the development of a suitable model.

2.6 Summary

The strut-and-tie model is a unified design concept that permits consistent treatment of all portions of a structure. It is a generalization of the well known truss analogy which has been used extensively as a conceptual model for concrete beams subjected to shear, bending, and torsion. Strut-and-tie models have their basis in the theory of plasticity, but they may be applied by using a consistent set of rules without the need of complex theories.

The method is especially helpful in detailing situations for which no rational design procedure exists. The designer must envision the flow of forces within a detail and provide a viable means of transferring the forces. This promotes a better understanding of actual structural action.

Despite the advantages of the strut-and-tie model, portions of it lack adequate definition and have not been extensively verified through tests. Further research in the application of strut-and-tie models to various design situations is needed. Specific areas in which further guidance is required include:

1. Distribution and spacing of reinforcement in ties

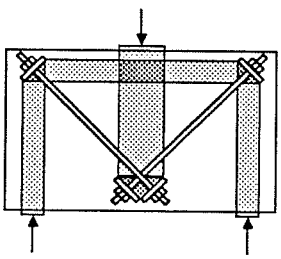

(a) Poor Model

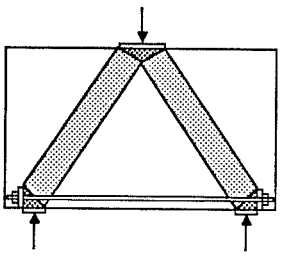

(b) Good Model

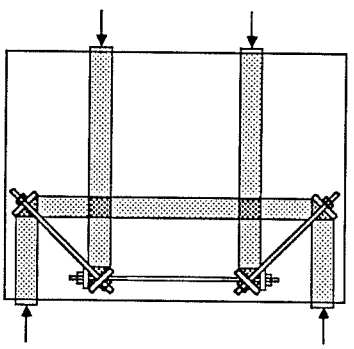

(c) Poor Model

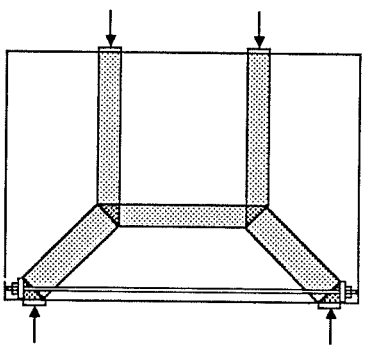

(d) Good Model

Fig. 2.29 Optimizing the Model (Adapted from Refs. 1 and 14)

2. Allowable concrete stress levels
3. Nodal zones
4. Serviceability criteria

In the next chapter, the experimental program investigating the behavior of a CTT-node is outlined. The test variables, specimen design and fabrication, and testing procedures will be described.

CHAPTER 3

TEST PROGRAM

3.1 Introduction

The purpose of the test program was to better quantify the nodal region behavior of the strut-and-tie model. In the early stages of this study, difficulties in designing members with the strut-and-tie model raised questions about the model's practical implementation. Particularly, the design work revealed that the existing state of knowledge did not allow the strut-and-tie model's application to complex detailing situations. The nodes were quite troublesome. There was difficulty in determining the size of the nodes which is a necessary part of concrete stress checks associated with the modelling procedure. The size of the area in which the strut and tie forces are redirected classifies nodes as either singular or smeared. Further problems involved assessing the configuration of the compression field, that is, whether it was a fan, bottle, or prism. Lastly, little information was available in determining the effect of differing compression strut angles on the various nodes.

A test program was implemented to provide experimental verification for the nodal area problems mentioned previously. To compliment research being conducted on a full-sized, dapped beam, part of a larger research program, an investigation of an isolated node was proposed. The description of the research study for the full-sized, dapped beam used as the prototype specimen for the elemental tests is presented by Barton (17). In the following presentation, pertinent information concerning the prototype beam

is summarized in an effort to establish the relationship between the elemental and full-sized tests.

A Compression-Tension-Tension (CTT) node was selected for the elemental study because it was a critical node type appearing often in structural members and it was one of the four principal nodes mentioned in the work Schlaich, Schäfer, and Jennewein (1). It appeared that it could be readily duplicated in laboratory tests. The CTT-node is an intersection of a concrete compressive strut and two tensile ties. In this study, mild steel reinforcement was used for all tensile ties. Every effort was made in trying to duplicate the prototype specimen's boundary conditions in the elemental study of the CTT-nodes.

Nine isolated CTT-node tests were conducted on two series of specimens. In one series, high strength concrete specimens were used while in the other series low strength concrete specimens were used. The design concrete strength for the specimens in the high strength series was 6000 psi - the same strength as in the full-sized, dapped beam. Half of this strength, or 3000 psi, was chosen as the design concrete strength for the low strength series. It was thought that this would give a suitable range for investigating the influence of concrete strength on CTT-node behavior. One specimen in each series incorporated a reduced compression strut width for determining the allowable concrete stress at the node boundary and the configuration of the compression stress fields. To study the effect of lateral confinement, each series contained specimens with differing confining reinforcement details. Other specimen variations included: 1) changing the anchorage detail for a

high strength specimen; and 2) changing the angle of inclination of the compression strut for a low strength specimen. A replicate specimen was also tested to provide information about the repeatability of the testing procedure. The specimen size, location and type of instrumentation, method of fabrication, and testing procedure were similar for all the specimens

3.2 Specimen Identification

A systematic pnemonic identification system was developed for this study. Each isolated CTT-node was designated by an identification scheme in the form of "XXXX-X". Identification of each letter modifier is given as follows:

1. First Modifier-Concrete Strength

   "**H**" - **H**igh
   "**L**" - **L**ow

2. Second Modifier-Strut Width

   "**F**" - **F**ull (10.6 in.) width
   "**H**" - Approximately **H**alf (4.0 in.) width

3. Third and Fourth Modifiers-Reinforcement and Strut Angle

   "**SR**"- **S**tandard **R**einforcing Detail-Confining transverse reinforcement, hooked longitudinal steel, and 45° strut angle
   "**NC**"- **N**on-**C**onfining transverse reinforcement with 45° strut angle
   "**AC**"- **A**ngle **C**hange 45° to 30° and standard reinforcing detail
   "**SB**"- **S**traight **B**ar anchorage on the longitudinal steel with confining transverse reinforcement and 45° strut angle

4. Fifth Modifier-Suffix for Specimens HFSR-A and HFSR-B only.

   "**A**" - First companion specimen
   "**B**" - Second companion specimen

The full-sized, dapped beam is not identified by the pnemonic system; however, it will be formally identified as the Prototype Beam Specimen henceforth.

3.3 Specimen Design

Each isolated node specimen was designed to duplicate as closely as possible the boundary conditions that existed in the full-sized, dapped beam. The placement and amount of steel in the Prototype Beam Specimen and the node specimens were identical although differing anchorage details were used in some of the node specimens. The prototype and node specimens also had the same width. The principle design criteria for the isolated CTT-node was its physical geometry. Proposals presented by Schlaich et al. (1), Schlaich and Schäfer (20), and Marti (15) give some insight as to the dimensioning of nodes and were used as a basis for choosing the specimen's size. The design method used is essentially the "state of the art" as explained in current literature combined with a fair amount of engineering judgement.

The physical dimensions of the node specimen were governed by the layout of the original strut-and-tie model developed for the full-sized, dapped beam (See Fig. 3.1 (a)). The corresponding placement of reinforcement is shown in Fig. 3.1 (b). The isolated CTT-node is shown in Fig. 3.1 (c). From this point on, tensile ties in the isolated CTT-node shall be identified by their purpose in the full-sized, dapped beam. Tensile ties 1 and 2 shall be designated as transverse and longitudinal ties, respectively.

The requirement of applying tension to each tie demanded that the reinforcing steel protrude from the node specimen an appropriate amount so

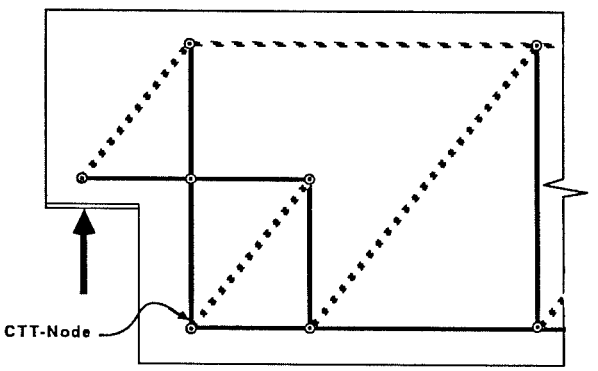

(a) Strut-and-Tie Model for Full-Sized Dapped Beam

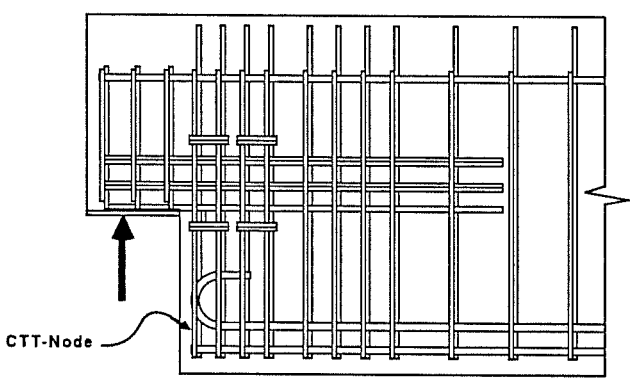

(b) Corresponding Placement of Reinforcement

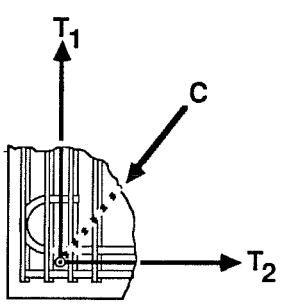

(c) Isolated CTT-Node

Fig. 3.1 Scope of Elemental Study

that it could be anchored to the test setup's loading system. The loading expectations were quite demanding and required the fabrication of heavy steel members for loading the isolated specimens. Holes in the steel members were drilled in a pattern corresponding to the pattern of the reinforcement. The loading system was inflexible in that it could not accept another reinforcement pattern without fabrication of another steel loading member. For this reason, identical reinforcement patterns were used for all specimens tested in this study.

As previously discussed, the strut-and-tie model designates nodes as either singular or smeared depending on the size of the area in which the strut and tie forces are redirected. Because of the close proximity of the transverse reinforcement in tensile tie 1, a smeared node approach was used. The dimension of this section of the node was governed by the stress field produced by tensile tie 1. The boundaries of the stress field produced by the longitudinal steel in tensile tie 2 were chosen to extend from the bottom of the beam an equal distance away from the center of gravity of the longitudinal steel. The points of intersection of the two stress fields are labeled A and B in Fig. 3.2 (a). The geometrical center of the CTT-node was considered to be the centroid of the two tension fields. A 45° dashed line corresponding to the inclination of the compression strut was drawn through the node's centroid. Equidistant lines parallel to the 45° inclined line were extended from A and from B until the transverse tie boundary, marked by point C was reached. Thus, the width of the compression strut was determined and extends between the points C and D shown in Fig. 3.2 (b).

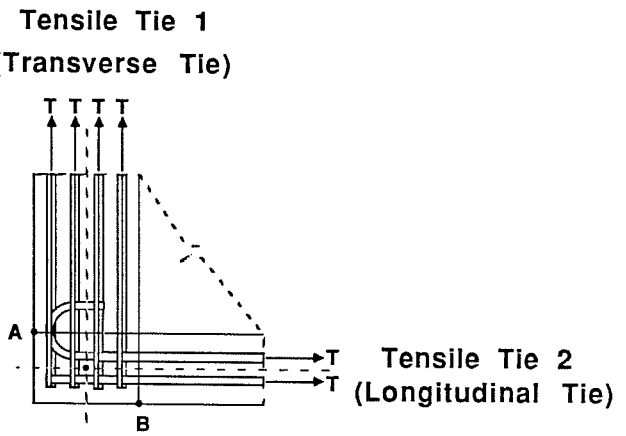

a) Points of Intersection of Tensile Stress Fields

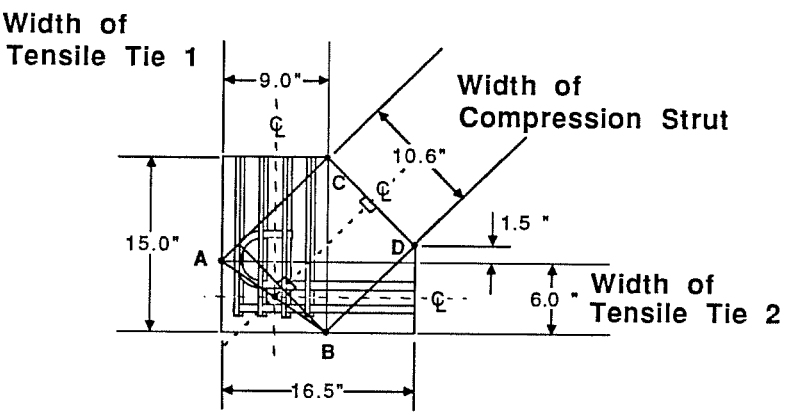

(b) Geometry of CTT-Node

Fig. 3.2 Determination of Node Boundaries

3.4 Specimen Details

Specimens HFSR-A, HFSR-B, and LFSR used identical steel reinforcement details as the full-sized, dapped beam. Of the nine node tests, Specimens HFSR-A and HFSR-B most closely resembled the CTT-node in the full-sized, dapped beam. They had similar concrete strengths, as well as comparable compression strut widths. Specimen HFSR-A was the first node specimen tested in this study and was used to demonstrate the applicability of the test method. Specimen HFSR-B was a companion specimen to HFSR-A and provided information about the repeatability of the tests. Specimen LFSR had the same reinforcement pattern as HFSR-A and HFSR-B but had a reduced concrete strength. Figure 3.3 shows the geometries for Specimens HFSR-A, HFSR-B, and LFSR.

Two specimens, one with high strength concrete (HHSR) and one with low strength concrete (LHSR), used reduced compressive strut widths. Reducing the strut width was accomplished by decreasing the bearing area at the compression face of the specimen. The strut width was chosen so that the average compressive stress was equivalent to f'c in the lower strength concrete specimen near the test setup's loading capacity. The same strut width was used in Specimen HHSR so the two could be compared. Except for a decreased bearing area, Specimens HHSR and LHSR had the same dimensions and steel placement as HFSR-A, HFSR-B and LFSR. Figure 3.4 shows the difference between the two sizes of bearing areas. Identical specimen size facilitated casting and specimen construction. Also, it reduced the number of test variables when comparing test results. The strut width was decreased by

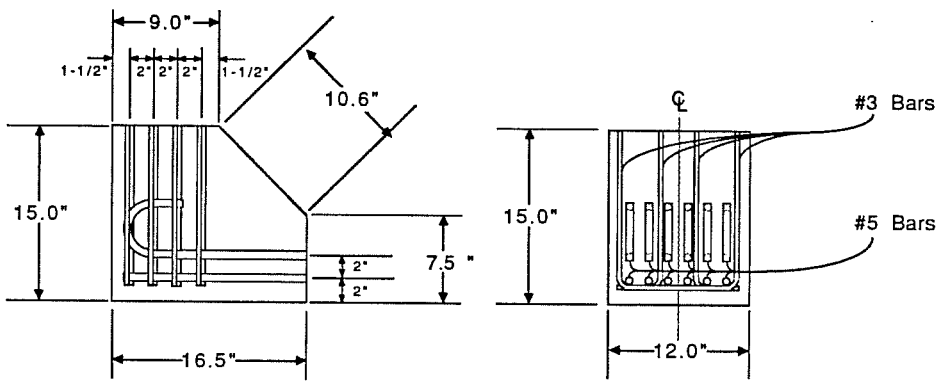

(a) Side View (b) End View

Fig. 3.3 Geometry and Placement of Steel for Specimens HFSR-A, HFSR-B, and LFSR

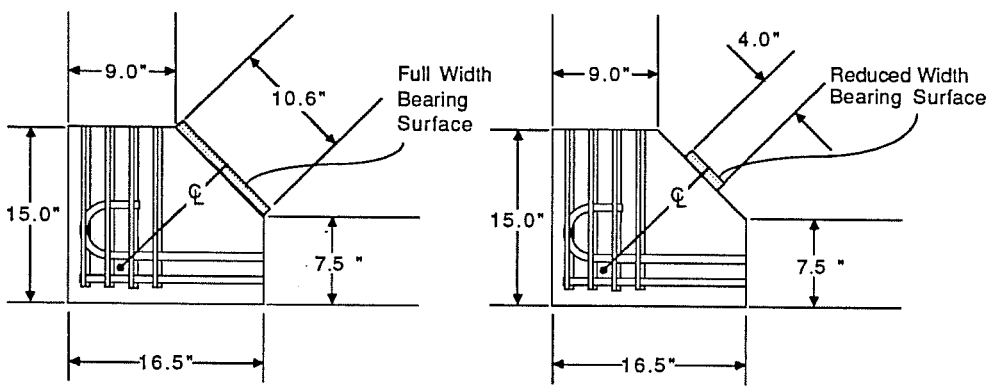

(a) Typical Full Width Bearing Surface (b) Reduced Bearing Surface for Specimens HHSR and LHSR

Fig. 3.4 Bearing Surfaces Used for Isolated Tests

gluing styrofoam strips adjacent to the bearing area at the specimen compression face. The styrofoam allowed only small bearing stresses to develop and thus concentrated compressive forces on the reduced bearing surface.

Each series contained specimens that were detailed with and without confining reinforcement to study the effect of lateral confining pressure on node behavior. Figure 3.5 (a) shows that confinement of the CTT-node was accomplished by placing U's and 90° hooks perpendicular to the longitudinal bars. Identical reinforcement details were used in the isolated node and the Prototype Beam Specimen. Specimens LFNC and HFNC were designed and constructed to minimize the effect of lateral confinement. Transverse reinforcement anchorage hooks were turned nearly parallel to the longitudinal bars. This detail is shown in Fig. 3.5 (b).

Specimen HFSB was tested to determine the behavior of a CTT-node with a different anchorage detail for the longitudinal steel. Specimen HFSB is identical to HFSR except the 180° hook was removed from the top longitudinal steel. The reinforcement used in Specimen HFSB is shown in Fig. 3.6.

Specimen LFAC was the only specimen in this study that was subjected to unequal forces in the tension ties. The purpose of the unequal force was to induce a different compression strut angle into the specimen. A 30° angle from the horizontal was chosen so the force in the longitudinal steel would be approximately 1.7 times the force in the transverse reinforcement. This angle would assure that the transverse steel would not reach its limiting capacity. Figure 3.7 shows the line of action of the compression strut force

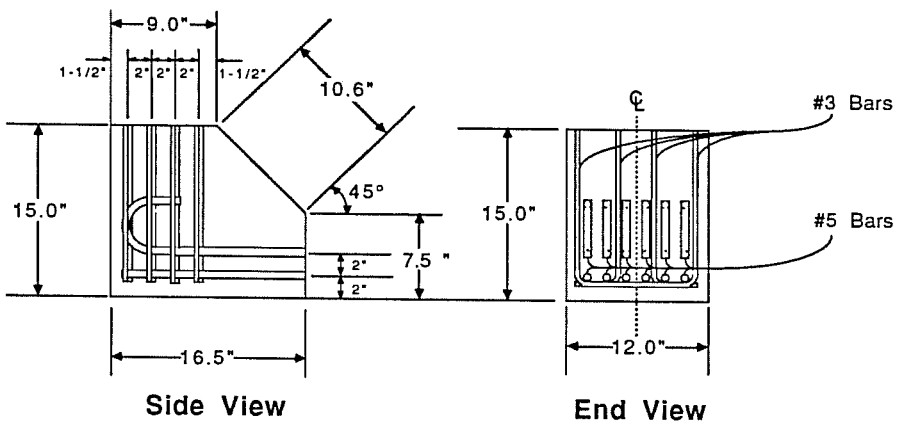

(a) Typical Confining Reinforcement Detail

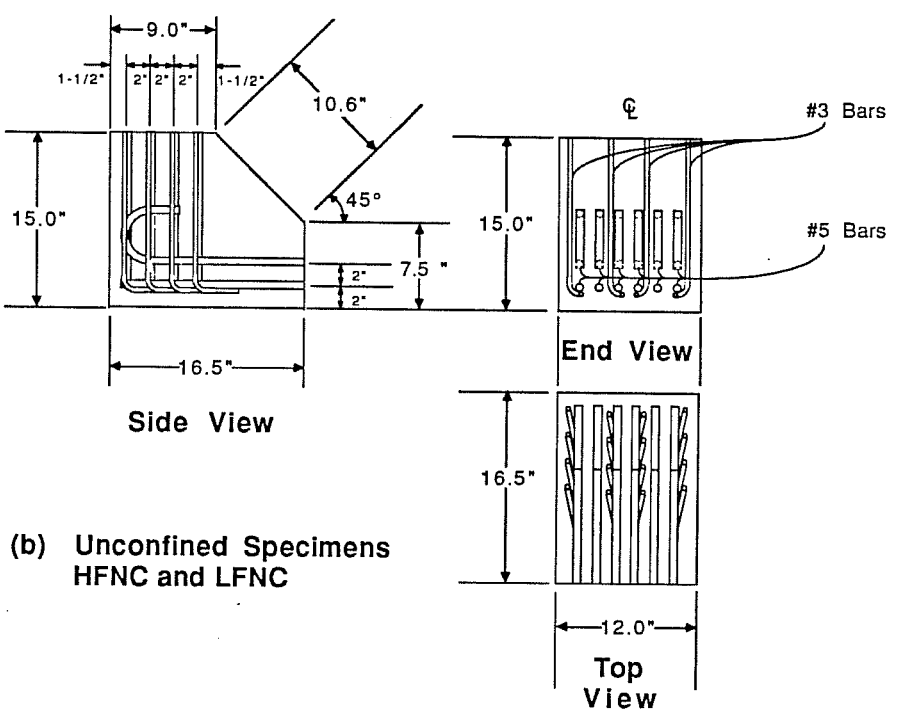

(b) Unconfined Specimens
HFNC and LFNC

Fig. 3.5 Details to Provide and Minimize Confinement

used in Specimen LFAC and all the other node specimens. Specimen LFAC was identical in construction to Specimen LFSR (See Fig. 3.8).

Specimen details for the two series of test specimens, along with the Prototype Beam Specimen, are summarized in Table 3.1.

3.5 Materials

3.5.1 Concrete. All test specimens were cast with concrete mixes complying with Texas Highway Department Standard Specifications. This standard specifies a maximum 5 in. slump, although actual slumps for different batches ranged from 3 to 6 inches. Concrete for Specimen HFSR-A and Specimen LFAC were mixed at the laboratory using a 6 cu. ft. drum type mixer. Batches for Specimen HFSR-A and Specimen LFAC were 5 and 6 cu. ft., respectively. Both mixes used Type I Portland cement with washed Colorado River sand as the fine aggregate. Coarse aggregate for Specimen HFSR-A consisted of crushed limestone with 1/2 in. maximum aggregate size. Coarse aggregate for Specimen LFAC was crushed dolomitic limestone with a 5/8 in. maximum aggregate size. All other specimens were cast using commercially available ready mix concrete. This concrete consisted of Type I Portland cement, washed Colorado River sand and gravel with a maximum aggregate size of 3/4 in. Tables 3.2 thru 3.5 give the concrete mix designs for each of the four batches. Figures 3.9 - 3.12 give the compressive strength versus time developed for each concrete mix. Compression tests were performed at 7 days and on each test day to develop the strength curves. Compression tests were also performed at 28 days if the specimen test day was not within one day of the concrete's 28 day age.

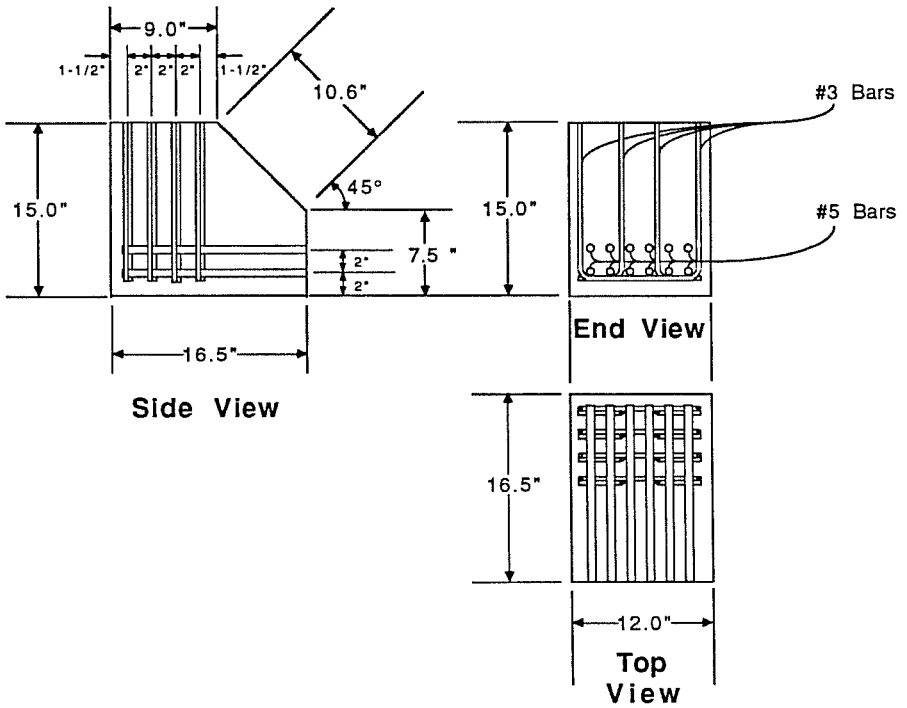

Fig. 3.6 Geometry and Placement of Steel for Specimen HFSB

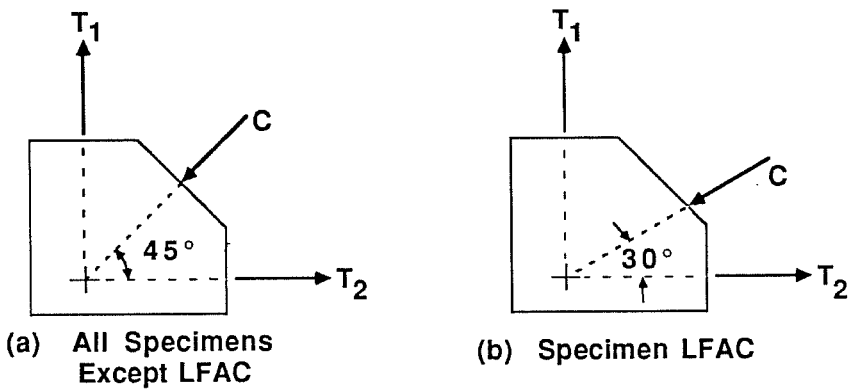

Fig. 3.7 Comparison of Specimen Strut Angles

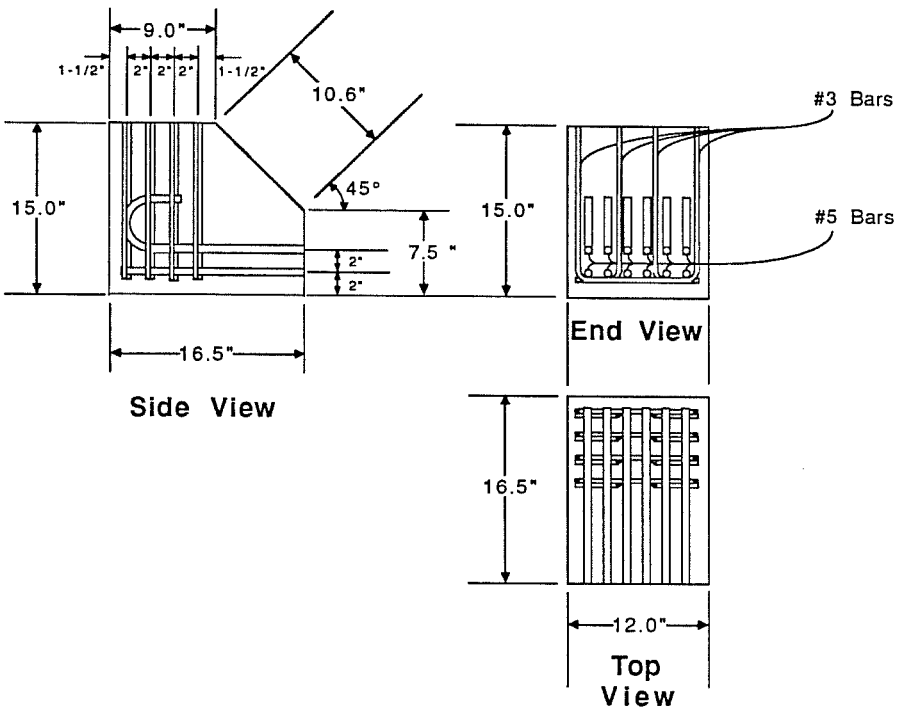

Fig. 3.8 Geometry and Placement of Steel for Specimen LFAC

Specimen	f'c (psi)	Strut Width (in.)	Conf. Trans. Reinf.	Angle of Loading	#3 Bars fy (ksi)	#5 Bars fy (ksi)	#5 Bar Anchorage Detail	Splitting Tensile Strength (psi)
Prototype Beam Specimen	6280	Not Applicable	Yes	51°-Design	66.8	60.5	180° Hook	Not Tested
HFSR-A	7010	10.6	Yes	45°	66.8	Not Applicable	180° Hook	440
HFSR-B	5780	10.6	Yes	45°	66.8	59.6	180° Hook	490
HHSR	5780	4.0	Yes	45°	66.8	59.6	180° Hook	490
HFSB	5780	10.6	Yes	45°	66.8	59.6	Straight Bar	490
HFNC	5780	10.6	No	45°	66.8	59.6	180° Hook	490
LFSR	3720	10.6	Yes	45°	66.8	59.6	180° Hook	410
LHSR	3720	4.0	Yes	45°	66.8	59.6	180° Hook	410
LFNC	3720	4.0	No	45°	66.8	59.6	180° Hook	410
LFAC	3920	10.6	Yes	30°	66.8	59.6	180° Hook	390

Table 3.1 Summary of Test Specimens

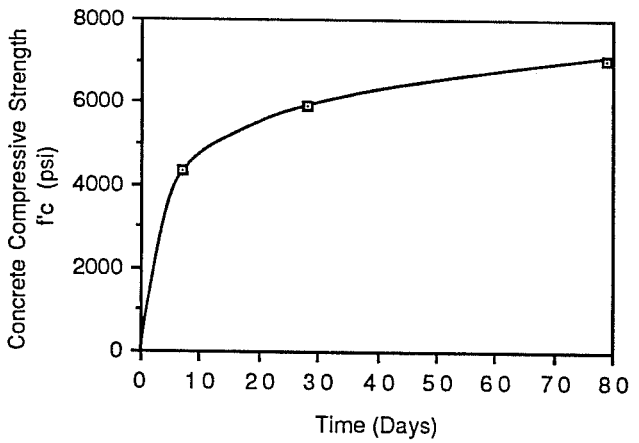

Time (Days)	f'c (psi)
7	4320
28	5930
79	7010

Fig. 3.9 Concrete Strength vs. Time for Specimen HFSR-A

Material	Batch Design			Final Batch Weights lbs./cu. yd.
	Volume cu. ft./sack	% Volume	Weight lbs./sack	
Coarse Aggregate	1.67	38	261	1568
Water	0.83	19	52	313
Cement	0.49	11	94	564
Fine Aggregate	1.40	32	230	1382

Cement Factor=6.00 sack/cu. yd.

Water Factor=6.25 gal/sack

Water/Cement Ratio (by Weight)=0.55

Slump=6.5"

Table 3.2 Concrete Mix Design for Specimen HFSR-A

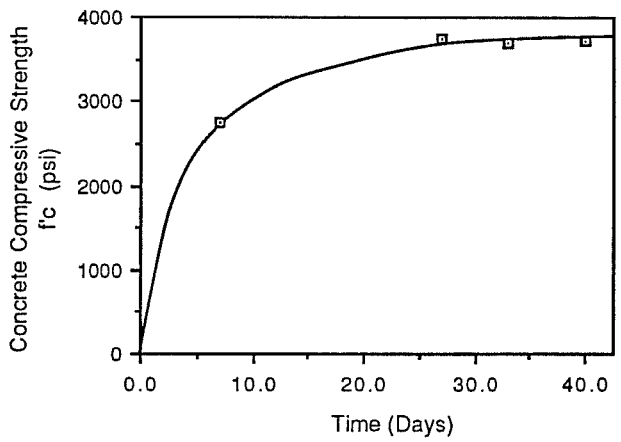

Time (Days)	f'c (psi)
7	2760
27	3740
33	3700
40	3720

Fig. 3.10 Concrete Strength vs. Time for Specimens LFSR, LHSR, and LFNC

Material	Batch Design			Final Batch Weights lbs./cu. yd.
	Volume cu. ft./sack	% Volume	Weight lbs./sack	
Coarse Aggregate	3.25	45	507	1886
Water	1.14	16	71	266
Cement	0.49	7	94	350
Fine Aggregate	2.34	32	386	1439

Cement Factor=3.75 sack/cu. yd.

Water Factor=8.5 gal/sack

Water/Cement Ratio (by Weight)=0.76

Slump=3.0"

Table 3.3 Concrete Mix Design for Specimen LFSR, LHSR, and LFNC

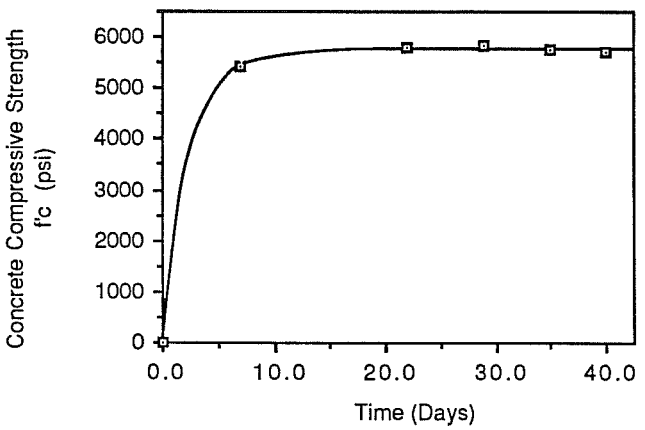

Time (Days)	f'c (psi)
7	5420
22	5780
29	5850
35	5780
40	5720

Fig. 3.11 Concrete Strength vs. Time for Specimens HFSR-B, HHSR, HFNC, and HFSB

Material	Batch Design			Final Batch Weights
	Volume cu. ft./sack	% Volume	Weight lbs./sack	lbs./cu. yd.
Coarse Aggregate	2.40	45	374	1870
Water	0.80	15	50	250
Cement	0.49	9	94	470
Fine Aggregate	1.68	31	277	1385

Cement Factor=5.00 sack/cu. yd.

Water Factor=6.00 gal/sack

Water/Cement Ratio (by Weight)=0.55

Slump=6.0"

Table 3.4 Concrete Mix Design for Specimen HFSR-B, HHSR, HFNC, and HFSB

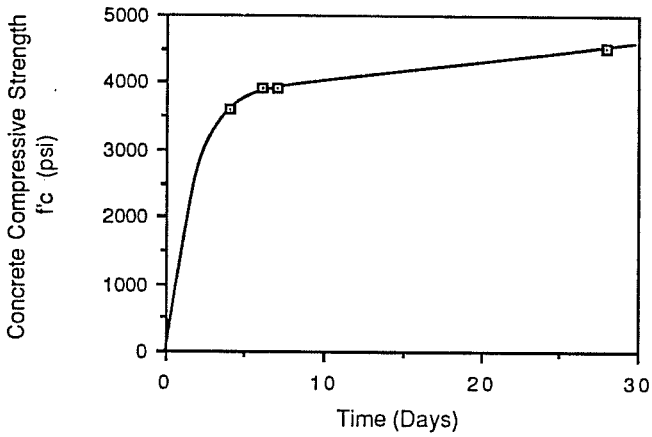

Time (Days)	f'c (psi)
4	3600
6	3920
7	3930
28	4520

Fig. 3.12 Concrete Strength vs. Time for Specimen LFAC

Material	Batch Design			Final Batch Weights lbs./cu. yd.
	Volume cu. ft./sack	% Volume	Weight lbs./sack	
Coarse Aggregate	1.82	38	285	1568
Water	0.80	17	50	275
Cement	0.49	10	94	517
Fine Aggregate	1.68	35	277	1521

Cement Factor=5.5 sack/cu. yd.

Water Factor=6.00 gal/sack

Water/Cement Ratio (by Weight)=0.53

Slump=4.5"

Table 3.5 Concrete Mix Design for Specimen LFAC

Split cylinder tests were conducted in order to determine the tensile strength of the concrete. Tests were conducted according to ASTM C496 with 1 in. wide x 1/8 in. thick birch plywood pads and a loading rate of 15,000 pounds per minute. Results of these tests are summarized in Table 3.1.

3.5.2 Reinforcing Steel. All node specimens used standard deformed bar reinforcing steel conforming to ASTM-A615. Grade 60 #3 bars used as transverse reinforcement in all the isolated CTT-nodes were produced in the same heat. Stress-strain characteristics of the #3 bars are shown in Fig. 3.13. Grade 60 #5 bars used as longitudinal reinforcement in Specimen HFSR-A were also from the same heat and have the stress-strain characteristics shown in Fig. 3.14. Because of the lack of a definite yield plateau, these bars were not used in further tests. Subsequent tests used Grade 40 #5 bars having the typical stress strain characteristics shown in Fig. 3.15. The Grade 40 reinforcement had a definite yield plateau and a yield point near 60 ksi.

Tensile coupons chosen from different bar lengths were obtained from each heat to determine the reinforcement's stress-strain characteristics. A mechanical test machine was used to conduct all tensile tests. Two coupons were loaded at a constant rate to obtain a good estimate of the yield point and ultimate stress. The remaining coupons from each heat were fitted with electrical resistance strain gages to monitor strain. Two gages, placed on opposite sides of the bar, were used on the #3 coupons and the Grade 60 #5 coupons to compensate for the effects of bending. The actual strain was the average of two readings. It was found that the effect of bending was quite

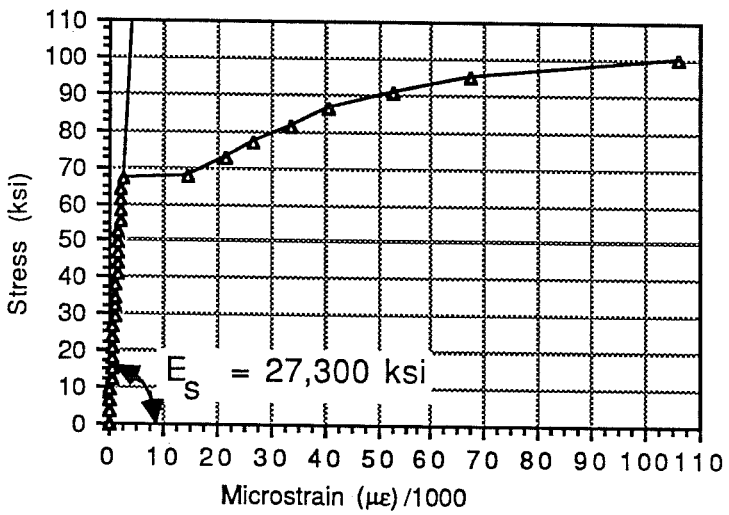

Fig. 3.13 Stress-Strain Curve for #3-Grade 60 Reinforcement

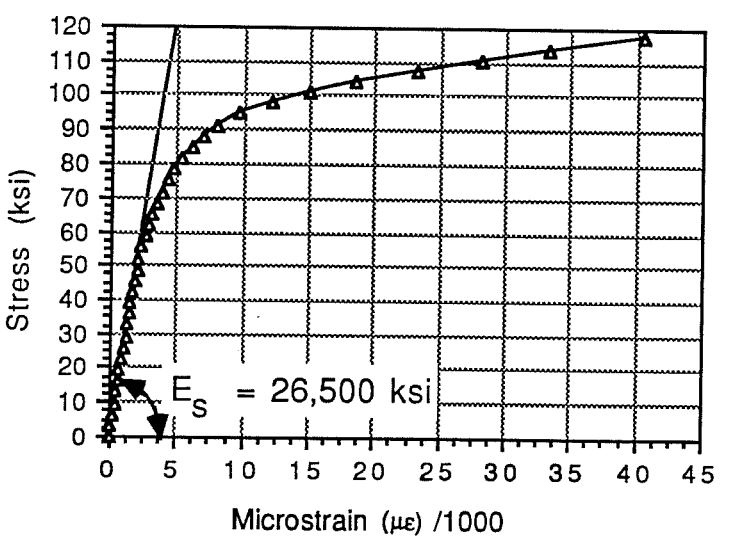

Fig. 3.14 Stress-Strain Curve for #5-Grade 60 Reinforcement

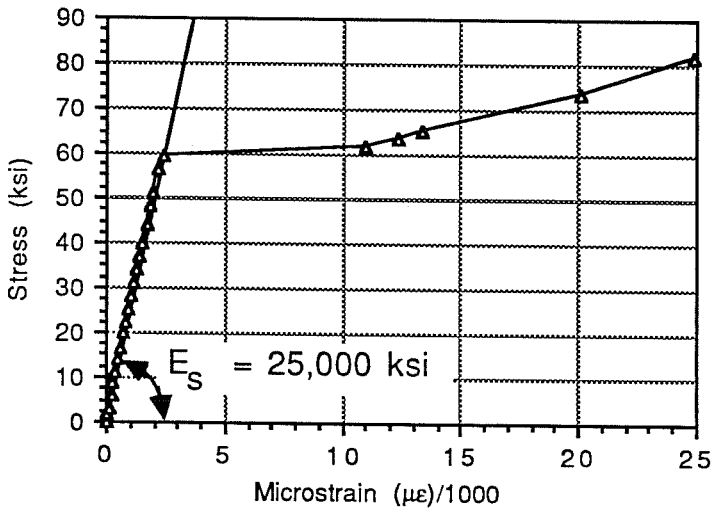

Fig. 3.15 Stress-Strain Curve for #5-Grade 40 Reinforcement

small for #5 coupons when they were properly centered in the jaws of the testing machine. Therefore, modulus tests on Grade 40 #5 coupons used only one gage. Because the strain gages would sometimes give erratic readings after 5000 $\mu\varepsilon$, the average strain after yield was determined by monitoring extension over a premeasured gage length. This method of measuring strain after yield was only used for the #3 coupons because knowledge of the complete stress-strain relationship was not required for the #5 steel reinforcement. Since only one or two gages were being monitored, several modulus tests were conducted using a portable strain indicator; however, this test procedure produced consistently high strain readings and these test results were disregarded. The portable strain indicator was replaced by a computerized data acquisition system in further tests. One modulus test using the computerized data acquisition system was conducted for each of the two heats of Grade 60 steel. Two modulus tests using the computerized data acquisition system were performed for the Grade 40 steel and the results of these tests were averaged to determine the modulus to elasticity. The yield and ultimate stresses for the various types of steels were obtained by averaging the results of the appropriate tests.

3.5.3 Mechanical Connectors. To allow easy removal of the isolated CTT-node from the test setup and to equalize the stresses in the bars before testing, each reinforcing bar protruding from the specimen was fitted with a mechanical connector with an integral adjusting nut. An Erico LENTON® connector was used for this purpose. All bar ends were threaded with tapered threads at the Erico Products Inc., Cleveland, Ohio facility. The mechanical

connector with adjusting nut was reused after each test. The mechanical connector could develop a bar stress of 85 ksi before the threads stripped. The limiting capacity of the threaded anchor was arbitrarily set at a bar stress of 75 ksi which assured the reinforcement would be well past yield when the test was concluded and also gave a 13% safety factor against connector failure. Adjusting threads on the exterior of the mechanical connector were cut at a close tolerance and had suitable length to prevent stripping of the adjusting nut. Figure 3.16 shows the mechanical connector with the adjusting nuts and the rebar threaded end.

3.6 Instrumentation

3.6.1 Strain Gages. All specimens in this study were heavily instrumented with electrical resistance strain gages mounted to the longitudinal and transverse steel. Interior gage locations were chosen to give information about the behavior and the transfer of forces within the node. Interior gages in the prototype and node specimens were placed in identical locations although more bars in the node specimen were instrumented. Location of the interior gages for all node specimens is shown in Figs. 3.17 - 3.20. Exterior strain gages were mounted on all protruding bars approximately 2 in. from the concrete. The exterior gages were used to obtain a uniform stress level prior to testing, and they also monitored bar stress levels during testing.

All gages mounted to the reinforcing steel had a foil backing and a gage length of 5 mm. Bar deformations were ground off and the area was sanded smooth before mounting the gages. The amount of sanding was kept to a

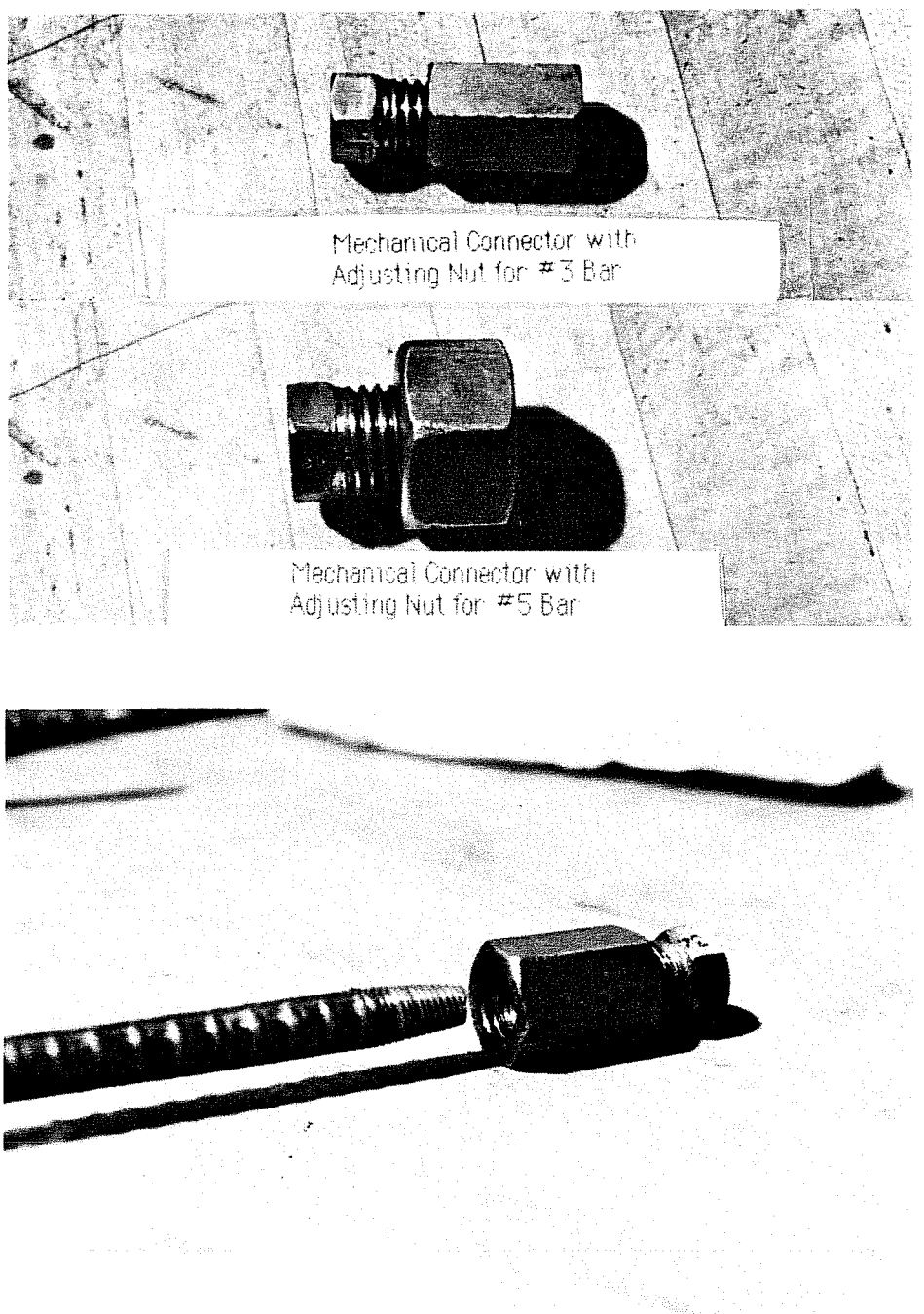

Fig. 3.16 Mechanical Connectors with Adjusting Nuts for #3 and #5 Bars

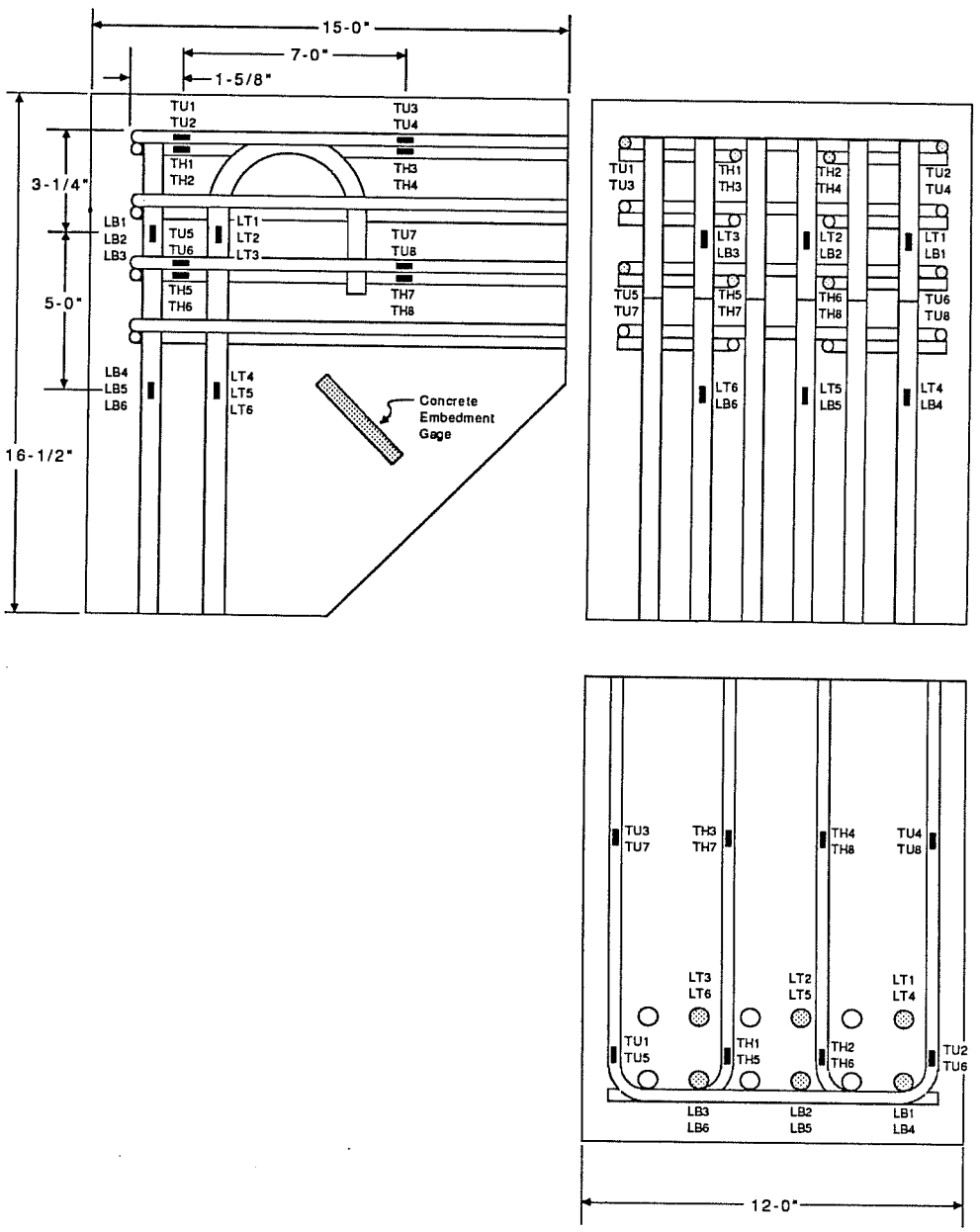

Fig. 3.17 Interior Gage Locations for Specimen HFSR-A

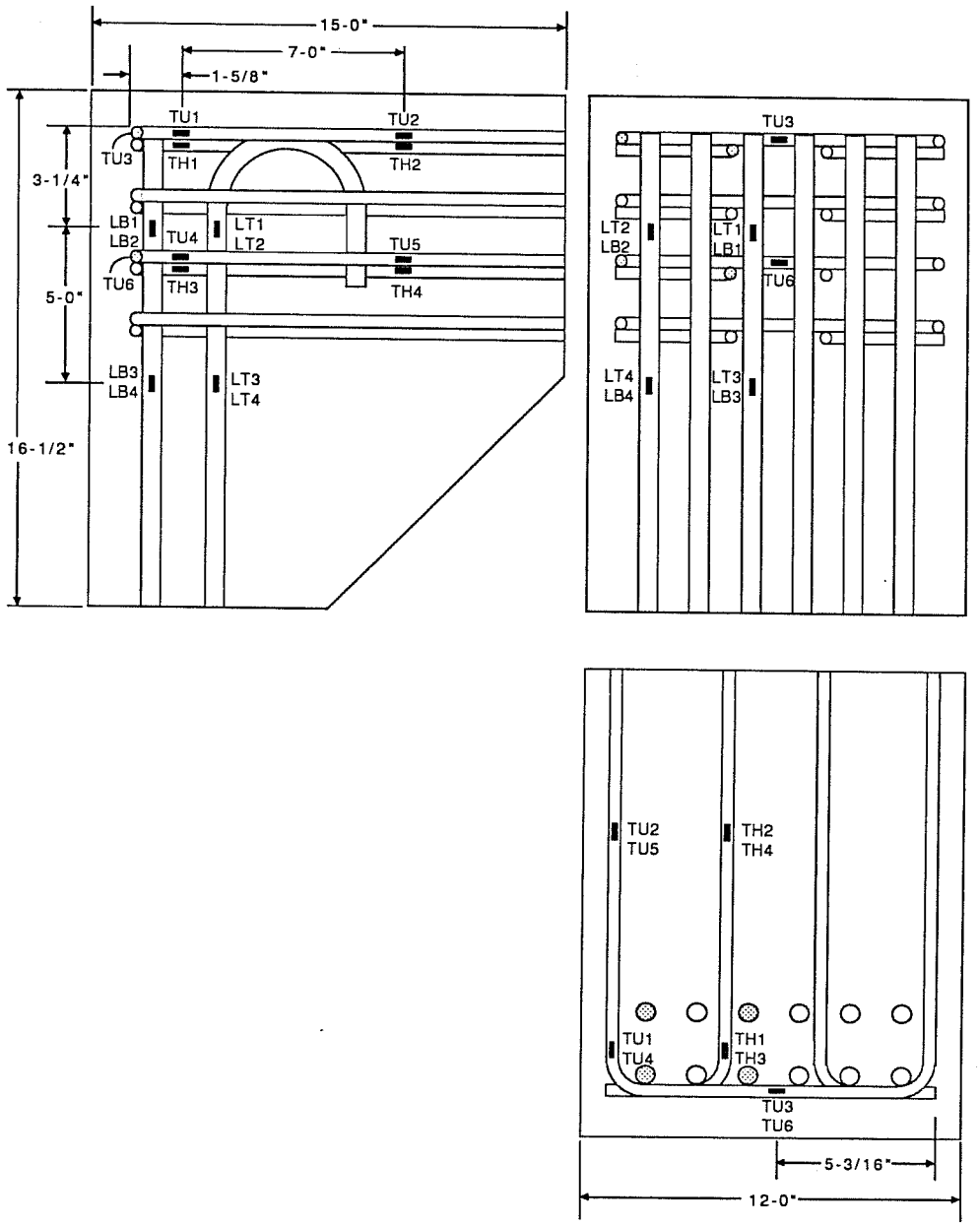

Fig. 3.18 Interior Gage Locations for Specimen HFSR-B, HHSR, LFSR, LHSR, LFAC

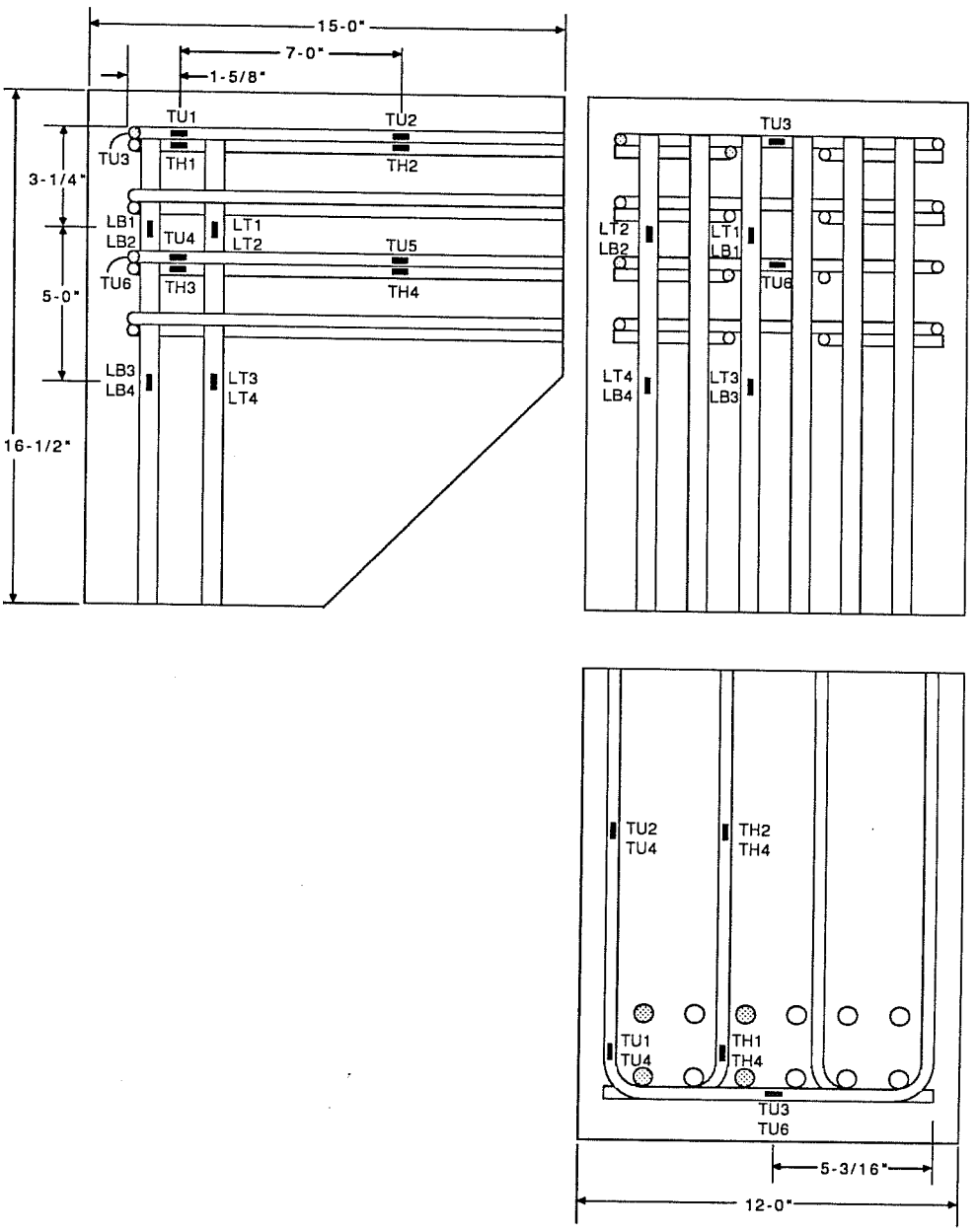

Fig. 3.19 Interior Gage Locations for Specimen HFSB

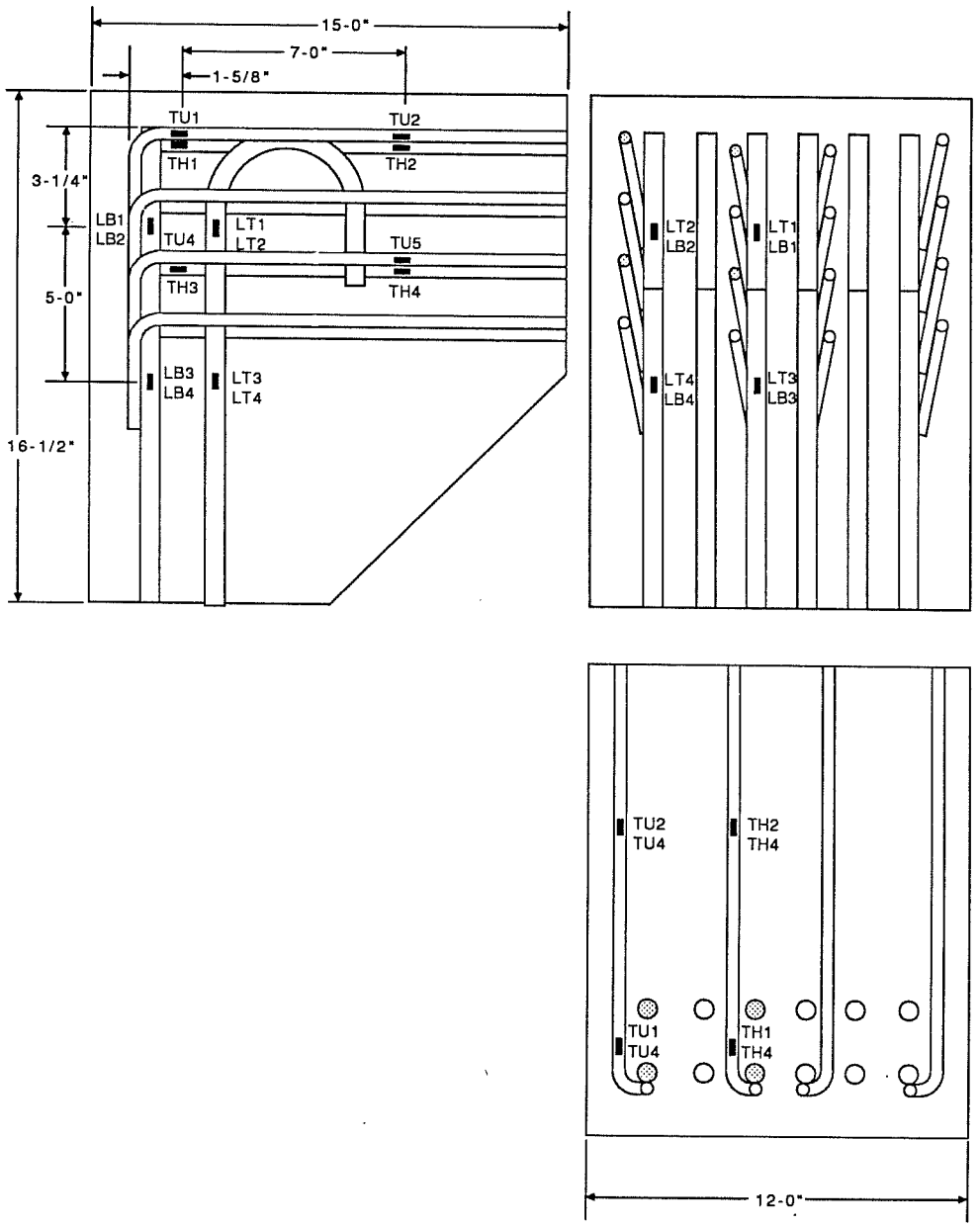

Fig. 3.20 Interior Gage Locations for Specimen HFNC and LFNC

minimum to reduce changes in the bar's cross sectional area. Exterior and interior gage locations for each specimen were ground and sanded at the same time. Interior gages were mounted immediately after sanding to reduce material oxidation. The sanded surface was first cleaned with acetone. A mild acid conditioner was then applied to this surface followed by a neutralizing solution. The surface was again cleaned with acetone prior to application of the gage. Gages were mounted using a special glue resin and universal catalyst. Special care was take to align the gage with the longitudinal axis of the bar. Once the gage was securely glued in place, 24 gage-3 conductor lead wires were solder connected to complete the circuit. A three-wire quarter bridge connection, which compensates for temperature effects in the lead wires, was made by twisting two of the lead wires together to make them common. A silicone rubber sealant was applied to waterproof the gage and lead wire connections. Plastic, self-locking ties were used to attach the lead wires to the bar to prevent the them from being pulled off. A pliable rubber sealant and neoprene rubber pad were placed over the gage to supply extra waterproofing and protect the gage from vibrators used during placement of concrete. The gages were checked with a multimeter for continuity and lead wires were properly tagged for identification.

An embedment strain gage was used in the Specimen HFSR-A to determine the strain in the concrete compressive strut. The embedment gage had a 60 mm gage length and was encased in a polyester/resin mold (125 x 13 x 5 mm) with a coarse grit surface. The embedment gage did not function

properly in the first test (Specimen HFSR-A) and was not used in further tests.

3.6.2 Hydraulic Force and Pressure Measurements. The specimen was loaded using double acting center hole rams with hand operated pumps. The applied load was determined by multiplying the hydraulic pressure by the effective area of the ram. Electronic pressure transducers, used in conjunction with a portable strain indicator, measured hydraulic pressure. A mechanical pressure gage was employed to assist in monitoring pressure during tests, but no attempt was made to run accurate cross checks between the pressure transducer and pressure gage.

Rams and pressure transducers used to apply and monitor load were all calibrated in a mechanical testing machine. During calibration, the head of the testing machine was held stationary as load was increased. Thus, the frictional characteristics of the ram packing were neglected. This procedure was felt quite valid because of the small deformations involved through most of the specimen test. Calibration plots are shown in Figs. 3.21 - 3.22.

A single loop system was used to load all specimens except LFAC. Pressure was applied to each ram through a single manifold; hence, equal forces were produced by each ram. The manifold pressure was monitored by a calibrated pressure transducer and strain indicator, a pressure transducer and data acquisition system, and a mechanical pressure gage. In contrast, a two loop system was used for Specimen LFAC. Each ram was loaded by a separate hydraulic system with no interconnection between the two. Hydraulic pressure in the separate loops was monitored by a calibrated

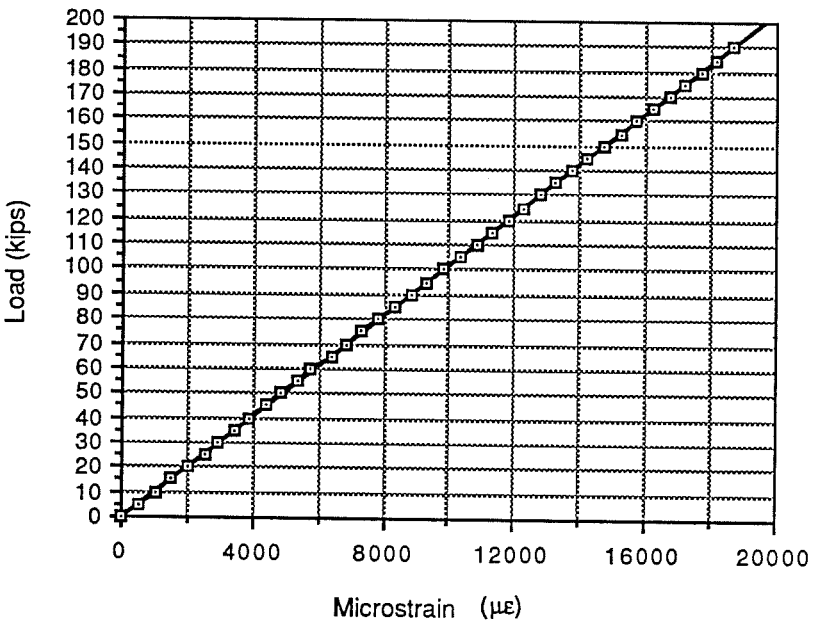

Fig. 3.21 Calibration Plot for Horizontal Pressure Transducer

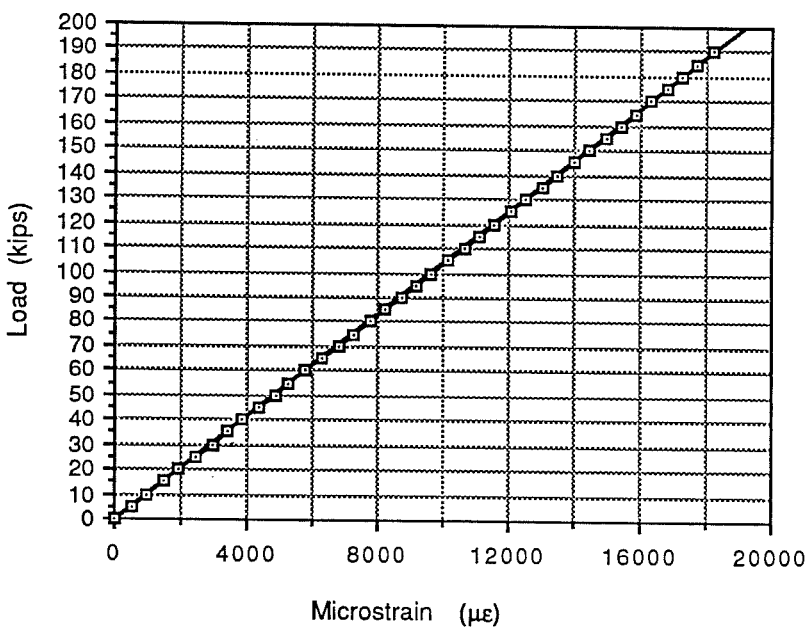

Fig. 3.22 Calibration Plot for Vertical Pressure Transducer

pressure transducer and strain indicator, pressure transducer and data acquisition system, and a mechanical pressure gage. Diagrams showing the scheme for applying and monitoring hydraulic force and presented in Fig. 3.23.

3.6.3 Linear Potentiometers. Electronic linear potentiometers monitored all deflections during testing. The linear potentiometers were located at the centerline of each stress field as shown in Fig. 3.24. The computerized data acquisition system processed and recorded the deflection readings. Potentiometers had a length of 2.00 in. with a standard linearity tolerance of $\pm$0.50%. This means the instruments were precise to the nearest 1/100 of an inch.

Removable brackets were epoxied to the test setup and were used to mount the linear potentiometers. If was felt the bracket distortion induced by strain in the test setup during specimen loading would be small. Also, the brackets were beneficial in removing clutter around the specimen and test setup.

3.6.4 Data Acquisition System. A Hewlett-Packard 3497A computerized data acquisition system was used to collect and record all test data. Constant voltage power supplies furnished the excitation voltage across unbalanced full and quarter bridge circuits. The data acquisition system used a high resolution digital voltmeter to measure the output voltage of each bridge circuit. The computer calculated the value for strain, deformation, or pressure from appropriate bridge circuit equations. Scans of instrument readings were initiated manually from the computer keyboard and this data

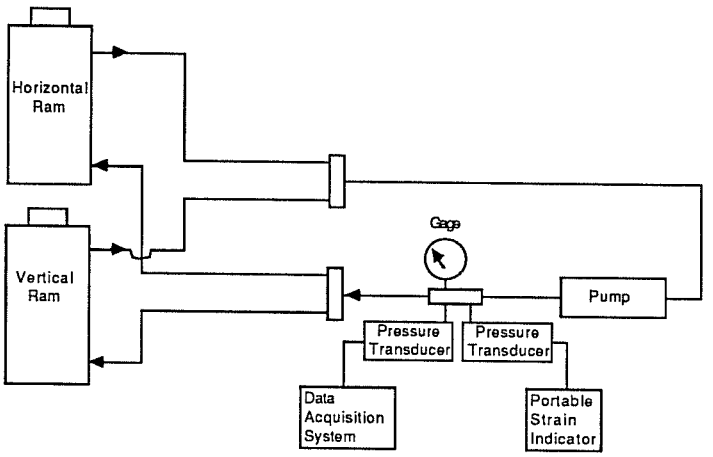

(a) Single Loop System

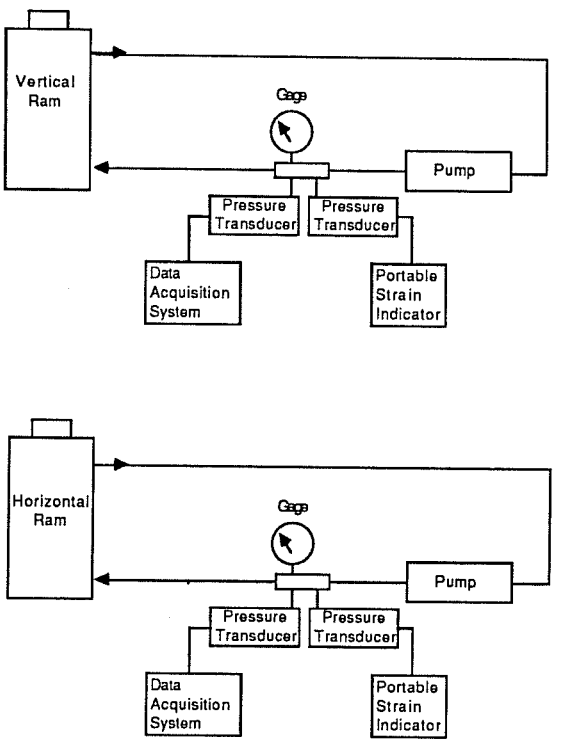

(b) Two Loop System

Fig. 3.23 Hydraulic Load Application and Monitoring System

was stored on computer disk. Hard copies of test data were also made with each scan.

3.7 Specimen Fabrication

Steel reinforcement for the specimens was cut to the proper length and was threaded for attachment of the mechanical connectors. Bars were detailed according to ACI Specifications. All reinforcement was bent cold.

Surface preparation at all gage locations and mounting of interior gages were performed prior to assembly of the steel cage. Exterior gages were not mounted; however, locations were given a light coat of lacquer to prevent oxidation of the sanded surface. Lead wires for the internal gages were tied together in an efficient manner to reduce interference with other reinforcement and internal vibrators. Lead wire bundles running out of the top of the specimen were wrapped in plastic bags.

Formwork for all specimens was constructed of 3/4 in. plywood reinforced with 2 in. x 4 in. studs at the corners. Inside form faces were puttied and sanded to remove irregularities. Form faces were painted with lacquer to waterproof them and reduce water absorption. A very light film of a light colored grease was applied to inside faces of the form to aid in removal. Side forms were bolted together at the corners. The bottom form was nailed to the side forms. The 45° corner form was glued in place using silicone caulk. All joints in the formwork were sealed with silicon caulk to prevent leaking.

The protruding reinforcement passed through holes predrilled in two sides of the formwork. These sides were bolted together first to serve as a

guide for placing the reinforcing steel. Standardized templates were drawn and followed when drilling to assure proper spacing of all the reinforcement. Longitudinal reinforcement was placed first, followed by the transverse reinforcement. The steel cage was tied together with 16 gage tie wire. Protruding reinforcement was aligned and restricted in movement by 3/4 in. plywood pattern pieces slipped over the bar ends. Special care was taken in aligning the reinforcement and guaranteeing its position. Grease was applied to bar ends to prevent rusting of the threads while the specimen cured. Figure 3.25 shows the assembled formwork and reinforcing cage for a typical specimen.

Slump tests initiated the casting operation. It was not necessary to add water to any of the mixes to increase slump. Concrete was placed and then consolidated using flexible shaft internal vibrators (See Fig. 3.26). The exterior of the forms were vibrated lightly to remove air bubbles. 6 in. x 12 in. test cylinders were cast simultaneously with the test specimens. The casting operation ended when all specimens and cylinders were troweled smooth.

Specimens were covered with wet burlap as soon as their surface was resistant to marring. This usually occurred after 4 hours. The burlap was, in turn, covered with a polypropylene plastic sheet to inhibit evaporation. Cylinders were capped with plastic covers. Removal of formwork for all specimens, except HFSR-B, HFNC, HHSR, and HFSB, occurred on the day following casting. The forms for HFSR-B, HFNC, HHSR, and HFSB were removed 3 days after casting. Cylinders were removed from the molds when

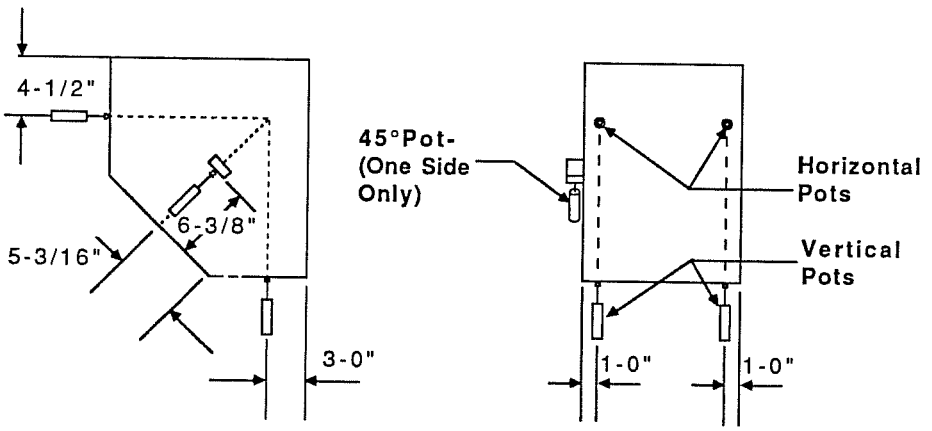

Fig. 3.24 Location of Linear Potentiometers

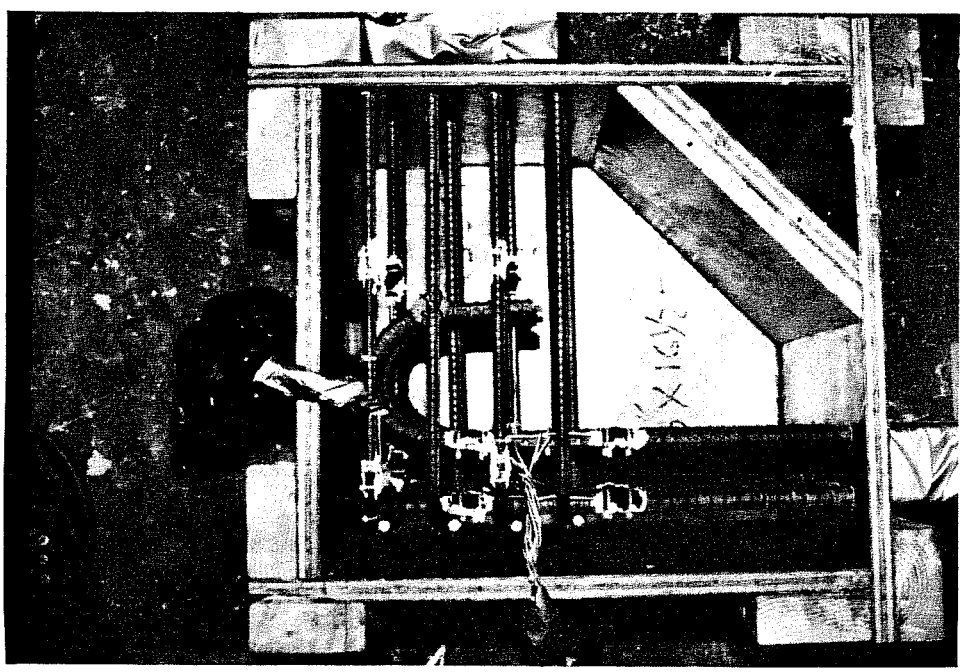

Fig. 3.25 Assembled Formwork and Reinforcing Cage

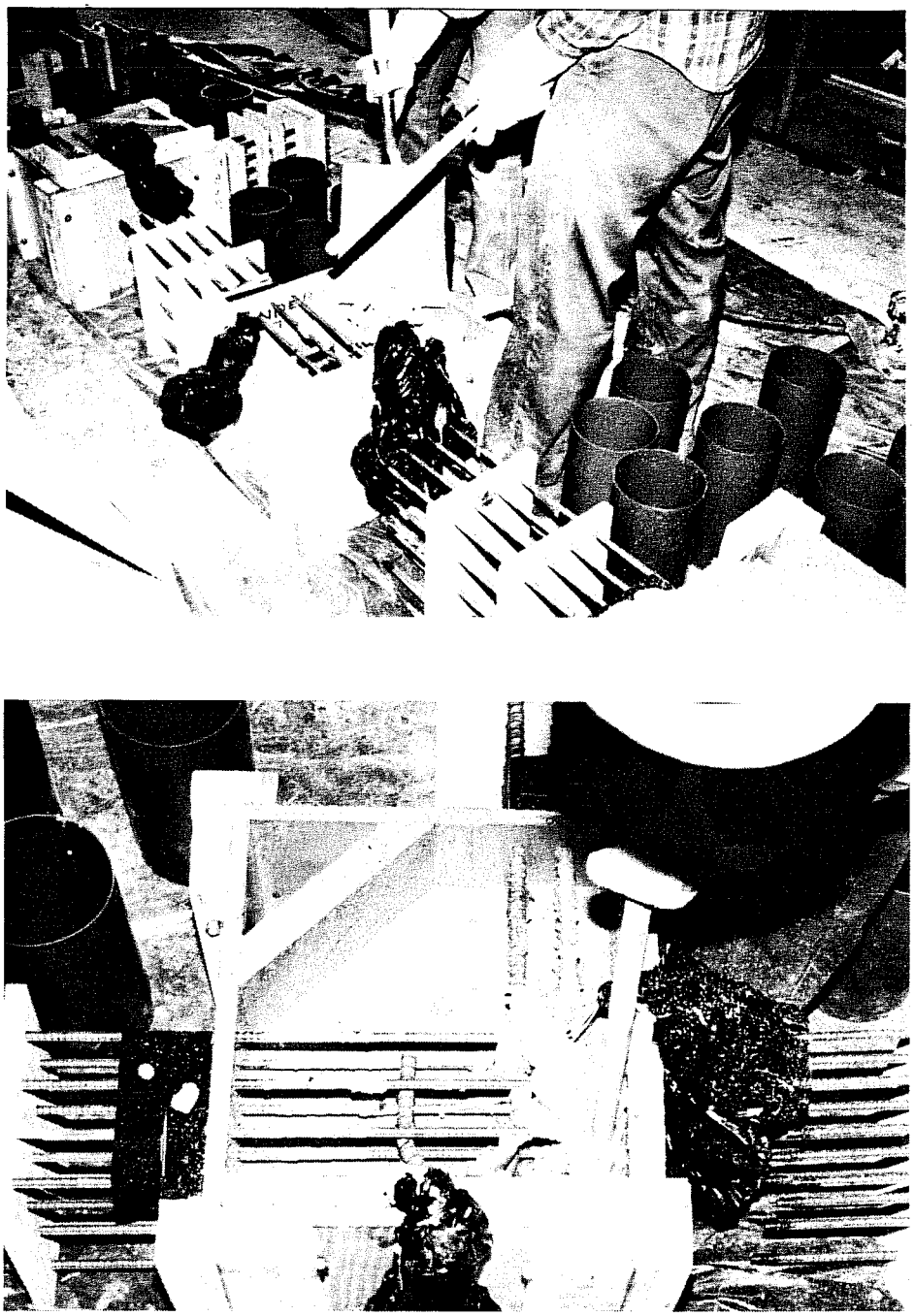

Fig. 3.26 Placement and Consolidation of Concrete

the formwork was removed. Moist curing ended with formwork removal except for Specimen HFSR-A which was moist cured 28 days. Destruction of the forms was necessary for removal because of the closely spaced, protruding reinforcement essentially clamped the forms into place. Care was taken to prevent damage to the specimen when prying off the formwork. Shrinkage cracks sometimes resulted because the formwork resisted movement of the reinforcing bars. These cracks were marked prior to specimen testing; however, the behavior of the specimen during testing did not seem to be affected by the shrinkage cracks. Therefore, they will not be discussed in the presentation of test results in Chapter 4.

The last step in specimen fabrication involved mounting the exterior gages. Gage locations were already sanded and coated with lacquer before casting and form removal. The lacquer coating was readily removed with acetone and the exterior gages were attached in the same manner as described in Sec. 3.6.1. Duct tape replaced neoprene as a protective covering for the exterior gages.

3.8 Test Setup

3.8.1 Concrete Reaction Block. A concrete reaction block was constructed for the purpose of transferring the load from the compression face of the test specimen to the floor and wall reaction system. The reaction block consisted of two components, the base block and the extension block. The extension block was designed to be removable so different angles of inclination of the compression strut could be investigated. An elevation view of the concrete reaction block is presented in Fig. 3.27.

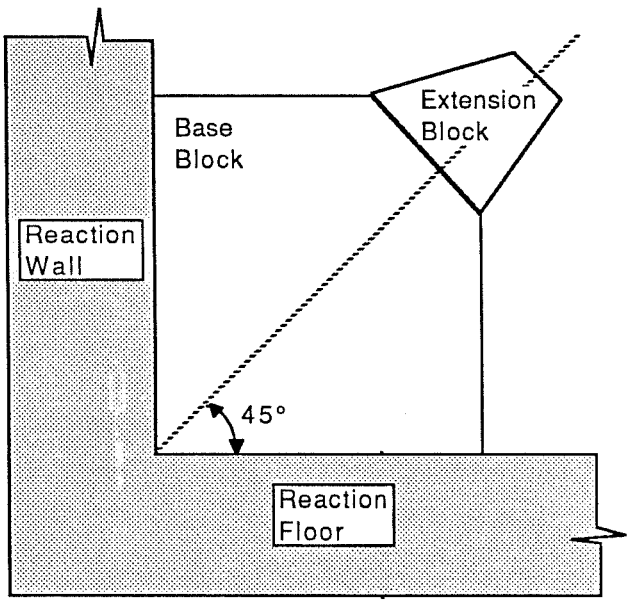

Fig. 3.27 Elevation View of Concrete Reaction Block

The extension block was post-tensioned to the base block using the Dywidag threadbar system and plate anchorages. First, a cement, water, and sand grout was thoroughly mixed by hand. A layer of the grout was then troweled onto the base block. The grout mixture was fairly stiff so that it would not slide off the base block's inclined surface. The extension block was then lowered into place using an overhead crane. Four 1 in. diameter, 150 ksi yield strength, Dywidag bars were used for post-tensioning. The bars were inserted through 2 in. ducts and plate anchors with anchor nuts were fastened hand tight at each end. Final alignment checks were made before the anchor nuts were further tightened by wrench. Because of construction tolerances, the alignment (in plan) of the base block and the extension block was off about 1/2 in. Corrections for misalignment were made during the specimen grouting operation and did not impede subsequent testing operations. Additional post-tensioning was accomplished using a center hole ram and hand operated hydraulic pump. The Dywidag threadbar was passed through a jack stand, then the center hole ram and was made snug with another nut. Each bar was tensioned to a force of 25 kips as monitored by a mechanical pressure gage. Extrusion of grout from the joint indicated that a uniform bearing was achieved. The post-tensioning force was checked after 3 days. If necessary, the Dywidag threadbars were retensioned to account for losses occurring in the newly hardened concrete grout.

Both the base block and extension block were designed and constructed to ensure a stiff setup. Concrete strength for the two pieces was 7800 psi at 28 days. Reinforcement and ductwork used for each piece is shown in Figs.

3.28 and 3.29. The extension block was designed for a uniaxial load of 650 kips which was approximately twice the test setup's loading capacity. Closely spaced ties were used to provide column confinement and for shear reinforcement should an unbalanced loading condition occur. The base block contained 2% temperature and shrinkage steel as its primary reinforcement. The base block's reinforcement was placed orthogonal to the 45° post-tensioning to prevent splitting along the diagonal.

The reaction block was bolted to the strong wall to resist the compressive forces developed during the tests. A cement, water, and minus 20 mesh sand were used to grout the reaction block to the floor. Construction tolerances required the use of shim plates at the vertical wall to allow for proper positioning of the reaction block. Hydrostone was placed between the reaction block and the reaction wall in the opening left by the shim plates. Both grouting measures were taken to provide uniform bearing surfaces under compressive load. A theodolite was "wiggled in" to establish the centerline of the two bolt groups used during testing. The reaction block was positioned by crane and plumbed with the theodolite so all three specimen reaction points would be in alignment.

3.8.2 Loading and Reaction System. The test setup allowed direct tension loading of the node specimen's protruding reinforcement in the horizontal and vertical directions. The tensile loading produced an equilibrating compression reaction at the specimen's bearing face. Space requirements and magnitude of loading did not permit insertion of tensile pull rams between the specimen and the strong wall and floor. Therefore, a

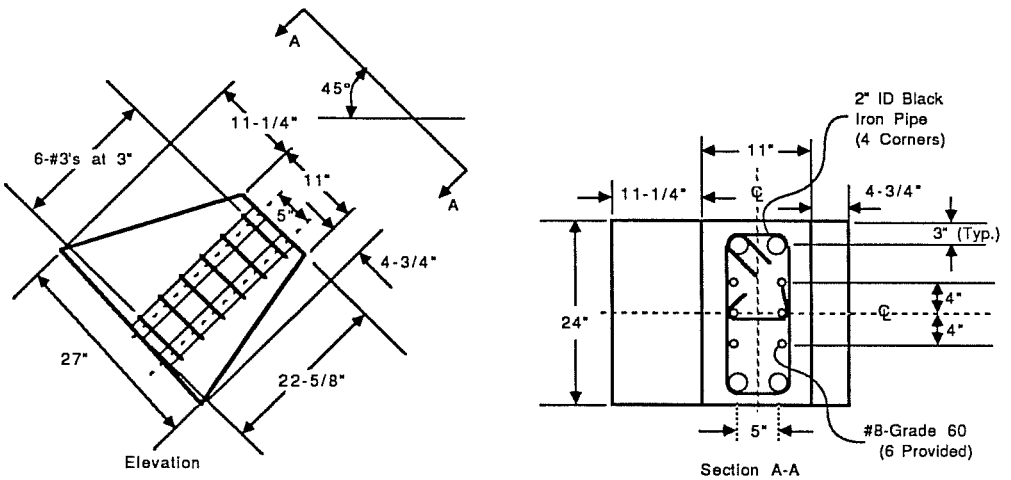

Fig. 3.28 Reinforcement of Extension Block

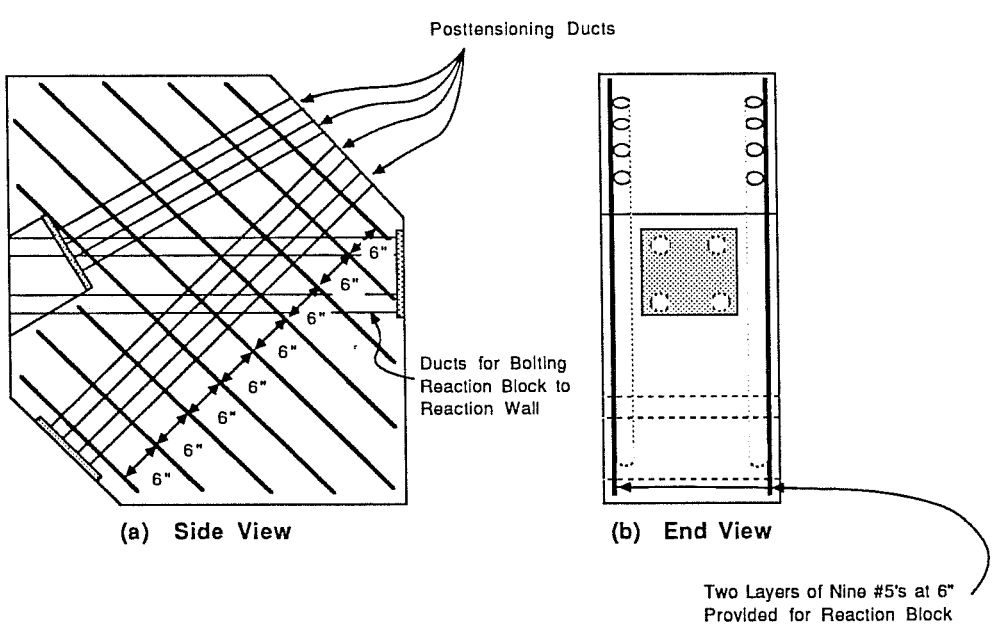

Fig. 3.29 Reinforcement of Base Block

loading system consisting of fabricated steel members and connected rods was assembled to allow tensile loading of the specimen by compressive rams. Elevation and plan views of the complete loading system are shown in Fig. 3.30 and 3.31, respectively. A photograph of the actual test setup is shown in Fig. 3.32. The top plates were anchored to the reaction wall and floor by means of connecting rods. When a ram was extended, it reacted against the top plate and bearing beam. Rods connecting the bearing beam and grasping beam transferred tensile force to the specimen's protruding reinforcement.

The grasping beams were 8 in. x 12 in. x 1/2 in. ASTM-A500 Grade B cold formed structural tubing. The tubes were stiffened at various locations to prevent buckling. A 3/4 in. cover-plate was added to increase strength and provide a smooth, flat bearing surface for the adjustable connectors. Holes were drilled through each grasping beam in a reinforcement pattern marked with standardized templates. After the holes were drilled, the stiffeners were welded in place. Pipe lengths were also welded in place for the purpose of guiding the specimen's protruding reinforcement through the section. A W14 x 120 ASTM A36 steel section was used as the bearing beam for the rams. Placing the ram between the flanges of this section made efficient use of space. Stiffeners were welded in place at the bearing beam reaction points to preclude web buckling. The top plates were 2 in. thick ASTM-A572 Grade 50 plate built up at the points of maximum flexural stress. 1-1/4 in. diameter ASTM-A193 Grade B7 rods connected loading system components. The bearing beams and top plates were load tested to a load of 190 kips prior to specimen testing.

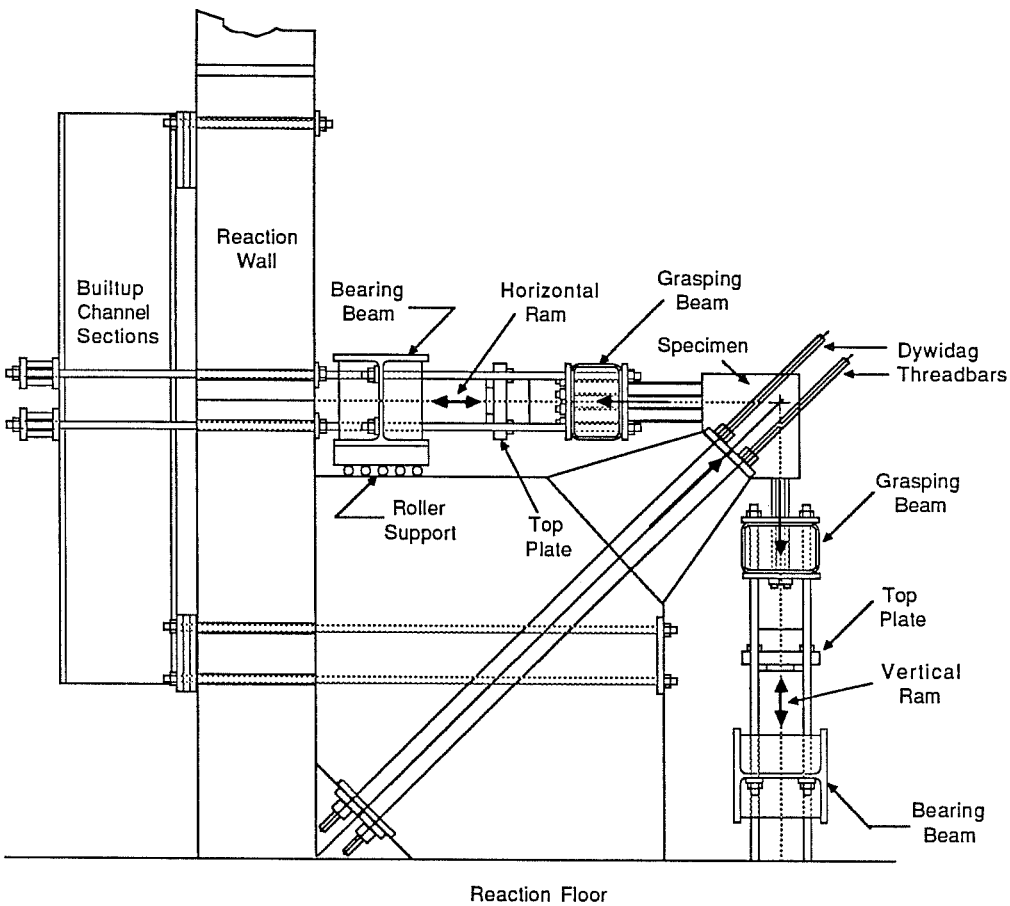

Fig. 3.30 Elevation View of Test Setup

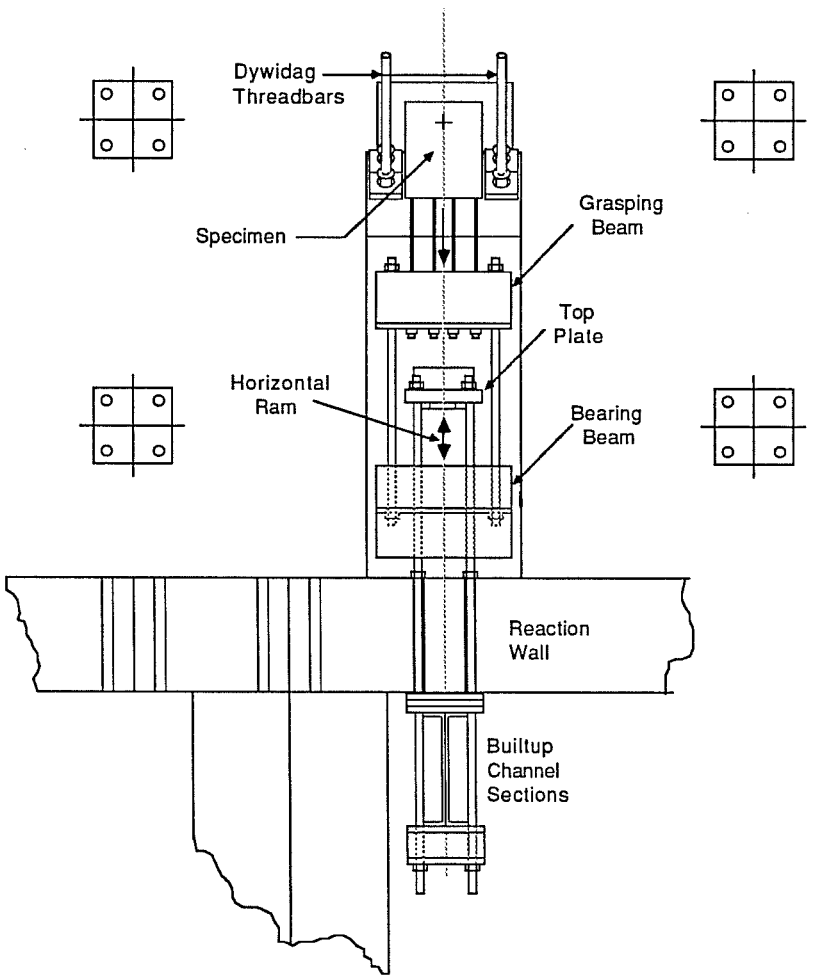

Fig. 3.31 Plan View of Test Setup

The horizontal bearing beam and ram rested on a wooden carriage fitted with ball bearing rollers. The carriage rolled atop the concrete base block. The roller support, shown in Fig. 3.33, allowed the bearing beam and ram to move horizontally when the ram was extended while negating the detrimental effects of friction.

Since the reaction wall was capable of resisting 100 kips per bolt group, two built-up channel sections were placed back to back to to distribute the horizontal force behind the wall. The channels were post-tensioned into position with approximately 15 kips of force in each of the connecting rods. Stiffeners were welded at channel beam reaction points to prevent web crippling and insure lateral stability.

3.9 Preparation for Testing

3.9.1 Positioning the Specimen.

Because of its small size, lifting lugs were not embedded into the specimen. A special lifting harness was designed and constructed that would allow the specimen and grasping beams to be properly positioned. Specimens were prepared by first slipping one of the steel grasping beams over the #5 longitudinal bars. Mechanical connectors were attached to the longitudinal bars after this procedure. Part of the lifting harness was then bolted to the specimen. Styrofoam was used at areas of stress concentration to prevent cracking of the concrete when the harness was tightened. Once this portion of the harness was in place, the specimen was tilted upright and the transverse bars were passed through the second grasping beam. Mechanical connectors were attached to the #3 bars as well. The remaining components of the lifting harness were bolted into position.

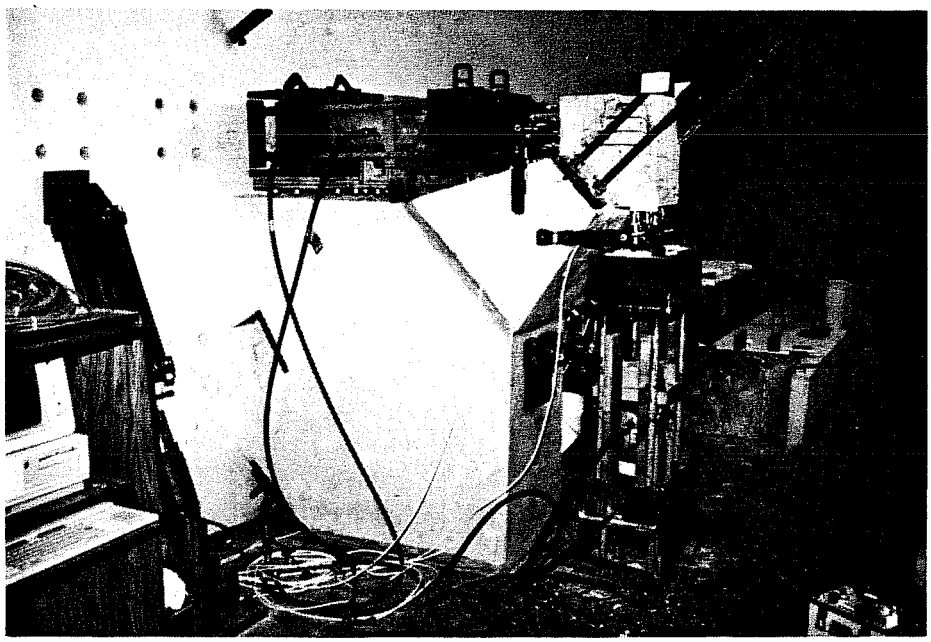

Fig. 3.32 View of Actual Test Setup

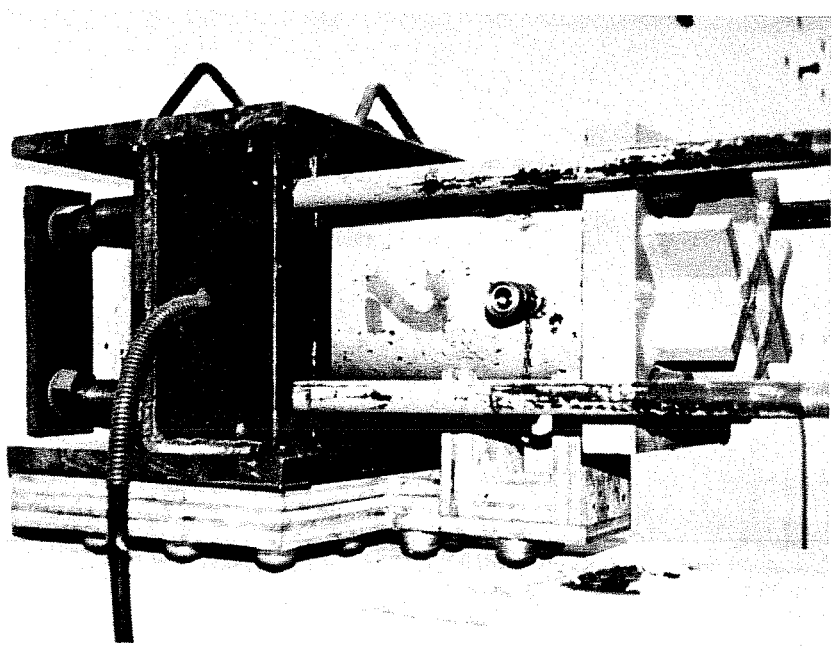

Fig. 3.33 Roller Support for Horizontal Bearing Beam and Ram

The transverse grasping beam was clamped into place to prevent movement during lifting and transport. Figure 3.34 shows a photograph of a specimen being lifted into position.

It was important to provide uniform bearing pressure at the compression face of the specimen. The construction tolerances of the specimen and test setup did not permit direct bearing between the two pieces. Therefore, a thin layer of hydrostone functioned as a grout to provide a uniform bearing surface between the specimen and test setup. Small hardened hydrostone shims served as bearing points when the test specimen was moved into position. The main purpose of the shims was to produce a gap of about 3/8 in. between the bearing faces of the specimen and the extension block. Usually only two 1 in. square bearing points were used. The specimen with grasping beams was lowered into position and connecting rods were tightened until the specimen's position was secure. The harness was then removed to provide access to the gap produced by the hydrostone shims. Next, plastic was wrapped around the longitudinal grasping beam for cleanliness. Hydrostone, about the consistency of putty, was then dry packed into gap at the sides and bottom corners of the specimen. Clear, flexible plastic tubing was inserted at gaps at the bottom corners of the specimen. The gap at the top of the specimen was left ungrouted. Silicone caulk was smeared at the junction of the tubing and hydrostone to further prevent leaking. After the appropriate gaps were sealed, the nozzles of hand operated caulking guns were taped to the plastic tubing. A flowable, but not runny, mixture of hydrostone and water was prepared. Two caulking guns were immediately filled with the

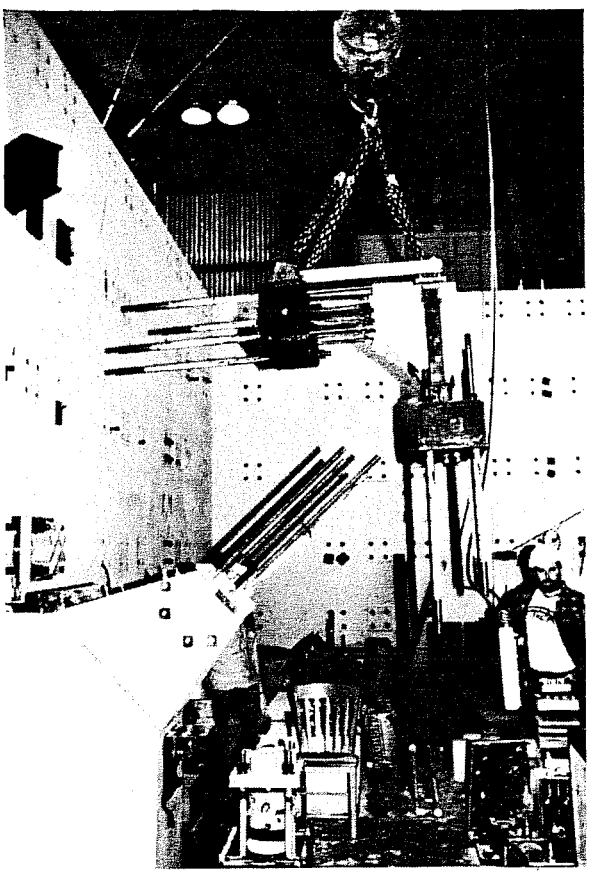

Fig. 3.34 Positioning of Specimen

mixture and each was connected to a nozzle. Hydrostone was then pumped into the gap until it flowed out of the space at the top of the specimen. This procedure is shown in Fig. 3.35. The flexible tubes were clamped and the guns were unscrewed from the nozzles and were immediately washed to prevent hydrostone from setting up and ruining their mechanism. After a sufficient time, the plastic tubes were removed. Hydrostone "putty" was dry packed into the voids left by the tubes. When the hydrostone had setup (usually within 15 minutes after mixing) a 3 in. x 3 in. steel angle was used to clamp the specimen in place and prevent any movement. It was placed over the corner of the specimen and was bolted down using the Dywidag threadbars as shown in Fig. 3.36. Styrofoam was placed between the angle and specimen to prevent cracking of the specimen caused by stress concentrations.

3.9.2 Equalization of Reinforcement Stresses. With the specimen held in place by the angle clamp, all connecting rods and adjustable couplings were loosened. They were then retightened by hand until snug. The vertical ram bearing beam was lifted from wooden support blocks by tightening the vertical connecting rods. Thus, the specimen's longitudinal steel was subjected to a dead load of approximately 1.5 kips which included the grasping beam, ram bearing beam, ram, and top plate. The transverse steel was not subjected to significant gravity loading because loading members were either self supporting or rested on supports. At this point, all gages, transducers, and potentiometers were zeroed. The specimen was loaded to trial loads far below cracking; 20 kips for the low strength concrete series and 30 kips for the high strength concrete series. Stresses at this load were

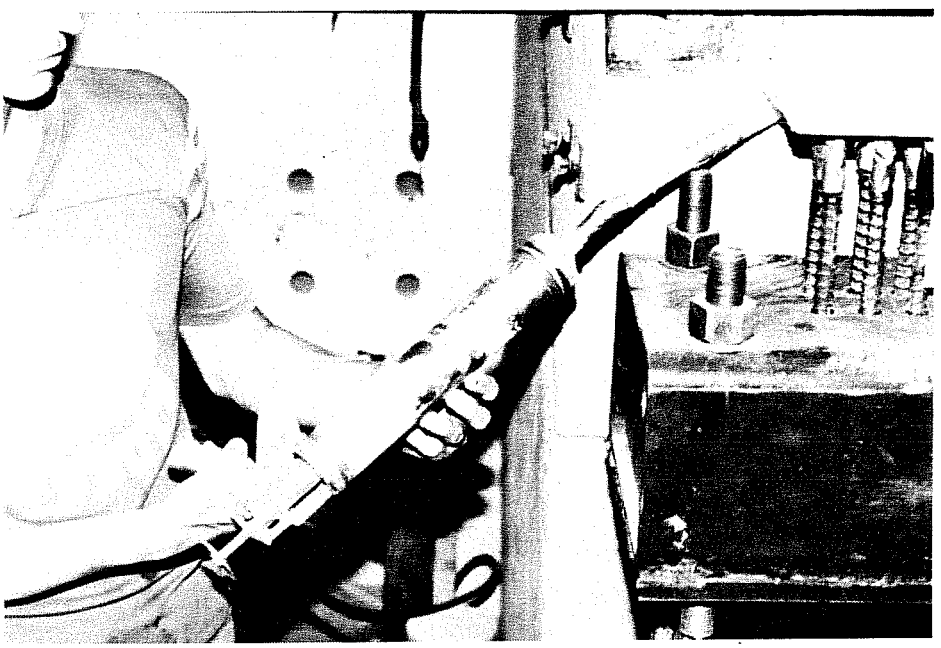

Fig. 3.35 Hydrostone Grouting Procedure

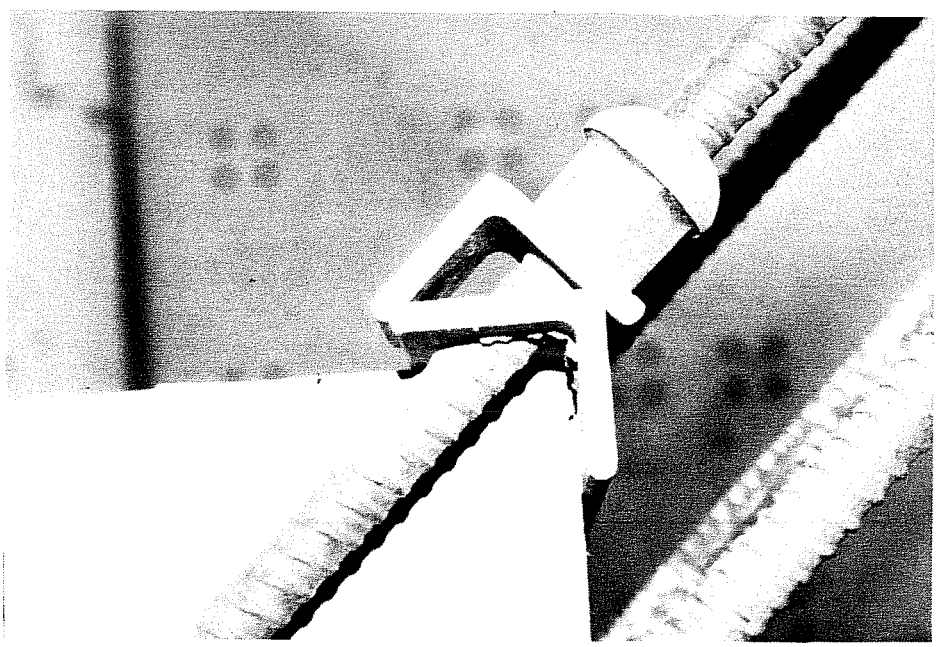

Fig. 3.36 Specimen Angle Clamp

compared and adjustments were made in the stress level of the bars by tightening or loosening the the adjusting nuts on the mechanical connectors. Because bending stresses were induced by the slightest specimen misalignment, the change in stresses from a low load point, usually 1 kip, to the trial load point were made to agree. This procedure assumes the strain gage reading is both axial and bending stress and the bending stresses are not changing as load is applied. The validity of this assumption should not be scrutinized too closely since the goal of the stress equalization process was to try to balance the bar stresses in each group to within 10% of each other. After numerous computer scans and adjustments, an acceptable level of equalization was achieved. The load was then reduced to 1 kip and scans were taken immediately before and after the angle clamp was removed.

3.10 Test Procedure

The testing procedure was essentially the same for all specimens. Equal loads were applied to the transverse and longitudinal reinforcement except for Specimen LFAC where a 30° strut angle was established by varying the loads appropriately. The procedure for applying the varying load will be expanded upon later in this section.

After the angle clamp was removed, zero readings were taken at an initial force of 1 kip equal tension force in each loading direction. The load was not reduced to zero for the unclamped specimen because of concern of possible slippage between the specimen and test setup. The slippage would be caused by the load imbalance set up by the dead weight of the ram, grasping beam, bearing beam, and top plate on the specimen's longitudinal bars. The 1

kip starting point assured adequate friction force would develop at the interface between the specimen and test setup. The initial load was small compared to the capacity of the specimen and was easily corrected for when analyzing the data and presenting the results.

Tensile loading of all specimens, except LFAC, was applied equally in the longitudinal and transverse directions so that a 45 ° equilibrating compressive reaction would result. Load levels were increased at 5 kip intervals until the specimen had sustained cracks crossing most of the transverse and longitudinal steel. This load varied with the concrete strength but ranged from 40 kips with the low strength concrete to 80 kips for the high strength specimens. After cracking, the load level was reduced at 10 kip intervals to a load of 10 kips. The next load stage was at 15 kips; after which, the load level was increased at 10 kip intervals until the cracking loads had been exceeded. 5 kip intervals were used after this load level and were continued until failure occurred or the limiting capacity of the mechanical couplings was achieved. All loads were applied using a manual hydraulic pump and were monitored by a calibrated electronic pressure transducer used in conjunction with a strain indicator.

Specimen LFAC was loaded similarly to all other specimens except ram forces varied in each direction in an attempt to change the angle of the compression strut. The free body diagram of the specimen's ultimate capacity loading forces is shown in Fig. 3.37. The zero reading for Specimen LFAC was 1 kip equal pull in each ram as with all the other specimens. Loads were equally increased to 10 kips; after which, the vertical tensile force was

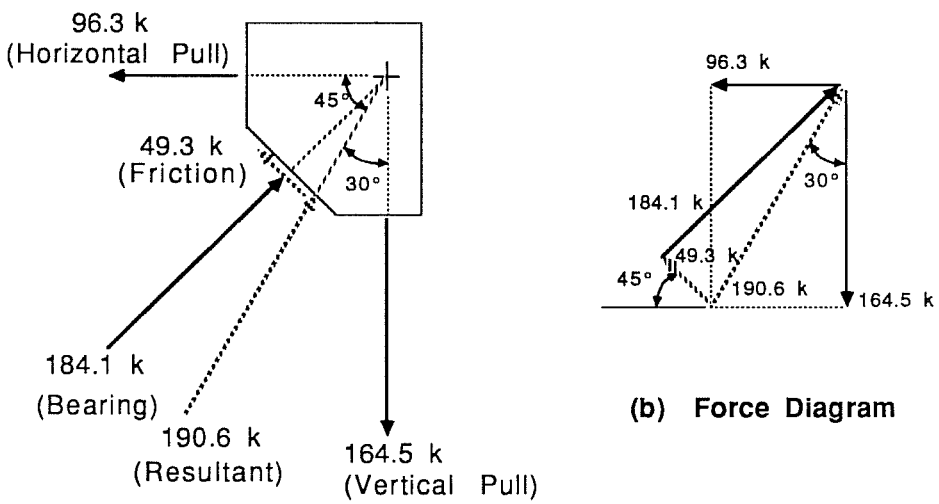

Fig. 3.37 Loading Forces at Specimen LFAC's Ultimate Capacity

increased to induce a 30° strut angle. The vertical loads (longitudinal direction) were used to reference load stages for Specimen LFAC. The horizontal loads (transverse direction) were 0.577 or tan 30° of the vertical loads. Load levels were increased at 5 kips intervals to 80 kip (vertical) until cracks had crossed both the transverse and longitudinal reinforcement. Load levels were then reduced to 20 kips (vertical) by 10 kip intervals. The next load stage was 25 kips (vertical); after which, the load level was increased at 10 kip intervals to 85 kips (vertical). The specimen was loaded after this point by 5 kip intervals until failure. Each ram was loaded with separate manual hydraulic pumps that were each monitored using a calibrated electronic pressure transducer and a strain indicator. Table 3.6 gives a summary of the load stages used for Specimen LFAC.

Plots to monitor deflection vs. load and stress vs. load in both the vertical and horizontal directions were kept during all tests. The plots gave a graphical representation of the behavior of the specimen and were used to detect a malfunction or instability in the setup.

Cracks at each load stage were highlighted and labeled using felt tipped markers. Crack width readings and photographs were taken at varying load levels depending on the specimen. Standard points of reference used in all specimens except LFAC were at vertical loads of 100 kips and 115 kips. Generally, the time interval between load stages was less than 10 minutes. All tests were concluded on the day they were started. The testing process usually took about 6 hours.

Load Stage	Vertical Load (kips)	Horizontal Load (kips)	Angle of Resultant (Deg.)
Clamping Load	1.0	1.0	45
1	6.0	5.0	45
2	11.0	10.0	45
3	16.0	10.0	32
4	21.0	12.1	30
5	26.0	15.0	30
6	31.0	17.9	30
7	36.0	20.8	30
8	41.0	23.7	30
9	46.0	26.6	30
10	51.0	29.4	30
11	56.0	32.3	30
12	61.0	35.2	30
13	66.0	38.1	30
14	71.0	41.0	30
15	76.0	43.9	30
16	81.0	46.8	30
17	71.0	41.0	30
18	61.0	35.2	30
19	51.0	29.4	30
20	41.0	23.7	30
21	31.0	17.9	30
22	21.0	12.1	30
23	26.0	15.0	30
24	36.0	20.8	30
25	46.0	26.6	30
26	56.0	32.3	30
27	66.0	38.1	30
28	76.0	43.9	30
29	86.0	49.7	30
30	91.0	52.5	30
31	96.0	55.4	30
32	101.0	58.3	30
33	106.0	61.2	30
34	111.0	64.1	30
35	116.0	67.0	30
36	121.0	69.9	30
37	126.0	72.7	30
38	131.0	75.6	30
39	136.0	78.5	30
40	141.0	81.4	30
41	146.0	84.3	30
42	151.0	87.2	30
43	156.0	90.1	30
44	161.0	93.0	30
45 (Ultimate)	165.4	96.3	30

Table 3.6 Load Stages for Specimen LFAC

3.11 Data Reduction and Interpretation

Data reduction for all the specimens involved plotting the load vs. strain graphs for the individual gages. Plots of the average strain at the various gage locations were also made to reduce the complexity of the strain graphs. Bar graphs were prepared to show the percentage of applied horizontal or vertical force reaching the interior gage locations. The cracking patterns, strain graphs, and bar graphs were compared in order to establish the configuration of the node's compression strut and to identify the force distribution within the node. The test results will be presented in Chapter 4.

3.12 Summary

The purpose of the test program was to better quantify the behavior of a critical node of the strut-and-tie model. An isolated node study which complimented a full-sized test of a dapped beam was undertaken. The study aimed at providing information about the following criterion: 1) physical dimensions of the node; 2) configuration of stress fields; 3) allowable concrete stresses; 4) detailing considerations; and 5) effects of strut angle change. A CTT-node was selected, modelled and designed. Nine specimens were tested in the experimental program. Variables selected included concrete strength, confinement, strut width, reinforcement details, and strut angle. Specimens were similarly designed and constructed using standard laboratory methods and basic construction materials. A loading and reaction system suitable for loading the specimen in two directions was designed, constructed, and assembled. Tests were made on heavily instrumented

specimens. The specimen was loaded until cracking, unloaded to a low load, and reloaded until the ultimate capacity of the specimen or the limiting capacity of the test setup was reached. Data reduction was carried out to understand the transfer of forces within the node.

CHAPTER 4

TEST RESULTS

4.1 Introduction

Selected test results and a detailed summary of observed physical behavior of the specimens are presented in this chapter. The scope of the test results includes: 1) nine node specimens tested in this study; and 2) one full sized, dapped beam specimen tested by Barton (17) which will be presented and compared to the node tests. The specimens incorporate varying concrete strengths, reinforcement confinement details, reinforcement anchorage details, strut widths, and strut angles as outlined in Chapter 3. A critical evaluation of the strut-and-tie model, discussed in light of the test results presented in this chapter, will be undertaken in Chapter 5.

4.2 Interpretation of Individual Test Results

4.2.1 General. To aid in the interpretation of test results, the following figures have been prepared for each specimen:

1) Crack patterns showing the development of cracks for four faces of the specimens are presented in "unfolded" views. When the test was concluded, crack locations were mapped. In specimens where large amounts of damage occurred at failure, photographs were used to determine crack locations.

The reference loads used in these figures were not corrected for the $\pm$1 kip initial load; thus, the actual load was approximately 1 kip more than the reference load. For Specimen LFAC, where forces applied to the

transverse and longitudinal ties are unequal, the longitudinal force was used as the reference load (See Table 3.6).

2) The large amount of strain gage data from each test is presented in graph form. The total transverse (T) or longitudinal (L) force, defined in Fig. 4.1, was plotted on the vertical axis and the reinforcement strain was plotted on the horizontal axis. Data points were corrected for the ± 1 kip initial load. To assess the ductility of the specimens and to facilitate strength comparisons, the ultimate and/or maximum capacity of the specimens is expressed in the graphs in terms of T_y and L_y which are the transverse and longitudinal tie yield loads.

The orientation of the node specimen during testing was 90° from that of the full sized, dapped beam. As shown in Fig. 4.1, layers of transverse reinforcement are parallel to the horizontal plane while the layers of longitudinal steel are oriented vertically. Throughout the following discussion, the outer layers of reinforcement located closest to the surface of the specimen shall be identified as the first layer of transverse or longitudinal reinforcement, respectively. Layers of bars will be identified in ascending order from the exterior to the interior of the specimen (See Fig. 4.1).

The graphs do not follow the exact load histories used during testing. The specimen was loaded until visible cracks appeared, unloaded to a low load, and reloaded until the ultimate capacity of the specimen or limiting capacity of the mechanical connectors was attained. The repeated loading produced a typical reloading curve where the load/strain path returned to a common

point where the load was first reduced. The loops were not included in order to simplify the graphs.

For each specimen, separate strain graphs were plotted for the longitudinal and transverse reinforcement. Plots of the average strain at the selected locations were made to reduce the complexity of the strain graphs. If only one gage was functional at a particular location, its reading was plotted instead of the average strain. The average strains were, in general, a reliable indicator of the strain at each location. In some cases, however, certain gages varied substantially from companion gages at the same location. For this reason, graphs showing the relationship of load versus strain for individual gages as well as the averages of strain gages at particular locations have been included in this chapter or in the Appendix for completeness.

The strain graphs contain supplementary items to assist in their interpretation. Legends on the right side of the strain graphs distinguish each set of data points. Inset diagrams show the location of the strain gages. For the plots of average strains the inset diagram also contains a superimposed crack pattern from the specimen's south face. This aids in identifying changes in the slope of the data points due to cracking of the concrete. The ultimate load of the specimen, or the maximum load in cases where the specimen did not fail upon conclusion of the test, are noted. As discussed previously, the ultimate and/or maximum load is also expressed in terms of the yield load of the respective ties. The graphs show the yield strain of the tie reinforcement where appropriate. The average external bar strain, produced by the applied tensile loading, is plotted to show the significance of

internal force transfer mechanisms including concrete tensile strength, strut-and-tie action, shear friction (aggregate interlock), and dowel action. For the node specimen strain graphs, the average external bar strain is identified with a solid line and referenced in the graph legend by "Ext.". For the Prototype Beam Specimen, where the strut of the CTT-node is inclined at 51°, the average tie strain was calculated from the strut-and-tie design model and is referenced in the graph legend as "51° S-T".

Average external bar strains based upon the applied tensile load were plotted in lieu of the measured strain readings from the exterior gages because the latter were somewhat inconsistent. The measured external bar strains were susceptible to bending effects and were influenced by specimen cracking. This is especially true of the external longitudinal gages. Figures 4.2 - 4.4 present reinforcement external strain gage data for Specimen HFSB. Figure 4.2 shows strains for the external transverse bars are fairly well grouped. In contrast, Fig. 4.3 shows that considerably different strain rates were indicated by external longitudinal gages. The second layer of bars, closest to the interior of the specimen, displayed higher strain rates than the first layer of bars. The average of the external strains for the first and second layers of longitudinal reinforcement are shown in Fig. 4.4. The average external strain produced by the applied longitudinal force is also shown in the figure. A divergence between the strain rates for the two layers of longitudinal reinforcement occurred after first cracking. The external reinforcement strain behavior exhibited by Specimen HFSB was generally typical of all the node specimens and appeared to be influenced by the location

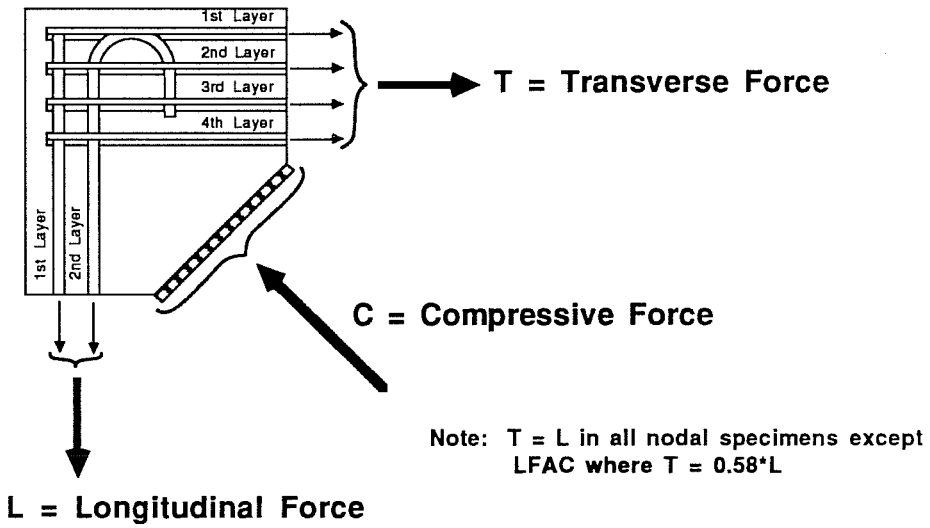

Fig. 4.1 Node Specimen Force Designation

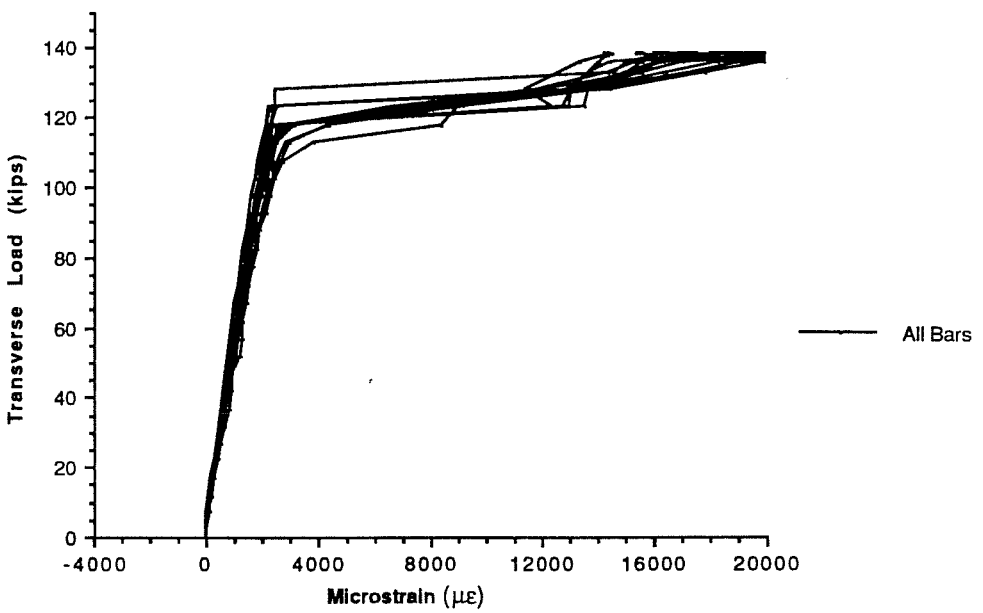

Fig. 4.2 External Transverse Bar Strains for Specimen HFSB

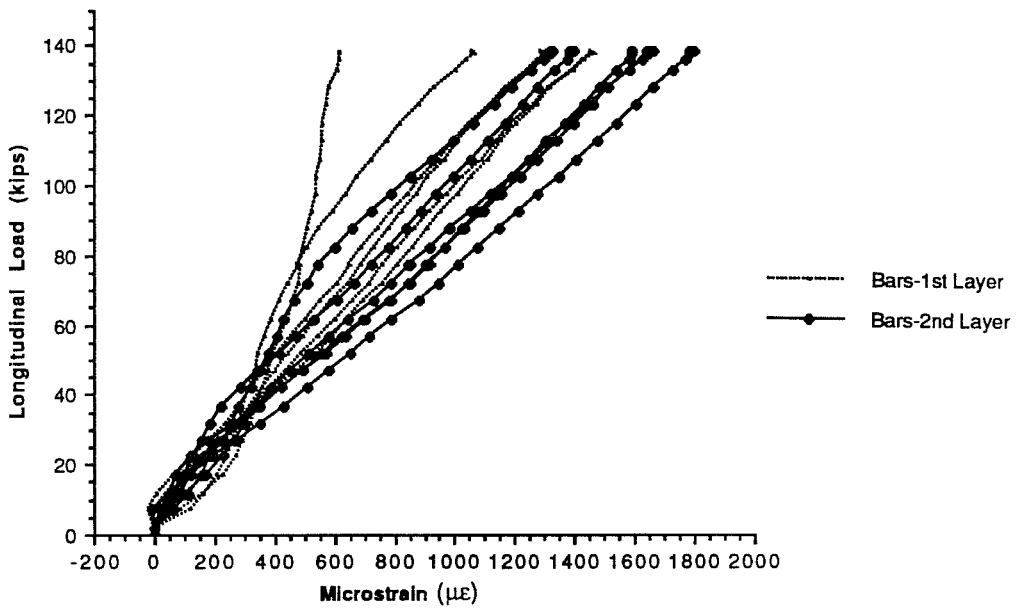

Fig. 4.3 External Longitudinal Bar Strains for Specimen HFSB

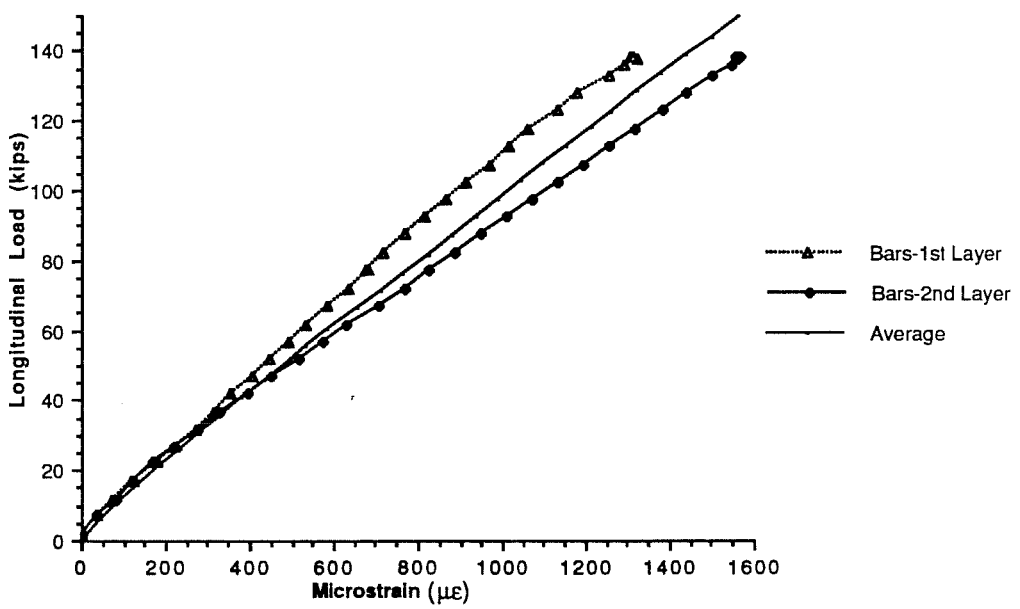

Fig. 4.4 Average External Longitudinal Bar Strains for Specimen HFSB

of major cracks. This behavior pattern will be discussed further in Sec. 4.3.9.

3) The percentage of applied transverse or longitudinal load at a particular location is presented in a bar graph. The stress in the bars was determined from a stepped function reconstructing the various portions of the stress-strain relationship. Thus, nonlinear stress-strain characteristics of the reinforcement were included. The percentage of total applied load at a particular location was determined by:

$$\% \text{ of Total Applied Load at Location} = \left(\frac{\sigma_{int}}{\sigma_{ext}}\right) * \left(\frac{B_{gl}}{B_{tot}}\right) \qquad (4.1)$$

where

σ_{int} = Internal stress determined from the average internal strain at location.

σ_{ext} = External reinforcement stress produced by the applied longitudinal or transverse load.

B_{gl} = Number of bars in group at location.

B_{tot} = Total transverse or longitudinal bars in tie.

Determining the bar stress from the stress-strain relationship assumes the reinforcement is axially stressed. This may not always be the case because slip and/or dowel action sometimes produce reinforcement bending strains. The strain reading may be higher or lower than the average strain if the gage is located away from the neutral axis.

The graphs also show the percentage of load corresponding to direct tension at each location. With direct tension, the internal stress (σ_{int}) equals the external stress (σ_{ext}). For the transverse reinforcement the average strain at each location was assumed to affect 4 of the 16 bars. A

particular transverse location would see 4/16's of 100% or 25% of the applied force if it was subjected to direct tension. The percentages for the longitudinal reinforcement were similarly determined. At locations LA and LB, 6 of 12 bars were affected by the load; thus, direct tension corresponds to 50% of the applied force. Direct tension corresponds to 100% of the applied force at location LC where all the reinforcement is included in the bar group.

The bar forces were most helpful in assessing the role of different internal force transfer mechanisms. At early load stages, concrete tensile strength and bond forces were mobilized resulting in very stiff responses. The locations normally indicated a low percentage of the applied tensile force being transmitted by reinforcement. After cracking, new static systems developed. Bond gradually deteriorated and the bars slipped. Higher loads were eventually carried through strut-and-tie action. Strut-and-tie action could be identified when the percentage of applied load at a location was observed to remain constant for increasing load stages. If shear friction, dowel action, or the breakdown in bond resulted in the straining of reinforcement, the percentage of applied load increased with increasing load stages. The first two mechanisms sometimes produced stresses in excess of direct tension.

Section 4.2.2 is included to demonstrate in detail the procedures used in interpreting the individual test results. The example specimen, HFNC, displayed important behavioral patterns evidenced by other specimens in the

study; however, it did not exemplify behavior typical of all specimens. The detail in the explanation is merely provided to assist the reader.

4.2.2 Comprehensive Interpretation of Test Results for Specimen HFNC. Specimen HFNC was part of the high strength concrete series with f'c=5780 psi. The transverse reinforcement provided minimal lateral confinement to the node. A 180° hook was used to anchor the second layer of longitudinal reinforcement. The specimen had a strut width of 10.6 in. and a strut angle of 45° from the longitudinal tie. Equal forces were applied in the transverse and longitudinal directions during the test.

From a 1.3 kip starting point the specimen was loaded in 5 kip increments to 71.3 kips. At this point the specimen had sustained visible cracks crossing the transverse and longitudinal bars. The load was then decreased in 10 kip increments to 11.3 kips. The next load stage was 16.3 kips; after which, the load was increased in 10 kip increments to 76.3 kips. Subsequent loads were increased in 5 kips increments until the specimen experienced a final failure with spalling of the south cover over the transverse reinforcement hooks and a sudden drop in the transverse bar force. The specimen capacity of 132.5 kips corresponds to $1.13*T_y$ and $0.60*L_y$. The concrete stress at the bearing surface was 1470 psi or 0.25*f'c when the cover splitting failure took place. Figures 4.5 and 4.6 show crack patterns and photographs of the specimen. The crack widths at various load stages are summarized in Table 4.2.

Some differences in strain for companion gages at each location are indicated in Fig. 4.7. The most significant variation was between gages TU1

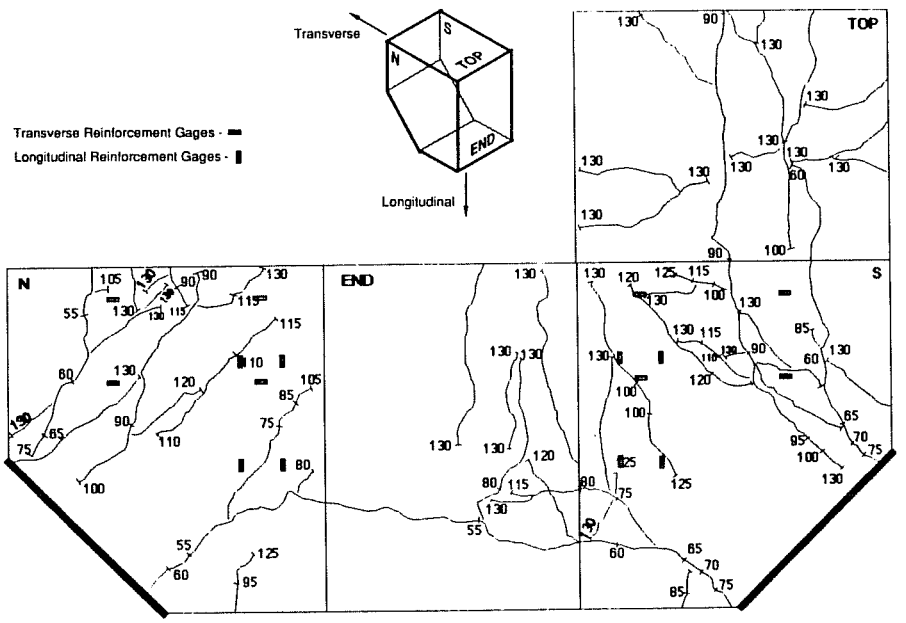

Fig. 4.5 Crack Patterns for Specimen HFNC

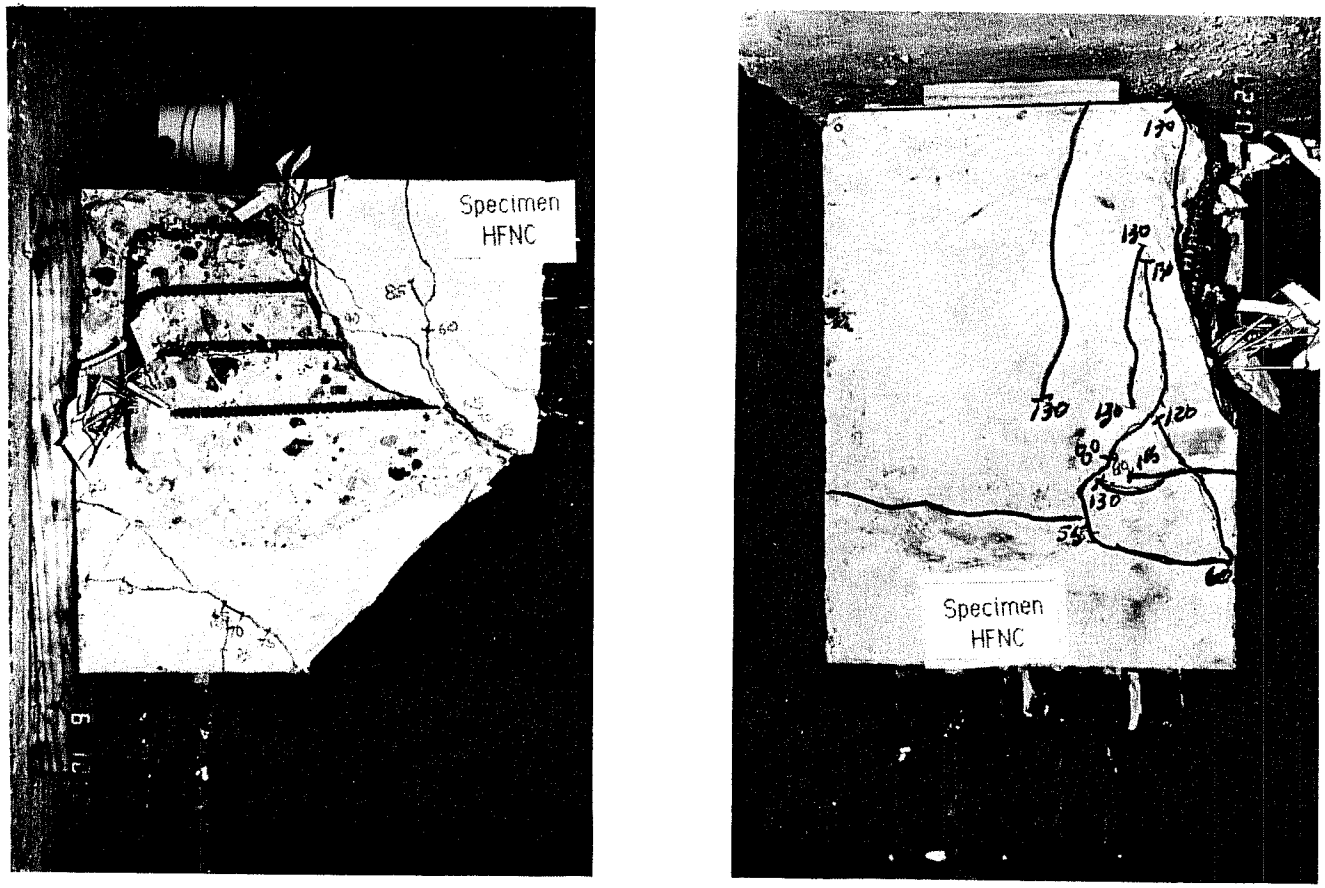

Fig. 4.6 Specimen HFNC at Failure (South and End Faces)

and TH1. Gage TU1 was strained much more than gage TH1 after the load exceeded 95 kips. This behavior was exhibited by all but two of the test specimens (the Prototype and HFSR-A) and occurred in conjunction with a second crack crossing the transverse reinforcing bars. A possible explanation for the flattening of the strain curve for gage TU1 is that once the second crack crossed the transverse bars, the corner bars slipped as a result of the increased tensile force. Because of its location, the corner bar was least confined and slipped more than other transverse reinforcement. Bearing stresses developed at the bend and forced it to open slightly as illustrated in Fig. 4.8. The strain read by the gage located near the inside of the bend was the summation of axial and bending strains. The strain at gage TU1 exceeded that of TU2 in some tests. This further suggested the presence of significant bending strains at the 90° bend. Visible splitting or bond cracks produced by slip in the corner bar were not apparent at this load stage. At 130 kips; however, bond cracks at the same plane as the corner bar appeared at the specimen's top, end, and south faces. A cover splitting failure at this location occurred shortly thereafter at 132.5 kips.

Figure 4.7 also shows that gage TU2 was strained to approximately 350 $\mu\varepsilon$ at 56 kips. Concrete cracks were not visible at this load which indicated slip and/or microcracking were affecting this gage. Either occurrence could have developed during equalization of bar stresses. Shrinkage cracks may have also influenced behavior in this way. Gage TU2 essentially mirrored its companion gage TH2 at loads stages above 60 kips.

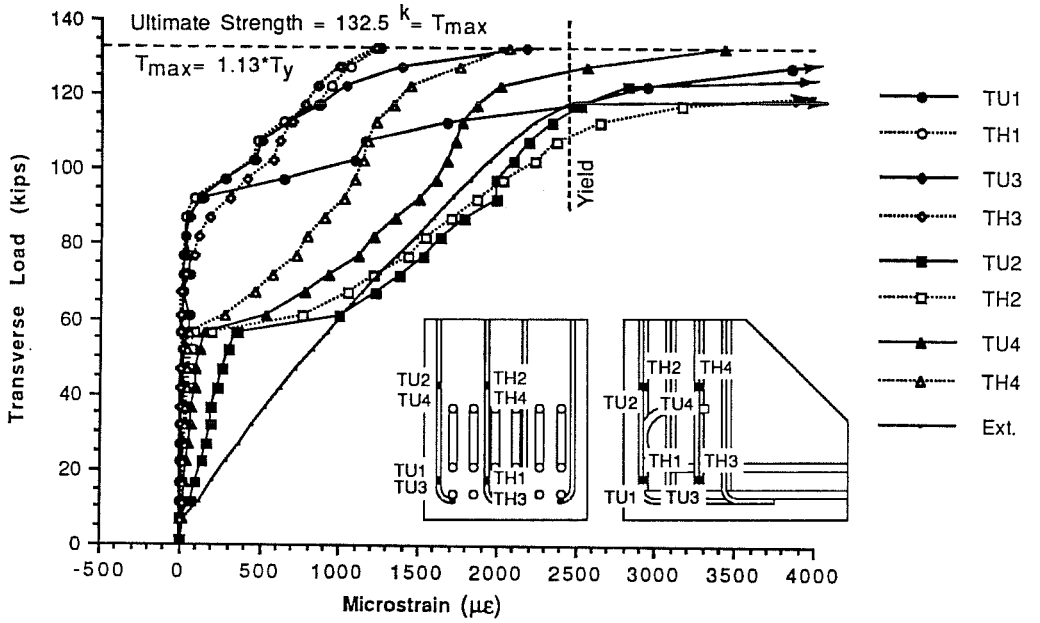

Fig. 4.7 Specimen HFNC-Reinforcement Strain Data for Individual Transverse Gage Locations

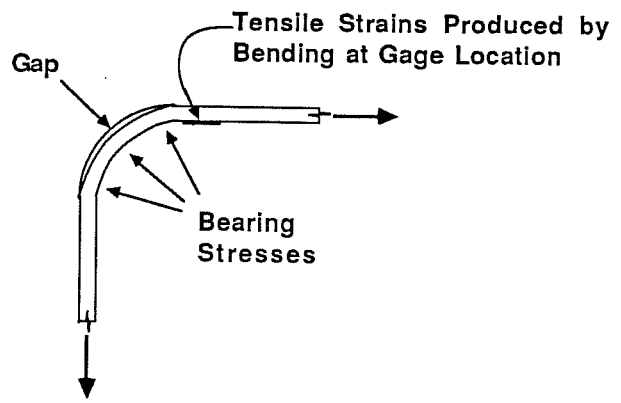

Fig. 4.8 Tensile Strains Resulting from Slip at 90° Bend

This suggested that some strain resulting from slip and/or microcracking did not significantly affect strain readings after visible cracks appeared.

The change in the average strain at each transverse location with cracking of the concrete is shown in Fig. 4.9. At 52 kips, the first crack crossing the transverse bars developed and reduced the slope of the strain curves for locations TC and TD. Locations TA and TB were affected by the formation of a second crack crossing the transverse bars at 92 kips. Locations TA, TC, and TD showed reinforcement yield before failure of the specimen. Once cracking occurred, the slope of the strain curves for locations TB,TC, and TD were about the same as that of the average external bar strain produced by direct tension. This would imply that the bars were loaded basically as predicted by strut-and-tie action.

Figure 4.9 shows a very interesting behavior pattern exhibited by all the node specimens and the Prototype Beam Specimen. Even though the applied forces at locations TC and TD are equal, location TC shows significantly higher strains than location TD after the specimen cracks. Similarly, the strain indicated at location TA is higher than that shown at location TB although the strain paths do not separate until cracks form closer to the termination point of the transverse bars at approximately 95 kips. This strain variation for parallel locations shows that the location of the layers of transverse reinforcement greatly affect their straining. This occurrence is identified as a "distance effect" because layers of transverse reinforcement closest to the surface of the specimen are strained more than layers closer to the specimen's interior. Particularly, the reinforcement

strain is influenced by the cracks which develop at the edge of the specimen and cross the outer layers of steel first.

Averages of the individual longitudinal strains are plotted in Fig. 4.10. For location LC, the strain jumped at 56 kips with the formation of a crack crossing the longitudinal bars. Slip caused rounding of the strain curves from 60 to 100 kips for locations LA and LB. A small inclined diagonal tension crack developed at 100 kips which appeared to decrease the strain rate for locations LA and LB. Less anchorage was available after this crack formed which reduced the bars' ability to carry tensile force and increased the slope of their strain curves. Location LA shows more strain than location LB and illustrates another "distance effect" involving development. Because diagonal tension cracks intersect the second layer of longitudinal bars at a greater distance from the reinforcement's free end than in the first layer of bars, it is afforded a longer development length. Thus, it is able to carry more of the applied tensile force. This behavior could result from the hooked anchorage being more efficient than the straight bar; however, similar behavior was exhibited by Specimen HFSB where both layers of longitudinal reinforcement anchored with straight bars. This behavior pattern will be discussed in further detail in Sec. 4.3.9. After cracking, Fig. 4.10 shows the slope of the strain curves for all interior locations were quite similar to the average external strain. There is a fairly consistent 250 $\mu\varepsilon$ offset between the strain curve of location LC and that of the average external strain at higher loads. This not only suggests that the

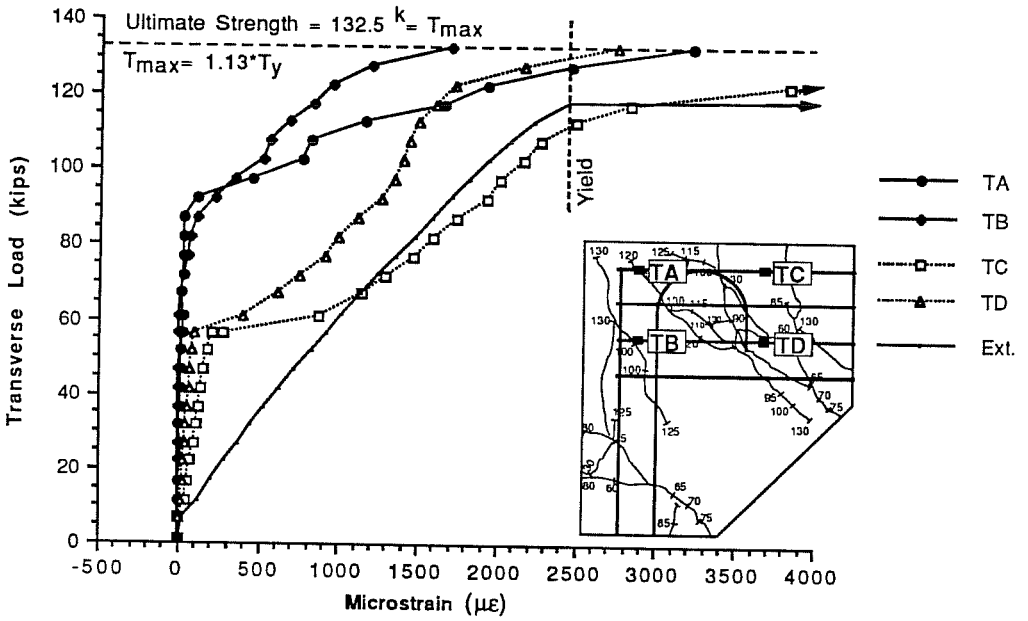

Fig. 4.9 Average Strain at Transverse Locations for Specimen HFNC

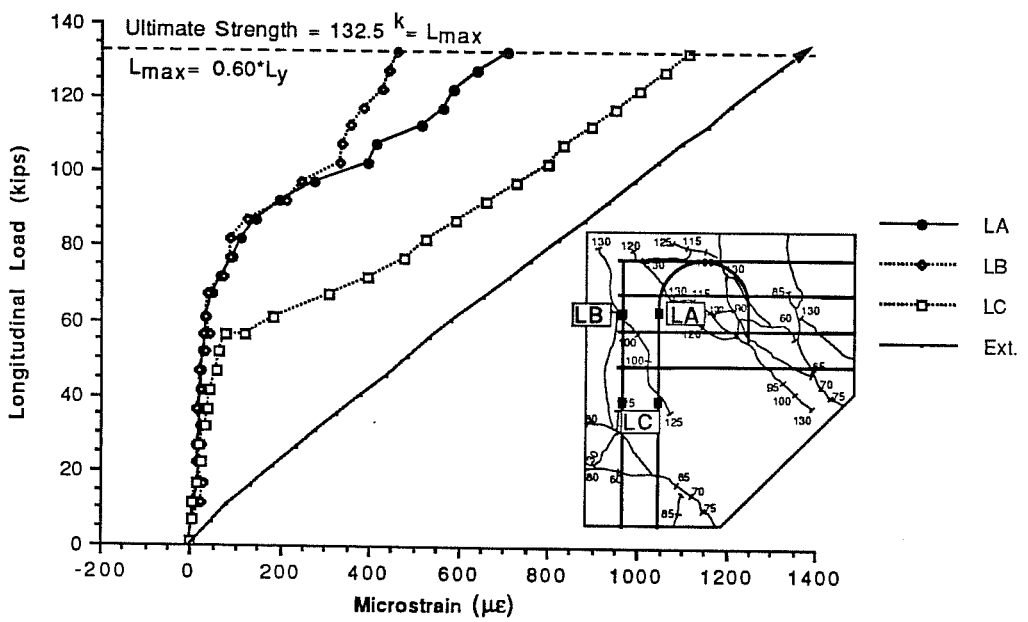

Fig. 4.10 Average Strain at Longitudinal Locations for Specimen HFNC

internal longitudinal bars are strained mainly through strut-and-tie action, but also that other internal force transfer mechanisms are present.

Bar graphs presented in Figs. 4.11 and 4.12 show the significance of internal force transfer mechanisms. If strut-and-tie action accounted all internal force transfer, the percentage of applied load at a particular location would remain constant and the locations would account for 100% of the applied tensile force. Specimen HFNC shows that strut-and-tie action dominates only when the tie reinforcement yielded. At 50 kips, the concrete tensile strength was effective in resisting most of the applied load and the percentages of applied load seen by the bars were small. A big increase in the percentage of applied load at locations TC, TD, and LC at 75 kips is attributable to the formation of the first specimen cracks; however, small percentages of load are still observed at locations TA, TB, LA, and LB. After the transverse reinforcement yielded and when the specimen was thoroughly cracked at 125 kips, additional load was resisted mainly through strut-and-tie action. This is evidenced by the percentage of the applied load at a particular location staying constant as the load was increased. For the transverse reinforcement shown in Fig. 4.11, the locations TA,TC, and TD see roughly 22% of the load at 125 kips. Because the percentages of applied force at locations TA, TC, and, TD are nearly equal to direct tension, it is apparent that bond forces have broken down along the length of the bar and allow practically all the applied load to be carried through to these locations. The first layer of transverse reinforcement resists nearly all the applied force through anchorage of the hooks and U. The percentage of force at

location TB is 13% at 125 kips. This is just over half the direct tensile force and shows that bond, and possibly other mechanisms, are effective in resisting a portion of the applied load for the third layer of transverse reinforcement. The percentages level off after 115 kips for the longitudinal locations shown in Fig. 4.12. At 125 kips, 25% of the load is measured at location LA which is the second layer of longitudinal steel with a 180° hook anchorage. This is 7% more than the first layer of straight bars carry at the same load. Location LC sees 82% of the 125 kip load. The longitudinal reinforcement has not yielded and bond has not deteriorated entirely along the length of the reinforcement. This explains why the percentage of applied longitudinal force at locations is approximately half of direct tension at locations LA and LB.

4.3 Specimen Behavior

4.3.1 General.

In this section, important physical behavior patterns exhibited by each specimen are summarized. A summary of the test results for all of the specimens is presented in Table 4.1. Many specimens experienced a large amount of damage; however, none of the failures were explosive. It is noted that three of the specimens were not loaded to failure. These tests had to be terminated at the rated capacity of the mechanical couplers used to anchor the reinforcement to the test setup. The maximum load applied to the specimens that did not fail was well above the transverse yield force (T_y). Crack widths at various load stages are summarized in Table 4.2. Generally, wider cracks appeared on the south face of the specimen.

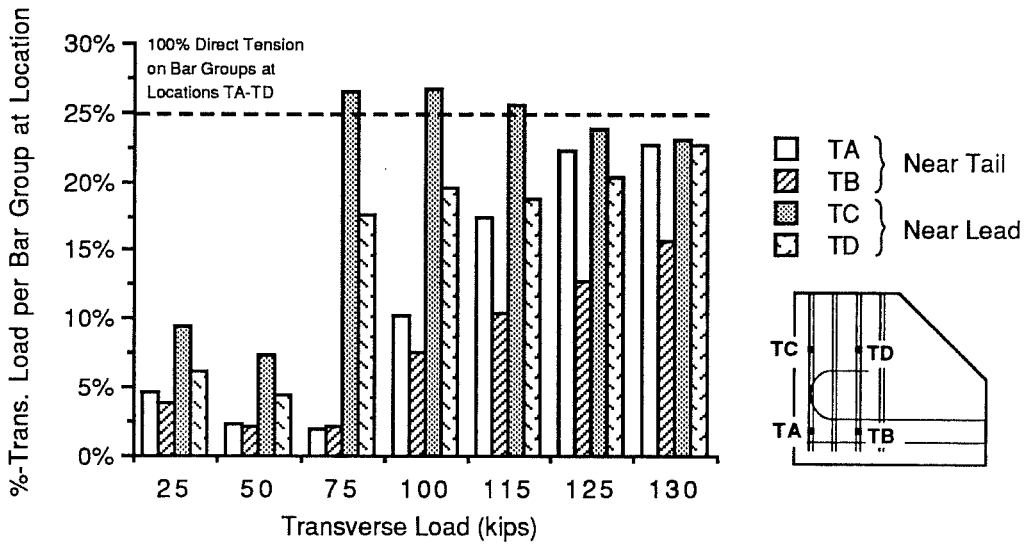

Fig. 4.11 Specimen HFNC-Percentage of Applied Force at Transverse Locations

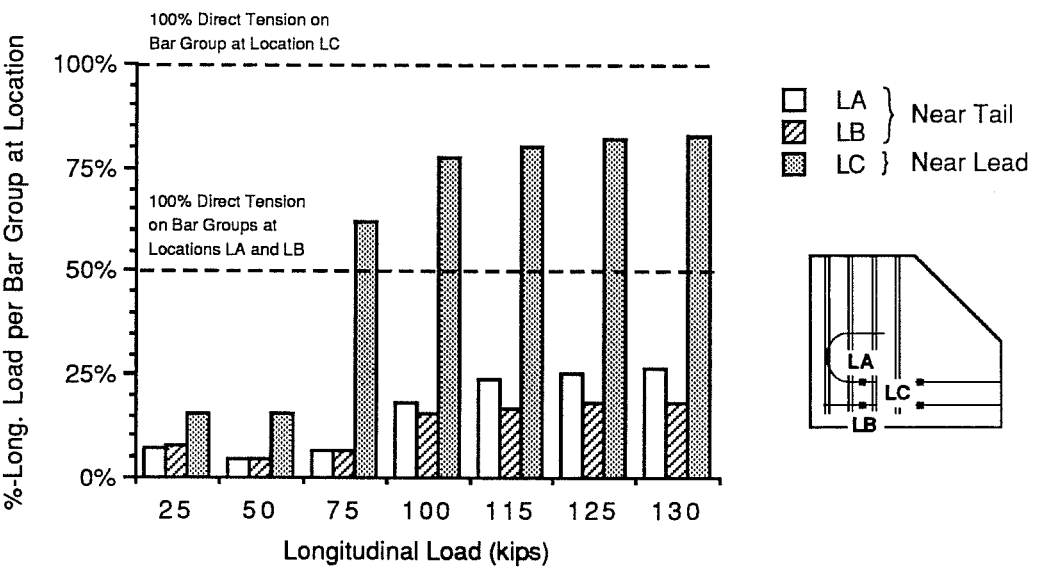

Fig. 4.12 Specimen HFNC-Percentage of Applied Force at Longitudinal Locations

Specimen	L max (kips)	Type of Failure	Bearing Stress at C max (ksi)	(Bearing Stress)/f'c	Tmax /Ty	Lmax /Ly
HFSR-A	127.4	None-Cap. of Setup	1.42	0.20	1.08	N/A
HFSR-B	137.5	None-Cap. of Setup	1.53	0.26	1.17	0.62
LFSR (1)	117.4	Development-Trans.	1.31	0.35	1.00	0.53
HFNC	132.5	Cover Splitting	1.47	0.25	1.13	0.60
LFNC	117.8	Cover Splitting	1.31	0.35	1.00	0.53
HHSR	139.0	None-Cap. of Setup	4.10	0.71	1.18	0.62
LHSR	130.2	Strut Crushing	3.84	1.03	1.11	0.59
HFSB	138.1	Gross Slip-Trans.	1.54	0.27	1.17	0.62
LFAC (1)	165.4	Development-Long.	3.19 (2)	0.81 (2)	0.82	0.74

Notes:

(1) Specimens failed before design capacity governed by yielding of transverse or longitudinal tie.

(2) Based on 5 in. strut width.

N/A-Not applicable-Reinforcement did not have definite yield point.

Table 4.1 Summary of Node Specimen Test Results

Specimen	100 Kips (Longitudinal)						115 Kips (Longitudinal)						Crack Widths at Noted Longitudinal Load						
	Transverse		Diagonal Tension		Longitudinal		Transverse		Diagonal Tension		Longitudinal		Applied Load	Transverse		Diagonal Tension		Longitudinal	
	North	South	North	South	North	South	North	South	North	South	North	South	(kips)	North	South	North	South	North	South
HFSR-A	0.009	NMS	DNF	DNF	0.016	NMS	0.015	NMS	DNF	DNF	0.015	NMS							
HFSR-B	0.003	0.003	0.002	0.001	0.003	0.006	0.005	0.008	0.003	0.002	0.003	0.009	135	0.040	0.050	0.005	0.005	0.007	0.013
LFSR	0.005	0.010	0.005	0.010	0.007	0.010	NMS	NMS	NMS	NMS	NMS	NMS							
HFNC	0.007	0.007	DNF	DNF	0.005	0.002	0.010	0.010	DNF	DNF	0.009	0.005	125	0.020	0.016	DNF	DNF	0.009	0.007
LFNC	0.009	0.007	0.005	0.010	0.009	0.013	NMS	NMS	NMS	NMS	NMS	NMS							
HHSR	0.005	0.009	0.005	0.007	0.002	0.002	0.007	0.010	0.006	0.003	0.003	0.009	135	0.040	0.040	0.010	0.010	0.030	0.030
LHSR	0.005	0.009	0.009	0.016	0.003	0.007	0.016	0.013	0.013	0.025	0.005	0.007							
HFSB	0.005	0.009	DNF	DNF	0.009	0.006	0.007	0.016	0.002	DNF	0.010	0.009	125	0.013	0.040	0.003	DNF	0.013	0.013
LFAC	0.003	0.003	DNF	DNF	0.010	0.013	0.010	0.009	DNF	DNF	0.020	0.016	150	0.010	0.013	DNF	DNF	0.025	0.025

Notes:

All measurements are in inches.
DNF-Crack did not form.
NMS-Crack not measured

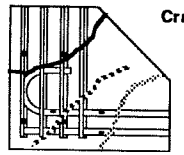

Crack Key:
- —— **Transverse**
- -·-·- **Diagonal Tension**
- ····· **Longitudinal**

Table 4.2 Crack Widths

Inspection of the crack patterns, strain plots, and bar graphs for each test revealed behavioral similarities. For the sake of brevity and conciseness, figures and descriptions of individual tests are presented in this section as needed to make distinctions between the specimens and their behavior. Supplemental figures illustrating typical behavior patterns are located in the Appendix. In this section, the observed cracking and/or failure behavior of the specimens is emphasized. Much of the information from strain graphs and bar graphs for the individual specimens has been summarized in a reduced number of key figures located in Sec. 4.4. The specimens are grouped according to geometry and placement of steel in the following presentation of results. The results for Specimen HFNC which were discussed in Sec. 4.2.2 will not be presented in this section.

4.3.2 Prototype Beam Specimen. The strut-and-tie model and corresponding placement of reinforcement for the Prototype Beam Specimen tested by Barton (17) were described in Sec. 3.4. In this presentation, the CTT-node located at the lower corner of the specimen (See Fig. 3.1) is examined. The overall behavior of the dapped beam will be discussed only briefly.

The specimen was constructed of high strength concrete with f'c=6280 psi. The transverse reinforcement of the CTT-node was detailed to provide lateral confinement. The theoretical strut angle of the CTT-node was 51° from the longitudinal tie. A 180° hook anchored the CTT-node's second layer of longitudinal reinforcement.

The dapped beam specimen was loaded in 5 kip increments until it experienced a shear compression failure at 149.1 kips. This load corresponds to $1.43*T_y$ and $0.68*L_y$ based upon a 51° CTT-node strut angle. Diagonal tension cracks extended into the beam and reduced the area of the compression zone until the concrete crushed. A photograph of the specimen near failure is shown in Fig. 4.13. Crack patterns for the CTT-node are given in Appendix Fig. A1.1. A large amount of damage was sustained by the specimen and the failure was not abrupt or explosive. The largest cracks were over 1 in. wide at failure. The CTT-node did not experience appreciable damage. Crack widths at this location were not measured.

Average strain versus load for the transverse and longitudinal locations are shown in Figs. 4.14 and 4.15. Strain graphs for the individual gages are located in the Appendix. The development of visible cracks coincided with jumps in strain and changes in slope of the strain curves. Much can be learned by comparing the average strain at particular locations with the theoretical tie strain also shown in the figures. As previously discussed, the theoretical tie strain would develop if the tie reinforcement were subjected to the tie force calculated from the strut-and-tie design model. A 51° strut angle was used to determine the tie strains and this is identified as "51° S & T" in the graph legend. The slope of the strain curves for the longitudinal locations were quite similar to that of the theoretical strain above the 80 kip node cracking load. This suggested that strut-and-tie action was the dominant internal force transfer mechanism after cracks formed near the intersection the longitudinal and transverse tie reinforcement. There is a consistent

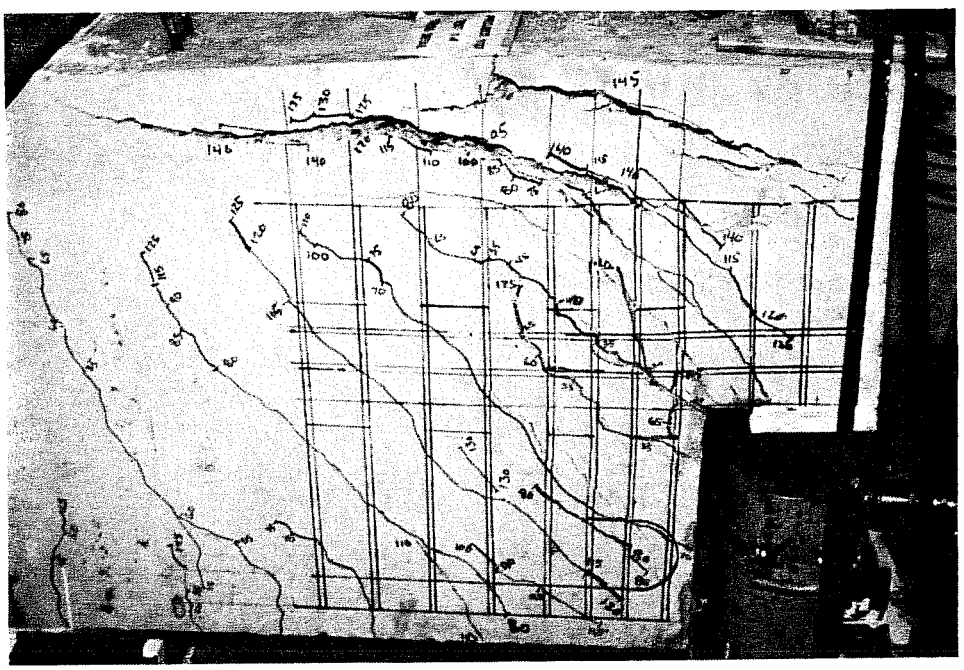

Fig. 4.13 Prototype Beam Specimen Near Failure

500 με offset between the strains of locations LA and LC after 80 kips. Strut-and-tie action and other internal force transfer mechanisms reduced the amount of strain at location LA.

While Fig. 4.14 shows that the slope of the theoretical tie strain compared well with the measured values, Fig. 4.15 shows that the transverse strains varied substantially from the theoretical strain after approximately 106.5 kips. This load was the design strength of the member governed by yielding of the transverse tie. It was observed that strains for locations TA, TB, and TC remained nearly constant from 120 to 145 kips. The rational explanation for this is that after yielding of the transverse ties, force transfer to the CTT-node through strut-and-tie action required large deformations. As the member deformed, other internal force transfer mechanisms including shear friction and dowel action were indeed mobilized in addition to strut-and-tie action. The CTT-node did not sustain a large amount of damage before the shear compression failure of the specimen took place. Excessive deformations took place above and away from the dapped end. Above T_y, the deformation necessary to increase the transverse tie force in the CTT-node did not occur.

Figure. 4.16 shows that the percentage of theoretical tie force at transverse locations decreased after first yield (96.1 kips). For the longitudinal locations shown in Fig. 4.17, the percentages were nearly constant after first yield. Using Eq. 4.1, bar groups at locations TA, TB, and TC respectively saw 5.0%, 3.7% , and 27% of the theoretical transverse tie

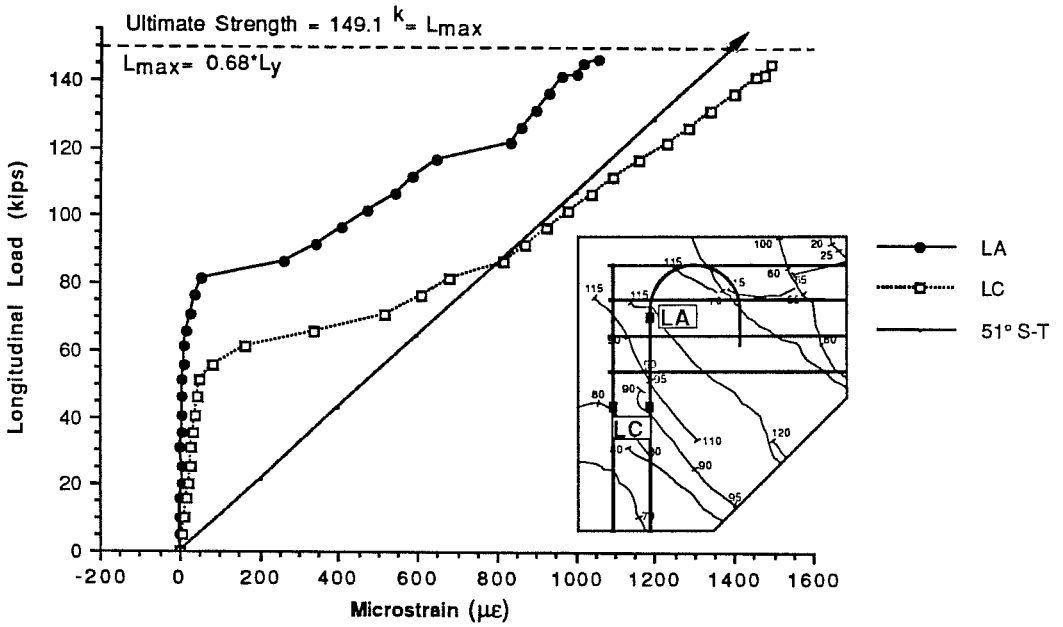

Fig. 4.14 Average Strain at Longitudinal Locations for Prototype Beam Specimen

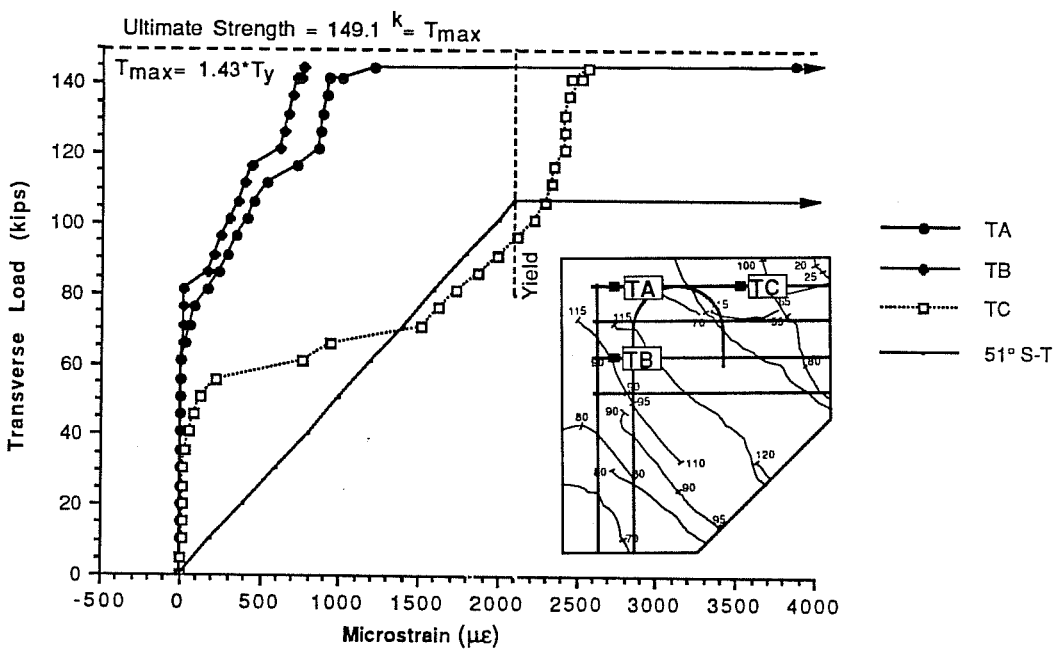

Fig. 4.15 Average Strain at Transverse Locations for Prototype Beam Specimen

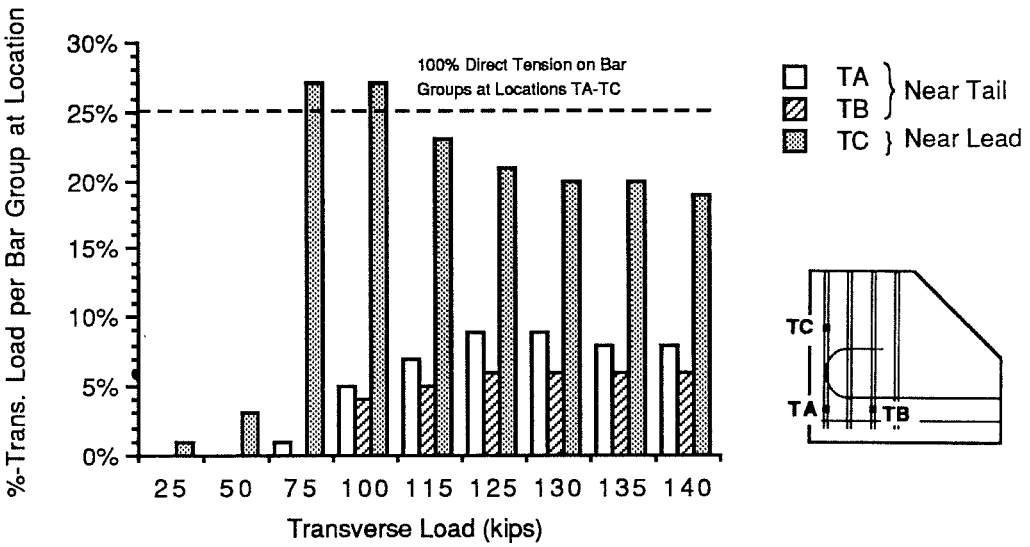

Fig. 4.16 Prototype Beam Specimen-Percentage of Applied Force at Transverse Locations

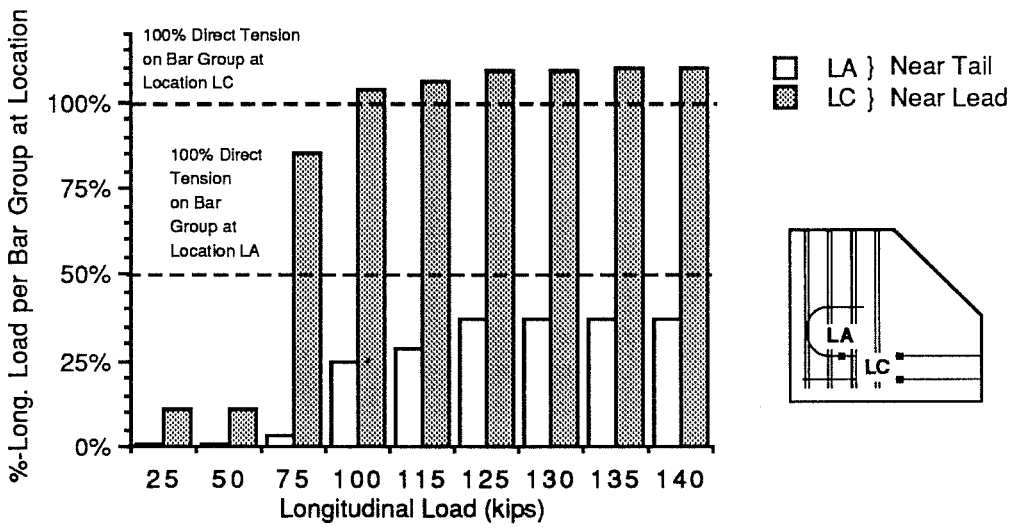

Fig. 4.17 Prototype Beam Specimen-Percentage of Applied Force at Longitudinal Locations

force at 100 kips. Bar groups at location LA saw 31% and location LC saw 128% of the theoretical longitudinal tie force at the same load.

4.3.3 Specimen HFSR-A. Specimen HFSR-A used steel reinforcement details identical to the CTT-node of the Prototype Beam Specimen. The transverse steel provided lateral confinement and a 180° hook anchored the second layer of longitudinal reinforcement. Concrete strength of Specimen HFSR was 7010 psi. The compression strut was 10.6 in. wide at an angle of 45° from the longitudinal tie. The geometry and placement of steel for Specimen HFSR-A were shown in Fig. 3.3.

Using the standard loading procedure described in Sec. 3.10, Specimen HFSR-A was subjected to a maximum tie force of 127.4 kips which is equal to $1.08*T_y$. The specimen did not fail at this load; rather, the test was concluded to prevent overload of the mechanical connectors. This was the first isolated node test and a lower factor of safety was used in calculating the limiting capacity of the mechanical connectors in subsequent tests after confidence had been developed in the testing apparatus and procedure. Crack patterns are shown in Fig. 4.18. The crack widths at various load stages are summarized in Table 4.2.

Average strains for the transverse locations are shown in Fig. 4.19. Except for location TD, the strain curves are fairly typical of other specimens in the study. After 120 kips, the strains for location TD decreased. This load was just over yielding of the external transverse location which occurred at 117.6 kips. After close inspection, it was not possible to develop a rational explanation for the average strains measured at

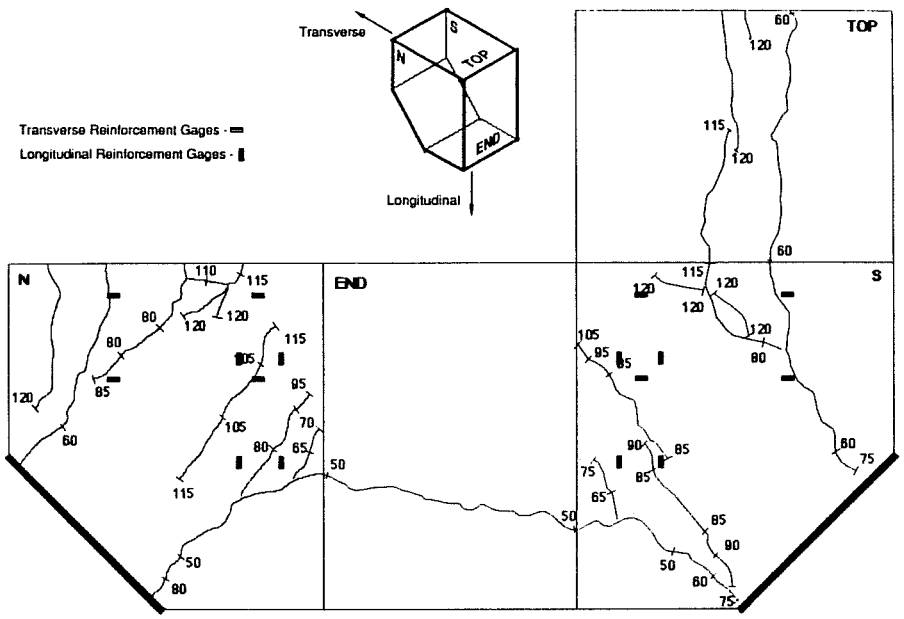

Fig. 4.18 Crack Patterns for Specimen HFSR-A

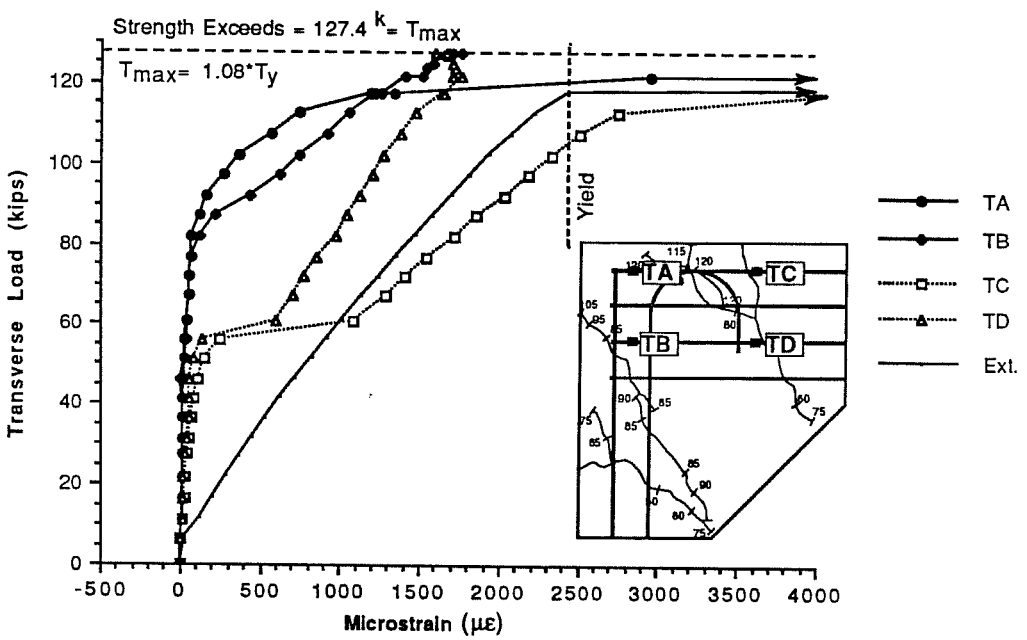

Fig. 4.19 Average Strain at Transverse Locations for Specimen HFSR-A

location TD for loads above 120 kips. There was no experimental evidence to link the decrease in strain to pull-out or slippage of these bars, nor did the decrease appear to be caused by other internal force transfer mechanisms, such as dowel action or shear friction.

4.3.4 Specimen HFSR-B. Specimen HFSR-B was part of the high strength concrete series with f'c=5780 psi. It was a replicate of Specimen HFSR-A. As described in Sec. 3.4, lateral confinement was provided by the transverse reinforcement. The second layer of longitudinal reinforcement was anchored with a 180° hook. The specimen had a strut width of 10.6 in. and strut angle of 45° from the longitudinal tie.

Specimen HFSR-B did not fail prior to conclusion of testing. The maximum force resisted by the specimen was 137.5 kips, which in terms of the yield loads is $1.17*T_y$ and $0.62*L_y$. Figure 4.20 shows that crack patterns for Specimen HFSR-B were quite similar to those of Specimen HFSR-A. Crack widths for Specimen HFSR-B are summarized in Table 4.2. The measured crack widths for Specimen HFSR-B are much smaller than for Specimen HFSR-A. A small amount of this variation can be attributed to the variability of crack measurements made with a plastic card imprinted with comparison marks. Particularly, measurements are complicated because cracks are jagged in nature and vary in width along their length. More importantly, the number and location of cracks affects the crack width. More cracks appeared in Specimen HFSR-B which resulted in smaller crack widths.

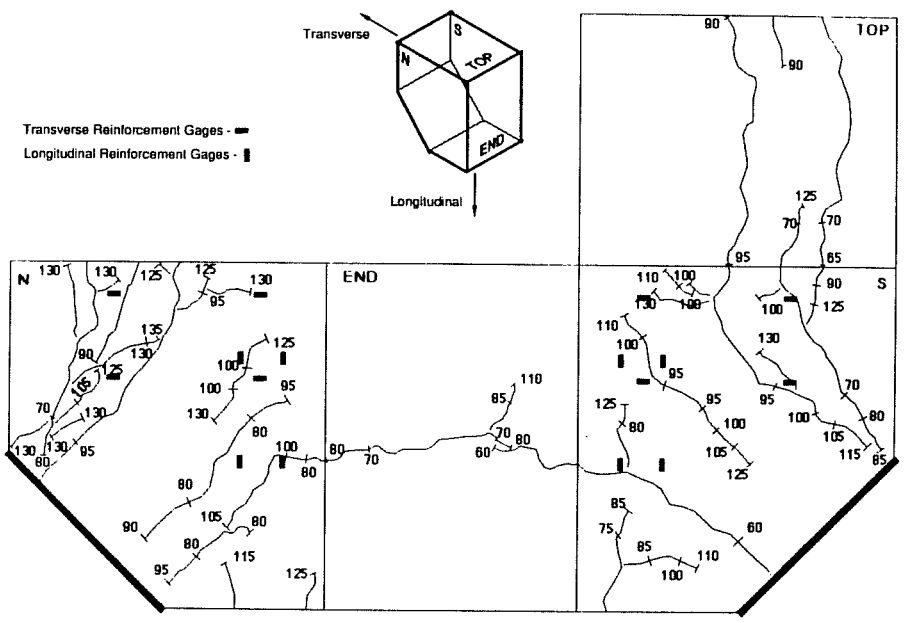

Fig. 4.20 Crack Patterns for Specimen HFSR-B

4.3.5 Specimen LFSR. Specimen LFSR was part of the low strength concrete series with f'c=3720 psi. As described in Sec. 3.4, Specimen LFSR used identical steel reinforcement details as the CTT-node of the full sized, dapped beam. Lateral confinement was provided by the transverse reinforcement and 180° hooks anchored the second layer of longitudinal reinforcement. The strut was 10.6 in. wide and was 45° from the longitudinal tie.

The specimen experienced a development failure of the transverse reinforcement at 117.4 kips which is essentially T_y (117.6 kips). The failure load was equal to 1.00*T_y and 0.53*L_y. The outer transverse U's split the end cover as illustrated in the photographs shown in Fig. 4.21 The widths of major cracks at various load levels are summarized in Table 4.2. The load was increased after cover splitting occurred. The maximum applied load was 125 kips; however, severe cracking and substantial redistribution of the transverse bar forces took place. The practical failure load was set at 117.4 kips which corresponds with cover splitting.

Specimen LFSR was the only low strength concrete specimen with a confining reinforcement detail that experienced a development failure of the transverse bars. Table 4.1 shows that Specimen LHSR, with identical concrete strength and reinforcement details, failed with crushing of the compression strut at a much higher load. The explanation for this was not clear; however, for Specimen LFSR there was an unusually high strain for gage TU2 at load levels where no visible cracking was observed. This indicated slip and/or microcracking affected the straining of the transverse U. The

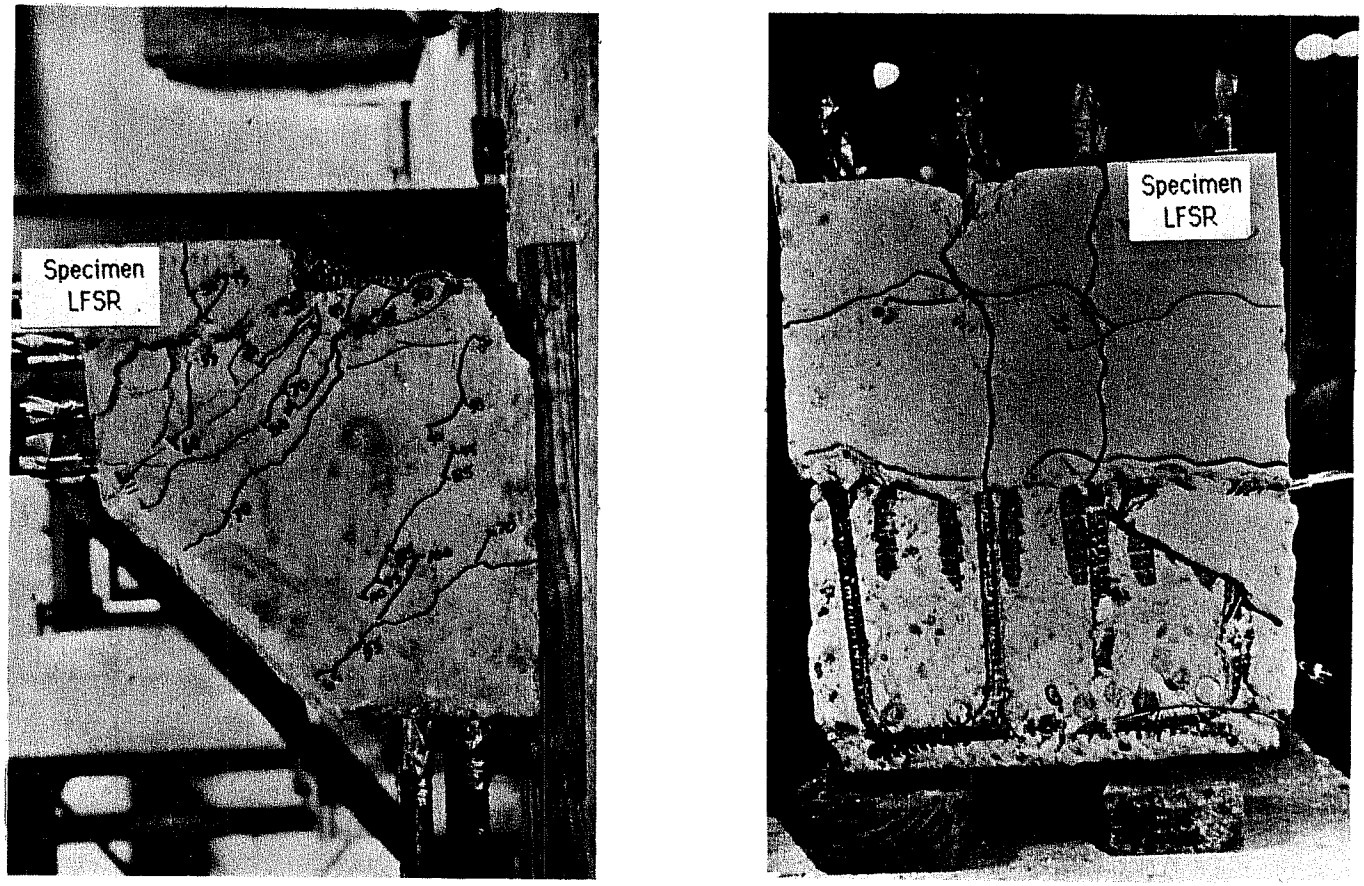

Fig. 4.21 Specimen LFSR-Development Failure of Transverse Reinforcement (North and Top Faces)

radial pressure produced by slip at the bend and along the straight portion of the U was great enough to split the specimen's concrete cover. Bond cracks, shown in Fig. 4.22, were oriented parallel to the transverse bars. A failure plane developed when the bond cracks joined with diagonal tension cracks.

From Fig. 4.23 it was noted that there was a decrease in strain at gages TU2 and TH2 after the development failure took place. It is also interesting to note that the strains at gage TU1 exceeded those of TU2 and TH2 after 90 kips. It is likely that the 90° bend opened and flexural strains added to strains produced by strut-and-tie action.

4.3.6 Specimen LFNC. Specimen LFNC was part of the low strength concrete series with f'c=3720 psi. As described in Sec. 3.4, the transverse reinforcement was detailed to provide minimal lateral confinement and a 180° hook anchored the second layer of longitudinal reinforcement. The compression strut was 10.6 in. wide at an angle of 45° from the longitudinal tie.

Specimen LFNC was tested in the manner described in Sec. 3.10. A cover splitting failure of the transverse bars occurred at 117.8 kips when the transverse bars split off the side cover on the north and south faces. This load was just 0.2 kips above the transverse reinforcement yield load (T_y). In terms of the yield loads for the ties, this would be $1.00*T_y$ and $0.53*L_y$ Photographs and crack patterns of the failed specimen are shown in Figs. 4.24 and 4.25, respectively. Bond cracks, parallel to the reinforcement, appeared when the development failure took place. Crack widths at various load stages are noted in Table 4.2.

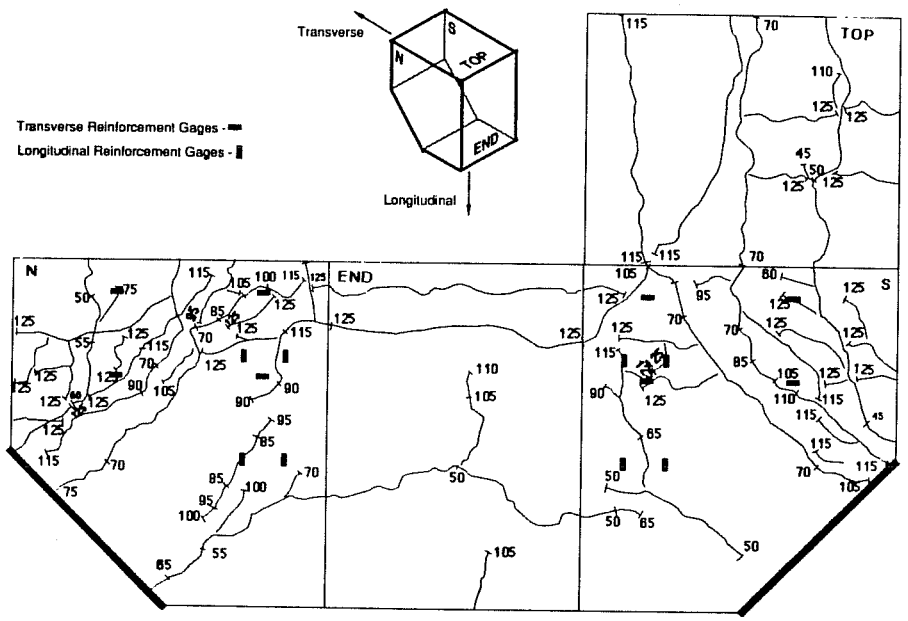

Fig. 4.22 Crack Patterns for Specimen LFSR

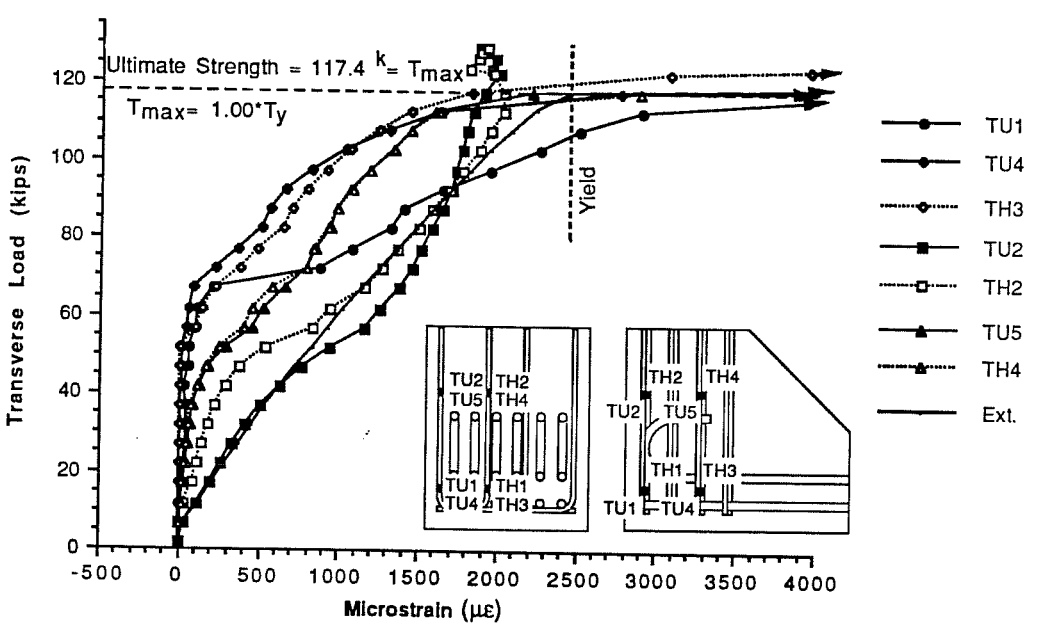

Fig. 4.23 Specimen LFSR-Reinforcement Strain Data for Individual Transverse Gage Locations

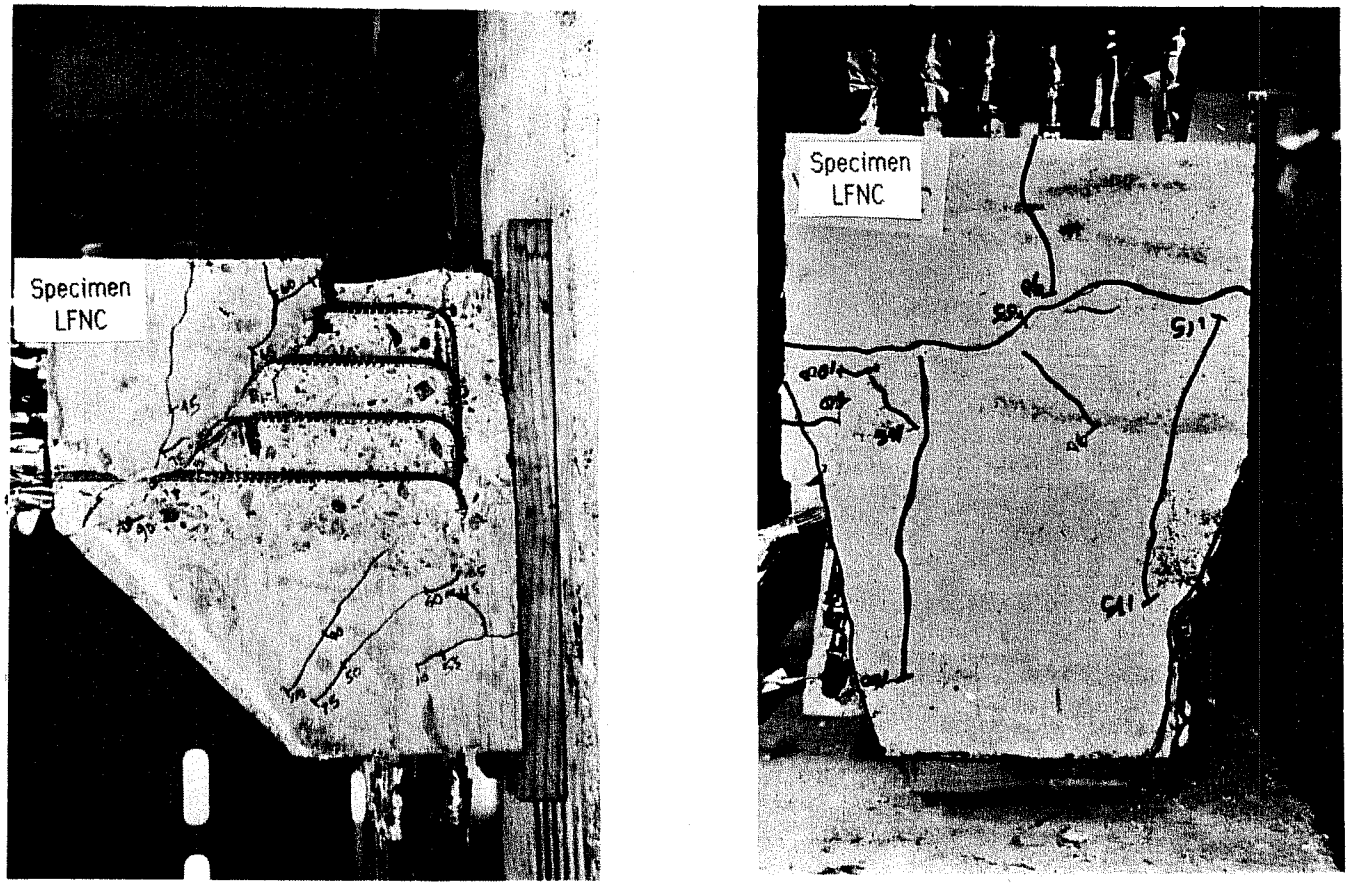

Fig. 4.24 Specimen LFNC-Cover Splitting Failure (North and End Faces)

4.3.7 Specimen HHSR. Specimen HHSR was one of two specimens described in Sec. 3.4 that had a compression strut width of 4.0 in. at the specimen's bearing surface. In other respects, it was identical to Specimen HFSR-B. It was part of the high strength concrete series with f'c=5780 psi. Lateral confinement was provided by the transverse reinforcement and the second layer of longitudinal reinforcement was anchored with a 180° hook. A strut angle of 45° from the longitudinal tensile tie was developed by applying equal forces to the transverse and longitudinal reinforcement.

Specimen HHSR withstood an applied force of 139.0 kips (equal to $1.18*T_y$ and $0.62*L_y$) without failing. At this load, the nominal concrete stress at the bearing surface was 4010 psi or 0.71*f'c. Figure 4.26 shows cracks generally were parallel to the 45° angle of the compression strut. This is an important factor in explaining the high effective concrete strength developed by the specimen and will be discussed the next chapter. Crack widths for Specimen HHSR are given in Table 4.2.

Load versus average strain for transverse and longitudinal locations are plotted in Figs. 4.27 and 4.28. The strains for locations TC and LA exceeded the average strain of external gages subjected to direct tension. Strains produced by local bending were likely measured in addition to those produced by direct tension.

4.3.8 Specimen LHSR. Specimen LHSR had a reduced compression strut width of 4.0 in. at its bearing surface. It was constructed of 3720 psi concrete with lateral confinement provided by the transverse steel. The second layer of longitudinal steel was anchored by a 180° hook. The strut

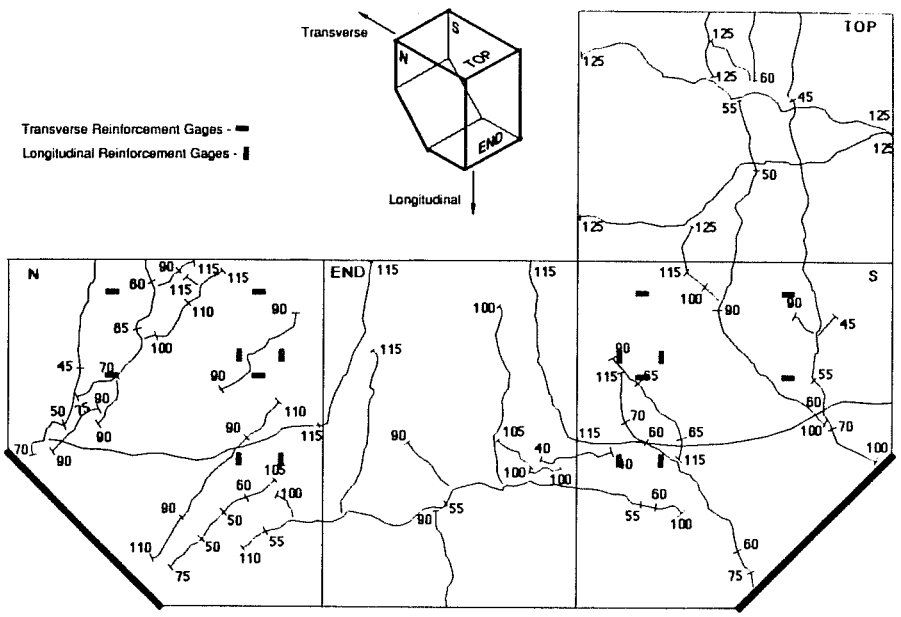

Fig. 4.25 Crack Patterns for Specimen LFNC

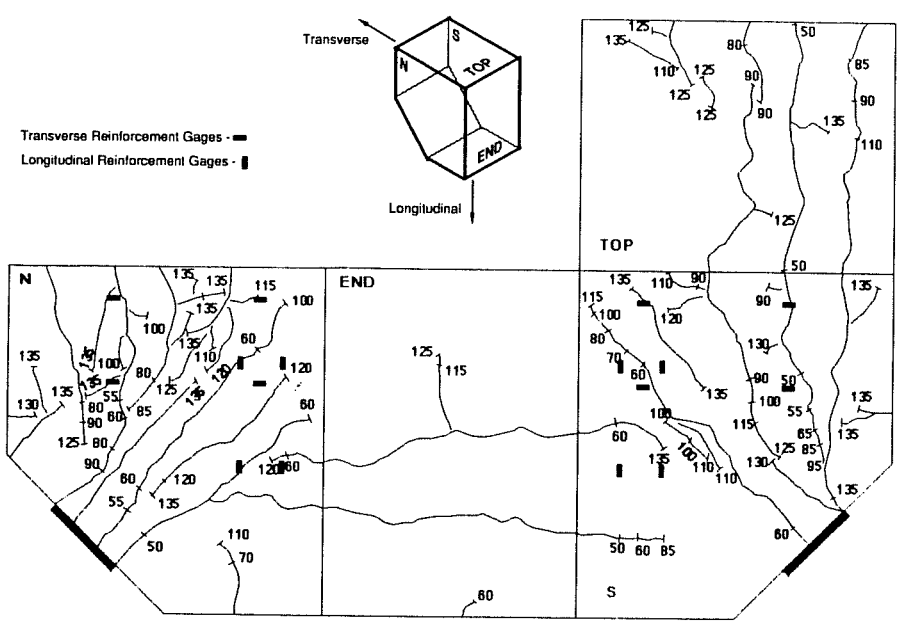

Fig. 4.26 Crack Patterns for Specimen HHSR

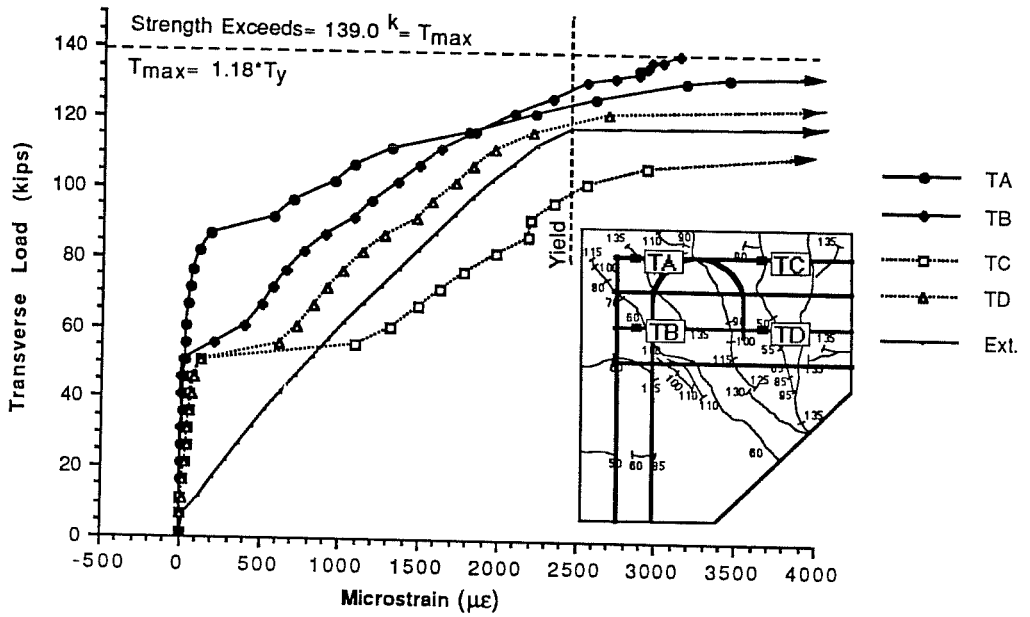

Fig. 4.27 Average Strain at Transverse Locations for Specimen HHSR

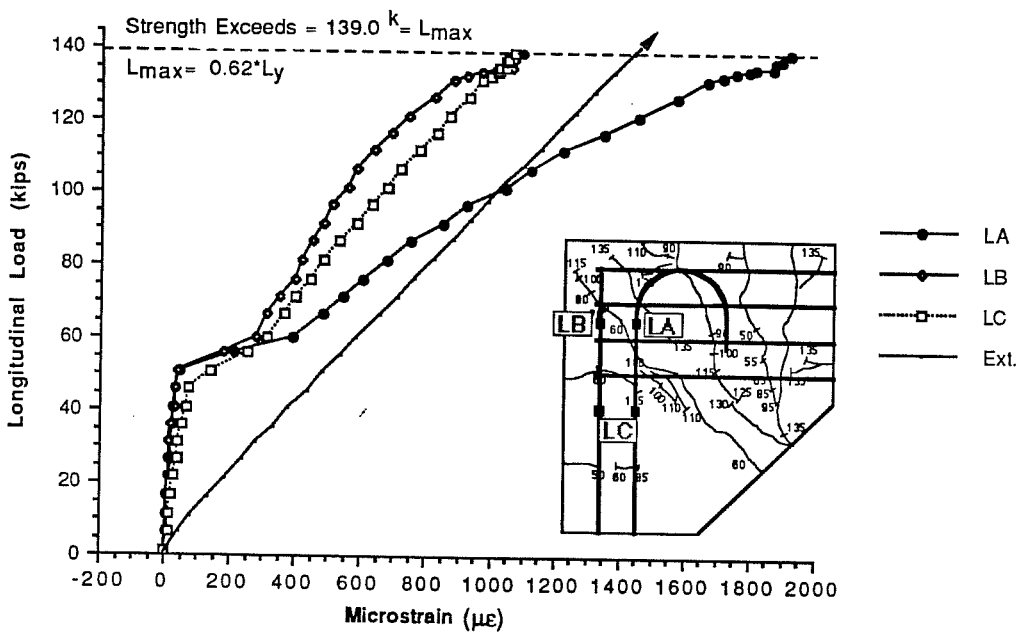

Fig. 4.28 Average Strain at Longitudinal Locations for Specimen HHSR

angle was maintained at 45° by applying equal transverse and longitudinal force to the specimen.

As with other isolated specimens, the load was applied according to the procedures described in Sec. 3.10. At 130.2 kips, a crushing failure of the concrete strut occurred at the specimen's bearing surface. This load corresponds to 1.11*T_y and 0.59*L_y. The nominal concrete stress at the bearing surface was 3840 psi or 1.03*f'c at the failure load. Figure 4.29 shows photographs of the specimen after failure. An indentation at the bearing surface can be distinguished. Cracks parallel to the strut angle are shown in Fig. 4.30. Crack widths are given in Table 4.2

4.3.9 Specimen HFSB. Specimen HFSB was the only specimen in this study that used a straight bar anchorage detail for the second layer of longitudinal steel. Concrete strength was 5780 psi. The transverse reinforcement was detailed to provide for lateral confinement (See Fig. 3.7). Equal forces applied in the longitudinal and transverse directions produced an equilibrating 45° strut angle at the 10.6 in. wide bearing face of the specimen. Specimen details were noted in Sec. 3.4.

At 138.1 kips, or 1.17*T_y and 0.62*L_y in terms of the tie yield loads, the specimen was no longer able to carry additional load. The specimen did not sustain a large amount of damage at failure ; however, Table 4.2 shows that cracks crossing the transverse reinforcement became quite wide. Additionally, bond cracks resulting from radial pressure produced by slip opened parallel to the transverse bars.

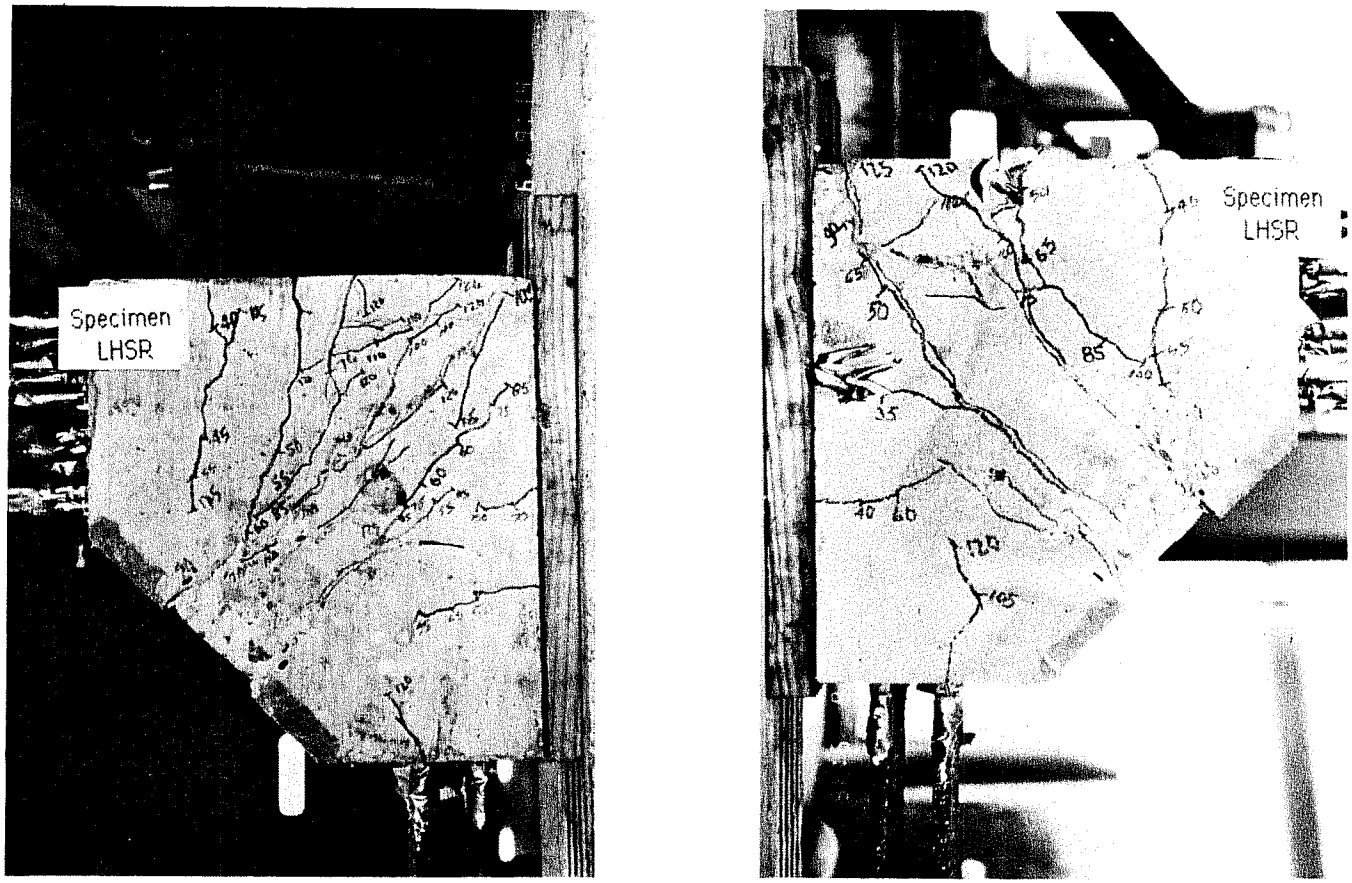

Fig. 4.29 Specimen LHSR-Compression Strut Crushing Failure (North and South Faces)

Figure. 4.31 shows the graph of average strains for the longitudinal steel. The strain curves were quite similar to other specimens with 45°, 10.6 in. wide struts. At 115 kips, the strain at location LA exceeded the strain at location LB. This behavior is identified as a "distance effect" and shows that diagonal cracks intersecting layers of bars at different locations along their length affected the straining of the reinforcement. When a diagonal tension crack crossed the longitudinal bars, the first layer of reinforcement had less available development length than the second layer (See Fig. 4.32). The second layer of reinforcement was strained more than the first layer because it slipped less and was better able to resist tensile forces. In other node specimens, the hook was not so important in providing anchorage to the longitudinal steel, rather it served to hold together the corner of the node. The hook was able to cross more transverse cracks than the straight bar. For the straight bar, the cracks opened wider which resulted in a deterioration of node strength.

4.3.10 Specimen LFAC. Specimen LFAC was part of the low strength concrete series with f'c=3920 psi. Lateral confinement was provided by the transverse reinforcement and a 180° hook was used to anchor the second layer of longitudinal steel. The specimen's strut width was 10.6 in. although during testing it appeared that the actual bearing area was much less. This will be expanded upon in the following discussion. A strut angle of 30° from the longitudinal tie was induced by applying a longitudinal force (L) equal to 1.73 times the transverse force (T).

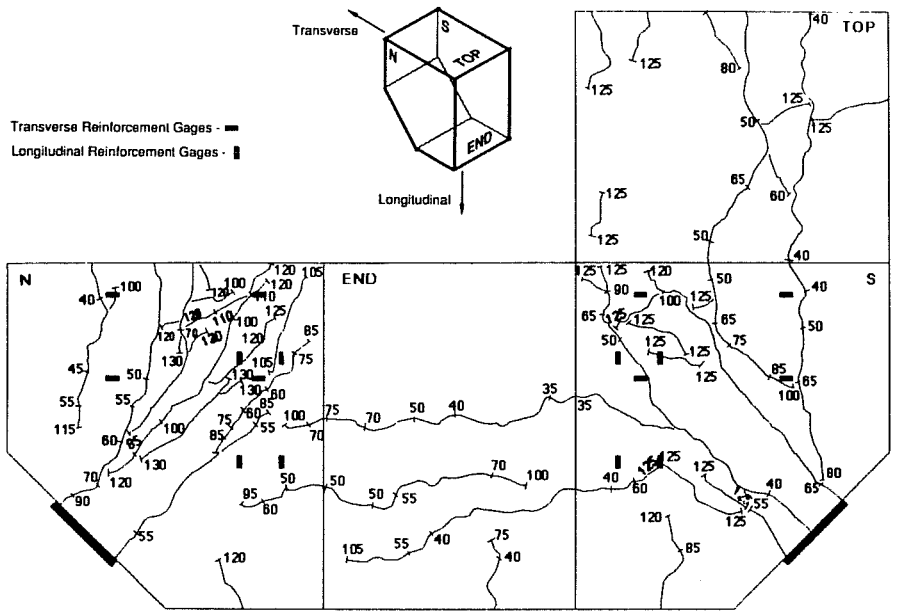

Fig. 4.30 Crack Patterns for Specimen LHSR

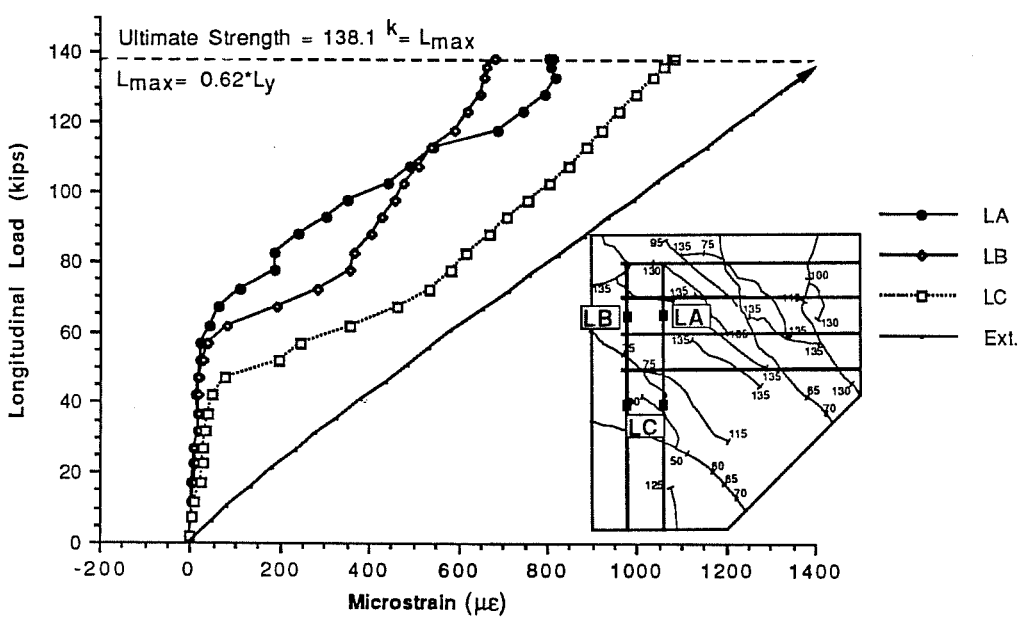

Fig. 4.31 Average Strain at Longitudinal Locations for Specimen HFSB

The application of loads to Specimen LFAC was outlined in Table 3.6. The first visible cracks crossing the longitudinal bars appeared at a longitudinal force of 60 kips. Cracks crossing the transverse bars appeared at 75 kips longitudinal force. The general crack direction followed the 30° resultant of the tie forces. Table 4.2 gives crack widths at various load stages. Crack patterns and photographs of the failed specimen are shown in Figs. 4.33 and 4.34, respectively. The specimen showed signs of distress at 160 kips longitudinal force when spalling occurred at its north face. The spalling was attributed to slip along a failure plane that originated at the lower corner of the specimen bearing surface and ran at a $\pm 30°$ angle through the theoretical centroid of the node defined in Sec. 3.4. Neither the longitudinal or transverse ties were able to reach their yield loads when the specimen reached its ultimate strength. At the failure load of 165.4 kips, the forces in the transverse and longitudinal ties were $0.82*T_y$ and $0.74*L_y$, respectively. A development failure of the longitudinal reinforcement was evidenced by slip along the failure plane and bulging of the specimen's north and south faces as the hooks unwound.

Cracking patterns indicated that the effective bearing surface was much less than 10.6 in. Because of the unbalanced loading in the transverse and longitudinal directions, a slight rotation of the specimen occurred. This produced a gap at the top face of the specimen and concentrated forces over the lower part of the bearing area. Through inspection of the cracks, it is estimated that the strut width was 5 in. The strut width was estimated by drawing lines parallel to the general crack directions. Figure 4.39 (b)

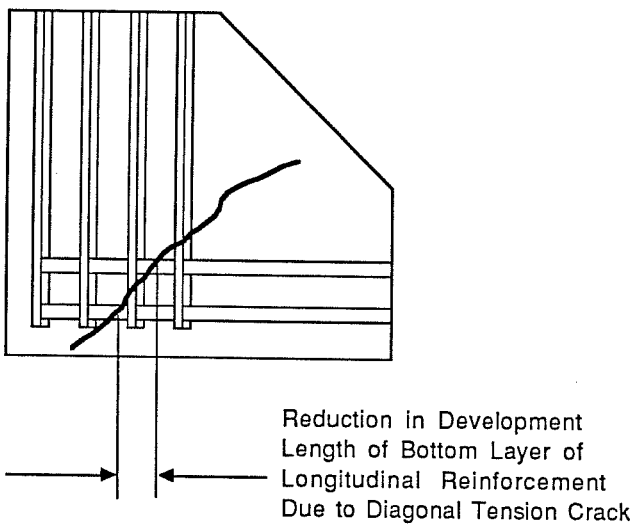

Fig. 4.32 Effect of Diagonal Tension Crack Upon Reinforcement Development Length

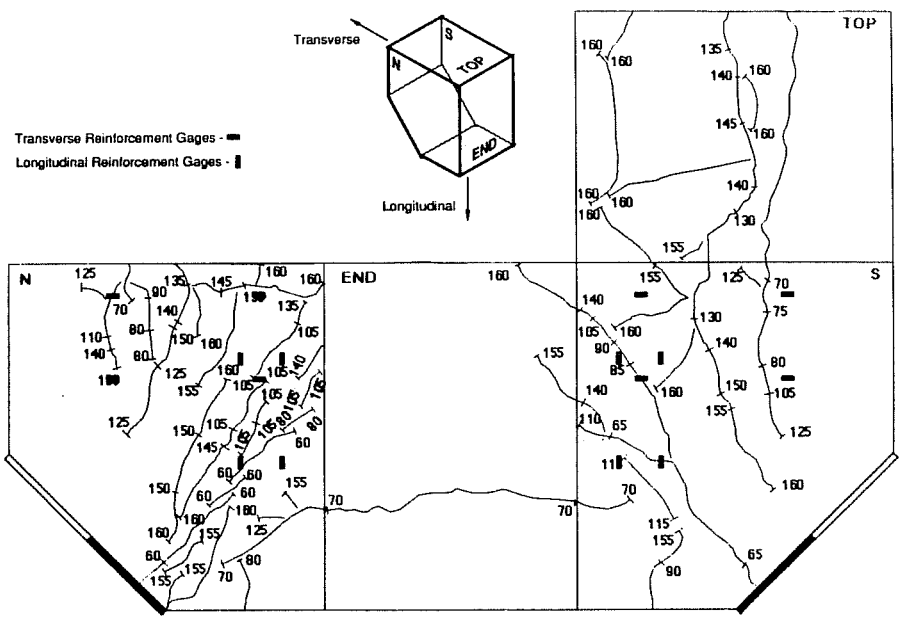

Fig. 4.33 Crack Patterns for Specimen LFAC

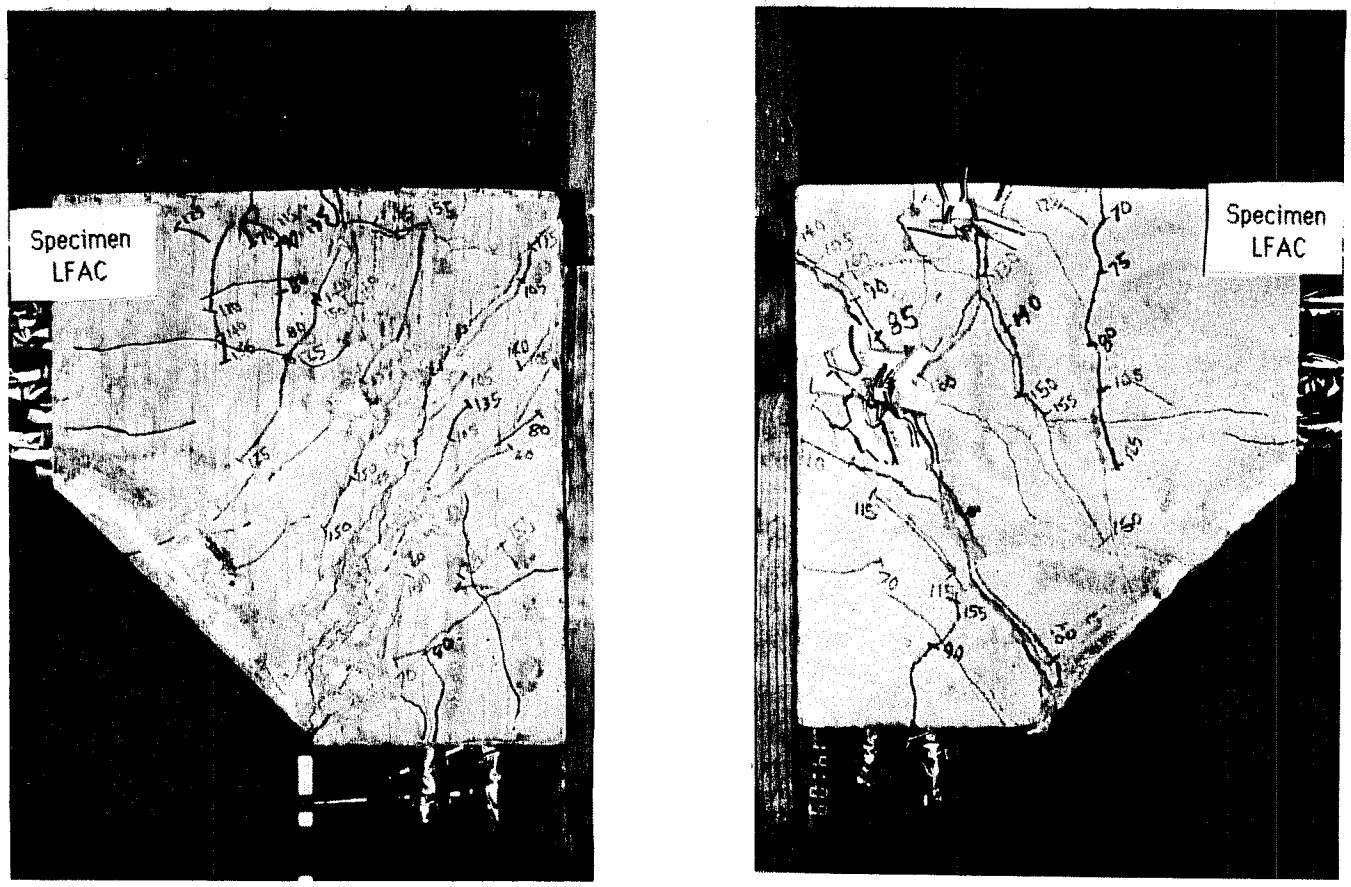

Fig. 4.34 Specimen LFAC-Development Failure of Longitudinal Reinforcement (North and South Faces)

shows that the boundaries of the effective bearing surface were indicated by the points where the outermost lines intersected the specimen's bearing face.

The average transverse strains for Specimen LFAC are shown in Fig. 4.35. At the ultimate transverse load of 96.3 kips, locations TA, TB and TC had yielded. If the transverse bars were only strained though direct tension, yielding would occur at 117.6 kips. The development failure of the longitudinal hook greatly affected these transverse locations. As the longitudinal bars slipped, the transverse gages were additionally strained through localized bending. Bending of the transverse U's was especially obvious when the longitudinal hooks opened up and split the side cover of the specimen.

Strain plots for individual longitudinal gages in Fig. 4.36 show that the specimen experienced a development failure. Companion gages LB3 and LB4 show a reduction in strain after approximately 140 kips. This behavior is caused by a lack of available development length for the first layer of bars. Force was redistributed to the second layer of hooked bars as the first layer of straight bars failed. Bar locations LT3 and LT4 yielded so it is obvious that sufficient development length is available for the hooked bars; still, their capacity is only slightly greater than yield. Overall, the two layers of the longitudinal tie develop only $0.74^{*}L_y$; thus, the failure type is classified as a development failure of the longitudinal tie. Gages LB1 and LB2 indicate higher strains than gages LB3 and LB4 near the failure load. This indicates that gages LB1 and LB2 were affected by local bending.

4.4 Comparisons of Specimen Behavior

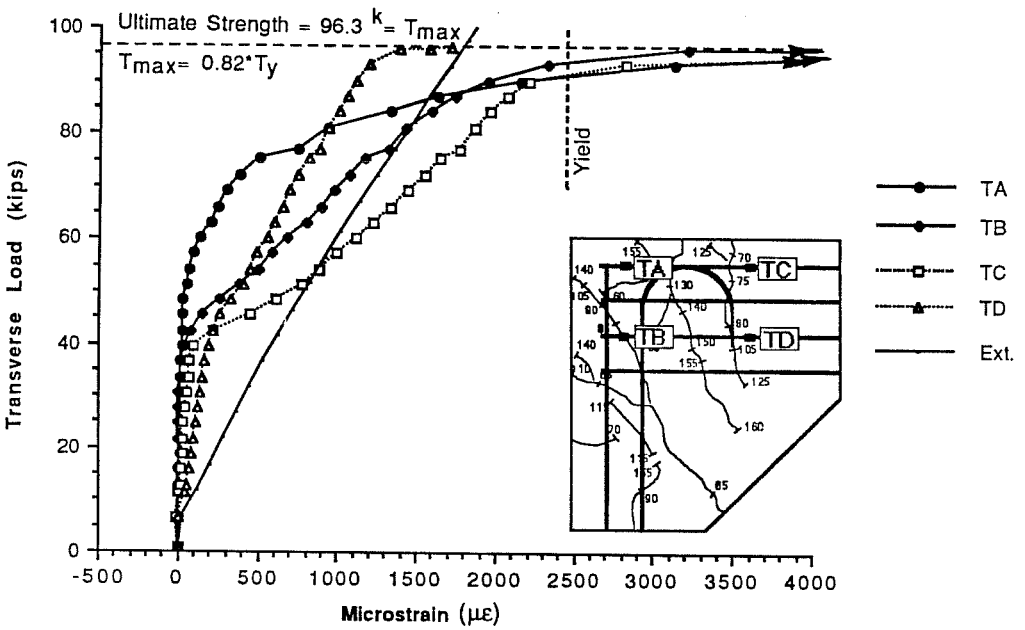

Fig. 4.35 Average Strain at Transverse Locations for Specimen LFAC

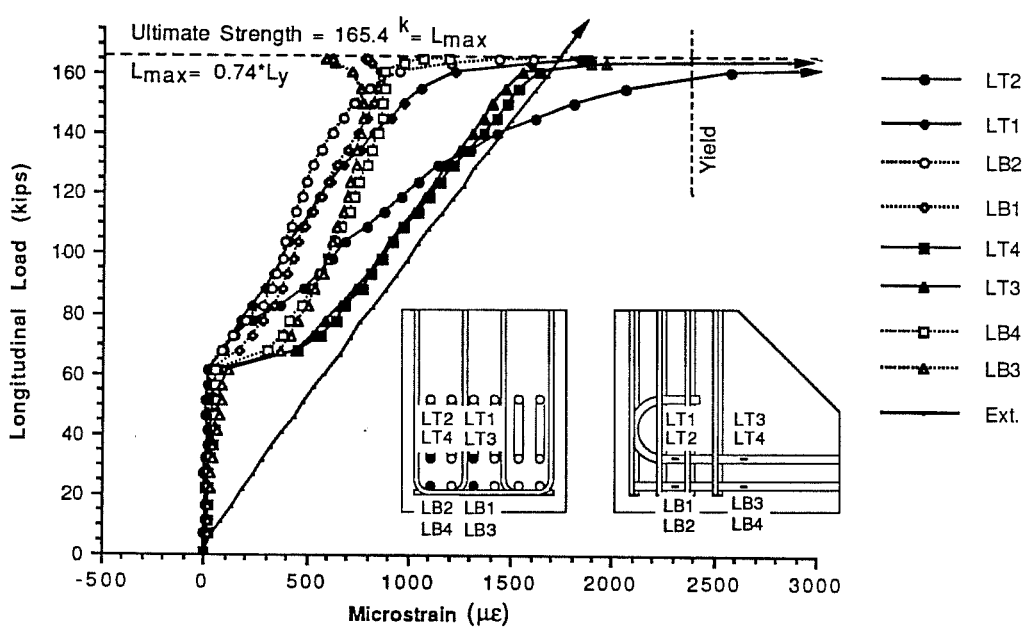

Fig. 4.36 Specimen LFAC-Reinforcement Strain Data for Individual Longitudinal Gage Locations

4.4.1 Crack Patterns. In Fig. 4.37 (a), 4.38 (a), and 4.39 (a) the crack patterns for different specimen types have been superimposed. The specimen types were separated by strut width and strut angle as follows:

1. 45°-strut angle; 10.6 in. strut width (Prototype Beam Specimen, HFSR-A, HFSR-B, LFSR, HFNC, LFNC, and HFSB)
2. 45°-strut angle; 4.0 in. strut width (HHSR and LHSR)
3. 30°-strut angle; 10.6 in. strut width (LFAC-not superimposed)

These figures show similar cracks reoccurred in the different types of specimens. In Figs. 4.37 (b), 4.38 (b), and 4.39 (b) bold lines were drawn to illustrate the general configuration of the compression fields in the different types of CTT-nodes. The lines were drawn parallel to the general crack directions. In all the specimens, the compression fields radiate from the bearing surface. The fan-shaped stress fields followed the theoretical strut angle.

The strut configurations and node dimensions will be further examined in Chapter 5 where the results will be compared to strut-and-tie model assumptions.

4.4.2 Comparison of Strains. In Figs. 4.40 - 4.46, average strains at selected locations are compared for all the specimens. Most of the variations in strain measurements between specimens were small and could be attributed to differences in cracking loads and crack locations. Still, significant variations in strain were exhibited by some specimens. Atypical strain curves in Figs. 4.40 - 4.46 were identified and linked to behavior patterns described in Sections 4.2 and 4.3. Observations and comments are summarized as follows:

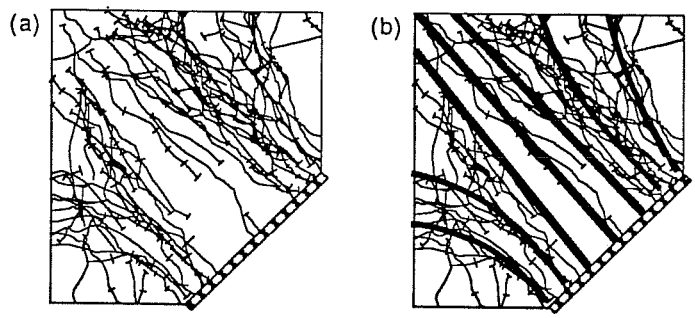

Fig. 4.37 Reoccurring Crack Pattern and Stress Field for Specimens with 45°-10.6 in. Compression Strut

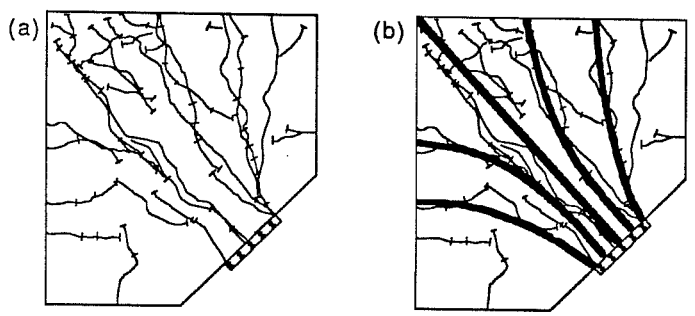

Fig. 4.38 Reoccurring Crack Pattern and Stress Field for Specimens with 45°-4.0 in. Compression Strut

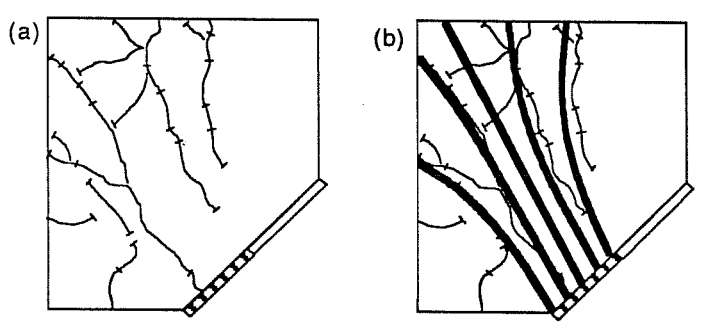

Fig. 4.39 Crack Pattern and Stress Field for Specimen LFAC with 30°-10.6 in. Compression Strut

1) In Figs. 4.40, 4.41, and 4.42, Specimen LFAC reached yield well before other specimens. The anchorage failure of the longitudinal tie described in Sec. 4.3.10 produced high strains at these transverse locations.

2) Specimens HHSR and LHSR are strained more than typical specimens in Figs. 4.41, 4.42, 4.44, and 4.45. This can be attributed to the diagonal tension crack that was sustained by the 4.0 in. strut width specimens. This crack occurred at low loads in these specimens.

3) The strain curves for the Prototype Beam Specimen are steeper than the curves for the node specimens in Figs. 4.40, 4.41, and 4.42. Between 120 kips and 140 kips, locations TA, TB, and TC saw almost no increase in strain for the Prototype Beam Specimen. It is obvious that these locations were not seeing all of the tensile force which was directly applied to the isolated specimens. As identified in Sec. 4.3.2, large deformations necessary to transfer force to the CTT-node realistically would not occur in the full sized, dapped beam.

4) The development failure of Specimen LFSR's first layer of transverse bars is evidenced in Fig. 4.42.

5) In Figs. 4.40 and 4.42, the strain curves for Specimen HFNC varied somewhat from other high strength specimens. The location of the first crack crossing the transverse bars caused the difference.

In Figs. 4.47 and 4.48, strains for lateral confinement bars are presented. There was a grouping of specimens according to concrete strength. Low strength concrete specimens strained much more than the high strength specimens. Location CB yielded only in Specimen LFSR. At low loads, small

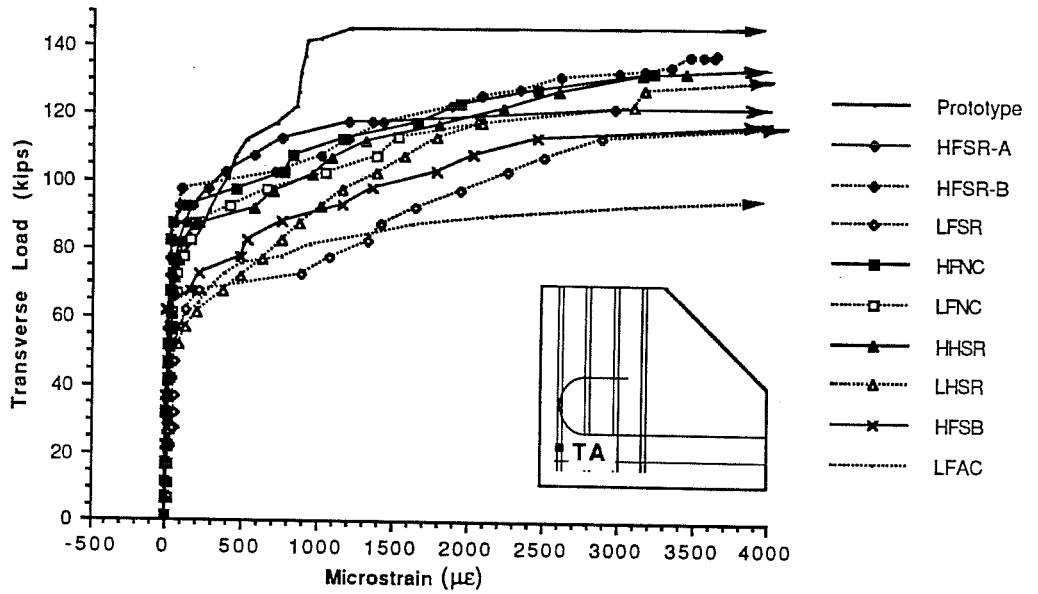

Fig. 4.40 Comparison Strain Graph for Location TA

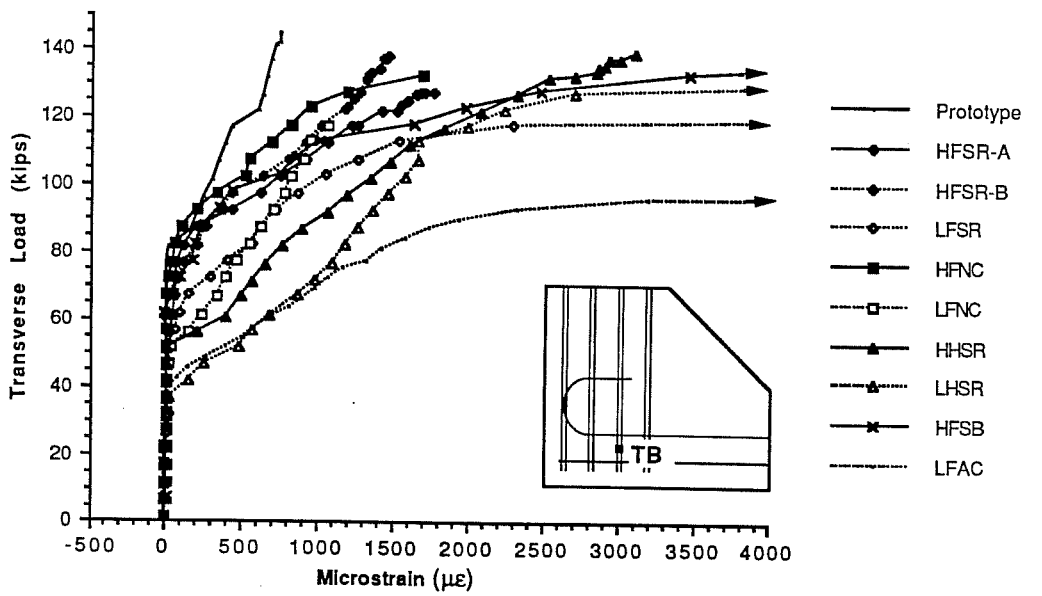

Fig. 4.41 Comparison Strain Graph for Location TB

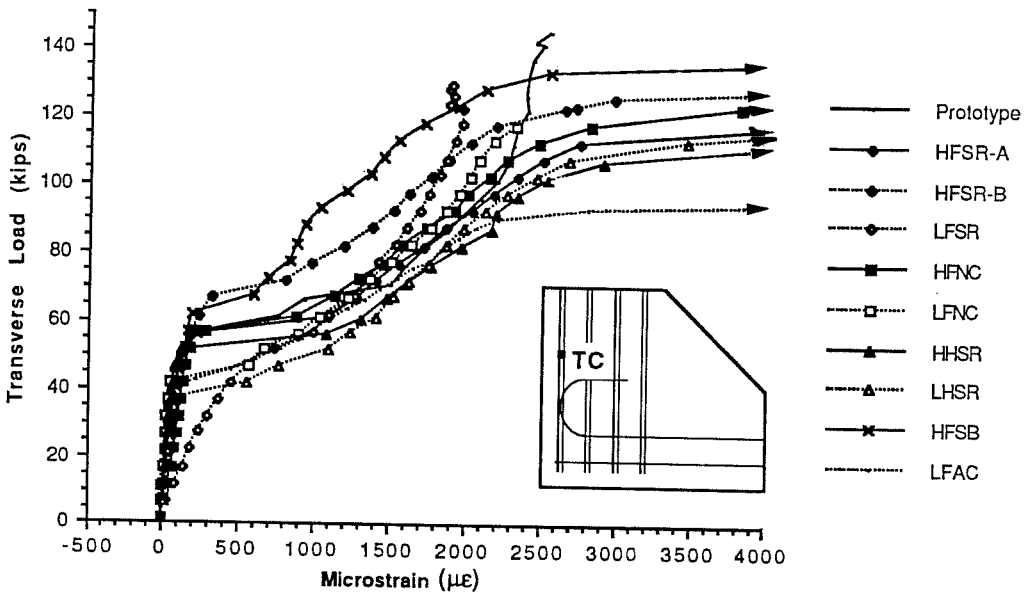

Fig. 4.42 Comparison Strain Graph for Location TC

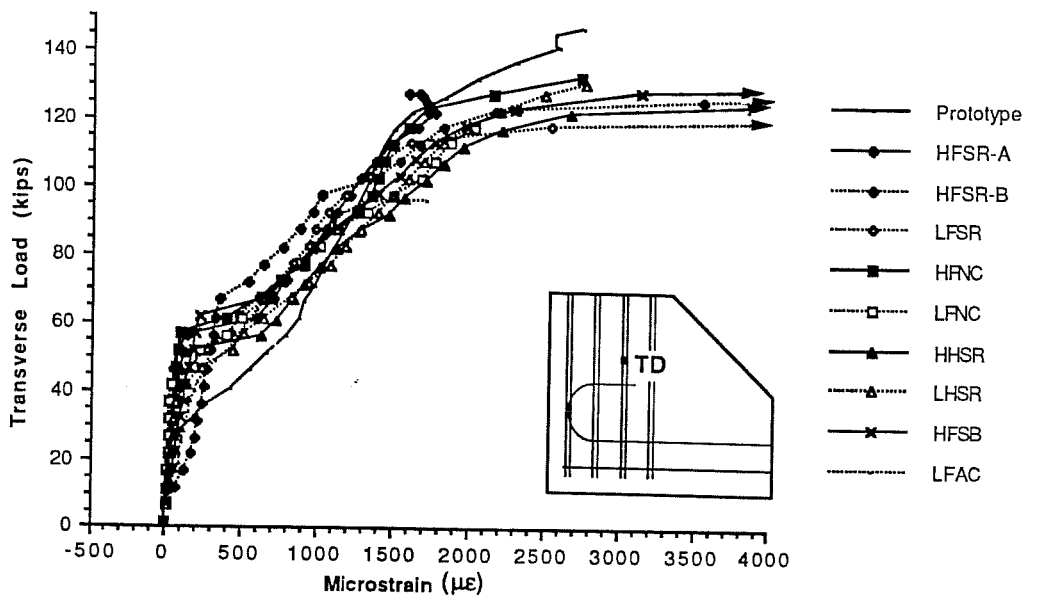

Fig. 4.43 Comparison Strain Graph for Location TD

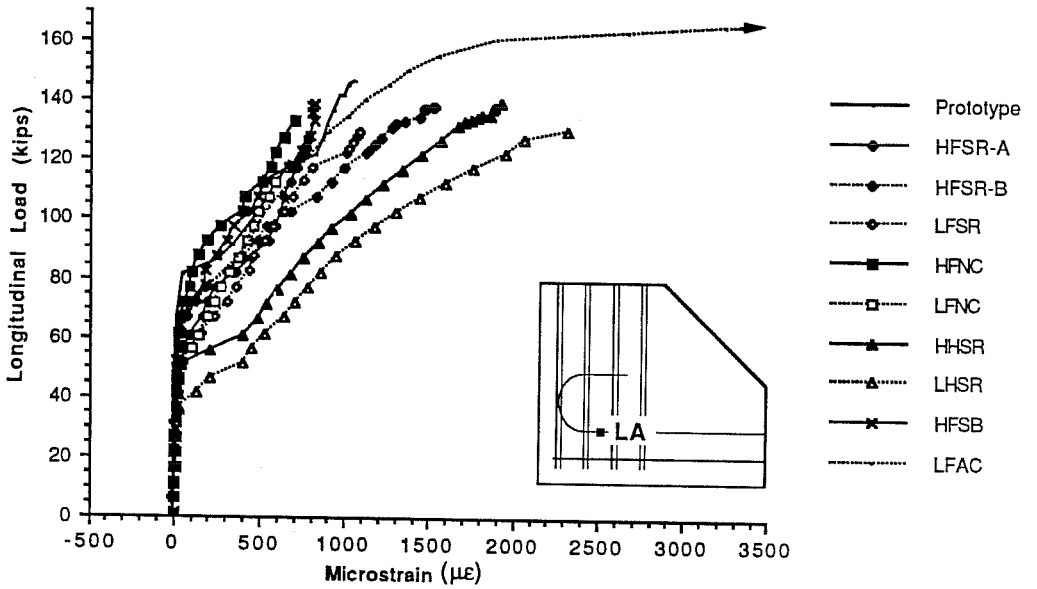

Fig. 4.44 Comparison Strain Graph for Location LA

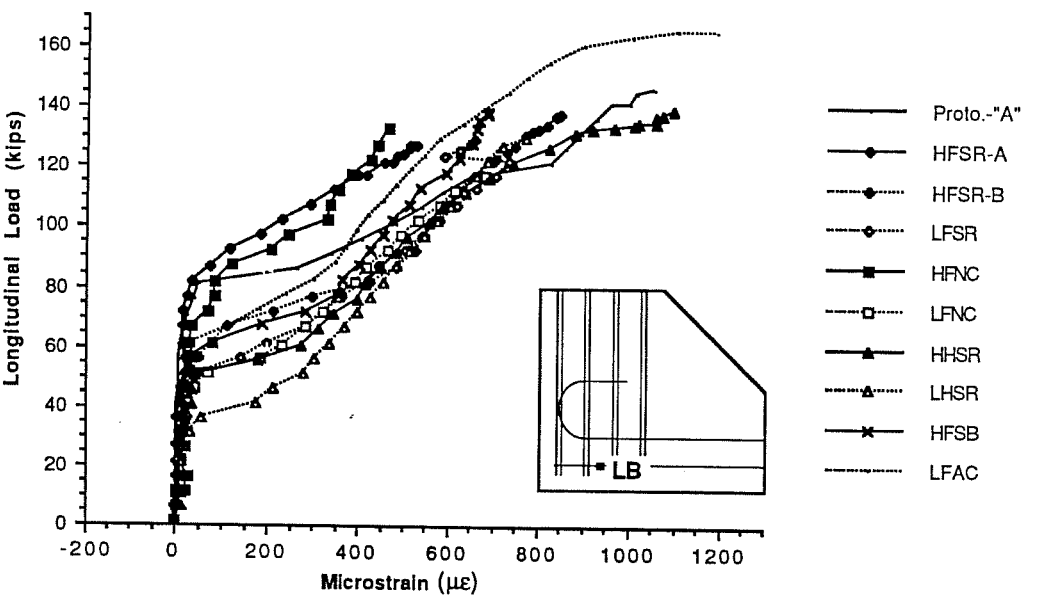

Fig. 4.45 Comparison Strain Graph for Location LB

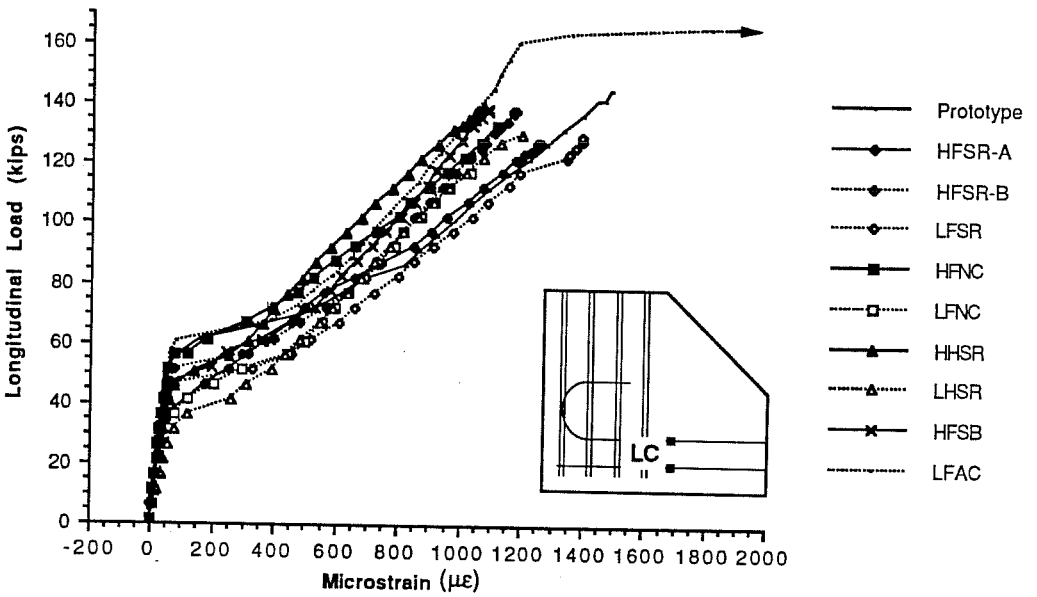

Fig. 4.46 Comparison Strain Graph for Location LC

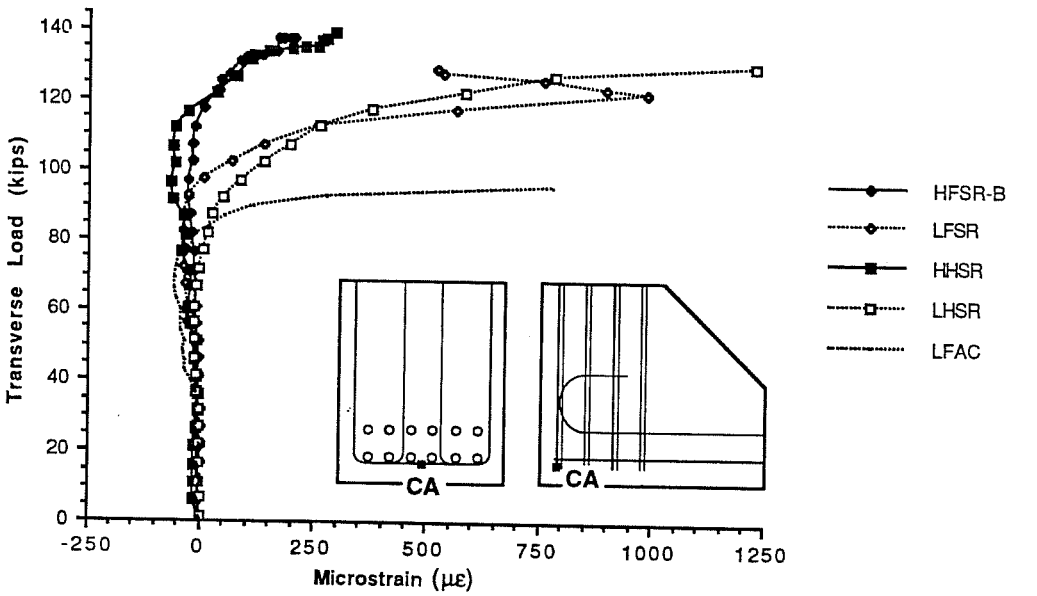

Fig. 4.47 Comparison Strain Graph for Location CA

compression strains were observed. As shown in Fig. 4.49, the confining detail creates compressive forces in the concrete. Tensile strains were observed after the 90° bends slipped and lost anchorage capacity.

4.4.3 Percentage of Applied Tensile Force at Bar Locations. Tables 4.3 and 4.4 summarize information from the bar graphs for each node specimen. Reference loads are 115 kips and 125 kips. The 115 kip reference point is just below 117.6 kips, the yield load (T_y) of the transverse tie. The information for the load of 125 kips is included for comparison purposes. These tables are particularly meaningful since they indicate the percentage of applied force reaching a particular location.

For the transverse locations shown in Table 4.3, the percentage of applied force reaching a particular location was quite similar for all the specimens. Locations TA and TB were the most variable; however, behavior patterns for one or more specimens were not apparent. Thus, the readings from all specimens have been averaged. The percentages for locations TA and TB are close to those for location TC and TD. It was also observed that a large percentage of the direct tensile force was transferred to each location.

The percentage of load reaching the longitudinal locations are summarized in Table 4.4. The specimens have been grouped according to strut width and strut angle in conformance to the data trends. For location LA, shear friction in Specimens HHSR and LHSR resulted in bar stress in excess of those produced by direct tension. The percentages for location LA are almost twice those observed in the 10.6 in. strut width specimens. The differences in percentage of load were not that great for other locations.

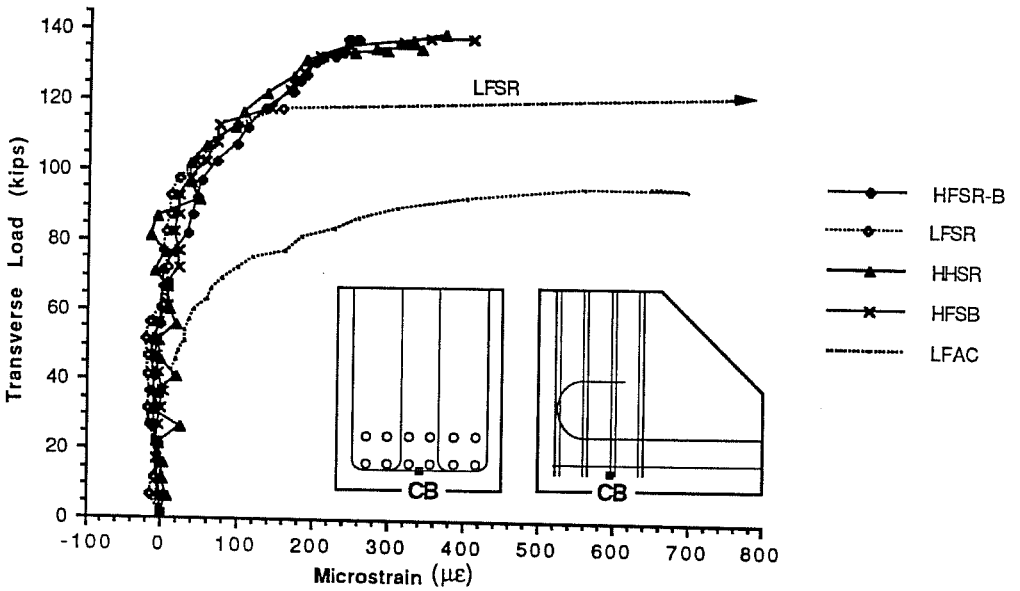

Fig. 4.48 Comparison Strain Graph for Location CB

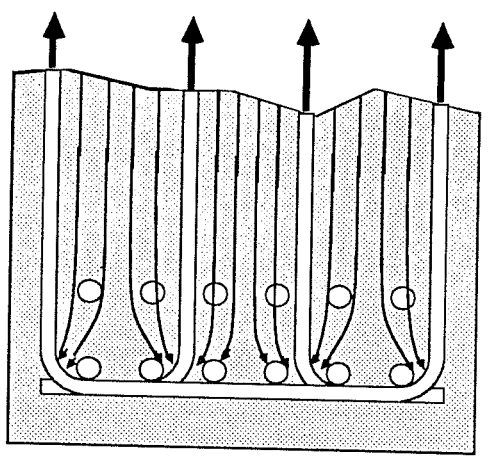

Fig. 4.49 Distribution of Compression Strut Force

Specimen	Location TA		Location TB		Location TC		Location TD	
	%-Applied Force		%-Applied Force		%-Applied Force		%-Applied Force	
	115 Kips	125 Kips	115 Kips	125 Kips	115 Kips	125 Kips	115 Kips	125 Kips
HFSR-A	13.0%	23.8%	14.7%	17.6%	25.6%	23.8%	18.9%	18.5%
HFSR-B	16.5%	21.3%	12.9%	14.4%	23.5%	23.6%	20.5%	23.6%
LFSR	25.7%	*	21.7%	*	22.1%	*	22.9%	*
HFNC	17.4%	22.2%	10.5%	12.8%	25.6%	23.8%	18.7%	20.4%
LFNC	21.0%	*	13.3%	*	24.5%	*	22.2%	*
HHSR	19.5%	23.5%	20.6%	22.5%	25.8%	23.9%	23.5%	23.7%
LHSR	22.1%	23.6%	21.2%	23.5%	25.7%	23.8%	21.8%	23.2%
HFSB	25.6%	23.8%	16.1%	22.2%	19.4%	20.9%	21.4%	23.5%
LFAC	*	*	*	*	*	*	*	*
Average	20.1%	23.0%	16.4%	18.8%	24.0%	23.3%	21.2%	22.2%
St. Dev.	4.4%	1.0%	4.3%	4.6%	2.3%	1.2%	1.8%	2.2%
Direct Tension	25.0%	25.0%	25.0%	25.0%	25.0%	25.0%	25.0%	25.0%
Ave. as % of Dir. Tens.	80.4%	92.1%	65.5%	75.3%	96.1%	93.2%	85.0%	88.6%

Table 4.3 Comparison of Percentages of Applied Force at Transverse Locations

Specimen	Location LA		Location LB		Location LC	
	%-Applied Force		%-Applied Force		%-Applied Force	
	115 Kips	125 Kips	115 Kips	125 Kips	115 Kips	125 Kips
HFSR-A	29.6%	30.3%	15.9%	19.6%	93.8%	96.0%
HFSR-B	41.4%	45.8%	28.4%	29.4%	82.9%	83.9%
LFSR	34.2%	*	30.1%	0.0%	100.0%	0.0%
HFNC	24.1%	25.2%	17.0%	18.1%	80.1%	81.8%
LFNC	27.8%	*	28.7%	0.0%	86.0%	0.0%
HFSB	27.0%	31.0%	25.1%	25.9%	78.3%	77.6%
Average	30.7%	33.1%	24.2%	23.3%	86.9%	84.8%
St. Dev.	6.2%	8.9%	6.2%	5.3%	8.4%	7.9%
Direct Tension	50.0%	50.0%	50.0%	50.0%	100.0%	100.0%
Ave. as % of Dir. Tens.	61.4%	66.2%	48.4%	46.5%	86.9%	84.8%
HHSR	55.2%	59.1%	29.7%	32.2%	71.0%	72.6%
LHSR	69.4%	75.3%	28.7%	28.5%	85.2%	86.7%
Average	62.3%	67.2%	29.2%	30.4%	78.1%	79.7%
St. Dev.	10.0%	11.5%	0.7%	2.6%	10.0%	10.0%
Direct Tension	50.0%	50.0%	50.0%	50.0%	100.0%	100.0%
Ave. as % of Dir. Tens.	124.6%	134.4%	58.4%	60.7%	78.1%	79.7%
LFAC	31.4%	33.9%	22.2%	22.8%	75.8%	75.2%
Direct Tension	50.0%	50.0%	50.0%	50.0%	100.0%	100.0%
Ave. as % of Dir. Tens.	62.8%	67.8%	44.4%	45.6%	75.8%	75.2%

*-Data Unavailable
Specimen Failed

Table 4.4 Comparison of Percentages of Applied Force at Longitudinal Locations

Except for Specimens HHSR and LHSR, it was observed that internal force transfer mechanisms reduced the applied tension force substantially at locations LA and LB.

4.4.4 Validity of Node Tests. The test results from the node specimens are only meaningful if they are representative of the behavior that would occur in the CTT-node of the full-sized, dapped beam. The test results for the Prototype Beam Specimen and applicable node specimens will be compared to assess the validity of the node tests.

The cracking patterns and reinforcement strains for the Prototype Beam Specimen and high strength node specimens with 45°-10.6 in. struts were quite similar. Figure 4.50 shows superimposed crack patterns for Specimen HFSR-A and the Prototype Beam Specimen. The cracks for the Prototype Beam Specimen are shown boldly. This figure shows the cracking pattern of the node specimen compares well with that of the full-sized, dapped beam specimen. The same cracks generally appeared in both specimens at approximately the same load. One exception was the diagonal tension crack perpendicular to the center of the bearing face in the Prototype Beam Specimen. It is thought that confinement at the bearing face prevented this crack from forming in Specimen HFSR-A. Adhesion and friction at the bearing surface probably reduced diagonal tensile strains as shown in Fig. 4.51.

Reinforcement strain comparisons in Sec. 4.4.2 showed some differences in the transverse strains of the full-sized and node specimens after the design strength was achieved. As previously mentioned, strains for

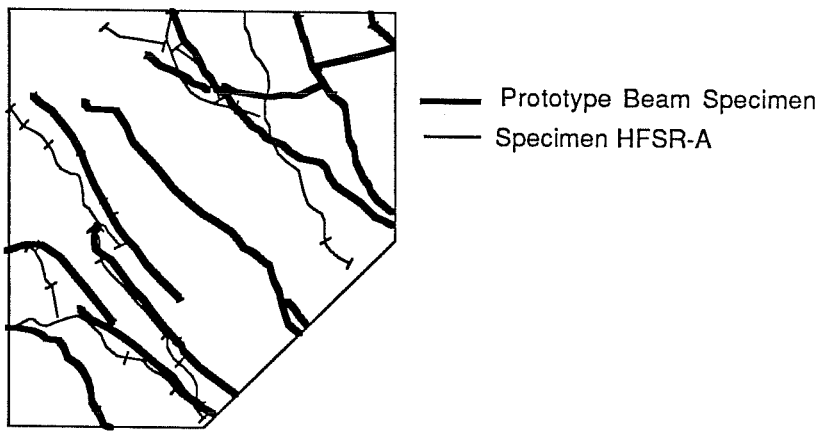

Fig. 4.50 Crack Pattern Comparison of Specimen HFSR-A and Prototype Beam Specimen

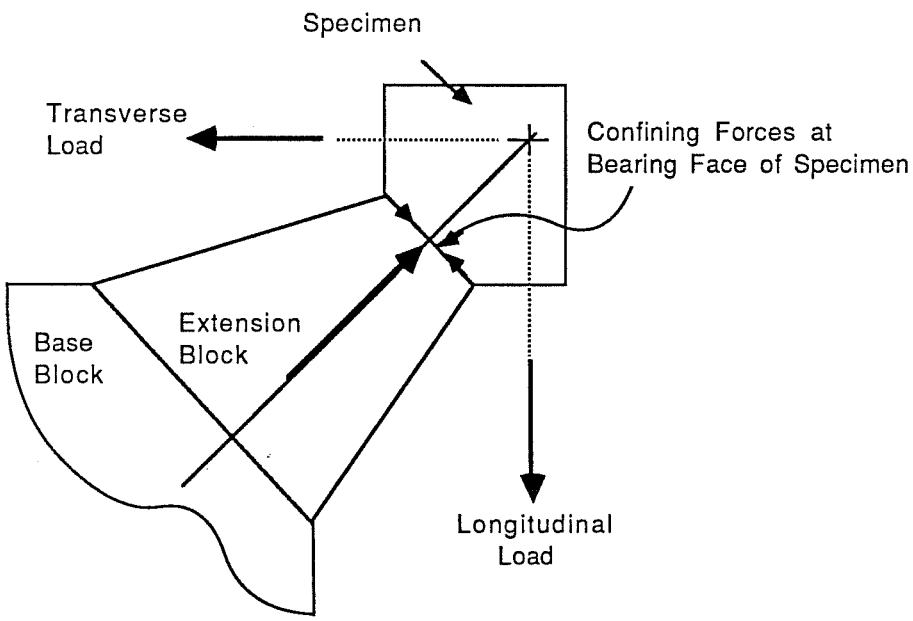

Fig. 4.51 Confining Forces Produced by Test Setup

the CTT-node transverse bars of the Prototype Beam Specimen did not increase after yielding of the transverse steel at the re-entrant corner. Damage in the Prototype Beam Specimen was above and away from the nib of the dap; therefore, additional forces were never transferred to the CTT-node at the lower corner of the dapped beam. In the node specimen, the transverse tie force was increased through loading after the reinforcement yielded. Thus, transverse bar strains increased after the design strength of the specimen was achieved. While it is interesting to study the behavior of the node specimens after yielding of the transverse steel, it is unlikely that such strains would develop in an actual member. The deformation limit of the member would probably limit the amount of force that would be transferred to the CTT-node.

In summary, the node specimen behavior was felt to be characteristic of behavior of the CTT-node of the full-sized, dapped beam. Correlations between the behavior of the two types of specimens were quite good, especially before yield of the transverse steel. Certain behavioral patterns from the node specimens could be attributed to the method of testing; still, the test data appeared to be valid and relevant in describing CTT-node behavior.

4.5 Summary

The experimental portion of this study provided information about the distribution and transfer of forces within the CTT-node as well as the ultimate strength and behavior of the specimens. The results from one full sized, dapped beam and nine node specimens were presented. Eight specimens reached their design strength governed by yielding of tensile ties. Specimen

LFSR, although failing prematurely, was less than 1 kip from its design strength. Specimen LFAC experienced a development failure of the longitudinal tie at $0.74*L_y$ where L_y is the is the yield load of the longitudinal tie. Several specimens experienced post-yield failures including strut crushing, cover splitting, and gross slippage of reinforcement. Some specimens behaved similarly and could be grouped for comparison. The concrete strength affected the ultimate strength of the node; however, it did not affect cracking patterns and reinforcement strains as much as did the specimen geometry and placement of steel. Strut-and-tie action was identified as the dominant internal force transfer mechanism after yield.

In all the specimens, strains in the different layers of reinforcement making up the tie were influenced by crack orientation. This behavior pattern was identified as a "distance effect". Cracks generally originated at the surface of the specimen, were aligned with the inclination of the compression strut, and crossed the layers of bars at an angle. Layers of bars closest to the surface of the specimen generally were intersected by cracks close to their free or hooked end. Outer layers of bars which were anchored sufficiently reached higher strains than interior layers. In contrast, outer bars were strained less than interior bars if major cracks were close enough to the end of the bars to reduce their available development length.

CHAPTER 5

EVALUATION OF STRUT-AND-TIE MODEL

5.1 Introduction

Nodes are critical parts of the strut-and-tie model, yet they are not fully understood. The designer is generally able to adequately develop the overall strut-and-tie model for D- and/or B-regions of a structure; however, design checks for nodes, especially those anchoring tensile ties, are unclear. The main reason for this is that comprehensive proposals for dimensioning such nodes have yet to be developed. In particular, it is uncertain how present design models are to be consistently adapted to different reinforcement layouts.

Because the scope of the present study is limited to a narrow range of variables and a few tests, it is not possible to develop comprehensive design recommendations for CTT-nodes. Still, the node test results provide important information in an area where the strut-and-tie model is definitely lacking. Therefore, in this chapter the test results will be used to: 1) verify present proposals where possible; 2) identify behavior patterns not considered by present proposals; and 3) both substantiate and serve as a basis for CTT-node interim design guidance.

As mentioned in Chapter 2, an assessment of the node must be made during the final phase of design. Prior to that phase, a conceptual static system (strut-and-tie model) will have already been developed to represent the complex state of stress within the member in a simplified form. The designer must make two checks of the node which are normally based on the

actual reinforcement layout selected. First, the concrete stress in the node must be checked to ensure that it does not exceed the effective concrete strength limit of $f_{ce}=\upsilon f'c$. Second, the proper anchorage of tie reinforcement must be ensured. Further design iterations are not required if these conditions are satisfied.

Figure 5.1 shows similar design rationale for detailing a steel truss and for detailing a concrete member using the strut-and-tie model. After the members of the structural system are proportioned to carry the calculated forces, the nodes are detailed. Specifically, the nodes must transfer forces between elements. In the steel truss, bolts, welds, and possibly gusset plates are sized to safely transfer load between the members. In contrast, the node in a concrete member must rely on bond, anchorage, and other internal force transfer mechanisms to transfer strut and tie forces.

5.2 Dimensions and Configuration of the Compression Strut.

5.2.1 Stress Trajectories and Actual Crack Patterns.

It has been suggested (1) that the general layout of the strut-and-tie model should follow the elastic stress distribution. This is useful since available elastic analyses can be used to formulate the model. The magnitude and direction of the principle stresses determined from elastic analysis are helpful to the designer because the force flow within the member can be identified Hence, a strut-and-tie model which transfers the design load to the supports can be developed. Such use of elastic models is convenient although use of other models based on plasticity will usually lead to more efficient reinforcement patterns.

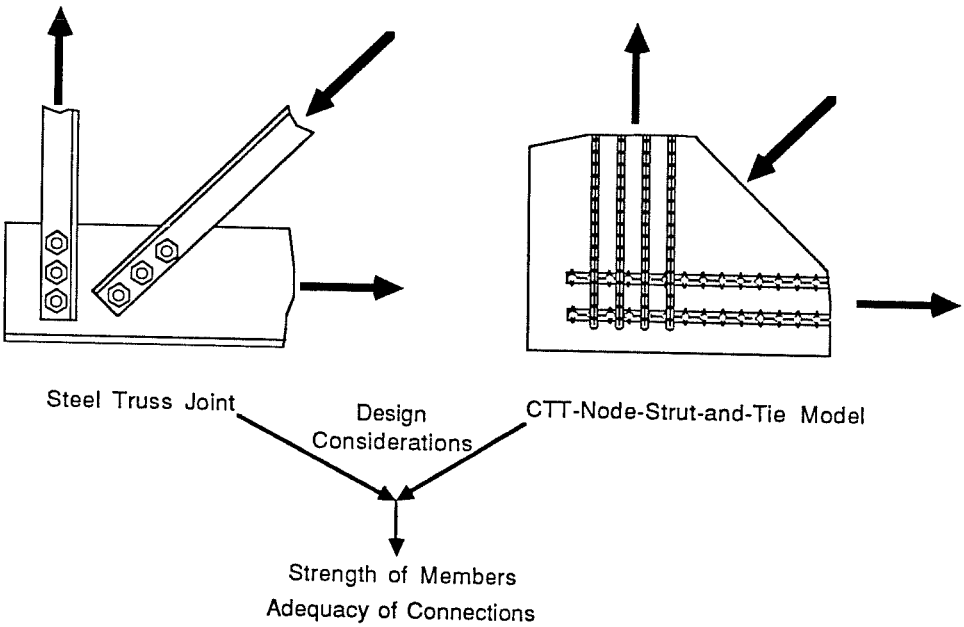

Fig. 5.1 Comparisons of Design Rationale Used for Nodal Region of Strut-and-Tie Model and Joint of Steel Truss

Figure 5.2 shows principle stress vectors and elastic stress trajectories for the Prototype Beam Specimen. The geometry of the CTT-nodal specimens has also been noted in the figure. After an elastic finite element analysis was used to generate the principle stress vectors shown in Fig. 5.2 (a), stress trajectories were developed by drawing lines parallel to the principal stress directions as illustrated in Fig. 5.2 (b). Stress trajectories should not be confused with stress contours where the lines trace paths of equal stress. The CTT-node is characterized by a fanning of the compressive stress trajectories. The tensile stress fields form a set of near parallel arcs. The compressive stress trajectories, which are orthogonal to the tensile stress trajectories, fan out as they cross the arcs. The narrowest portion of the fan region is subject to the highest compressive stress. A line of separation identifies the point where compressive stress trajectories change curvatures. This could be used to orient the compression strut of the CTT-node. It is interesting to compare the cracking patterns of the Prototype Beam Specimen (shown in Fig. 4.13) with the principal stress trajectories. It is seen that the actual cracks are nearly parallel to the principle compressive stress directions and hence normal to the principle tensile stress directions as would be expected. Cracks generally fan away from the vertical reaction point in the Prototype Beam Specimen. In the CTT-node, fanning of the compression struts predicted by the elastic analysis was evident in both the Prototype Beam Specimen and the node specimens. The angle of the major diagonal tension cracks in the CTT-node of the Prototype Beam Specimen is approximately 40° from the horizontal. This is

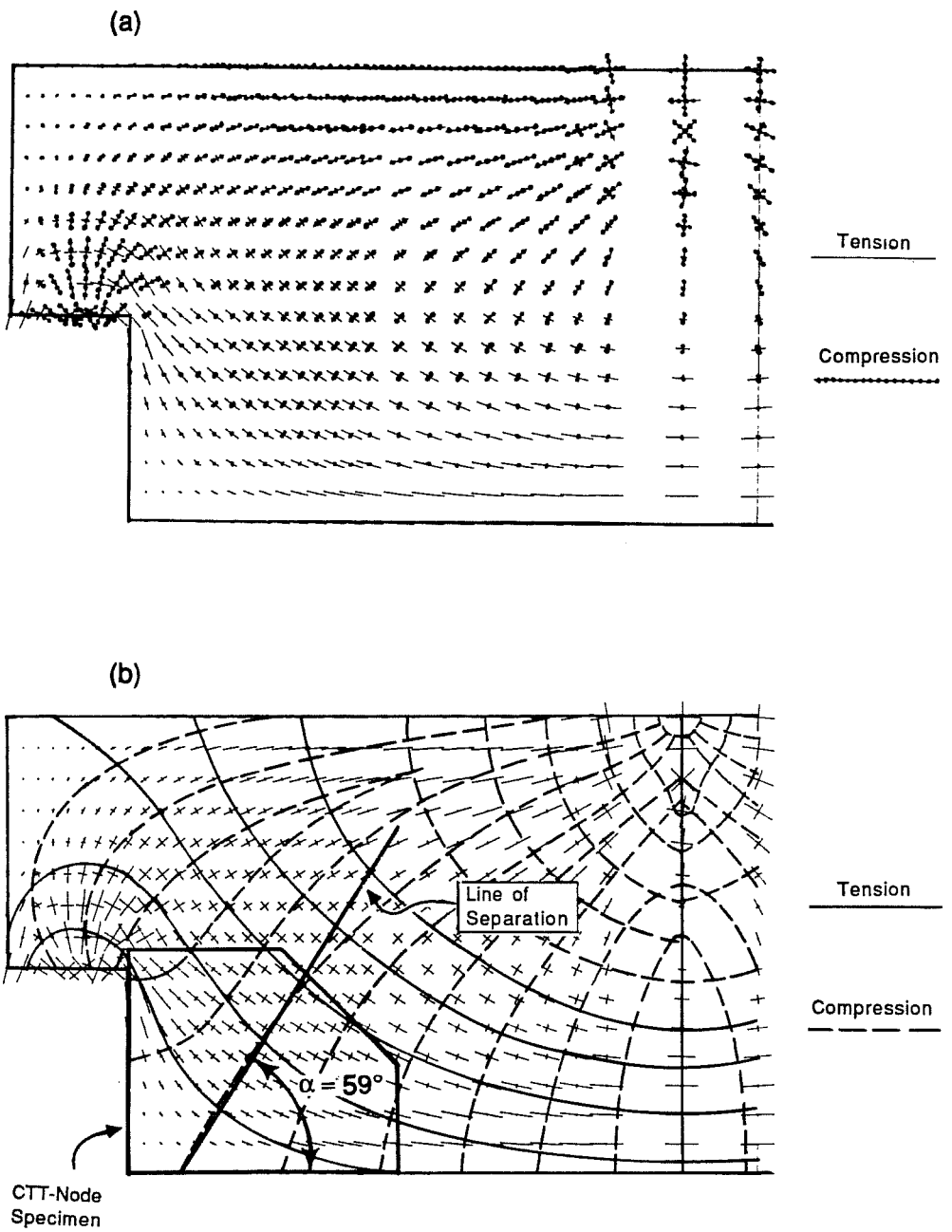

Fig. 5.2 Principal Stress Vectors and Elastic Stress Trajectories for Prototype Beam and CTT-Node Specimens

substantially less than the 59° angle defined by the line of separation in Fig. 5.2. It appears that a major diagonal strut developed between the vertical reaction point and the CTT-node and produced the flatter angle of crack inclination (See Fig. 5.3).

5.2.2 Estimating the Geometry of the Compressive Stress Fields.

Once concrete cracks, tensile stresses initially carried by concrete are transferred to reinforcing steel. The size and shape of the post-cracking stress fields in the member are affected by the placement of reinforcement. For instance, it is thought that the strut width increases if multiple layers of tie reinforcement are used (1,14,15). While the knowledge of elastic stress trajectories is helpful in developing the strut-and-tie concepts, the strut-and-tie model geometry must be based on the location of nodes anchoring the tensile ties which, in turn, must be defined by the spacing and distribution of the tie reinforcement.

For the node specimens, the fan-shaped cracking patterns indicated by the elastic analysis may not represent the flow of compressive forces. To avoid confusion, the estimated flow of forces within the cracked specimen shall be identified as the assumed stress field in contrast to the elastic stress field. As discussed in Chapter 4, forces in the the ties were determined from strains so that strut-and-tie action could be identified. It is logical that the stress field is defined by the layout of the transverse and longitudinal bars. After closely examining the reinforcement strains and the cracking patterns for the all the nodal specimens, estimates of the physical dimensions and

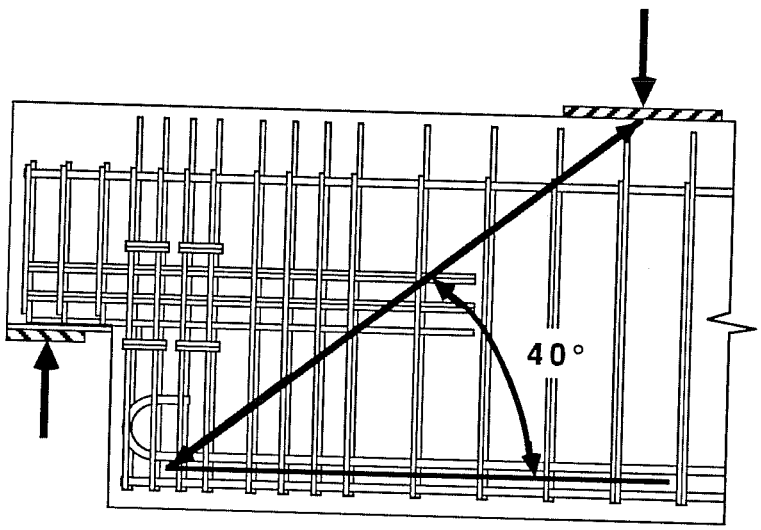

Fig. 5.3 Compression Strut Intersecting CTT-Node in Prototype Beam Specimen

configuration of the assumed stress fields for the several types of specimen geometries were made and are illustrated in Fig. 5.4.

The rationale for estimating the dimensions and configuration of the compressive stress fields is explained as follows. As a general rule, the compressive stress field was assumed to act at an angle α (corresponding to the effective angle of loading). The width was conservatively defined by the intersections of the outer transverse and longitudinal layers of tie reinforcement. However, when hooked bars were present, this width was increased as explained immediately below to consider the effect of the hooks. In addition, where reduced bearing plates were present, the width of the upper face of the compression field was reduced to that limiting width.

The cracking patterns in the nodes played an important role in making estimates of strut width and are superimposed on the nodes in Fig. 5.4. Specifically, the crack patterns showed that some extra consideration should be given to reinforcement layouts which used hooked bars. The hook is able to resist tensile force through a combination of bond and anchorage. When a hooked bar is loaded in tension, frictional forces are developed along the length of the bar and bearing stresses form at the hook's bend. In the nodes with hooked bars, defining the width of the actual stress field by using the point where the hook is tangent to the vertical bars appears to be reasonable.

It is important to observe that the estimated width of the assumed stress field is narrower than the effective bearing surface provided at the face of all node specimens except HHSR, LHSR, and LFAC. Because of this, it is unlikely that uniform bearing stresses were produced across the entire

10.6 in. bearing face of the nodal specimens with full width struts as originally thought. Instead, the distribution of bearing stresses would correspond to an assumed stress field. Outside the assumed stress field, small bearing stresses would develop because the majority of force would be distributed over the width of the assumed stress field. The estimated widths of the assumed stress fields are shown in Fig. 5.4. Estimated widths of the assumed stress fields and full effective widths of the bearing surface will both be used when making comparisons with effective concrete strength limits in Sec. 5.3.

The configuration of the compression field is also of interest in this study. As discussed in Sec. 2.4, "bottle" struts may have lower effective concrete strength limits due to transverse tensile strains perpendicular to the axis of the strut. Data from the node tests cannot conclusively show the shape of the actual stress fields because concrete strains were not measured. Still, crack patterns and reinforcement strain readings are helpful in **estimating** the configuration of the actual compression field. Cracks generally radiated from the bearing surface. At the same time, a large percentage of the applied tensile force was observed at the interior gage locations. As illustrated in Fig. 5.4, it is estimated that the configuration of the real stress field was prismatic for all specimens except HHSR, LHSR, and LFAC where fanned-shaped configurations are defined by the narrow effective width of the bearing surface.

Lastly, the width of the compressive stress field may also affect development. Schlaich, Schäfer, and Jennewein suggest that anchorage of the

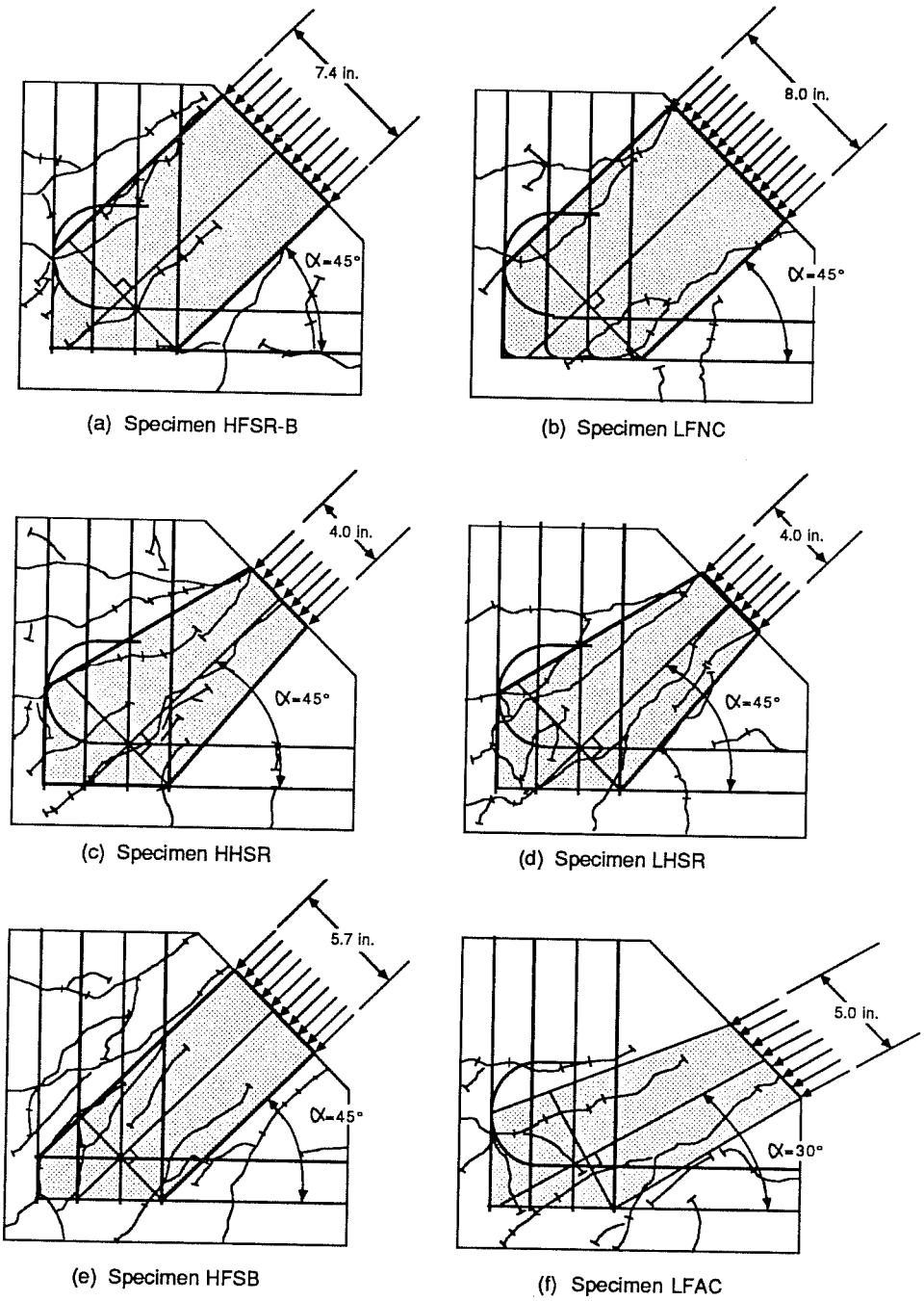

(a) Specimen HFSR-B

(b) Specimen LFNC

(c) Specimen HHSR

(d) Specimen LHSR

(e) Specimen HFSB

(f) Specimen LFAC

Fig. 5.4 Estimated Physical Geometries of Compressive Stress Fields in the Several Types of Node Specimens

tie reinforcement begins where the transverse compression stress trajectories of the struts meet the bar and are deviated (1). This implies that the boundaries of the compressive stress field define the critical section of reinforcement. This recommendation will be evaluated in Section 5.4.3 where the development provisions of ACI 318 (2) and AASHTO (3) will be compared with the geometry of the stress field and with the test results from the node specimens.

5.3 Comparison of Test Results with Effective Concrete Strength Limits

In Chapter 2 the effective concrete strength limit was defined as $f_{ce}=\upsilon f'c$ where υ is an efficiency factor and f'c is the cylinder strength. A comparison of node test results with recommended efficiency factors (υ) from selected authors is made in Tables 5.1 and 5.2. When making comparisons with effective concrete strength limits, the available widths of the bearing surface and the estimated widths of the stress fields shown in Fig. 5.4 are used in Tables 5.1 and 5.2, respectively. Maximum bearing stresses (Table 5.1) or compression field stresses (Table 5.2) are normalized using the actual concrete strength. Test results from Specimens HHSR, LHSR, and LFAC are excluded from Table 5.2 since their effective bearing surface width and estimated compression field width are identical.

In both Tables 5.1 and 5.2, test results for many nodes are inconclusive since predicted efficiency factors were not exceeded and crushing failures were not observed. More important are test results where the ratios of measured normalized stress to the recommended efficiency are greater than one. These results are presented in bold type and show that the

recommended effective concrete strength limits are conservative. In Table 5.1, Specimen LHSR is shown in bold, italic type because it was the only specimen that experienced a crushing failure of the compressive strut. Except for Specimen LHSR, concrete efficiencies are higher than those shown in the tables because crushing failures were not observed during the tests.

Specimens HHSR, LHSR, and LFAC provide the most meaningful information when evaluating recommended efficiency factors. These specimens showed surprisingly high effective concrete strength considering they had sustained substantial cracking parallel to their compression struts. Tensile stresses and subsequent cracking orthogonal to the compression strut are normally thought to be detrimental to the effective concrete strength (22). It is possible that some confinement was provided by: 1) friction at the bearing surface of the strut; and 2) the bulk of concrete which surrounded the relatively narrow strut. Still, the formation of cracks occurred at roughly the same loads in the node specimens and the Prototype Beam Specimen. This would would suggest that confining mechanisms in the node specimens were much the same as those in the full-sized, dapped beam.

The recommended efficiency factor proposed by Schlaich et al. (1) underestimates the measured efficiency of Specimen LHSR by over 50%. Effective concrete strength limits proposed by Ramirez (13) and Mitchell and Collins (12) are even more conservative. Extending the recommendations of Ramirez and Mitchell and Collins to more general applications, such as CTT-nodes, seems to be inappropriate since they were based on tests of continuous compression fields in beams and shear panels.

Specimen	(Bearing Stress)/f'c (Meas.)	Ramirez		Schlaich et al.		Mitchell & Collins	
		(Rec.)	(Meas./Rec.)	(Rec.)	(Meas./Rec.)	(Rec.)	(Meas./Rec.)
HFSR-A	0.20	0.36	0.56	0.68	0.29	0.54	0.37
HFSR-B	0.26	0.39	0.66	0.68	0.38	0.54	0.48
LFSR	0.35	0.49	0.71	0.68	0.51	0.54	0.65
HFNC	0.25	0.39	0.63	0.68	0.37	0.54	0.46
LFNC	0.35	0.49	0.71	0.68	0.51	0.54	0.65
HHSR	0.71	0.39	**1.80**	0.68	**1.04**	0.54	**1.32**
LHSR (1)	***1.03***	***0.49***	***2.09***	***0.68***	***1.51***	***0.54***	***1.91***
HFSB	0.27	0.39	0.68	0.68	0.40	0.54	0.50
LFAC	0.99 (2)	0.48	**2.07**	0.68	**1.46**	0.42	**2.34**

Notes:

(Rec.)-Recommended
(Meas.)-Measured
(1)-Experienced concrete strut crushing failure.
(2)-Based on 5 in. Strut Width

Table 5.1 Comparison of Node Test Results with Efficiency Factors (υ) from Selected Authors Based on Available Bearing Surface

Specimen	(Strut Stress)/f'c (Meas.)	Ramirez		Schlaich et al.		Mitchell & Collins	
		(Rec.)	(Meas./Rec.)	(Rec.)	(Meas./Rec.)	(Rec.)	(Meas./Rec.)
HFSR-A	0.29	0.36	0.81	0.68	0.43	0.54	0.54
HFSR-B	0.38	0.39	0.96	0.68	0.56	0.54	0.70
LFSR	0.50	0.49	**1.02**	0.68	0.74	0.54	0.93
HFNC	0.34	0.39	0.86	0.68	0.50	0.54	0.63
LFNC	0.47	0.49	0.95	0.68	0.69	0.54	0.87
HFSB	0.49	0.39	**1.25**	0.68	0.73	0.54	0.92

Notes:

(Rec.)-Recommended
(Meas.)-Measured

Specimens HHSR, LHSR, and LFAC are not included in Table 5.2 because their available strut width and estimated strut width are assumed to be equal.

Table 5.2 Comparison of Node Test Results with Efficiency Factors (υ) from Selected Authors Based on Estimated Strut Width

The state of stress in the isolated struts and nodes is quite different from that in continuous compression fields.

Effective concrete strength limits proposed by Mitchell and Collins are affected by the chosen strut angle of the strut-and-tie model. One of the goals of this study was to evaluate the effects of strut angle change in the nodal specimens. For Specimen LFAC, the reduced strut angle of 30° did not appear to reduce the effective concrete strength. This observation must be tempered somewhat because the direction of cracking in Specimen LFAC was parallel to the strut rather than inclined to the strut axis. If a 30° strut angle was chosen for the CTT-node in the full-sized, dapped beam specimen, initial cracks likely would be oriented at approximately 45° to 50° from the horizontal steel. Subsequent cracks would tend to form parallel to the 30° strut angle of the chosen strut-and-tie model. Cracks inclined to the axis of the compression strut, that is, skew cracks, are believed to be especially detrimental to the effective concrete strength of the strut (22). Consequently, Specimen LFAC may have exhibited a higher effective concrete strength than would exist in the full-sized specimen because of an absence of skew cracks. It appears that the empirical effective concrete strength limit of Mitchell and Collins which is based partially on the strut angle may not be suitable for nodes. The recommendations of Schlaich et al. (1) which differentiate between parallel and skew cracking may be more applicable. Skew cracks would be expected if the orientation of struts departs significantly from the elastic stress trajectories. Models where the strut

angle does not follow the elastic stress trajectories are penalized by lower effective concrete strength limits for the struts and nodes.

5.4 Comparison of Test Results with ACI and AASHTO Provisions for Development

5.4.1 General. The tests results showed that reinforcement details affected the ultimate strength of the node. Except for Specimen LFSR, unconfined specimens failed before confined specimens. Specimen HFSB, which had a straight bar anchorage on the top or first layer of longitudinal reinforcement, was the only high strength specimen with confining transverse reinforcement that failed.

Proponents of the strut-and-tie model state that ties should be suitably anchored at the node. Anchorage of straight or hooked bars requires sufficient bond forces to resist the computed tie force. Requirements for the development of straight and hook bars in tension are illustrated in Fig. 5.5. The development length l_d is the shortest length in which the maximum bar stress f_s can be developed. The development length l_d is measured from the critical section to the termination point of the bar.

One of the vital aspects of the anchorage check is the determination of critical section of the reinforcement. Unfortunately, the critical sections for ties anchored at CTT-nodes are not well defined in current proposals. As previously mentioned in Chapter 2, Schlaich et al. propose that development of the reinforcement begins where the boundary of compressive stress field intersects the axis of the bars; however, this recommendation not not been verified through physical tests. As an initial step towards developing more

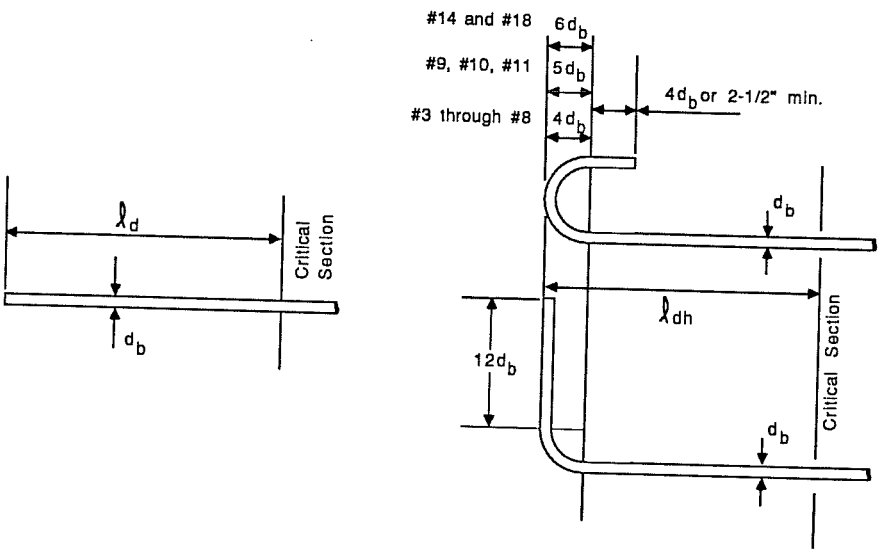

Fig. 5.5 Development Length for Straight and Hooked Bars

comprehensive design recommendations, the node test results are compared to ACI 318-83 (2) and AASHTO (3) design provisions for development.

5.4.2 Background of ACI and AASHTO Design Provisions for Development. Sections 12.2 and 12.5 of ACI 318 and Sections 1.5.14 and 1.5.17 of AASHTO provide design provisions for development of deformed bars and deformed wire in tension, as well as, standard hooks in tension. The design equations for development found in the AASHTO Specification essentially mirror those of the ACI Code. For the development of hooks, AASHTO uses a ξ factor which is a holdover from ACI 318-77 (23). For the diameters of reinforcement used in the node specimens, the AASHTO and ACI 318-83 provisions for hooks are essentially equal (24). The design equations of ACI Sections 12.2 and 12.5 are not entirely applicable when evaluating the test results of this study because they are based on lengths needed to develop 125 percent of yield. The substitution of $1.25*f_y$ for f_y in the equations is analogous to using a strength reduction factor of ϕ=0.8.

Equations 5.1 - 5.6 state the ACI and AASHTO requirements in a form that facilitates comparisons with the test results. These equations include the strength reduction factor ϕ. Multipliers which account for different conditions affecting development length are also included in Equations 5.1 - 5.6 and are identified by the symbol Ψ. Only multipliers which are applicable to this study are defined. The multiplier for excess reinforcement, equal to As required/As provided, is replaced by f_s/f_y . The ratios f_s/f_y and A_s required/A_s provided are equivalent; however, using the ratio f_s/f_y simplifies the development length calculations. Arbitrary Code

provisions outlining the minimum development length requirements for hooked bars (the smaller of $8d_b$ or 6 in.) were not considered when evaluating the specimen behavior.

The ACI and AASHTO development length equations for straight deformed bars in tension may be expressed as:

$$l_d = \frac{0.04 * A_b * f_y}{\sqrt{f'c}} * \frac{0.8}{\phi} * \Psi_1 \qquad (5.1)$$

$$\text{but not less than} \quad l_d = (0.0004 * d_b * f_y) * \frac{0.8}{\phi} * \Psi_1 \qquad (5.2)$$

where

l_d	=	Development length (in.)
A_b	=	Area of reinforcement (sq. in.)
f_y	=	Yield stress of the reinforcement (psi)
f_s	=	Maximum bar stress.
Ψ_1	=	(fs/fy) Modification factor for excess reinforcement.
ϕ	=	Strength reduction factor
f'c	=	Cylinder strength (psi)

Substituting f_s/f_y for Ψ_1, multiplying by $0.8/\phi$, and letting $\phi=1.0$ gives the nominal development length:

$$l_{dn} = \frac{0.032 * A_b * f_s}{\sqrt{f'c}} \qquad (5.3)$$

$$\text{but not less than} \quad l_{dn} = 0.0032 * d_b * f_s \qquad (5.4)$$

The ACI development length equation for hooked bars in tension is stated in a similar form as follows:

$$l_{dh} = \frac{0.02 * d_b * f_y}{\sqrt{f'c}} * \frac{0.8}{\phi} * (\Psi_1 * \Psi_2) \qquad (5.5)$$

where l_{dh} = Development length of standard hook in tension (in.)

d_b = Diameter of reinforcement (in.)

f_y = Yield strength of the reinforcement (psi)

fs = Maximum bar stress (psi)

Ψ_1 = (fs/fy) Modification factor for excess reinforcement.

Ψ_2 = (0.8) Modification factor for hooks enclosed vertically or horizontally within ties or stirrup-ties closely (< $3d_b$) spaced along the full development length l_{dh}.

ϕ = Strength reduction factor

f'c = Cylinder strength (psi)

Again, substituting f_s/f_y for Ψ_1, multiplying by $0.8/\phi$, and letting ϕ=1.0 simplifies the equation and gives the nominal development length:

$$l_{dhn} = \frac{0.016 * d_b * f_s}{\sqrt{f'c}} * \Psi_2 \qquad (5.6)$$

Equations 5.3, 5.4, and 5.6 may be rearranged to determine the capacity of an anchorage detail based upon the provided development length. For straight bars this is:

$$f_s = \frac{(l_{dn}) * (\sqrt{f'c})}{0.032 * A_b} \qquad (5.7)$$

$$\text{but not greater than } f_s = \frac{l_{dn}}{0.032 * d_b} \qquad (5.8)$$

Stating the formula for hooked bars in a similar form gives:

$$f_s = \frac{(l_{dhn}) * (\sqrt{f'c})}{0.016 * d_b} * \frac{1}{\Psi_2} \qquad (5.9)$$

Determining the nominal development length for the node specimens from Eqs. 5.3, 5.4 and 5.6 is straightforward. The material properties (f'c, f_y, d_b, and A_b) are known. The maximum bar stress f_s may be determined by : 1) dividing the applied tie force by the area of steel in the tie; or 2) the external strain gage readings. The first method produces the average f_s while the second is the measured or actual f_s. Theoretically, each method should produce identical results; however, as discussed in Chapter 4, the external strain gages showed an inequality of stresses for different layers of the longitudinal steel. The first layer of longitudinal reinforcement closest to the surface of the specimen had lower strains than the second layer. In contrast, similar strain rates were observed for different layers of transverse reinforcement. In later comparisons of specimen behavior and nominal development length, the average f_s is used for the transverse reinforcement. Both the average and measured values of f_s are used for the longitudinal steel.

5.4.3 Evaluation of Node Specimen Behavior. For the transverse reinforcement of the confined specimens, comparisons between the calculated nominal development length and the observed behavior are inappropriate. First, several of the confined specimens did not fail through mechanisms involving anchorage. Secondly, neither ACI nor AASHTO requirements are directly applicable for development of anchored U stirrups. It is normally thought that this type of detail does not require a specific development length check since it is fully anchored. Another complication involves the transverse hook in the confined specimens. The longitudinal bar in front of the hook is certainly beneficial to the hook's performance. Equations

presented in the previous section would overestimate the required development length for this case. For these reasons, comparisons are not made between the test results and ACI/AASHTO provisions for development in the confined specimens.

The determination of the development length of the transverse bars in the unconfined specimens, LFNC and HFNC, is complicated by the fact that the unconfined reinforcement detail violates ACI Code Section 12.5.4. The Code requires hooked bars with less than 2-1/2 inches of side or bottom cover to be enclosed within ties or stirrup ties along their full development length to prevent splitting failures. Specimens LFNC and HFNC were not enclosed and splitting failures occurred at 117.8 kips and 132.5 kips, respectively. Transverse bars of the unconfined specimens were sufficiently embedded to develop f_y; however, the ACI equations are not entirely appropriate since confining reinforcement was not provided. Nonetheless, comparisons between the observed and predicted behavior in the unconfined specimens are interesting. Calculated nominal development lengths for the unconfined specimens, based on the measured stress f_s at failure, are summarized in Table 5.3. Comparisons between the calculated nominal development length, cracking patterns, and the compressive stress field are shown in Fig. 5.6. For comparison, the critical section is defined by the boundary of the assumed stress field following the proposal of Schlaich and his co-workers. When the calculated nominal development length extends past the boundary of the compression stress field, the measured bar stress would be greater than estimates obtained from Eq. 5.9. In both specimens, the critical section

defined by the compressive strut intersects the first layer of transverse bars approximately 2 in. short of the calculated nominal development length. For the second layer of bars, the boundary of the actual stress field and starting point of development nearly coincide. The calculated nominal development length for the third and fourth layers of transverse bars lie within the stress field boundary. It would be expected that transverse bars in the unconfined specimens would experience a progressive failure. The first layer of bars would be most critical for development and would fail first. Unless the force could be redistributed to the remaining transverse reinforcement, the other layer of bars would fail sequentially.

The crack patterns for the specimens are also of interest since they certainly affect anchorage requirements. Major transverse cracks occurring in the specimens are shown boldly in Fig. 5.6. The major transverse crack occurs near the critical section in both specimens. It is not possible to establish this as a trend since the variability of crack location in concrete members is well known. However, a reasonable and significant observation is that the crack location produces a distinct "distance effect". The major cracks intersect layers of bars at different locations along their length. As noted in the previous paragraph, the first layer of transverse reinforcement nearest to the end of the member would be most critical for development while subsequent layers are afforded longer development lengths. Relief cracks which intersect the layers of transverse reinforcement close to end of the hooked anchorages are also shown in Fig. 5.6. The influence of these relief cracks is difficult to assess. It appears that the relief cracks were not

especially detrimental to anchorage capacity since the bars were still able to develop f_y. However, this comment must be tempered somewhat because a large percentage of the applied force reached the innermost gage locations and there was a gradual deterioration in anchorage as the specimens sustained more cracks. In general, the appearance of relief cracks parallel to the theoretical strut angle indicate that strut-and-tie action was mobilized. In turn, the role of other internal force transfer mechanisms would be diminished.

Specimen LFAC was the only specimen in which a loss of anchorage for the longitudinal reinforcement produced a side splitting failure. Anchorage first deteriorated along the first layer of straight bars and tie forces were gradually redistributed to the second layer of hooked bars until an anchorage failure of both layers of reinforcement occurred. At ultimate, the average stress of the longitudinal reinforcement was $0.74*f_y$ (44.5 ksi); however, external strain gage readings showed the hooked bars were stressed more than the straight bars. Average measured stresses from the external gages were 52 ksi for the hooked bars and 36 ksi for the straight bars. Table 5.4 is a summary of the calculated nominal development lengths for both the average and measured levels of stress. The measured stresses are surely the more correct, however, both have been included in the table for comparison because in design it is normally assumed that the different layers of the tie are equally stressed at the node. Using the same means of presentation as for the transverse reinforcement of Specimens HFNC and LFNC, the observed and predicted behavior for Specimen LFAC is compared in Fig. 5.7. Major cracks

Specimen	Average Stress= Tie Force/As fs (psi)	Nominal Development Length (in.)
HFNC	75,300	7.4
LFNC	66,900	6.6

Table 5.3 Nominal Development Lengths for Unconfined Specimens HFNC and LFNC

Bar Description	Average Stress= Tie Force/As fs (psi)	Nominal Development Length (in.)	Measured Stress (From Ext. Gages) fs (psi)	Nominal Development Length (in.)
Top (#5-180° Hook)	44,500	5.7	52,000	6.6
Bottom (#5-Straight)	44,500	8.9	36,000	7.2

Table 5.4 Nominal Development Lengths for Unconfined Specimen LFAC

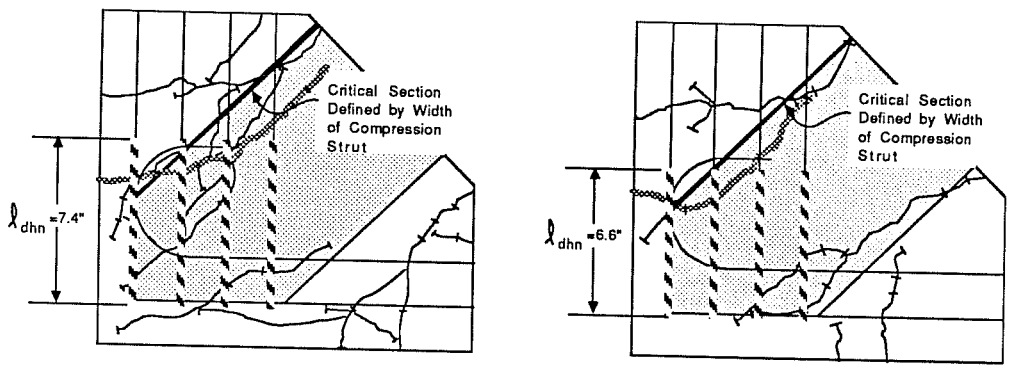

(a) Specimen HFNC (b) Specimen LFNC

Fig. 5.6 Comparisons of Transverse Reinforcement Nominal Development Lengths, Cracking Patterns, and Compressive Stress Fields for Specimens HFNC and LFNC

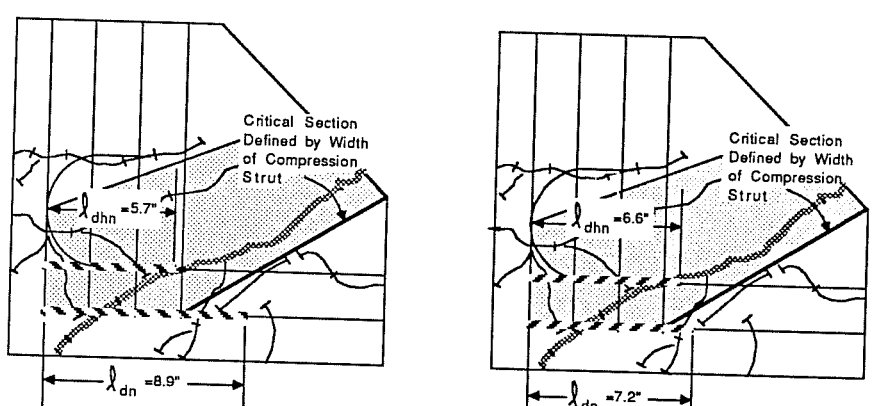

(a) Hooked and Straight Longitudinal Bars Equally Stressed at 44.5 ksi

(b) Unequal Longitudinal Bar Stresses; 52 ksi = Hook and 36 ksi = Straight Bar

Fig. 5.7 Comparisons of Longitudinal Reinforcement Nominal Development Lengths, Cracking Patterns, and Compressive Stress Fields for Specimen LFAC

and slip occurred along the failure plane which is shown boldly. It is surprising that calculated nominal development length for the layer of straight longitudinal bars extends past both the failure plane and the critical section defined by the compressive stress field. Strain gage readings show that the straight bars had a stress of 29 ksi at location LB (See Fig. A3.15). From Eq. 5.7, the required nominal development length for this level of stress is still 5.8 in. The measured distance from the failure plane to the termination point of the straight bar is roughly 2.5 in. It appears that Code equations overestimate the development requirements for the straight longitudinal bars; however, this may or may not be the case. First, the crack at the failure plane may not be the critical section for anchorage. Secondly, bond or anchorage is not always linear with length for short lengths such as 2.5 inches. Contrasting behavior is exhibited by the hooked bars. The end point of the nominal development length and the failure plane nearly coincide. However, the nominal development length falls well inside the boundary of the stress field.

An assessment of the applicability of defining the critical section for development by the boundary of the actual stress field is made in Table 5.5. The measured distance from the critical section to the termination point of the tie reinforcement has been used in Eqs. 5.7, 5.8, and 5.9 to predict the capacity of each tie. Layers of reinforcement with measured development lengths greater than necessary to develop f_y have capacities set equal to yield. The total calculated capacities for Specimens LFNC, HFNC, and LFAC are in turn compared with measured failure loads. For Specimens LFNC and HFNC,

ratios of measured to calculated capacities greater than one show the method is conservative for predicting the capacity of the tie. For Specimen LFAC, the total calculated capacity of the longitudinal tie is only 2% greater than the measured failure load. While it is difficult to develop comprehensive design recommendations for development based upon the test results from three nodal specimens, it appears that it is reasonable to define the critical section for development by the boundary of the compression field. Additionally, if the measured development length is greater than that required to develop f_y, the capacity of the layer of reinforcement should be governed by its yield stress. Further discussion regarding the design of ties anchored through development will follow in the next section.

5.5 Design Guidance for CTT-Nodes.

5.5.1 Classifying Tie Anchorage Details. As discussed in Chapter 2, researchers commonly idealize the tie anchorage detail as an end plate which distributes the tie force over the depth of the node. The end plate must be wide enough so that the stresses at the node face do not exceed $f_{ce}=\upsilon f'c$. The minimum area for the end plate may be defined by the effective concrete strength limit and tie force as follows:

$$A_{min} = \frac{T}{(\upsilon f'c)} \qquad (5.10)$$

where

A_{min} = Required minimum area for the end plate

T = Tie force

$\upsilon f'c$ = Effective concrete strength

Specimen	Meas. Dev. Length (From Comp. Field)	Eqs. 5.7-5.9	Accounting for Yielding of Steel Calculated Capacity (kips)
LFNC			
1st Layer	4.5	20.1	20.1
2nd Layer	6.5 (1)	29.1 (2)	28.5 (3)
3rd Layer	8.5 (1)	38.0 (2)	28.5 (3)
4th Layer	10.5 (1)	47.0 (2)	28.5 (3)
		Total Calc. Cap.	105.5
		Meas. Capacity	117.8
		Meas./Calc.	1.12
HFNC			
1st Layer	4.5	25.1	25.1
2nd Layer	6.5 (1)	36.2 (2)	28.5 (3)
3rd Layer	8.5 (1)	47.4 (2)	28.5 (3)
4th Layer	10.5 (1)	58.5 (2)	28.5 (3)
		Total Calc. Cap.	110.5
		Meas. Capacity	132.5
		Meas./Calc.	1.20
LFAC			
Straight Bars	6.0	55.8	55.8
Hooked Bars	9.5 (1)	137.7 (2)	111.2 (3)
		Total Calc. Cap.	167.0
		Meas. Capacity	164.5
		Meas./Calc.	0.98

Notes:

(1)-Greater than length necessary to develop fy
(2)-Based upon measured development length
(3)-Based upon fy

Table 5.5 Comparisons Between the Predicted Capacity of Tie Based Upon Development Length Measured from Boundary of Compression Field

Similarly, the tie force may be anchored with a continuous reinforcement detail, such as the U loops shown in Fig. 5.8. The U's must also be distributed over a minimum area of concrete so the stress in the node does not exceed the effective concrete strength limit $f_{ce}=\upsilon f'c$ (1,14,15,25). Cook and Mitchell (25) suggest that the effective width be taken as the distance between the end layers of the tie's reinforcement (See Fig. 5.9). The definition of the effective width of the U loop in the plane perpendicular to the U is also important. Cook and Mitchell assume that the concrete cover spalls off down to the centerline of the U's legs at the node. These assumptions have some validity since they are based upon observed test results. Still, design guidelines lack adequate definition. Where the tie reinforcement is spread out unevenly as shown in Fig. 5.10 or possibly consists of one layer, the determination of an effective concrete area is unclear. Results from the node tests are not particularly helpful in this regard because only one spacing of reinforcement was used. Implicit guidance is given by Code provisions governing minimum reinforcement bend diameters and cover requirements. Figure 5.11 shows another design consideration when using continuous reinforcement details in wide members (13,26,27). Strut-and-tie action will transfer forces to the bend of the U; however, a portion of the force may also cause splitting cracks if the center portion of the U is unsupported by a cross tie. Based on test results, Leonhardt and Walther (26,27) suggest that where large shear stress exist in the member, the lateral spacing of stirrup legs parallel to the web width "b_w" should not exceed 7.5 in. Where the member's nominal shear stress is small, it is proposed (26,27) that this

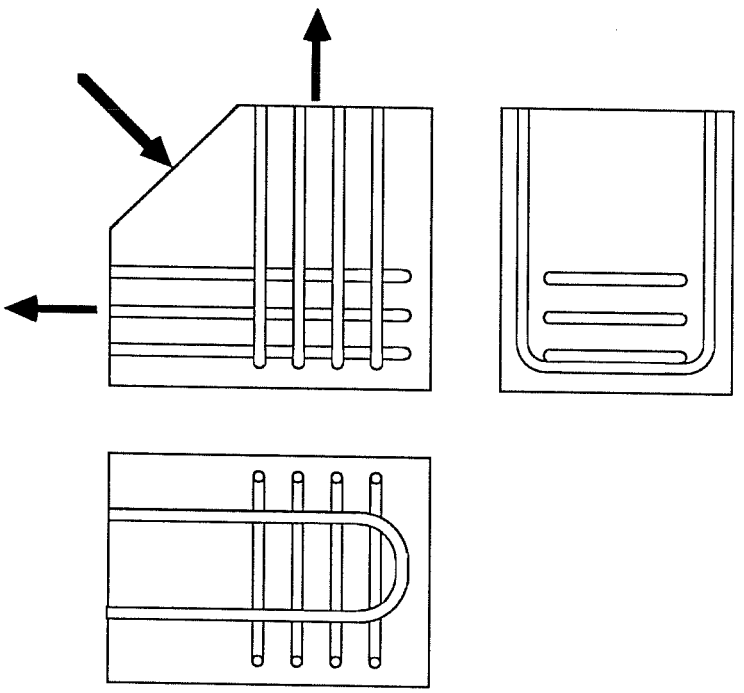

Fig. 5.8 Continuous Reinforcement Details for Anchoring Tensile Ties in CTT-Node

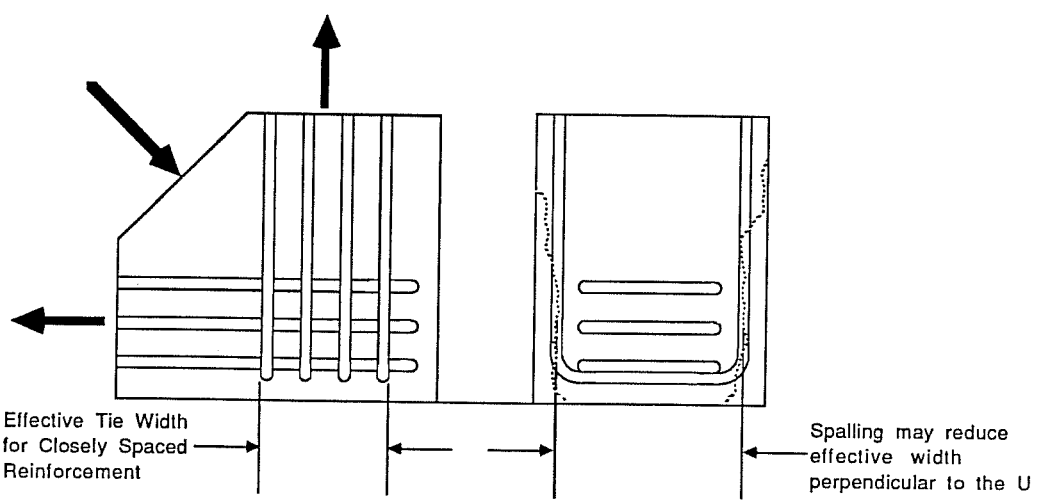

Fig. 5.9 Defining the Effective Width of Continuous Reinforcement Tie Anchors

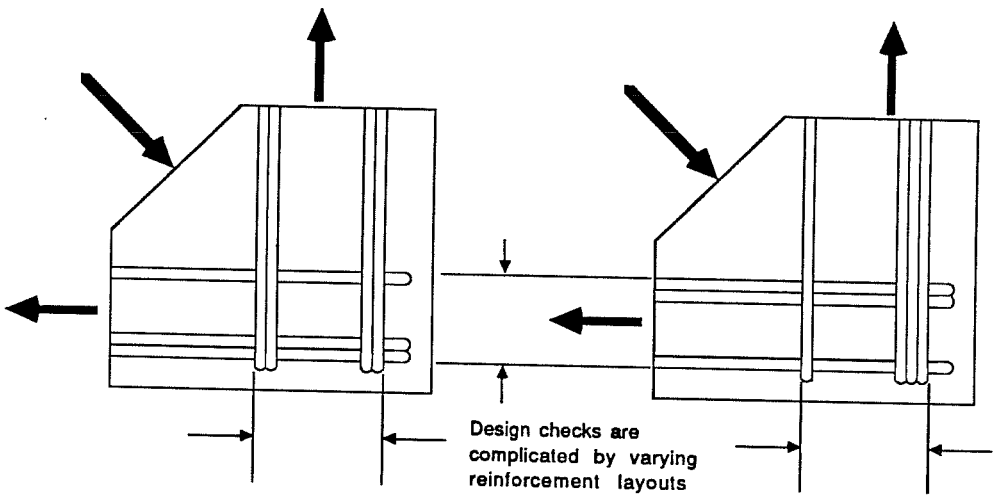

Fig. 5.10 Design Complications Resulting from Uneven Placements of Reinforcement

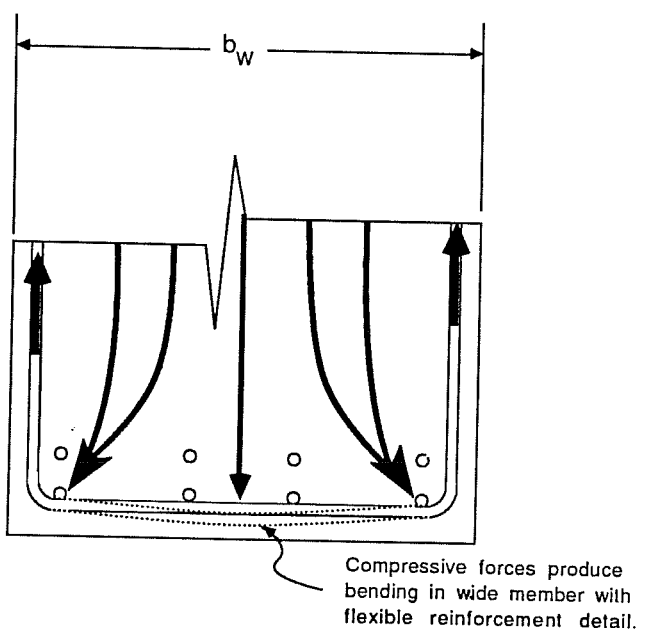

Fig. 5.11 Undesirable Effects Resulting from the Use of Continuous Reinforcement Details in Wide Members

distance may be increased to 15 in. or more but should not exceed the effective depth "d" of the member. For any continuous reinforcement detail, placing supplemental reinforcement at the bend of the U's is advantageous (15). Reinforcement perpendicular to the plane of the U not only controls splitting cracks caused by prying action, but also distributes radial pressures developed at the bends.

With end plates and continuous reinforcement details, the end detail transfers the tie force to the back of the node which, in turn, causes compression within the node. Development length failures are not of concern because proper detailing of end plates and continuous reinforcement assures that the tie reinforcement will be positively anchored. In contrast, development length is of utmost importance for ties anchored with straight or hooked bars. A case in point is illustrated by the CTT-node in Fig. 5.12 where single layers of straight bars anchor ties T_1 and T_2. The tie forces must be developed entirely through bond stresses which develop along the length of the straight bar. The concept of development length is based on a uniform distribution of bond stress although it is known that bond stresses vary along the length of the bar. For the purpose of this example, the development length for each layer of tie reinforcement is assumed to begin at the intersection point of the two ties. If insufficient development length is provided, the ultimate bond stress will be exceeded and the bar will pull out or initiate a cover splitting failure. Conversely, adequate development length will allow the tie forces T_1 and T_2 to fully develop. The CTT-node will not fail until: 1) the effective concrete strength in exceeded; or 2) tensile

capacity of the anchorage detail is achieved. The crux of this discussion is that crushing failures associated with end plates and continuous reinforcement details, resulting from the back face of the node being overstressed, would not occur with ties anchored through development. Local crushing may occur at the bar lugs as the bar slips; however, this behavior is associated with anchorage effects and does not change the effective concrete strength of the node. This subtle, yet significant, behavior pattern has not been addressed in the literature.

Because the behavior of the CTT-node is influenced by the tie anchorage detail, it is appropriate to make a distinction between anchorage details that may be chosen. In Fig. 5.13, tie anchorages have been separated by type. Positive anchorage details are those which do not rely appreciably upon bond stresses to resist the applied tensile force and include end plates and continuous reinforcement details. The positive anchorage detail must be designed so the tie force is distributed over a sufficient area to prevent the node from being overstressed. Development length anchorage details shown in Fig. 5.13 (b) include straight and hooked bars. For these details the designer must check the development length requirements of the tie reinforcement.

5.5.2 Design Checks for Ties Anchored Through Development Length. End plates and continuous reinforcement details are attractive from a design standpoint because they are fairly easy to evaluate. However, they are not necessarily required nor are they always desirable construction alternatives for anchoring tensile ties. Except for small diameter reinforcement, positive anchorage details are inherently more expensive and more difficult to

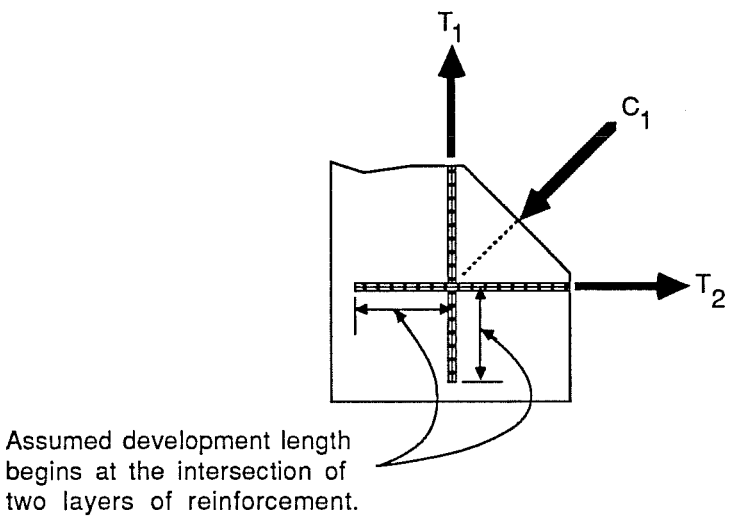

Fig. 5.12 Force Transfer in CTT-Node with Simple Reinforcement Layout

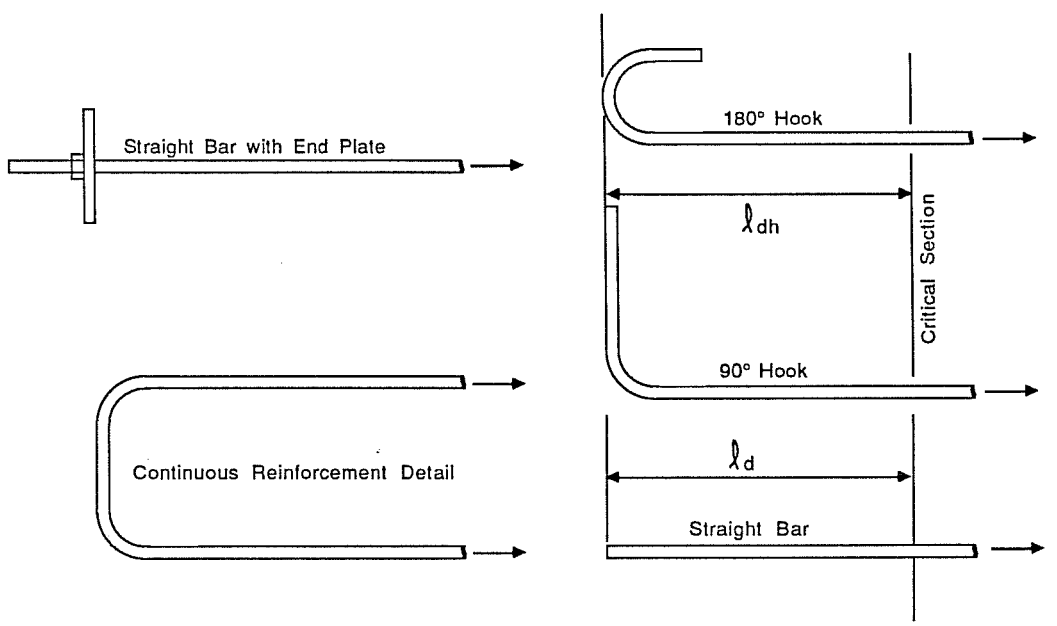

Fig. 5.13 Positive and Development Length Anchorage Details

construct than standard anchorage details such as straight bars or hooks. The key to the design process is being able to identify conditions severe enough to warrant the use of special anchorage details. Where the transfer of strut-and-tie forces is felt to be so abrupt that sufficient bond and anchorage forces cannot be developed, end plates or continuous reinforcement details should be provided.

The designer does not always have to use positive anchorage details if there is some flexibility in placing the tie reinforcement. A simple design situation is illustrated in Fig. 5.14 (a) where a strut-and-tie model has been developed for a CTT-node with two intersecting layers of reinforcement. One set of ties is continuous while the other is made up of straight bars. The centroid of the CTT-node is located at the intersection point of the two ties. The node implies an abrupt change in the direction of the forces. However, in the actual concrete member the transfer of force between strut and tie members would occur over some distance. It is logical to assume that the horizontal component of the strut force would have to be resisted by straight bar development measured from the centroid of the node. If the calculated capacity of the bar based on the measured development length is less than the bar stress $f_s=T_2/A_s$, the straight bar would fail in bond. Even with ties anchored with single layers of reinforcement, a check of the stress in the compression strut is required. Unfortunately, little guidance in determining the strut width for this case is provided from the results of the present study or from proposals found in current literature. It is known that the transfer of stress from a deformed bar to the concrete is accomplished mainly by the

mechanical locking of the lugs into the surrounding concrete. As shown in Fig. 5.15, the force transfer mechanism can be visualized by a strut-and-tie model with singular nodes at the ribs of the bar (1,28). The magnitude of the strut forces developed at the ribs depends upon the surface conditions of the bar and the angle "β" shown in the figure. Goto (29) found through experimentation that the value of β can vary substantially depending on whether the ribs are lateral, diagonal, or wavy with respect to the axis of the bar. Thus, the strut-and-tie model for bond forces is only helpful in a conceptual sense. As an interim design approach, the present study suggests that the boundaries of the compression strut should be determined from the beginning point of development and the intersection point of the layers of steel (See Fig. 5.14 (a)). This recommendation is again based upon the hypothesis that the force transfer to the bar at the node would occur over some distance.

A similar method could be used to evaluate the anchorage requirements for a CTT-node where each tie is made up of multiple layers of reinforcement. Following the premise that the critical section is defined by the compression field, wider spacings of tie reinforcement would increase the development lengths for the same bar extension beyond the node. The geometry of a typical design situation is illustrated in Fig. 5.14 (b). Again, anchorage would be adequate if the the capacity of the tie based on the measured development length exceeds the tie forces. The designer would also check the compression strut stresses based on the strut width defined by the outer layers of the horizontal and vertical layers of tie reinforcement.

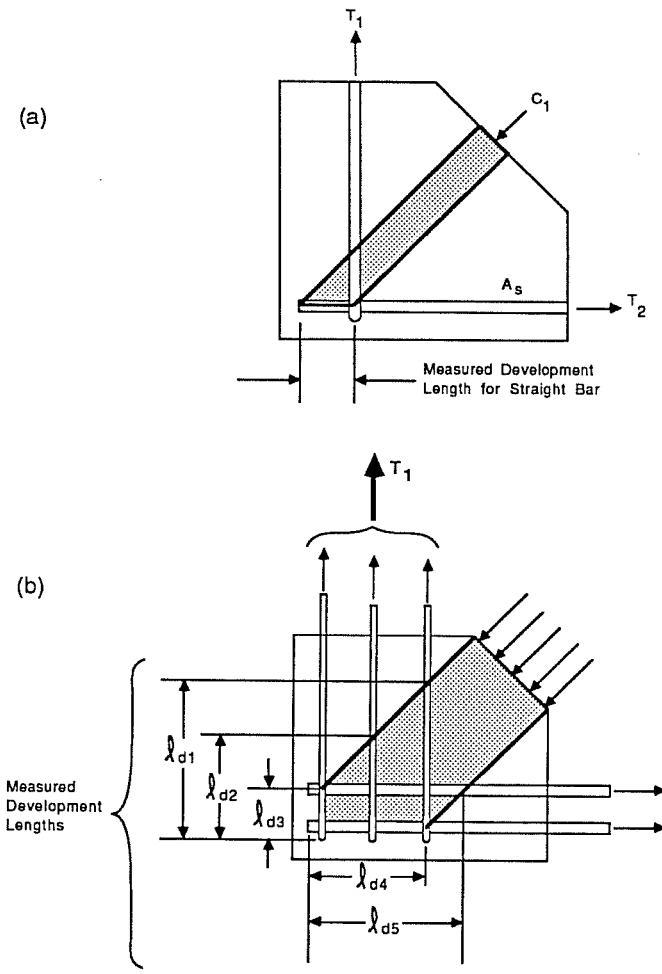

(c)

	Design Checks
Strut Stress	Calculated Strut Stress Based Upon Reinforcement Layout $\leq \forall f'c$ (Effective Concrete Strength Limit)
Anchorage	Calculated Tie Capacity Based Upon Measured Development Length $\geq$ Applied Tie Forces T_1 or T_2

Fig. 5.14 Design Checks for Ties Anchored with Single and Multiple Layers of Reinforcement

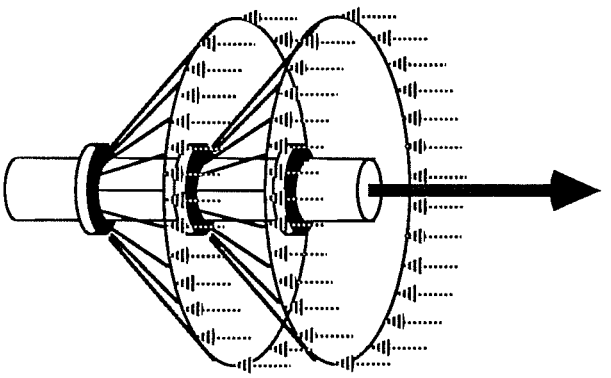

Fig. 5.15 Bond Force Transfer Mechanism (From Ref. 29)

Generally, increasing the spacing of the transverse reinforcement will lessen the development requirements of the longitudinal tie; however, it may create problems with the strut-and-tie design model. For the dapped beam, increasing the spacing of the transverse reinforcement too much will lead to an inefficient design model that does not agree well with the elastic flow of forces. Barton (17) has also shown through physical tests that the strains for tie reinforcement are less uniform if the bars are more widely spaced. Figure 5.16 shows how the spacing of transverse reinforcement affects the overall design model. Increasing the width of the tie results in flat strut angles α_1 and α_2. It is seen that the forces in the vertical tension ties, T_1 and T_2, are not affected by the change in the strut angle. In contrast, the forces in the horizontal ties, T_3 and T_4, are largely dependent on the strut angle. The most efficient model uses as steep a strut angle as possible to reduce the horizontal tie forces, thus, reducing the amount of tie reinforcement. It is apparent that the angle α_1 is constrained by the geometry of the dapped beam. The distance "x" must be large enough to accommodate the placement of steel required for the tie T_1. If the transverse reinforcement of tie T_1 is anchored with a continuous reinforcement detail, the reinforcement must be spread over a sufficient area to prevent crushing of the struts C_1 and C_2. Lastly, the anchorage requirements of the longitudinal reinforcement for tie T_3 must be assessed. As discussed in Chapter 2, an iterative design process would be used to: 1) coordinate the reinforcement scheme of the D-region with adjacent B-regions; 2) develop an efficient design model that satisfies equilibrium; 3) assure that the

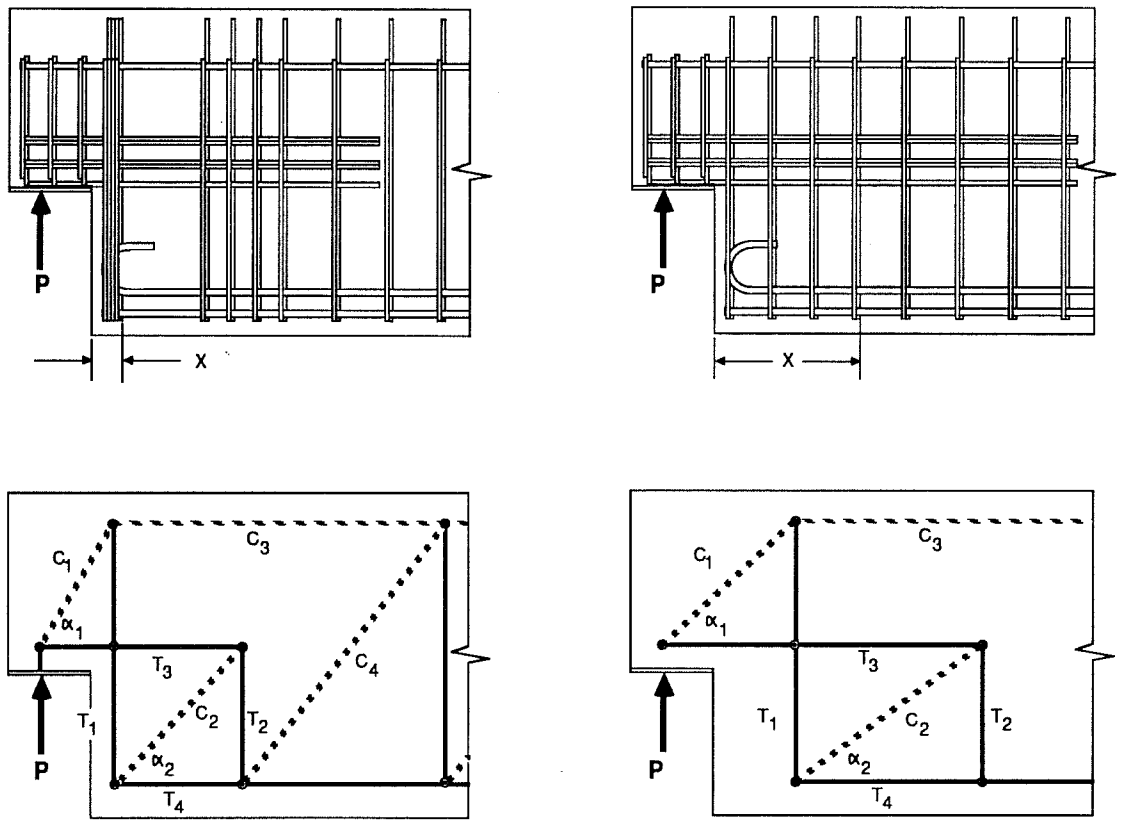

(a) Efficient Design Model Uses Closely Spaced Reinforcement for Tie T_1

(b) Widely Spaced Transverse Reinforcement Reduces the Efficiency of the Design Model

Fig. 5.16 Consequence of Reinforcement Spacing in Dapped Beam

crushing limits of the struts and nodes are not exceeded; and 4) provide adequate development lengths for tie reinforcement anchored with hooks and straight bars or use positive anchor details if necessary. A flowchart illustrating the design steps for the CTT-node is shown in Fig. 5.17.

5.6 Design Implications

5.6.1 Ramifications of Major Findings.

The strut-and-tie model requires an evaluation of the nodes during design. The stress at the face of the node must not exceed $f_{ce}=\upsilon f'c$ and proper anchorage of the tie reinforcement must be provided. Determining the geometry of the node is a prerequisite to making the design calculations. While conclusive design recommendations cannot be made from the results from this study, several inferences based upon the test data can be drawn.

First, the geometry of the compressive stress field appears to be governed by the placement of steel in the member. This follows the premise that at ultimate the majority of force is resisted through strut-and-tie action and the role of "concrete" mechanisms is diminished. In model development and subsequent placement of steel, the elastic stress trajectories are helpful, though not required, in determining the general flow of forces. For the CTT-node, the "line of separation" can be identified from the stress trajectories and appears to be reasonable estimate of the orientation of the compression strut.

Several node specimens had effective concrete strengths greater than values presented in current proposals. Specimen LFSR, the only specimen where a crushing failure of the strut occurred, was able to develop an

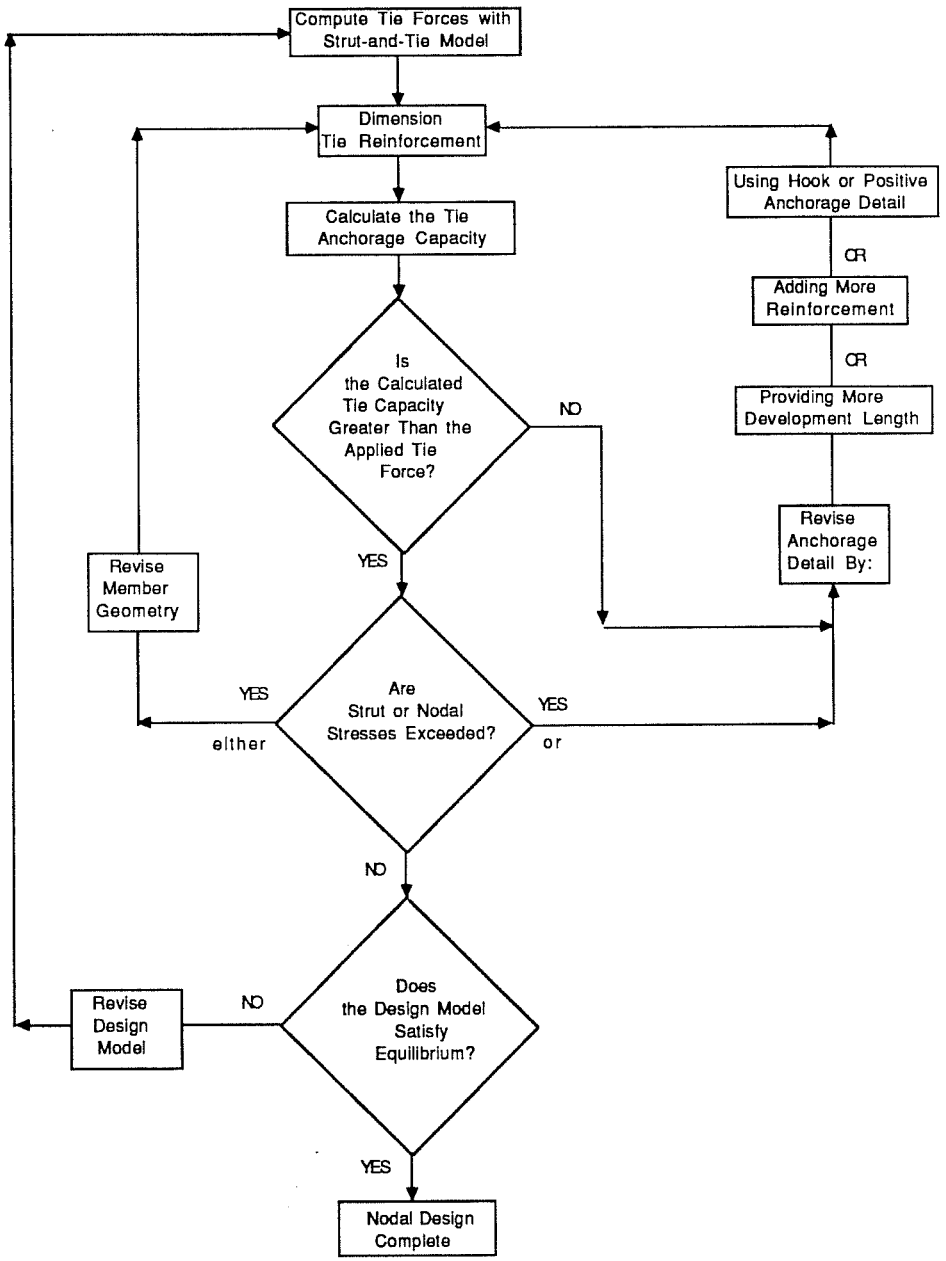

Fig. 5.17 Flowchart Illustrating Design Steps for CTT-Node

effective concrete stress of 1.03*f'c. Higher allowable concrete efficiencies for the CTT-node would greatly affect its design. Presently, nodes anchoring tensile ties in more than one direction are given lower efficiency factors than nodes bounded by compressive struts and those anchoring only one tie. If the effective concrete strength limits for the CTT-node matched recommendations for other types of nodes, the design process could be simplified.

While all the recommended efficiency factors show room for improvement, the extension of effective strength criteria for continuous compression fields to discontinuous regions appears most inappropriate. A case in point is illustrated by Specimen LFAC. This specimen had a 30° strut angle; however, it did not show decreased effective concrete strength as would be predicted by Mitchell and Collins (12). The concept of strain softened concrete needs further definition before it can be applied to D-regions.

Variations in the strains and in the anchorage requirements for different layers of tie reinforcement or "distance effects" were identified in the node tests. The forces in different layer of a tie are influenced by the location of major cracks. Major cracks initiated at the outside surface on the specimen, radiated diagonally across the tie, and generally intersected layers of bars at increasing distances along their length. Layers of reinforcement closest to the outside surfaces of the member appear to be most critical for development. It appears to be conservative to define the critical section for development of the tie reinforcement using the boundary of the compressive stress field. The capacity of each layer of reinforcement making up a tie can be based on development length from the critical section. Furthermore, if the

measured development length is greater than that required to develop f_y, the capacity of a particular layer of reinforcement should be limited by its yield stress.

Design guidance presented herein is intended to provide assistance to the designer and to serve as a basis for development of more comprehensive node design criteria. This study suggests that tie anchorage details should be classified by type, that is, positive and development anchorage details. For proper anchorage of the tensile ties, many proposals stress the use of positive anchorage details such as end plates or U's. The node tests showed these types of details may not always be necessary. Properly anchored straight or hooked bars can develop f_y. The key to the design process is the ability to identify conditions severe enough to warrant the use of positive anchorage details. In this regard, the designer must weigh the consequences of using wider spacings of tie reinforcement in order to provide suitable development. If the ties are too widely spaced, the design model will be inefficient and will not follow the elastic force distribution.

5.6.2 Practical Considerations. The test results show the importance of designing the CTT-nodes as three dimensional elements. Cover splitting failures in Specimens LFSR, HFNC, LFNC, and LFAC show planes of weakness often form normal to the plane of a hook or bend. For example, the transverse U provides good lateral confinement, but prying action at the 90° bend may produce splitting cracks which result in failure as in Specimen LFSR. Practical solutions for improving three dimensional confinement for the CTT-node in this study are shown in Fig. 5.18. The first and simplest

detail to control splitting cracks of the end cover involves extending the longitudinal bars a short distance past the transverse U's as shown in Fig. 5.18 (a). This detail would also provide the longitudinal tie with additional development length. Less economical details involve the placement of extra hoop reinforcement as shown Figs. 5.18 (b) and 5.18 (c). Confinement provided by hoops is beneficial to the performance of both the transverse and longitudinal steel. As a minimum, confining reinforcement as required by the ACI Code and the AASHTO Specification should be provided. The poor detail used in the unconfined specimens should be avoided.

Regarding the anchorage of ties, providing more reinforcement than is necessary for strength considerations reduces the required development length if the tie is anchored with a hook or straight bar. This was done for the Prototype Beam Specimen and involved carrying through the full amount of longitudinal steel to the CTT-node. This type of detail may add to material costs but the construction process is simplified because bar cutoff points are minimized.

Obviously, suitable cover is also very beneficial in preventing splitting failures and may possibly lessen the development requirements for ties. The steel layout and corresponding isolated strut-and-tie model at the termination point of the straight longitudinal bars in the node specimens is presented in Fig. 5.19. The strut-and-tie model shows that the forces are redirected at a point; however, the forces are not transferred instantaneously in the actual specimen. For example, it would not be expected that sufficient bond stresses could develop at the free end of the horizontal bar deviate the

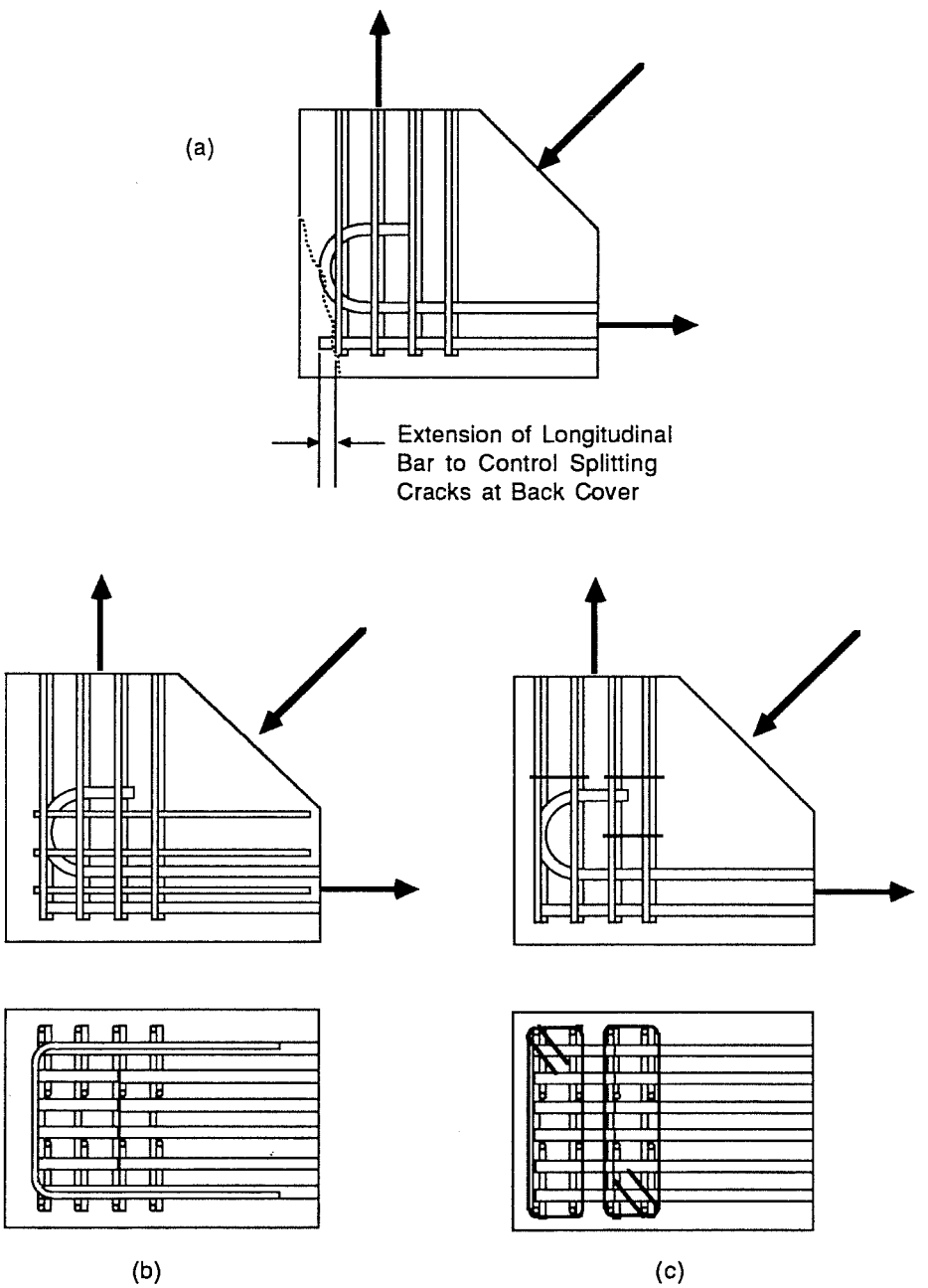

Fig. 5.18 Detailing the CTT-Node to Provide Three-Dimensional Confinement

strut force. It is also noted that concrete cover may be somewhat effective in maintaining equilibrium of the system. Indeed, the actual force flow is much more complex and relies on bond stresses distributed over some distance and on the tensile strength of the concrete (Fig. 5.20). The concrete cover acts as a tie and resists a portion of the horizontal strut force. Further tests are required before design recommendations regarding this behavior pattern can be proposed.

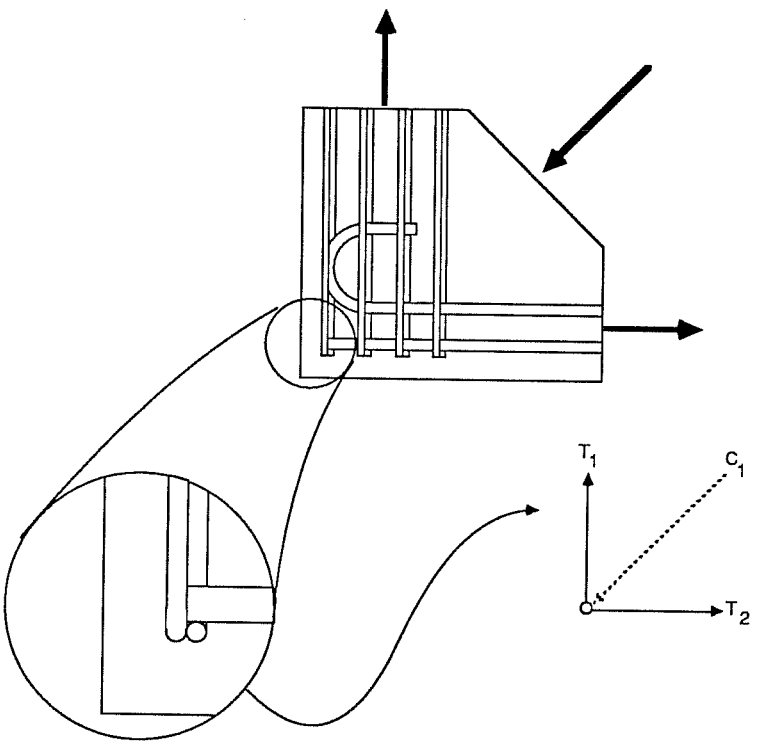

Fig. 5.19 Placement of Reinforcement and Corresponding Strut-and-Tie Model and Termination Point of Straight Bars

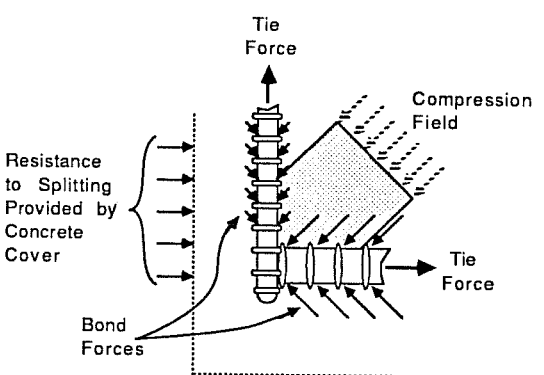

Fig. 5.20 Force Transfer Mechanisms at Intersection of Straight Bar with U Reinforcement

CHAPTER 6

SUMMARY AND CONCLUSIONS

6.1 Summary

The purpose of this study was to develop an in depth understanding of an isolated CTT-node. Portions of the strut and tie model dealing with nodes, especially those anchoring tensile ties, are not well defined, nor have they been subjected to comprehensive evaluation through tests. A laboratory investigation was implemented to verify current proposals, identify significant behavior patterns of the CTT-node, and develop design guidelines. In particular, the study was aimed at providing information about the following criterion: 1) dimensions of the node; 2) configuration of the compression strut; 3) allowable concrete stress; 4) detailing considerations, and 5) effects of strut angle change.

The prototype for the node tests was a full sized, dapped beam tested by Barton (17). The node specimens and the associated test setup were designed to duplicate, as closely as possible in the isolated node, boundary conditions that exist in the CTT-node of the full-sized, dapped beam. Nine isolated CTT-node specimens were fabricated and tested. Five of these were cast with concrete strengths ranging from 5800 to 7100 psi. Four specimens were cast with concrete strengths ranging from 3700 to 3900 psi. Other variables included lateral confinement provided by U-reinforcement, strut width, anchorage details, and strut angle. Tensile forces were applied in two directions which produced an equilibrating compressive force at the specimen's bearing face.

Cracking patterns and reinforcement strain behavior were the most important information obtained from the tests. Cracking patterns gave an indication of the dimensions and angle of the compression strut. Also, they were helpful in determining whether the node specimens were representative of the behavior of the full-sized specimen. Strain measurements aided in identifying the force transfer mechanisms of the CTT-node. From these measurements, the role of internal force transfer mechanisms in a strut-and-tie model could be identified.

6.2 Conclusions

The study provided valuable information in areas where current proposals offer limited guidance. While test data was collected from a relatively small number of tests, the following conclusions based on the experimental evidence are felt to be warranted.

1) Specimens were generally able to reach the design strength which was governed by yielding of tie reinforcement. The ultimate strength of the node was affected by concrete strength; however, internal force transfer mechanisms were more affected by the specimen geometry and placement of steel. Strut-and-tie action was identified as the dominant internal force transfer mechanism after yielding of tie reinforcement.

2) In all the specimens, different layers of tie reinforcement were observed to strain at different rates as a direct result of behavior patterns identified as "distance effects". With the strut and tie model, the reinforcement making up a single tie is normally thought to be similarly strained. All the test specimens showed that the straining of reinforcement

was affected by the location of major cracks. Cracks normally aligned with the resultant of the applied compressive force and reduced the available development length for bars closest to the perimeter of the specimen. Layers of reinforcement closest to the perimeter of the specimen and with sufficient anchorage strained at higher rates than interior layers of reinforcement. In the test specimens, this type of behavior was observed for the transverse tie which was anchored with U's and hooks. In contrast, the longitudinal tie in some of the test specimens saw reduced straining for layers of reinforcement closest to the specimen's perimeter. In these cases, the major cracks appeared to reduce the available development length enough to cause a deterioration in the tie's load carrying capacity. In design, layers of reinforcement closest to the outside surfaces of the member were shown to be most critical for development. This is because major cracks initiated at the surface of the specimen and generally followed the theoretical strut angle.

3) Correlations between the behavior of the node specimens and the prototype dapped beam specimen were quite good. This was evidenced by similar crack patterns and comparable reinforcement strains for the two types of specimens. Test data from the node specimens were most representative of the behavior of the full-sized specimen before the design strength of the member, governed by yielding of the tie reinforcement, was achieved. After yield, the deformation capacity of the full-sized member limited the amount of force that could be transferred to the CTT-node. This observation does not affect the design of the node significantly since the ties are designed to yield before crushing of the concrete.

Evaluation of the strut-and-tie model in the light of the test results of the present study gives rise to the following additional conclusions:

1) Fan-shaped cracking patterns indicated by the elastic stress trajectories were observed in the node specimens. Cracks generally followed the resultant of the compression strut.

2) For CTT-nodes with each tie composed of multiple layers of reinforcement, it appeared that the geometry of the strut is best defined by the strut angle and the width of the outer intersection of the tie reinforcement. In the case of hooked bars, the boundary of the strut is defined by the point were the hook is tangent to the reinforcement making up the opposite tie. Narrow bearing surfaces reduce the compression strut width.

3) Recommended effective concrete strength limits proposed earlier by several authors and mentioned in this study were conservative. Recommendations by Schlaich et al. (1) were closest to the measured compression strut strengths; however, test comparisons showed all the recommendations were rather imprecise. A shallow angle of the compression strut did not reduce the effective concrete strength as would be predicted by Mitchell and Collins (12). This conclusion must be tempered by the fact that the cracks in the node specimens were parallel to the resultant of the compression strut force and may account for the high measured strength.

4) It was estimated that the configuration of the compression strut was prismatic when sufficient available bearing surface was present. Fan-

shaped actual stress fields appeared to be produced in specimens with narrow bearing surfaces.

5) Defining the critical section of the reinforcement by the boundaries of the compression fields appeared to produce reasonable estimates of the capacity of ties anchored through development. If the measured development length (that is, the distance from the critical section to the termination point of the bar) was greater than that required to develop f_y, the estimated capacity of that layer of reinforcement would be governed by its yield stress.

6) Two types of tie anchorage details were identified. Positive anchorage details including end plates and U's ensure the tie is anchored without consideration of development along the bar. Development length anchorage details would include straight deformed bars and hooks. These details resist the tie force through a combination of bond and/or anchorage and require the designer to make an assessment of the available development length.

7) The splitting failures that occurred in Specimens LFSR, HFNC, LFNC, and LFAC underscored the importance of detailing the CTT-node as a three dimensional element. This implies that reinforcement should be provided across all planes of weakness to control cracking. Confining reinforcement normal to planes of hooks and bends is especially important.

6.3 Needs for Further Research

The present study is quite limited in scope since only one spacing of reinforcement was tested and no prestressed concrete details were

investigated. In order to develop comprehensive design criteria for the CTT-node, further tests are required. It is recommended that future studies of the CTT-node should include specimens with a number of different bar spacings and amounts of tie reinforcement. Test specimens with high percentages of reinforcement and narrow web widths are also suggested so that effective concrete strength limits could be evaluated more closely. Tests could also compare the behavior of specimens with anchor plates and straight or hooked bars. In addition, the effect of strut angle change should be studied more closely. Particularly, the effects of skew cracks on the effective concrete strength of the compressive strut should be determined.

The testing apparatus used for the present study could be used to test additional node specimens with minimal modifications. However, the type of specimen and test apparatus used in this study would not be appropriate for investigating the behavior of nodes in prestressed concrete specimens. Tests similar to beam or dapped beam tests would be more practical for prestressed concrete specimens.

REFERENCES

1. Schlaich, J., Schäfer, K., and Jennewein, M., "Towards a Consistent Design of Reinforced Concrete Structures," *PCI Journal*, Vol. 32, No. 3, May-June 1987, pp. 74-150.

2. American Concrete Institute, *Building Code Requirements for Reinforced Concrete (ACI 318-83)*, Detroit, 1983, 111 pp.

3. American Association of State and Highway and Transportation Officials, *Standard Specifications for Highway Bridges*, Thirteenth Edition, Washington, D. C., 1983.

4. *PCI Design Handbook, 3rd Ed.*, Prestressed Concrete Institute, Chicago, Illinois, 1985, 521 pp.

5. *Post-Tensioning Manual, 4th Ed.*, Post-Tensioning Institute, Phoenix, Arizona, 1987, 406 pp.

6. *Reinforcing Bar Detailing, 5th Ed.*, Concrete Reinforcing Steel Institute, Chicago, Illinois, 1986, 280 pp.

7. Ritter, W., "Die Bauweise Hennebique (The Hennebique Design Method)," *Schweizerische Bauzeitung* (Zurich), Vol. 33, No. 7, Feb.1899.

8. Mörsch, E., *Der Eisenbetonbau-Seine Theorie und Anwendung (Reinforced Concrete-Theory and Application)*, Verlag Konrad Wittwer, Stuttgart, 1912.

9. Leonhardt, F., "Über die Kunst des Bewehrens von Stahlbetontragwerken (About the Art of Reinforcing Detailing for Reinforced Concrete Girders)," *Beton-und-Stahlbetonbau*, Vol. 60, No. 8, 1965, pp.181-192; No. 9, pp. 212-220.

10. Neilsen, M. P., Braestrup, M. W., Jensen, B. C., and Bach, F., "Concrete Plasticity, Beam Shear-Shear in Joints-Punching Shear," *Special Publications*, Danish Society for Structural Science and Engineering, Technical University of Denmark, Lyngby, 1978, 129 pp.

11. Lampert, P., and Thürlimann, B., "Ultimate Strength and Design of Reinforced Concrete Beams in Torsion and Bending," *Publications No. 31-I*, International Association for Bridge and Structural Engineering, Zurich, 1971, pp. 107-131.

12. Collins, M.P., and Mitchell D., "Shear and Torsion Design of Prestressed and Non-Prestressed Concrete Beams," *PCI Journal*, Vol. 25 No. 5, Sept./Oct. 1980, pp. 32-100.

13. Ramirez, J.A., "Reevaluation of AASHTO Design Procedures for Shear and Torsion in Reinforced and Prestressed Concrete Beams", unpublished Ph. D. Dissertation, The University of Texas at Austin, 1983.

14. MacGregor, J.G., *Reinforced Concrete-Mechanics and Design*, 1988, Prentice-Hall, Englewood Cliffs, New Jersey.

15. Marti, P., "Basic Tools of Reinforced Concrete Beam Design," *ACI Journal*, Vol. 82, No. 1 Jan.-Feb., 1985, pp. 46-56.

16. Grob, J., and Thürlimann, B.,"Ultimate Strength and Design of Reinforced Concrete Beams under Bending and Shear", *Memoires*, International Association for Bridge and Structural Engineering, Vol. 36-II, 1976, pp. 105-120.

17. Barton, D.L., "Design of Dapped Beams Using the Strut-and-Tie Model," unpublished Master's Thesis, The University of Texas at Austin, December, 1988.

18. Marti, P., "Truss Models in Detailing," *Concrete International*, Vol. 7, No. 12, Dec., 1985, 1986, pp. 66-73.

19. C.E.B. Ad-Hoc Commission IV/VI, Contribution to the Revision of the C.E.B. Model Code 1990, C.E.B., June, 1986.

20. Schlaich, J., and Schäfer, K., "Towards a Consistent Design of Reinforced Concrete Structures", *Final Report*, 12th Congress, International Association for Bridge and Structural Engineering, Sept., 1984, pp. 8-15.

21. Rogowsky, D. and MacGregor, J., "Design of Reinforced Concrete Deep Beams," *Concrete International*, Vol. 8, No. 8, Aug., 1986, pp. 49-58.

22. Collins, M.P., and Vecchio, F., "The Response of Reinforced Concrete to In-Plane Shear and Normal Stresses," Publication No. 82-03, University of Toronto, March, 1982.

23. American Concrete Institute, *Building Code Requirements for Reinforced Concrete (ACI 318-77)*, Detroit, 1983, 111 pp.

24. Jirsa, J., Lutz, L., and Gergely, P., "Rationale for Suggested Development, Splice, and Standard Hook Provisions for Deformed Bars in Tension," *Concrete International*, Vol. 1, No. 7, July, 1979, pp. 47-61.

25. Cook, W., and Mitchell, D., "Studies of Disturbed Regions near Discontinuities in Reinforced Concrete Members," *ACI Structural Journal*, Vol. 85, No. 2 Mar.-Apr., 1988, pp. 206-216.

26. Leonhardt, F., and Walther, R., "Tests on T-Beams Under Severe Shear Load Conditions," Bulletin 152, Deutscher Ausschuss fur Stahlbeton, 1962, Berlin.

27. Leonhardt, F., and Walther, R., "Shear Tests on T-Beam with Varying Shear Reinforcement," Bulletin 156, Deutscher Ausschuss fur Stahlbeton, 1962, Berlin.

28. Schlaich, J., and Schäfer, K., *Beton-Kalender 1984, Konstruieren im Stahlbetonbau,* 1984, Wilhelm Ernst & Son, Berlin.

29. Goto, Y., "Cracks Formed in Concrete Around Deformed Tension Bars," *ACI Journal*, Vol. 68, No. 2 Mar.-Apr., 1971, pp. 31-36.

Appendix

This appendix is divided into four sections and contains supplemental information from the specimen tests. The data in each section is grouped according to the specimen's physical geometry and placement of steel.

A.1 Supplemental Crack Patterns

Figure Page

A1.1 Crack Patterns for Prototype Beam Specimen 232

A1.2 Crack Patterns for Specimen HFSB 232

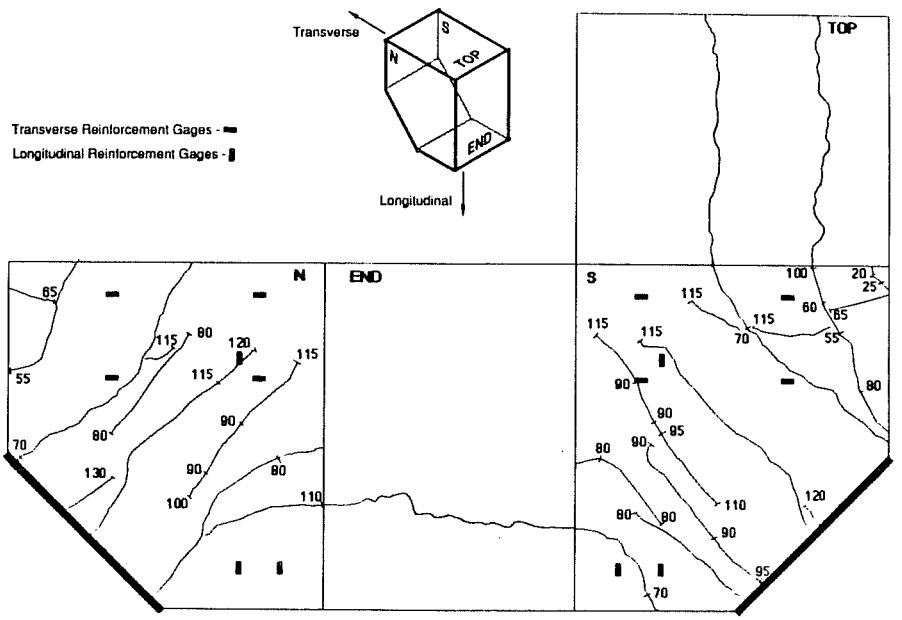

Fig. A1.1 Crack Patterns for Prototype Beam Specimen

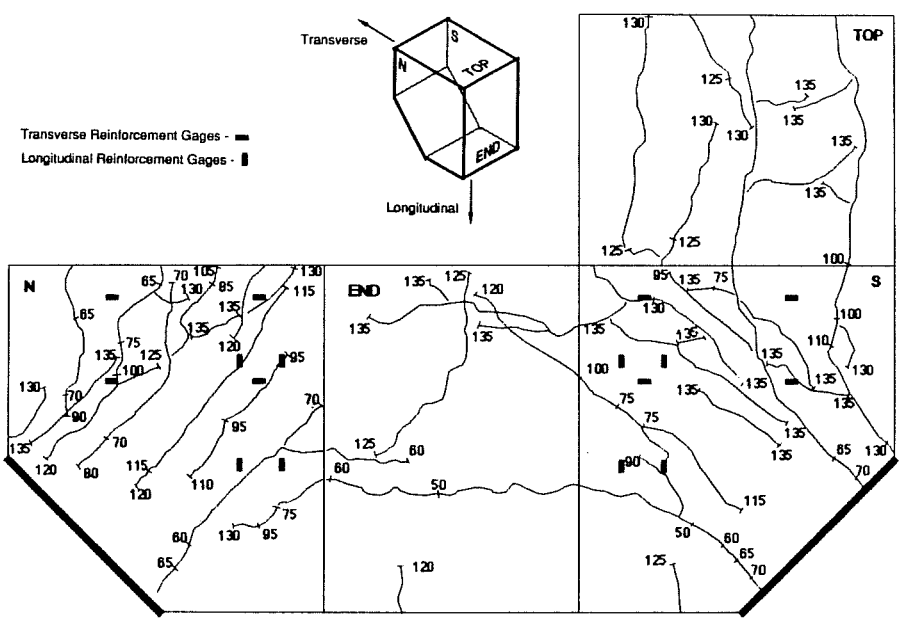

Fig. A1.2 Crack Patterns for Specimen HFSB

A.2 Supplemental Strain Graphs for Transverse Reinforcement

Figure		Page
A2.1	Prototype Beam Specimen-Reinforcement Strain Data for Individual Transverse Gage Locations	234
A2.2	Specimen HFSR-A-Reinforcement Strain Data for Individual Transverse Gage Locations	234
A2.3	Specimen HFSR-B-Reinforcement Strain Data for Individual Transverse Gage Locations	235
A2.4	Average Strain at Transverse Locations for Specimen HFSR-B	235
A2.5	Average Strain at Transverse Locations for Specimen LFSR	236
A2.6	Specimen LFNC-Reinforcement Strain Data for Individual Transverse Gage Locations	236
A2.7	Average Strain at Transverse Locations for Specimen LFNC	237
A2.8	Specimen HHSR-Reinforcement Strain Data for Individual Transverse Gage Locations	237
A2.9	Specimen LHSR-Reinforcement Strain Data for Individual Transverse Gage Locations	238
A2.10	Average Strain at Transverse Locations for Specimen LHSR	238
A2.11	Specimen HFSB-Reinforcement Strain Data for Individual Transverse Gage Locations	239
A2.12	Average Strain at Transverse Locations for Specimen HFSB	239
A2.13	Specimen LFAC-Reinforcement Strain Data for Individual Transverse Gage Locations	240

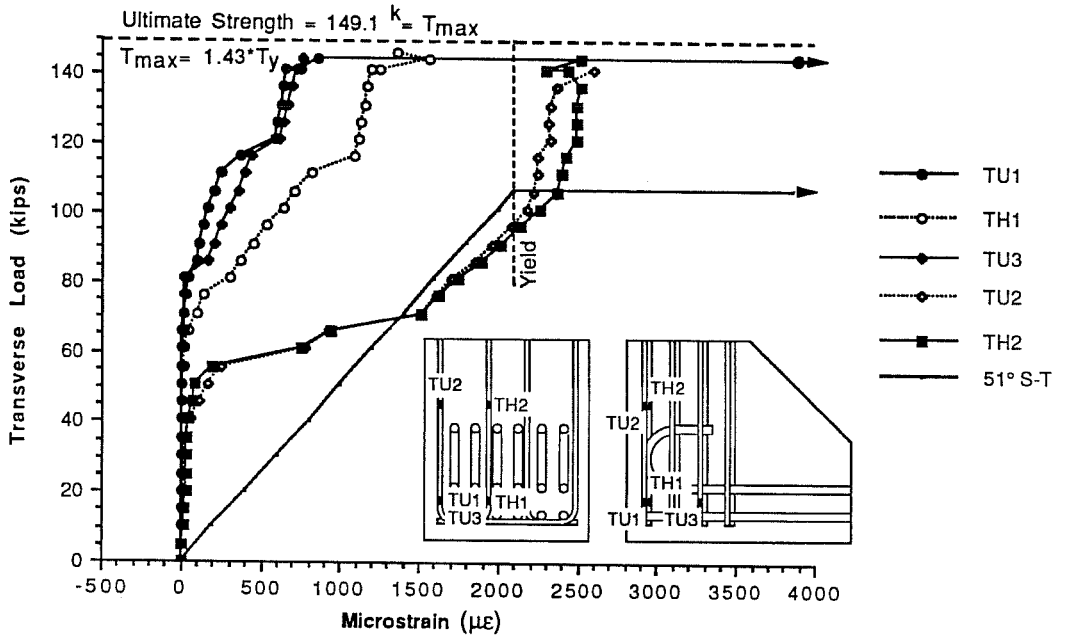

Fig. A2.1 Prototype Beam Specimen-Reinforcement Strain Data for Individual Transverse Gage Locations

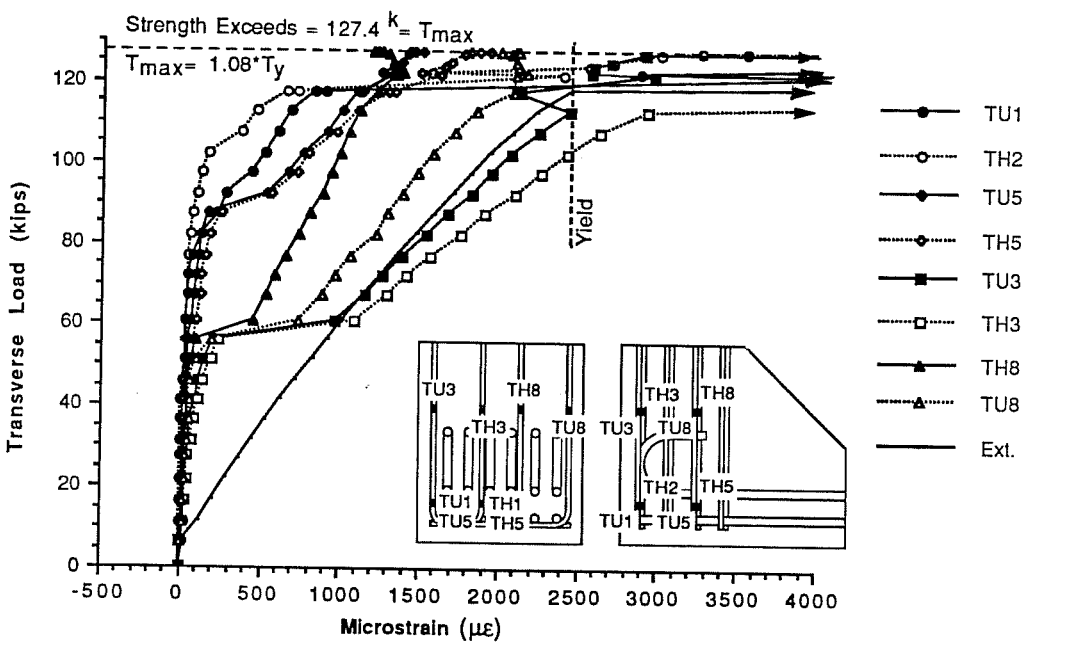

Fig. A2.2 Specimen HFSR-A-Reinforcement Strain Data for Individual Transverse Gage Locations

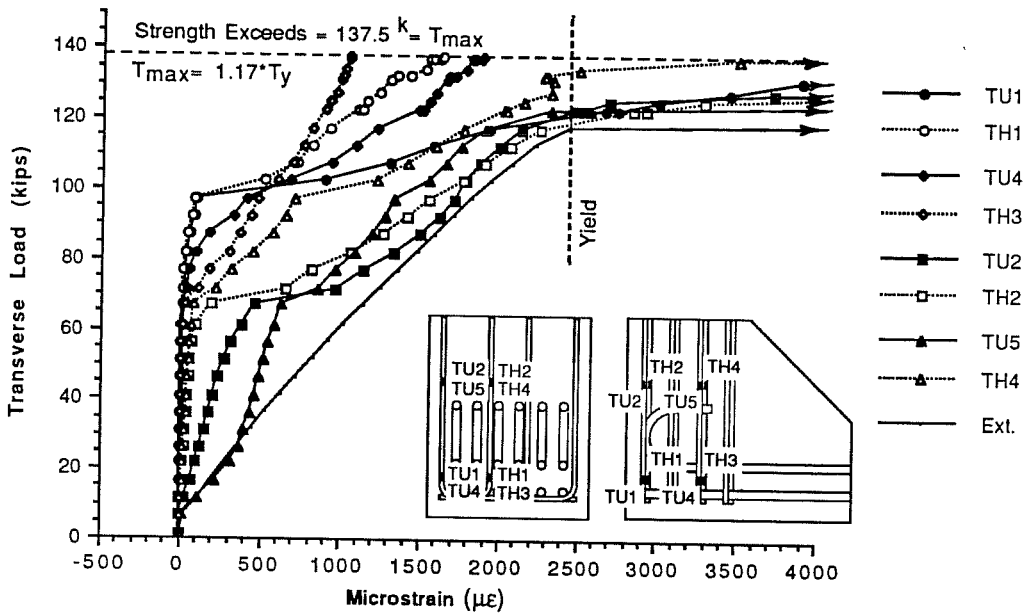

Fig. A2.3 Specimen HFSR-B-Reinforcement Strain Data for Individual Transverse Gage Locations

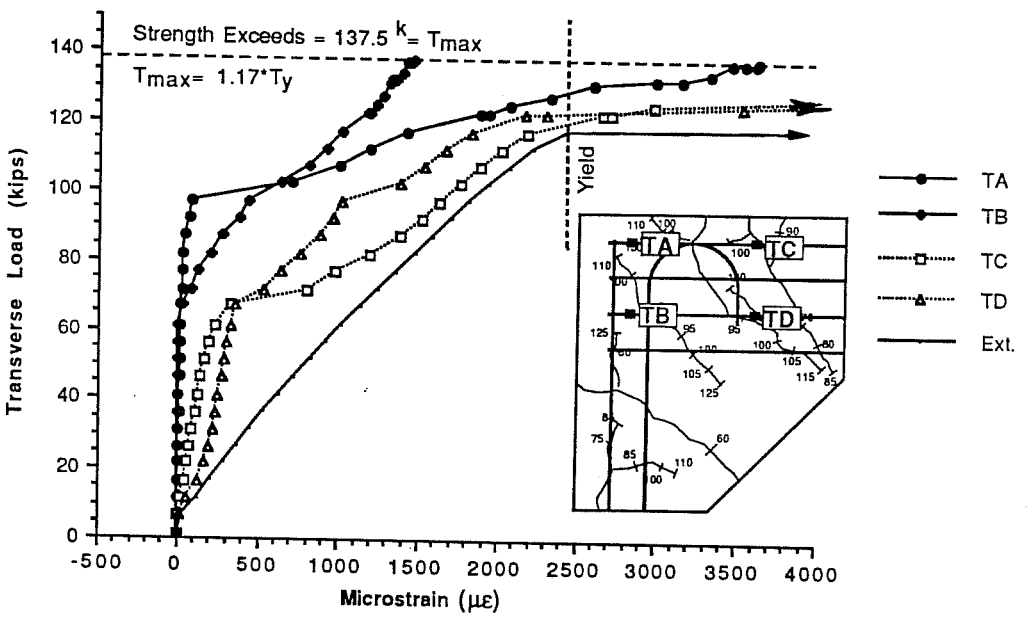

Fig. A2.4 Average Strain at Transverse Locations for Specimen HFSR-B

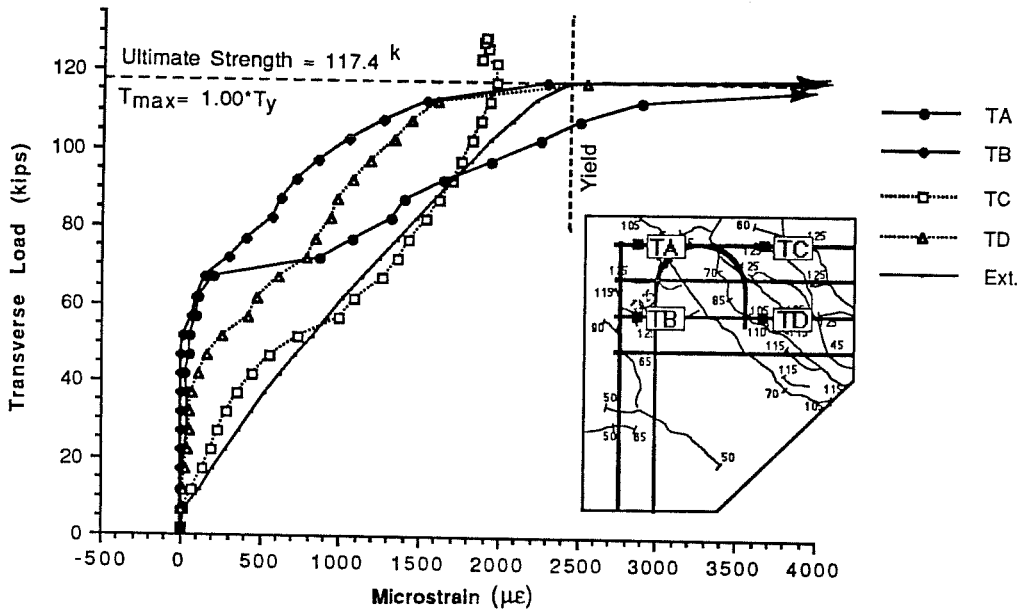

Fig. A2.5 Average Strain at Transverse Locations for Specimen LFSR

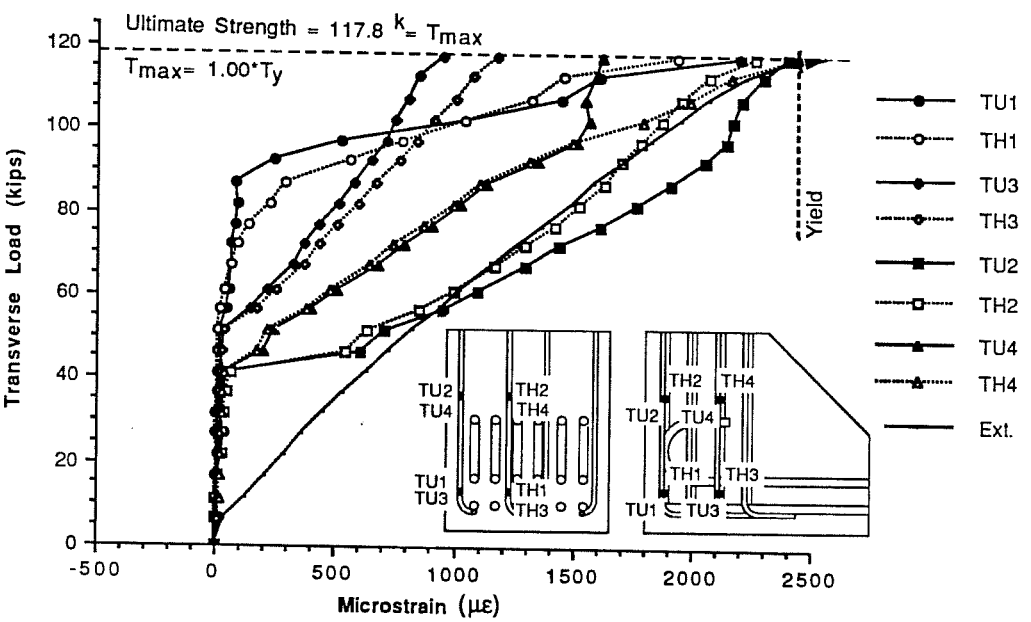

Fig. A2.6 Specimen LFNC-Reinforcement Strain Data for Individual Transverse Gage Locations

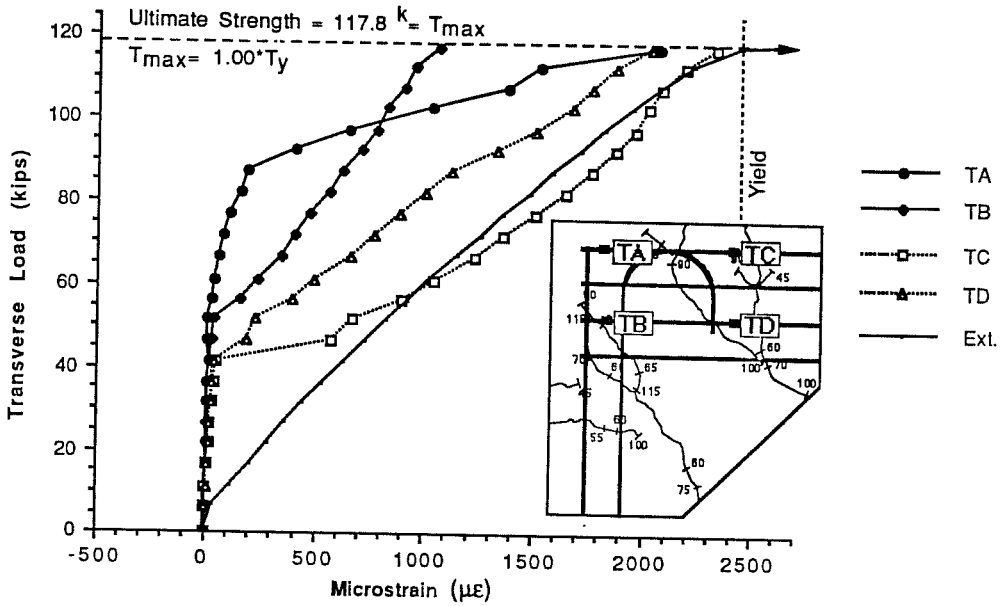

Fig. A2.7 Average Strain at Transverse Locations for Specimen LFNC

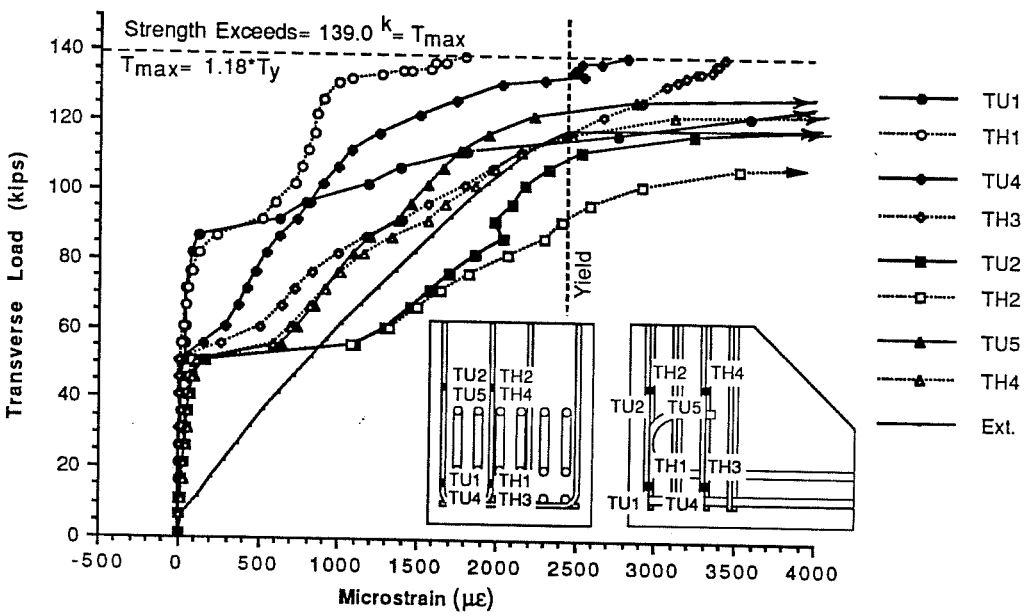

Fig. A2.8 Specimen HHSR-Reinforcement Strain Data for Individual Transverse Gage Locations

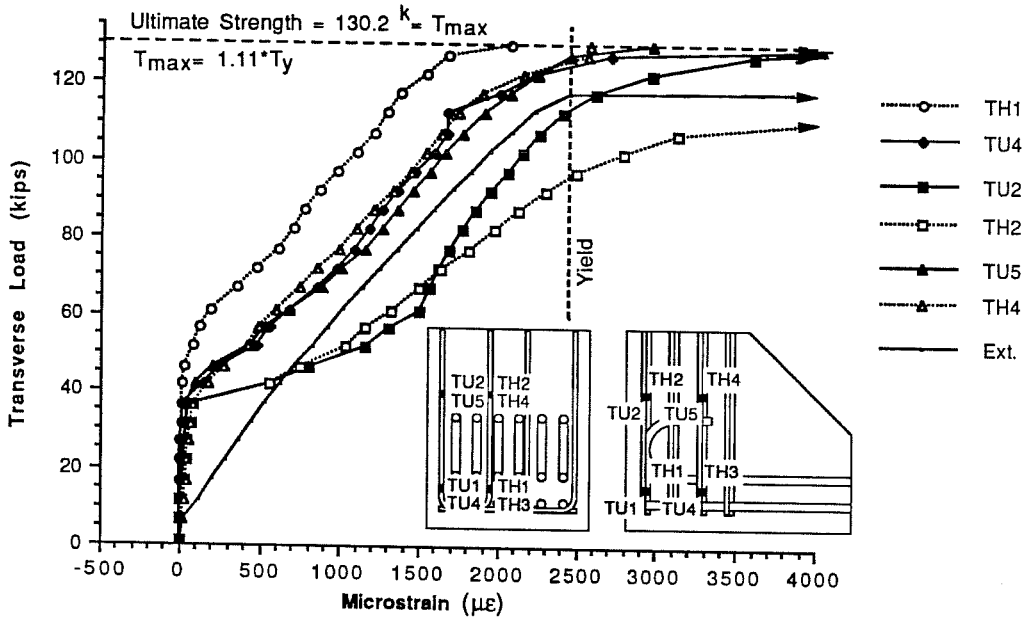

Fig. A2.9 Specimen LHSR-Reinforcement Strain Data for Individual Transverse Gage Locations

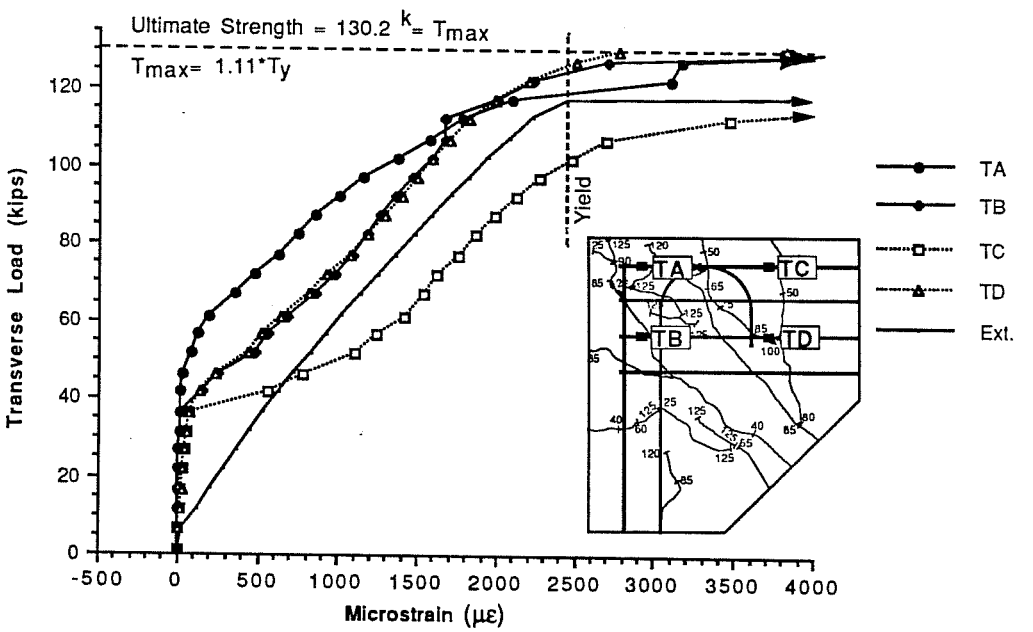

Fig. A2.10 Average Strain at Transverse Locations for Specimen LHSR

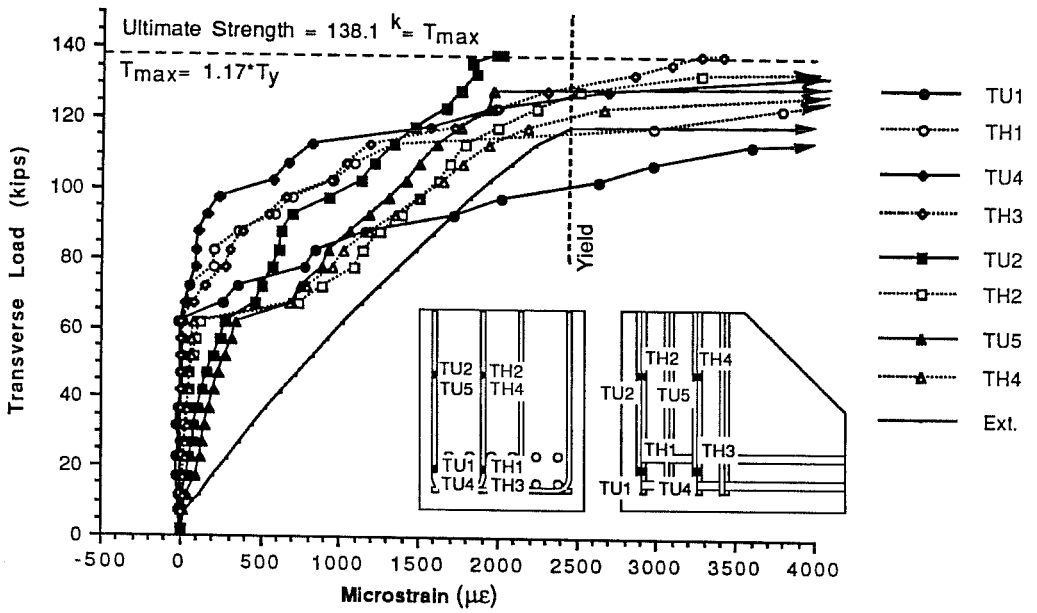

Fig. A2.11 Specimen HFSB-Reinforcement Strain Data for Individual Transverse Gage Locations

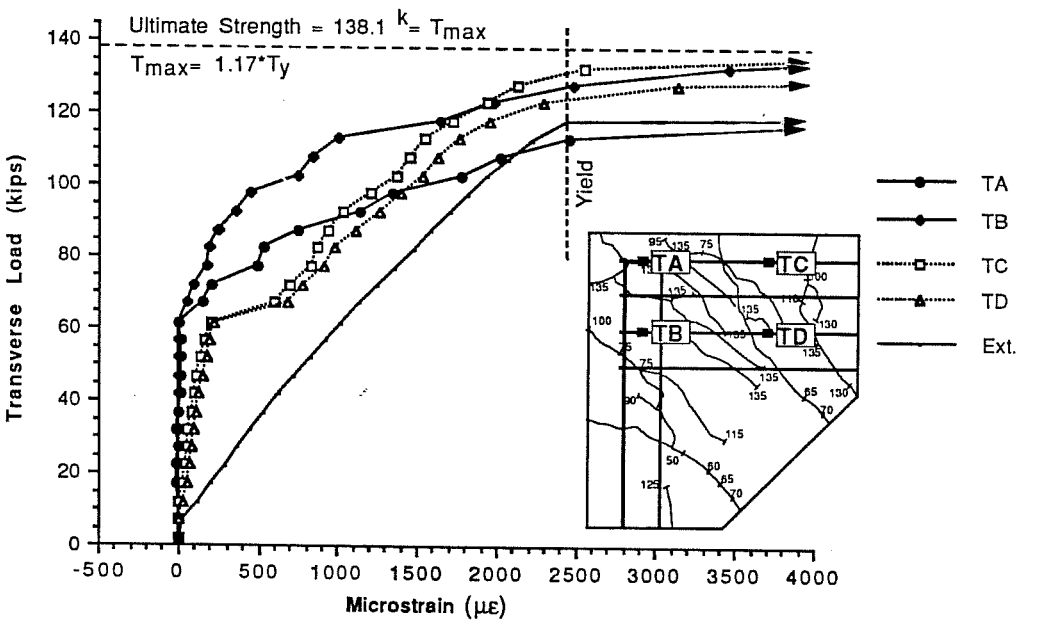

Fig. A2.12 Average Strain at Transverse Locations for Specimen HFSB

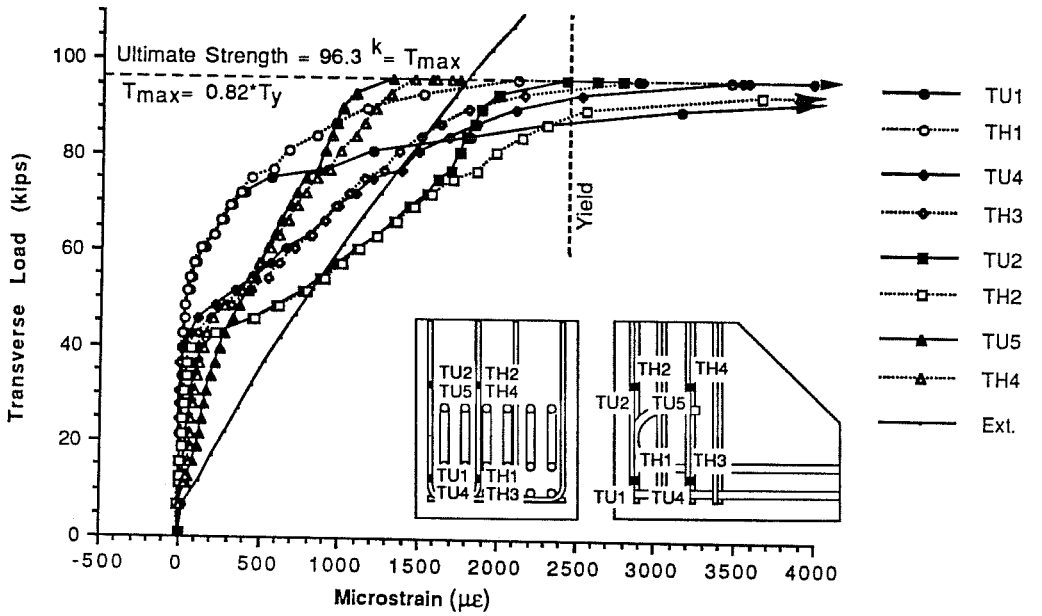

Fig. A2.13 Specimen LFAC-Reinforcement Strain Data for Individual Transverse Gage Locations

A.3 Supplemental Strain Graphs for Longitudinal Reinforcement

Figure — Page

A3.1 Prototype Beam Specimen-Reinforcement Strain Data for Individual Longitudinal Gage Locations 242

A3.2 Specimen HFSR-A-Reinforcement Strain Data for Individual Longitudinal Gage Locations 243

A3.3 Average Strain Data at Longitudinal Locations for Specimen HFSR-A 243

A3.4 Specimen HFSR-B-Reinforcement Strain Data for Individual Longitudinal Gage Locations 244

A3.5 Average Strain Data at Longitudinal Locations for Specimen HFSR-B 244

A3.6 Specimen LFSR-Reinforcement Strain Data for Individual Longitudinal Gage Locations 245

A3.7 Average Strain Data at Longitudinal Locations for Specimen LFSR 245

A3.8 Specimen HFNC-Reinforcement Strain Data for Individual Longitudinal Gage Locations 246

A3.9 Specimen LFNC-Reinforcement Strain Data for Individual Longitudinal Gage Locations 246

A3.10 Average Strain Data at Longitudinal Locations for Specimen LFNC 247

A3.11 Specimen HHSR-Reinforcement Strain Data for Individual Longitudinal Gage Locations 247

A3.12 Specimen LHSR-Reinforcement Strain Data for Individual Longitudinal Gage Locations 248

A3.13 Average Strain Data at Longitudinal Locations for Specimen LHSR 248

A3.14 Specimen HFSB-Reinforcement Strain Data for Individual Longitudinal Gage Locations 249

A3.15 Average Strain Data at Longitudinal Locations for Specimen HFSB 249

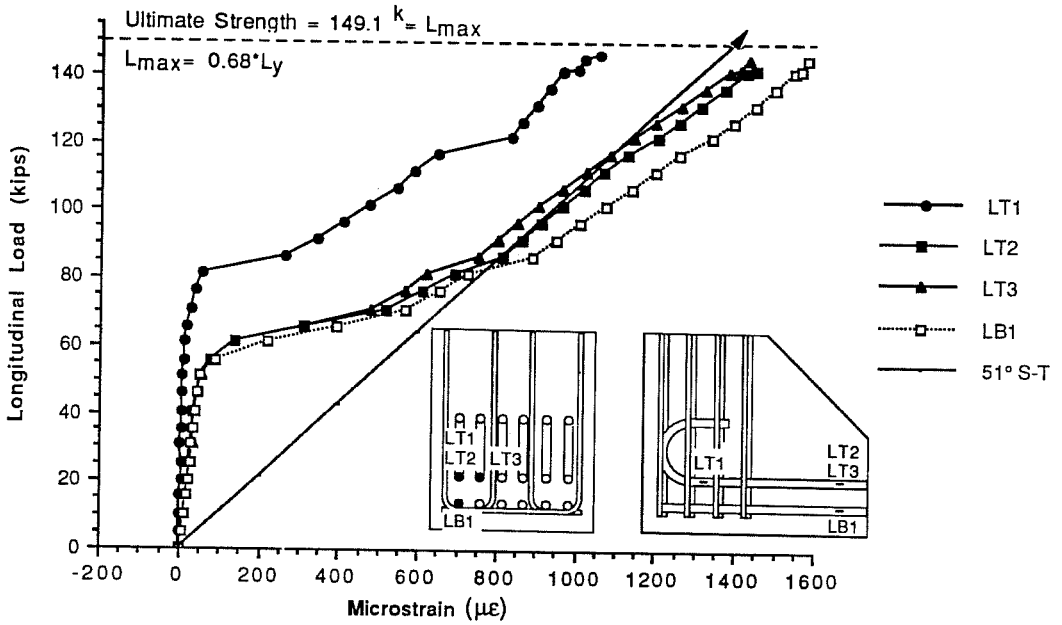

Fig. A3.1 Prototype Beam Specimen-Reinforcement Strain Data for Individual Longitudinal Gage Locations

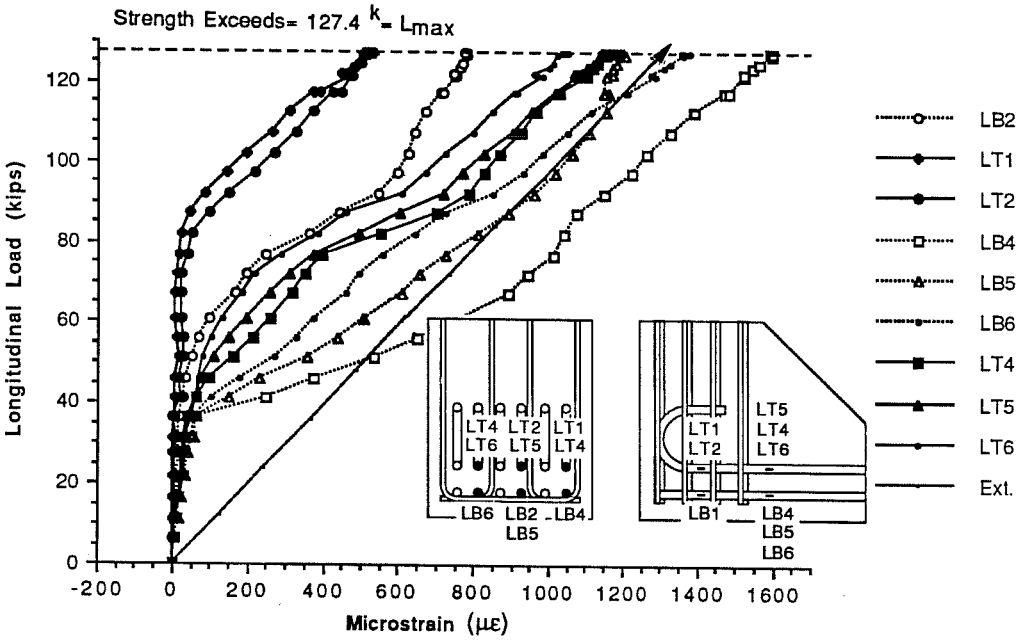

Fig. A3.2 Specimen HFSR-A-Reinforcement Strain Data for Individual Longitudinal Gage Locations

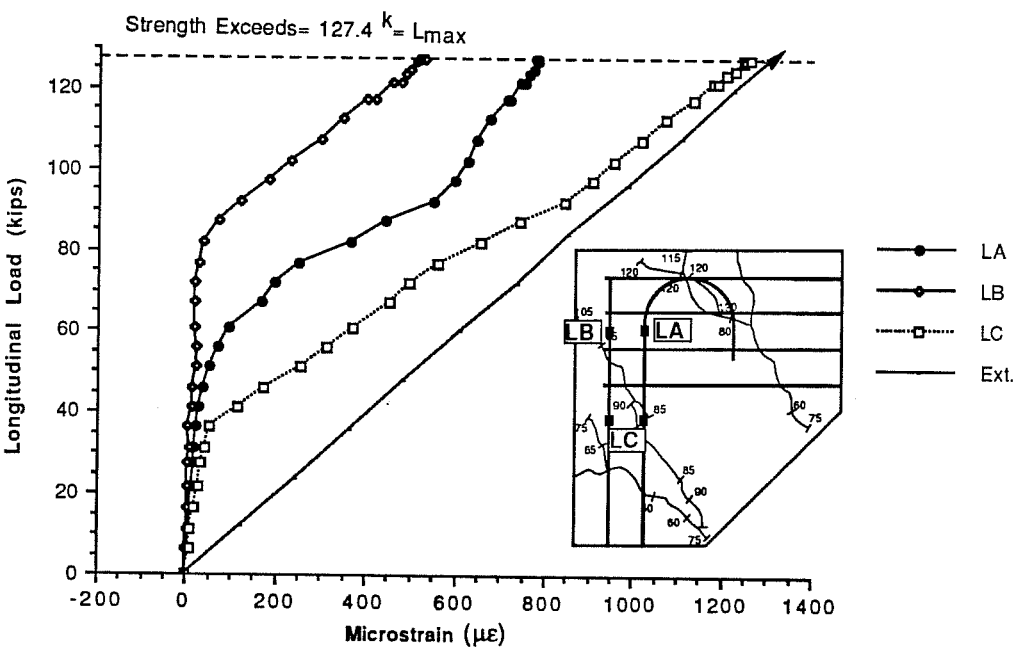

Fig. A3.3 Average Strain Data at Longitudinal Locations for Specimen HFSR-A

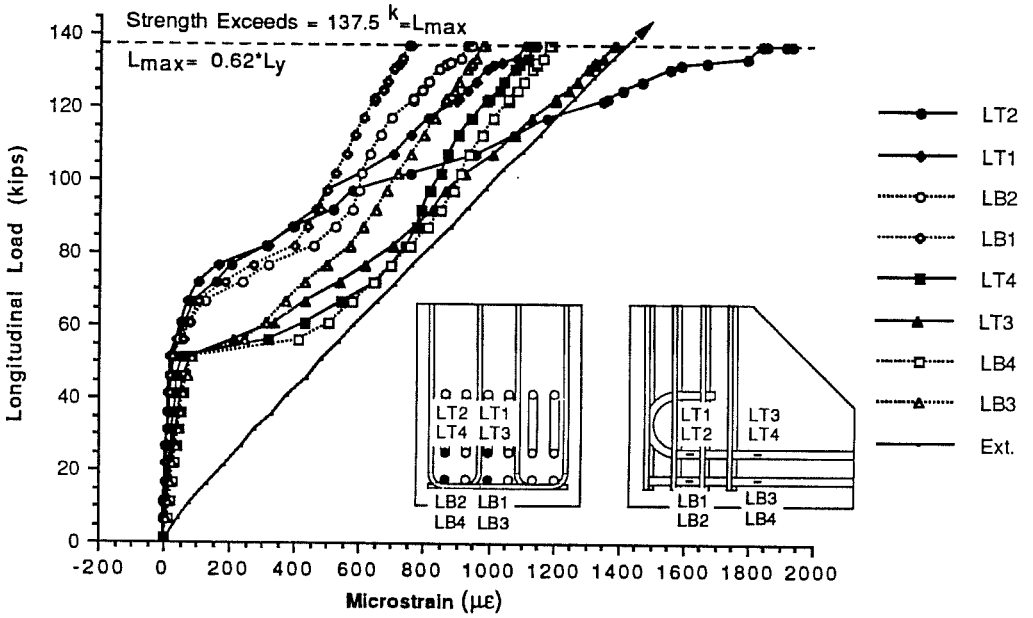

Fig. A3.4 Specimen HFSR-B-Reinforcement Strain Data for Individual Longitudinal Gage Locations

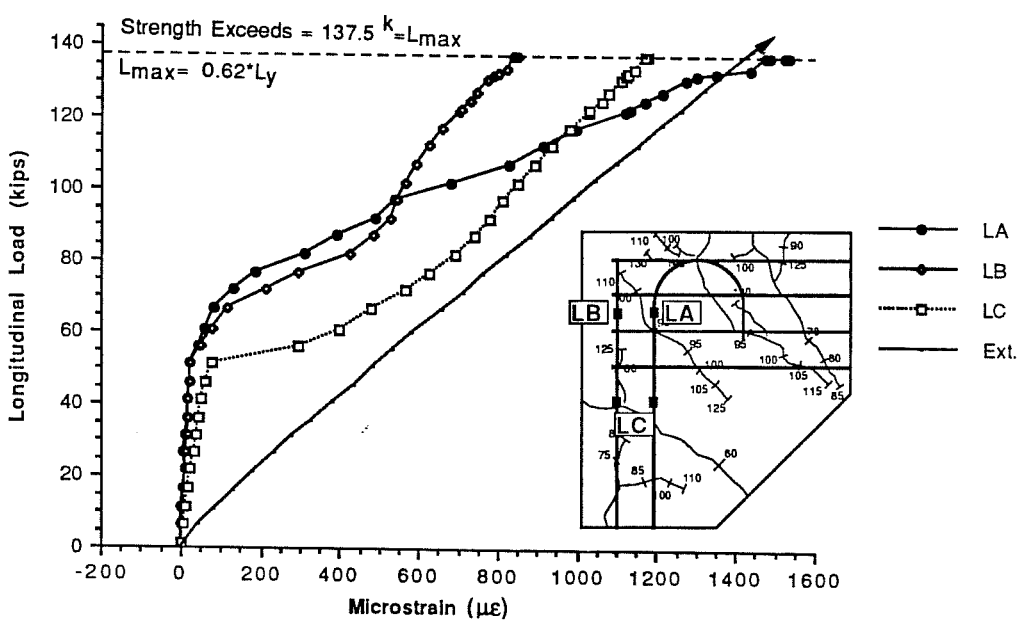

Fig. A3.5 Average Strain Data at Longitudinal Locations for Specimen HFSR-B

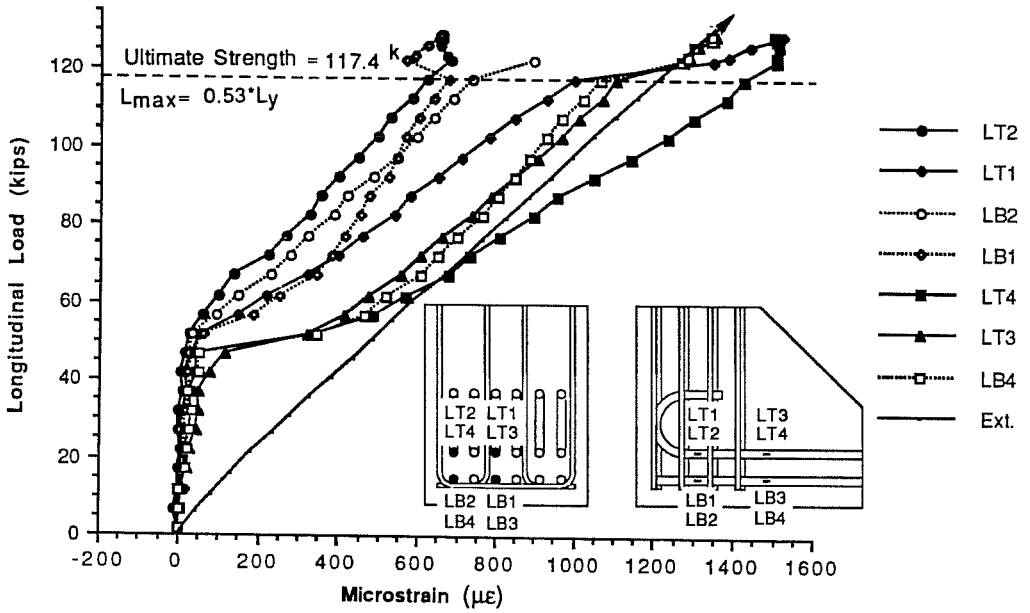

Fig. A3.6 Specimen LFSR-Reinforcement Strain Data for Individual Longitudinal Gage Locations

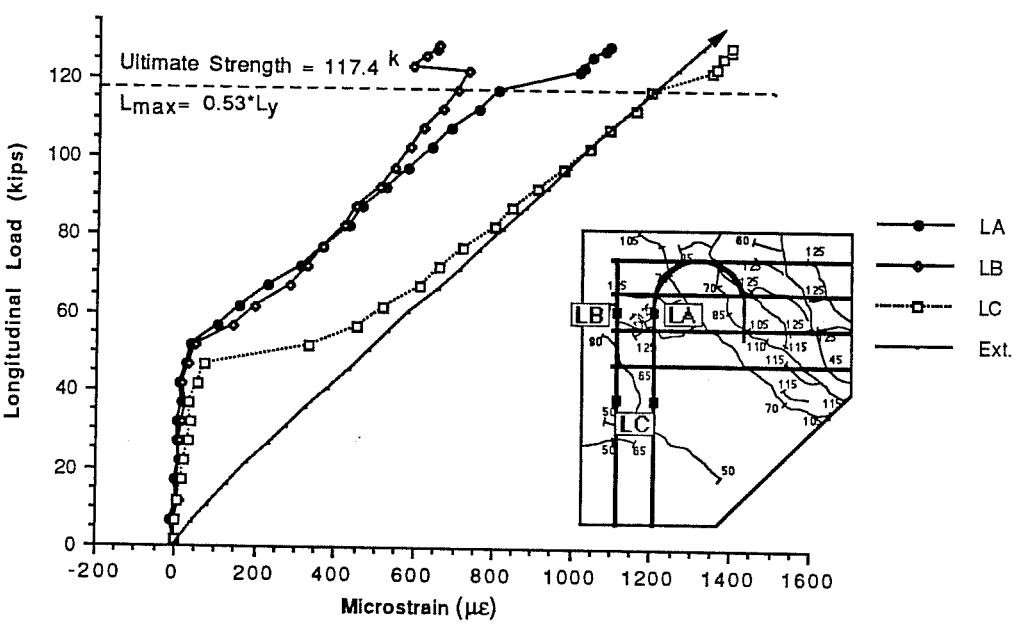

Fig. A3.7 Average Strain Data at Longitudinal Locations for Specimen LFSR

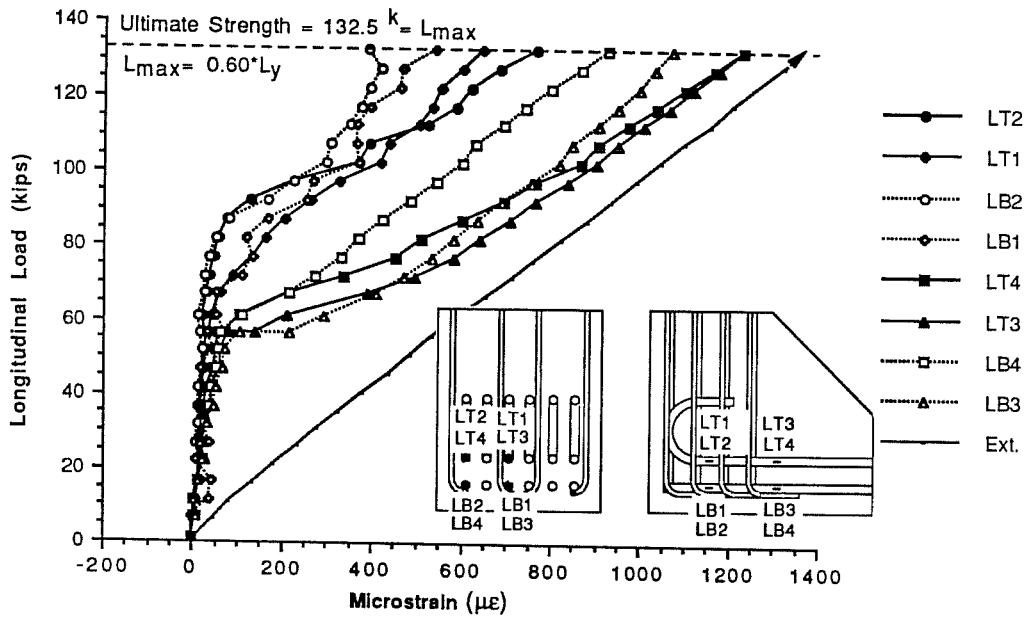

Fig. A3.8 Specimen HFNC-Reinforcement Strain Data for Individual Longitudinal Gage Locations

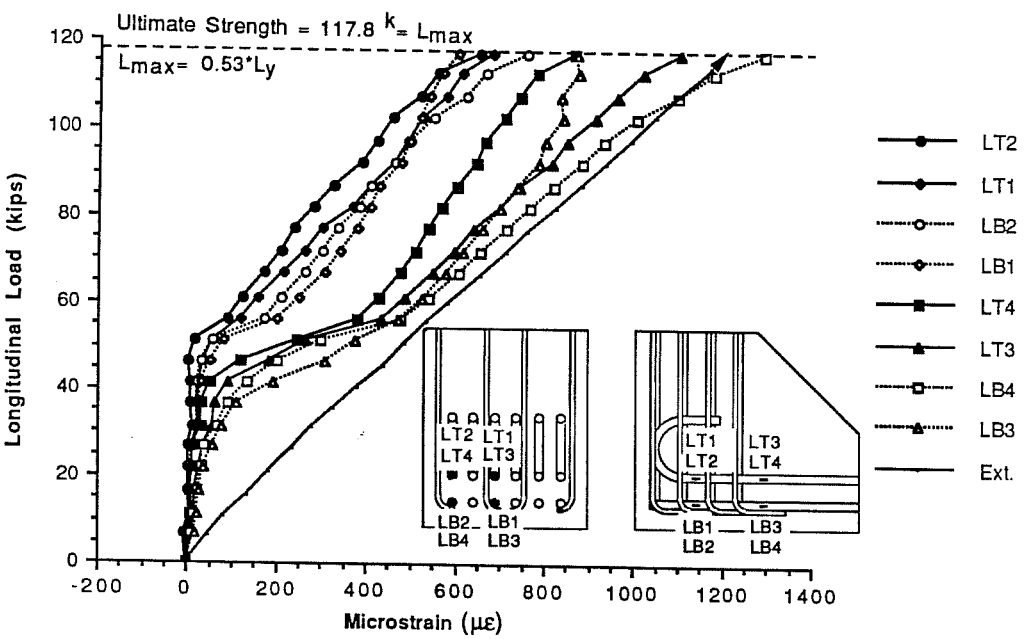

Fig. A3.9 Specimen LFNC-Reinforcement Strain Data for Individual Longitudinal Gage Locations

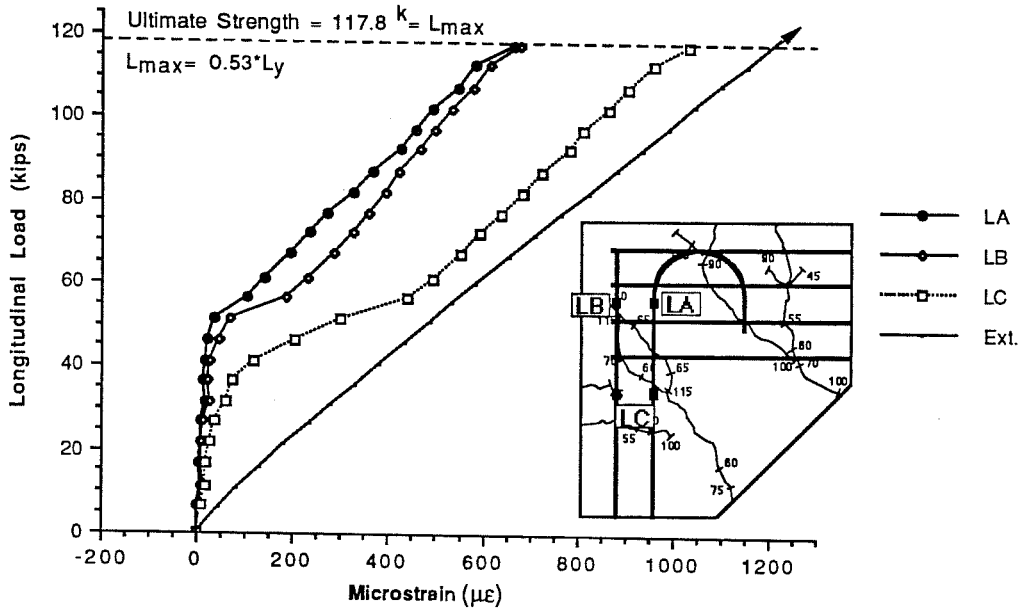

Fig. A3.10 Average Strain Data at Longitudinal Locations for Specimen LFNC

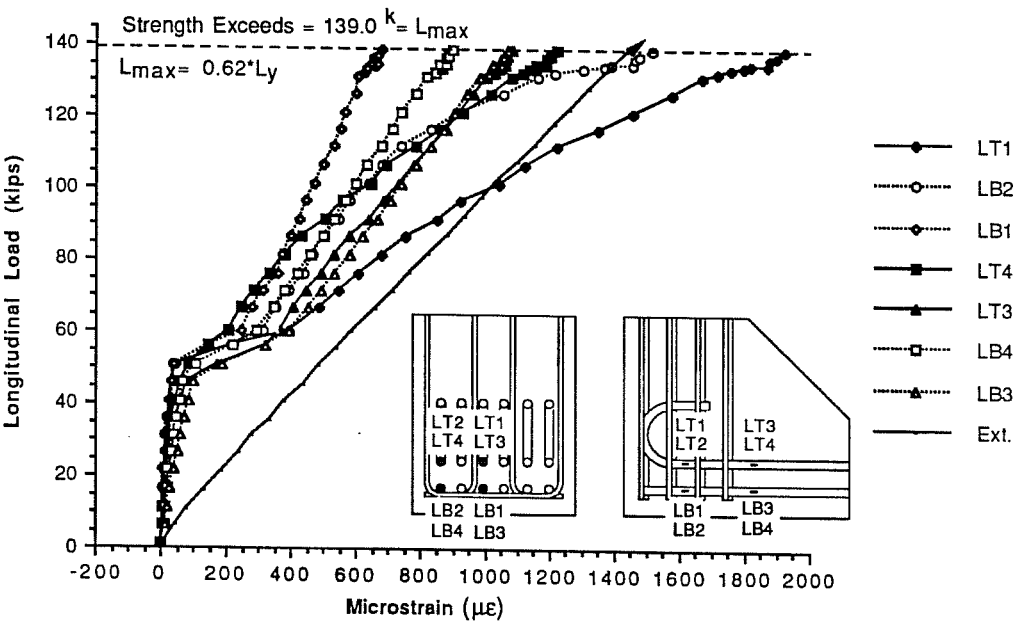

Fig. A3.11 Specimen HHSR-Reinforcement Strain Data for Individual Longitudinal Gage Locations

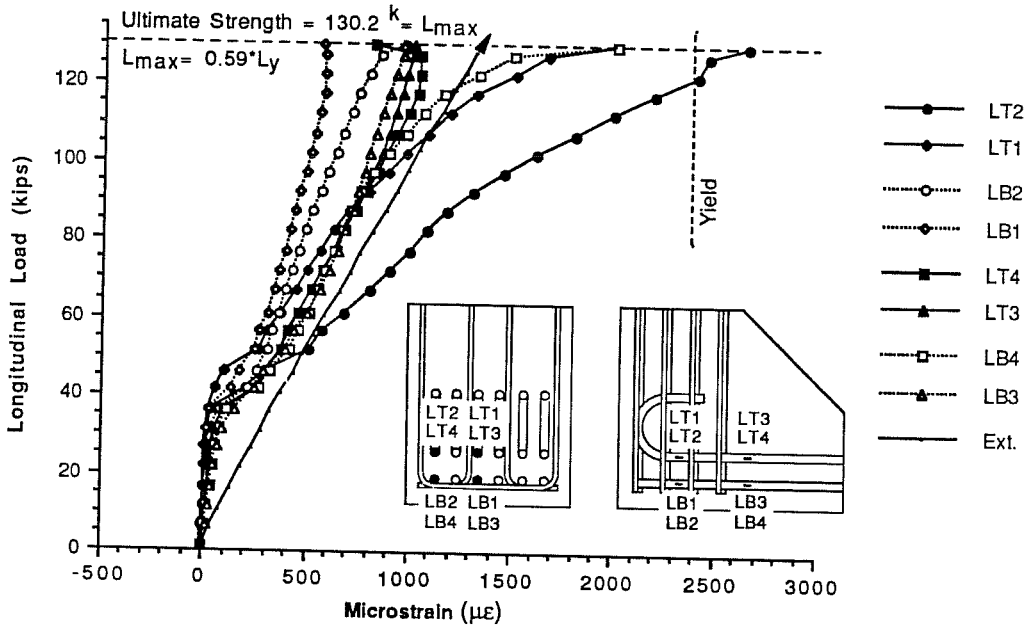

Fig. A3.12 Specimen LHSR-Reinforcement Strain Data for Individual Longitudinal Gage Locations

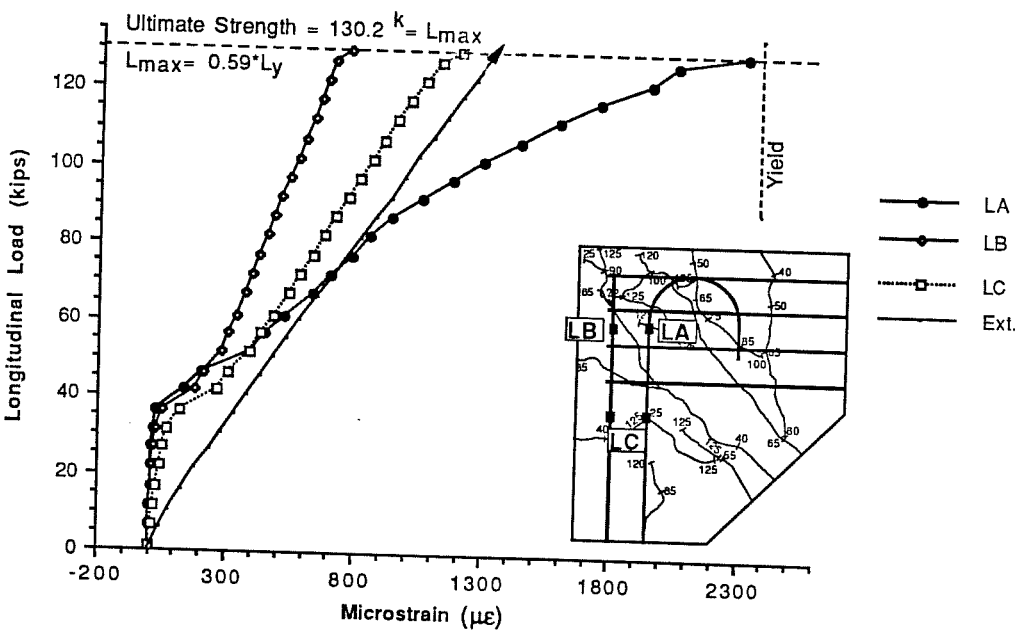

Fig. A3.13 Average Strain Data at Longitudinal Locations for Specimen LHSR

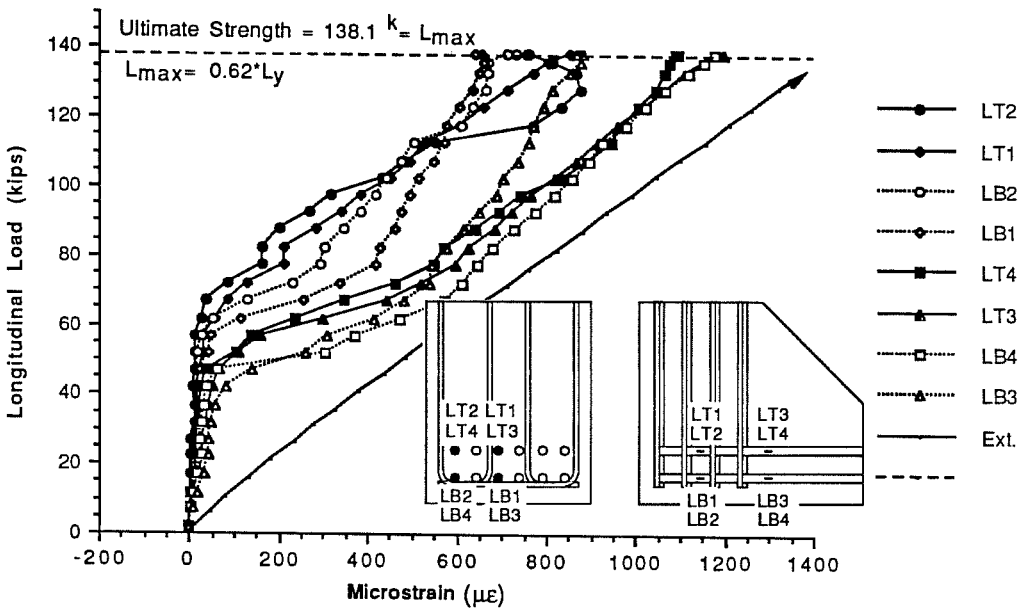

Fig. A3.14 Specimen HFSB-Reinforcement Strain Data for Individual Longitudinal Gage Locations

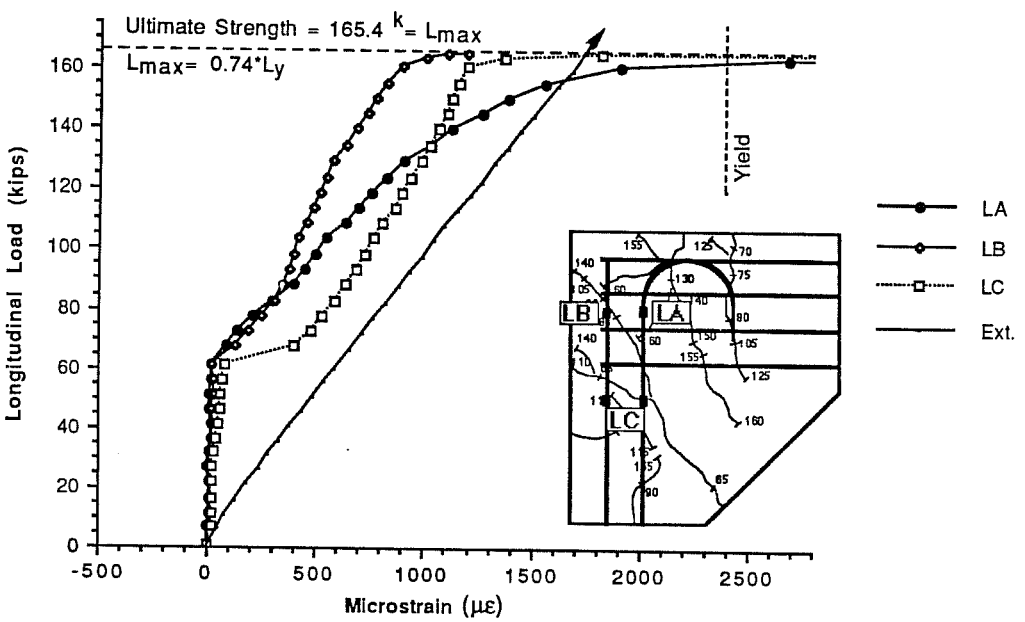

Fig. A3.15 Average Strain Data at Longitudinal Locations for Specimen HFSB

A.4 Supplemental Bar Graphs Showing Percentage of Load at Gage Locations

Figure — Page

A4.1 Specimen HFSR-A-Percentage of Applied Force at Transverse Locations 252

A4.2 Specimen HFSR-A-Percentage of Applied Force at Longitudinal Locations 252

A4.3 Specimen HFSR-B-Percentage of Applied Force at Transverse Locations 253

A4.4 Specimen HFSR-B-Percentage of Applied Force at Longitudinal Locations 253

A4.5 Specimen LFSR-Percentage of Applied Force at Transverse Locations 254

A4.6 Specimen LFSR-Percentage of Applied Force at Longitudinal Locations 254

A4.7 Specimen LFNC-Percentage of Applied Force at Transverse Locations 255

A4.8 Specimen LFNC-Percentage of Applied Force at Longitudinal Locations 255

A4.9 Specimen HHSR-Percentage of Applied Force at Transverse Locations 256

A4.10 Specimen HHSR-Percentage of Applied Force at Longitudinal Locations 256

A4.11 Specimen LHSR-Percentage of Applied Force at Transverse Locations 257

A4.12 Specimen LHSR-Percentage of Applied Force at Longitudinal Locations 257

A4.13 Specimen HFSB-Percentage of Applied Force at Transverse Locations 258

A4.14 Specimen HFSB-Percentage of Applied Force at Longitudinal Locations 258

Figure Page

A4.15 Specimen LFAC-Percentage of Applied Force at Transverse Locations 259

A4.16 Specimen LFAC-Percentage of Applied Force at Longitudinal Locations 259

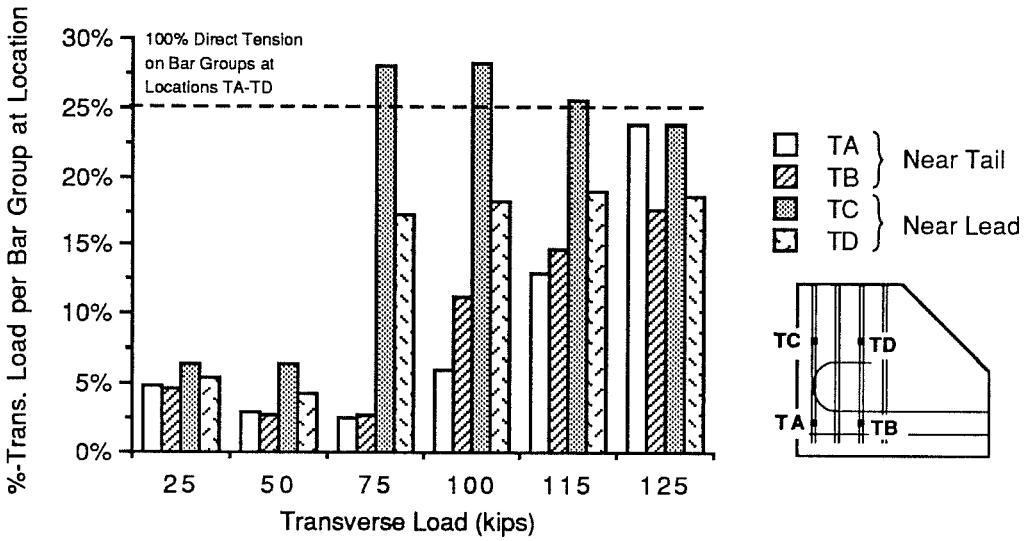

Fig. A4.1 Specimen HFSR-A-Percentage of Applied Force at Transverse Locations

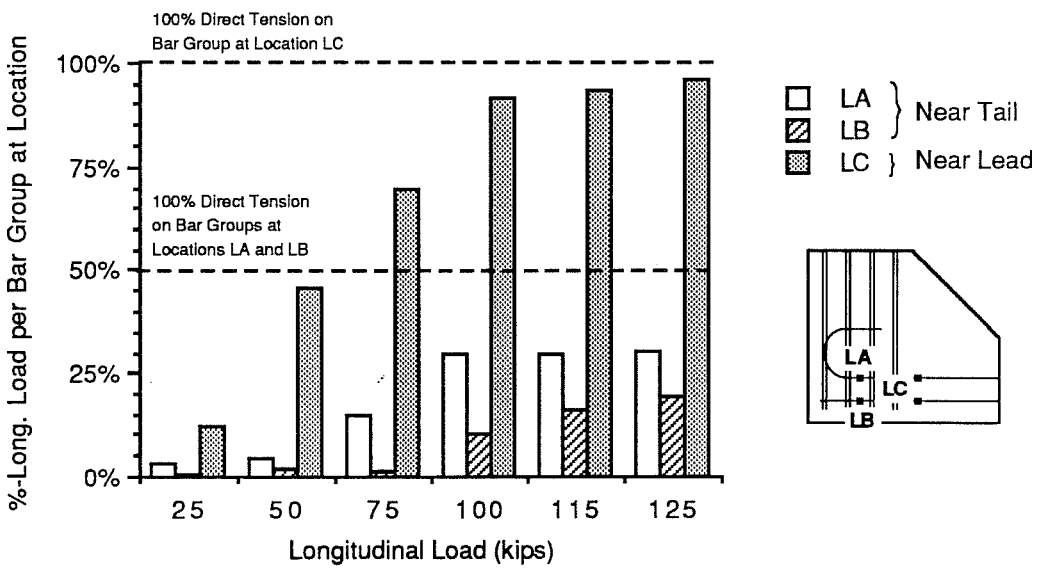

Fig. A4.2 Specimen HFSR-A-Percentage of Applied Force at Longitudinal Locations

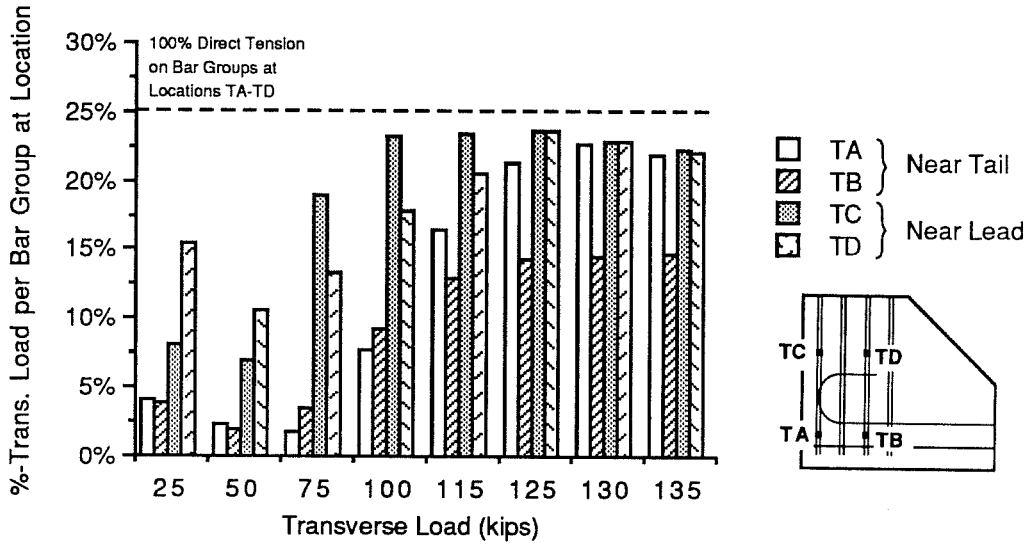

Fig. A4.3 Specimen HFSR-B-Percentage of Applied Force at Transverse Locations

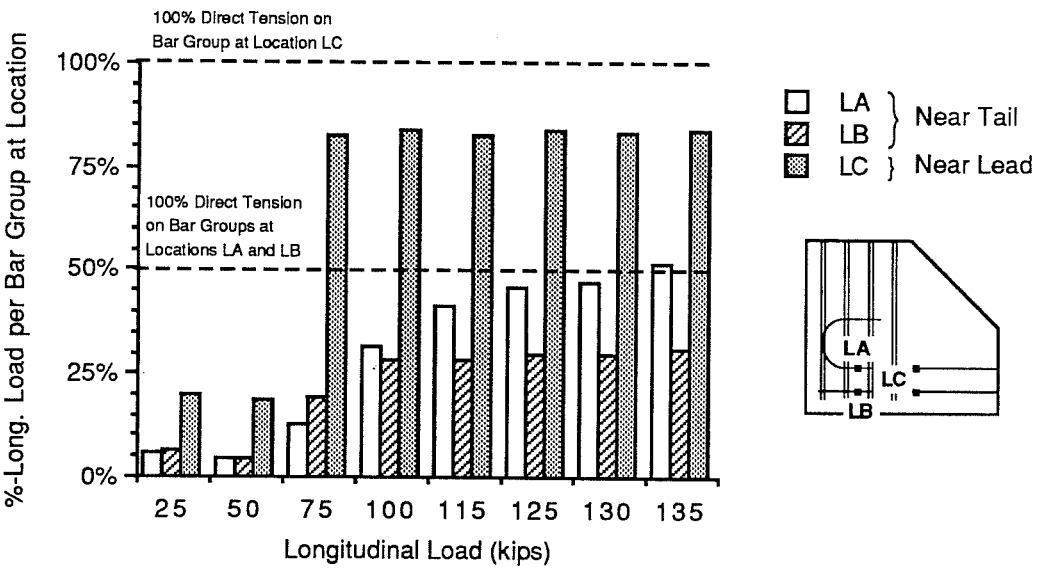

Fig. A4.4 Specimen HFSR-B-Percentage of Applied Force at Longitudinal Locations

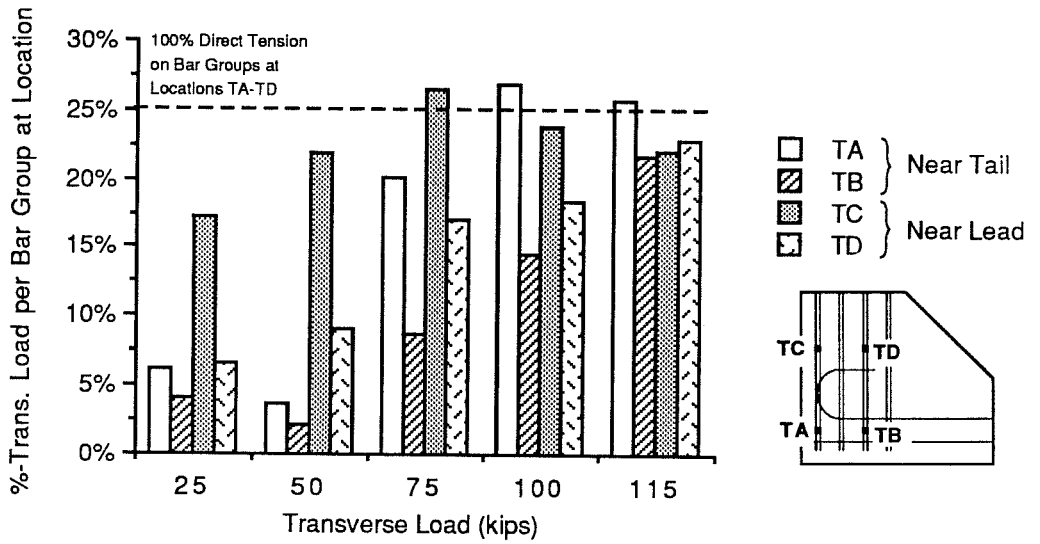

Fig. A4.5 Specimen LFSR-Percentage of Applied Force at Transverse Locations

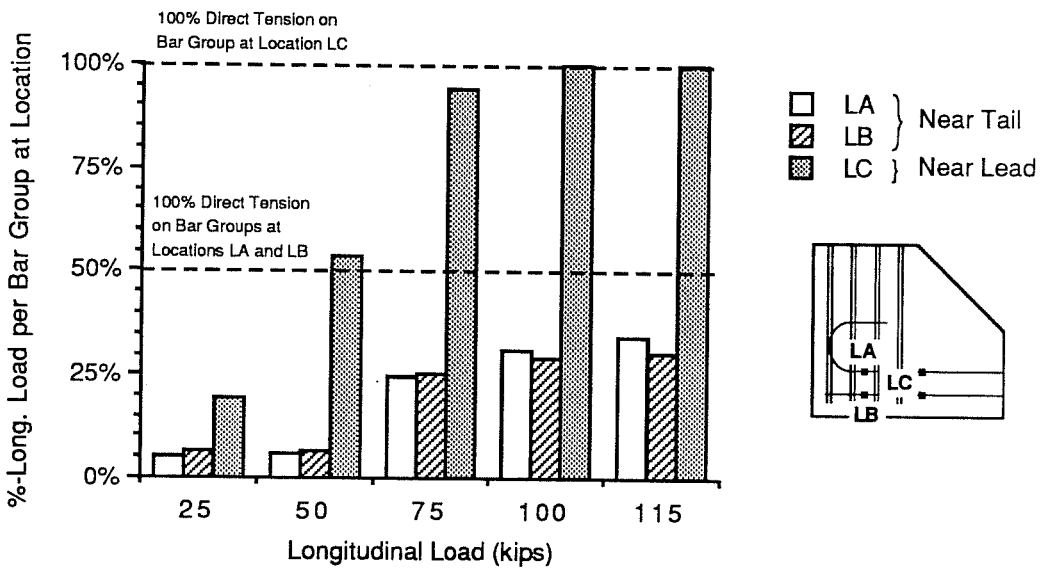

Fig. A4.6 Specimen LFSR-Percentage of Applied Force at Longitudinal Locations

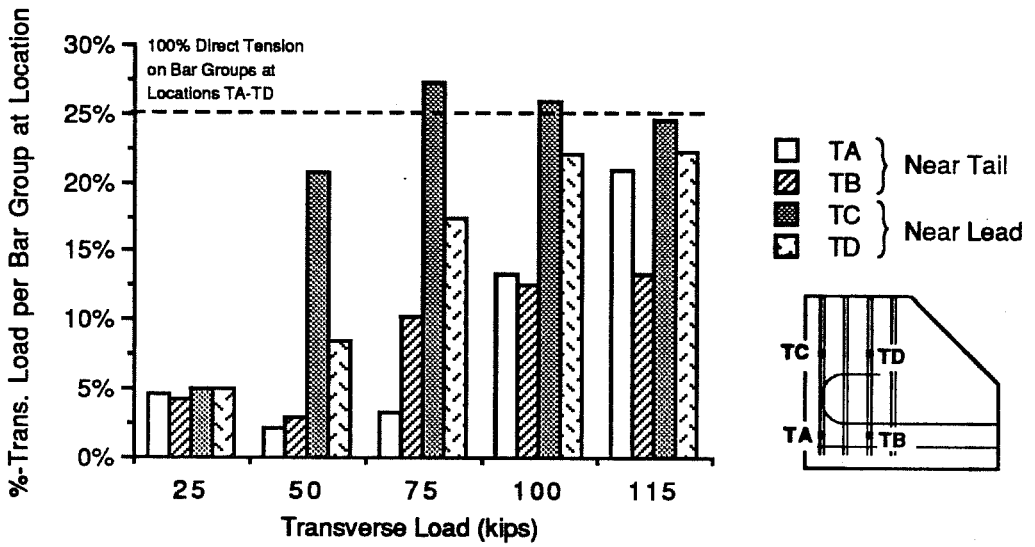

Fig. A4.7 Specimen LFNC-Percentage of Applied Force at Transverse Locations

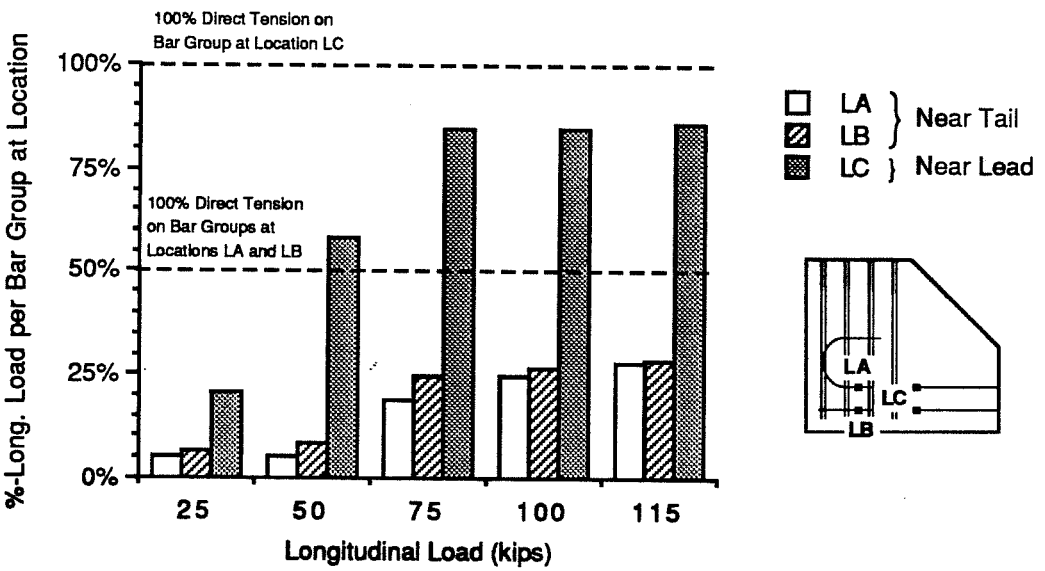

Fig. A4.8 Specimen LFNC-Percentage of Applied Force at Longitudinal Locations

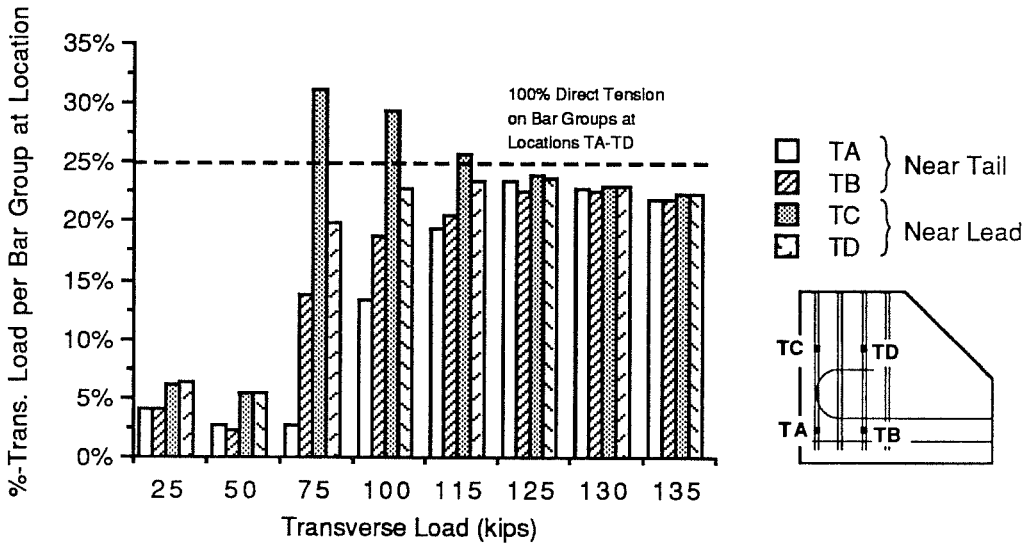

Fig. A4.9 Specimen HHSR-Percentage of Applied Force at Transverse Locations

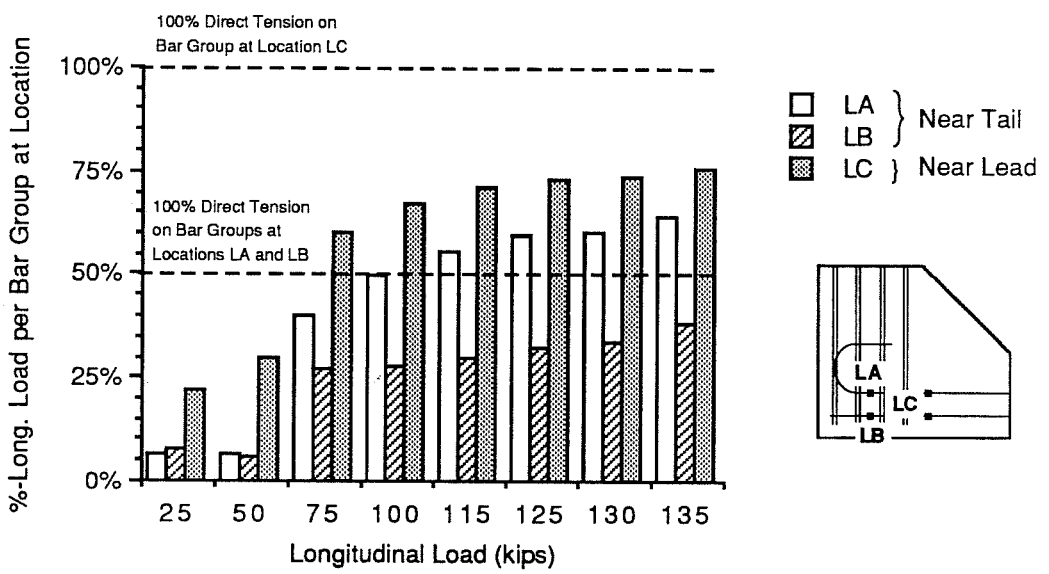

Fig. A4.10 Specimen HHSR-Percentage of Applied Force at Longitudinal Locations

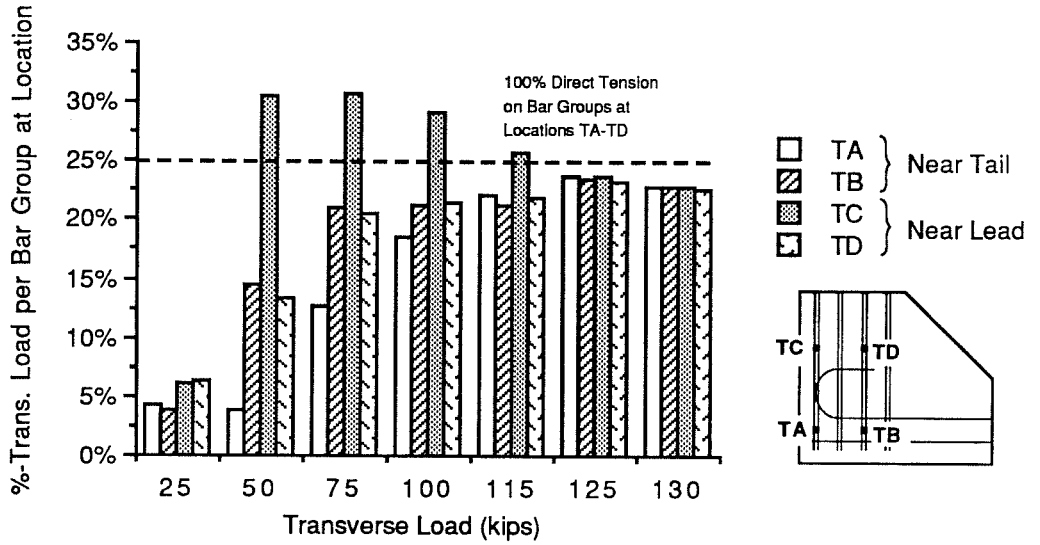

Fig. A4.11 Specimen LHSR-Percentage of Applied Force at Transverse Locations

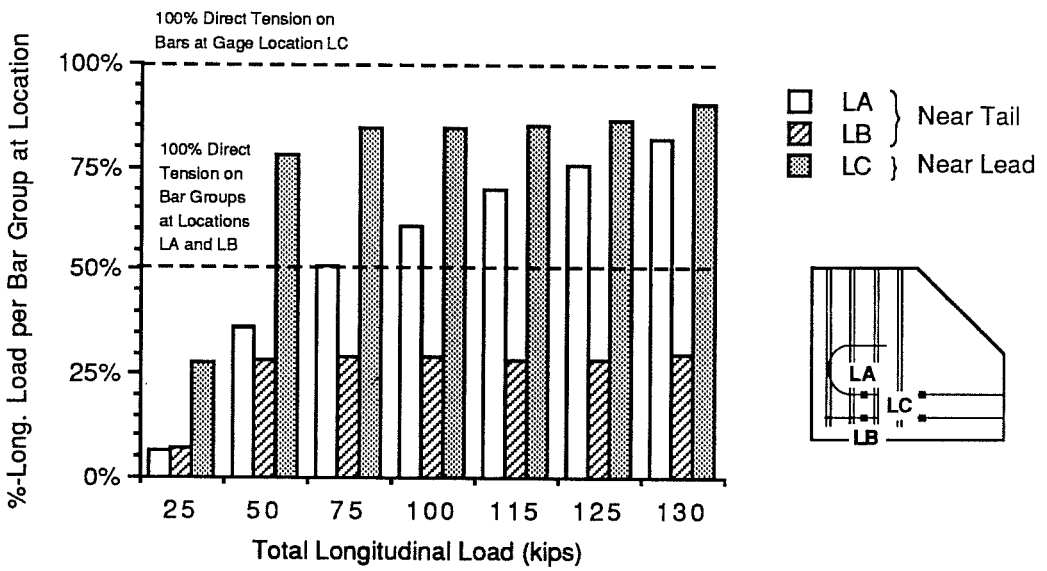

Fig. A4.12 Specimen LHSR-Percentage of Applied Force at Longitudinal Locations

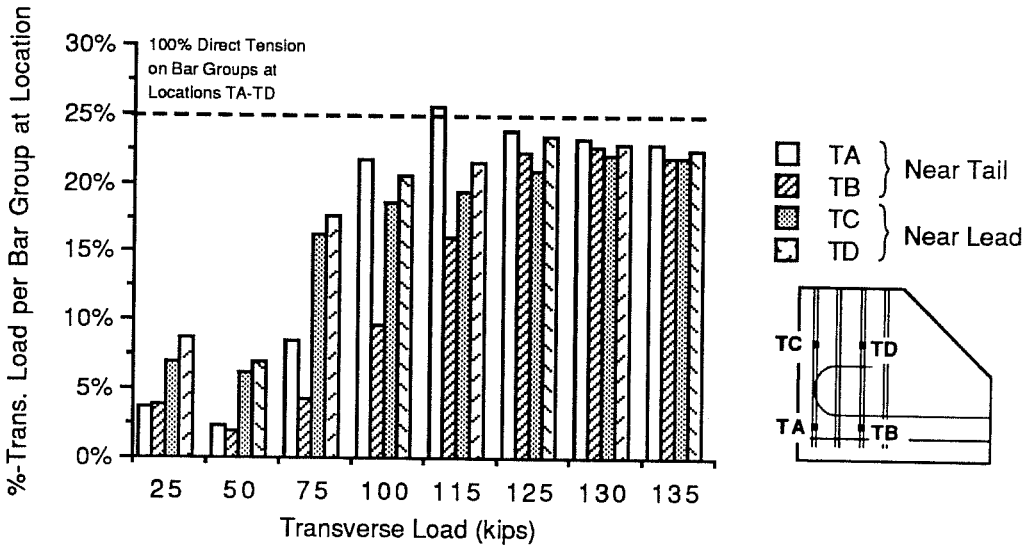

Fig. A4.13 Specimen HFSB-Percentage of Applied Force at Transverse Locations

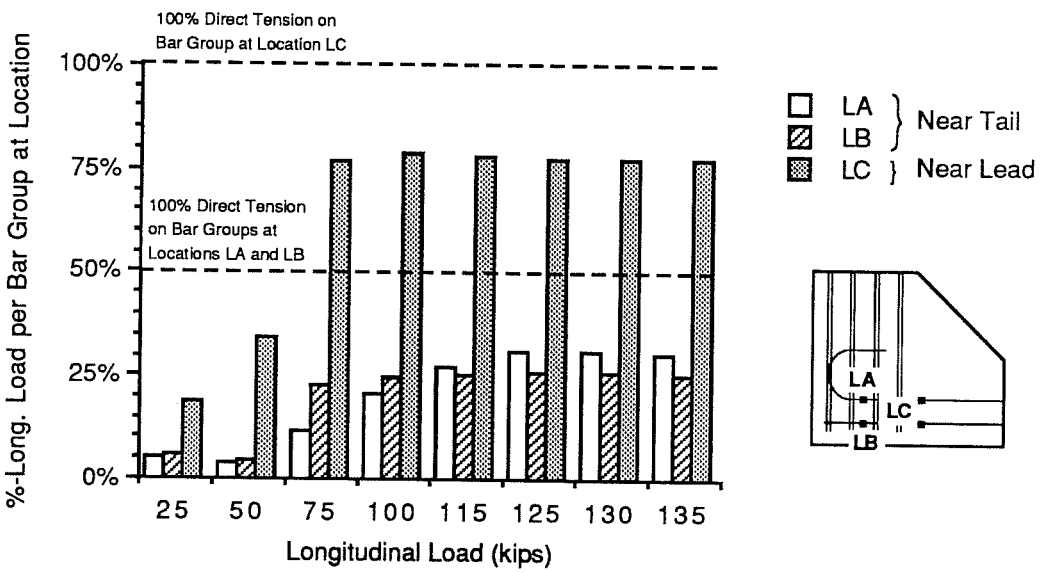

Fig. A4.14 Specimen HFSB-Percentage of Applied Force at Longitudinal Locations

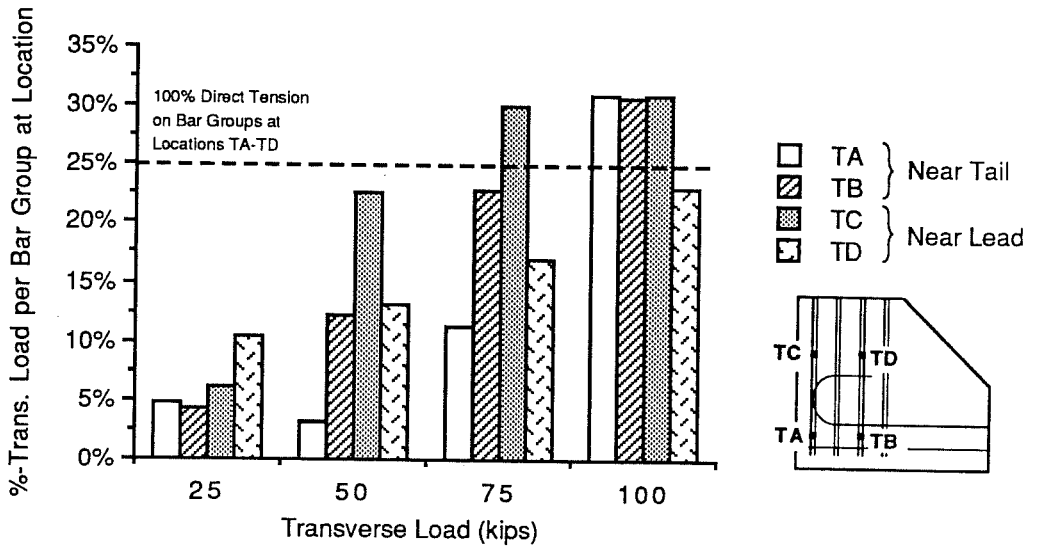

Fig. A4.15 Specimen LFAC-Percentage of Applied Force at Transverse Locations

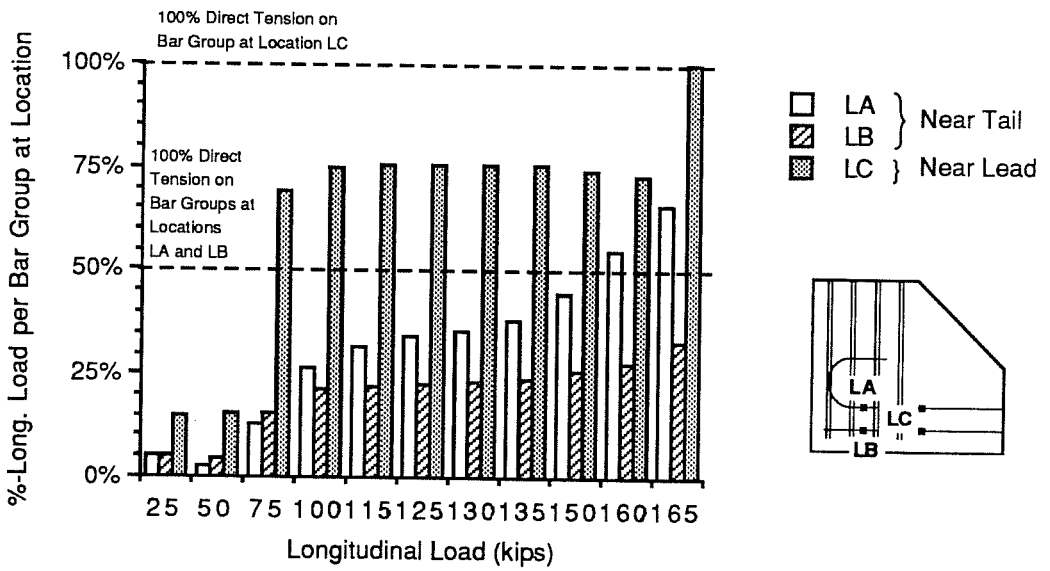

Fig. A4.16 Specimen LFAC-Percentage of Applied Force at Longitudinal Locations

VITA

Robert Bertram Anderson was born in Yankton, South Dakota, on January 9, 1961, the son of Curtis Lemoyne Anderson and Esther Newman Anderson. After completing his work at Viborg High School, Viborg, South Dakota, in 1979, he entered South Dakota State University in Brookings, South Dakota. He received the degree of Bachelor of Science in Civil Engineering from South Dakota State University in May, 1983. During the following year he was employed as a junior engineer for Northland Engineering and Land Surveying, Worthington, Minnesota. Subsequently, he was employed as a sales engineer for Kolberg Manufacturing, a subsidiary of Portec, Incorporated, Yankton, South Dakota. In August, 1986, he entered The Graduate School of the University of Texas at Austin.

Permanent Address: Rural Route 1 Box 124
Viborg, South Dakota 57070

This thesis was typed by Robert B. Anderson.